FACULTÉ DES ÉTUDES SUPÉRIEURES ET POSTDOCTORALES

uOttawa

L'Université canadienne
Canada's university

FACULTY OF GRADUATE AND POSTDOCTORAL STUDIES

Richard Gregory Green
AUTEUR DE LA THÈSE / AUTHOR OF THESIS

Ph.D. (Chemistry)
GRADE / DEGREE

Department of Chemistry
FACULTÉ, ÉCOLE, DÉPARTEMENT / FACULTY, SCHOOL, DEPARTMENT

Investigation of the Yttria Stabilized Zirconia (100) Surface by X-ray Photoelectron Spectroscopy and Scanning Probe Microscopy: Development of a Model Catalyst Support

TITRE DE LA THÈSE / TITLE OF THESIS

J. Giorgi
DIRECTEUR (DIRECTRICE) DE LA THÈSE / THESIS SUPERVISOR

CO-DIRECTEUR (CO-DIRECTRICE) DE LA THÈSE / THESIS CO-SUPERVISOR

EXAMINATEURS (EXAMINATRICES) DE LA THÈSE / THESIS EXAMINERS

D. Bryce

P. Mayer

E. Lai

P. Rowntree

Gary W. Slater
Le Doyen de la Faculté des études supérieures et postdoctorales / Dean of the Faculty of Graduate and Postdoctoral Studies

Investigation of the Yttria Stabilized Zirconia (100) Surface by X-ray Photoelectron Spectroscopy and Scanning Probe Microscopy: Development of a Model Catalyst Support

by
Richard Gregory Green
Two Mountains, QC

Thesis submitted to the
Faculty of Graduate and Postdoctoral Studies
In partial fulfillment of the requirements
For the PhD degree in Physical Chemistry
Department of Chemistry
Faculty of Science

Library and Archives Canada

Published Heritage Branch

395 Wellington Street
Ottawa ON K1A 0N4
Canada

Bibliothèque et Archives Canada

Direction du Patrimoine de l'édition

395, rue Wellington
Ottawa ON K1A 0N4
Canada

Your file Votre référence
ISBN: 978-0-494-59502-2
Our file Notre référence
ISBN: 978-0-494-59502-2

NOTICE:

The author has granted a non-exclusive license allowing Library and Archives Canada to reproduce, publish, archive, preserve, conserve, communicate to the public by telecommunication or on the Internet, loan, distribute and sell theses worldwide, for commercial or non-commercial purposes, in microform, paper, electronic and/or any other formats.

The author retains copyright ownership and moral rights in this thesis. Neither the thesis nor substantial extracts from it may be printed or otherwise reproduced without the author's permission.

AVIS:

L'auteur a accordé une licence non exclusive permettant à la Bibliothèque et Archives Canada de reproduire, publier, archiver, sauvegarder, conserver, transmettre au public par télécommunication ou par l'Internet, prêter, distribuer et vendre des thèses partout dans le monde, à des fins commerciales ou autres, sur support microforme, papier, électronique et/ou autres formats.

L'auteur conserve la propriété du droit d'auteur et des droits moraux qui protège cette thèse. Ni la thèse ni des extraits substantiels de celle-ci ne doivent être imprimés ou autrement reproduits sans son autorisation.

In compliance with the Canadian Privacy Act some supporting forms may have been removed from this thesis.

While these forms may be included in the document page count, their removal does not represent any loss of content from the thesis.

Conformément à la loi canadienne sur la protection de la vie privée, quelques formulaires secondaires ont été enlevés de cette thèse.

Bien que ces formulaires aient inclus dans la pagination, il n'y aura aucun contenu manquant.

Canada

To God for making the laws worth studying

To my parents for raising me to care

To my beloved and exceptional wife Ruth-Ann

for her unwavering support and kindness at every step

And to our daughter Julia Ruth Green for

being the best reason to just get it done

Table of Contents

List of Figures

Chapter 1

Chapter 2

Chapter 3

Chapter 4

Chapter 5

List of Tables

Chapter 2

Chapter 3

Chapter 5

Legend

Acronyms and Abbreviations

AFM – Atomic Force Microscopy

ASTM – American Society for Testing and Materials

Auger – Auger spectroscopy

BE – Binding Energy

HOPG - Highly Ordered Pyrolytic Graphite

LDOS – Local Density of States

LEED – Low Energy Electron Diffraction

LEIS – Low Energy Ion Spectroscopy

NIST – National Institute of Standards and Technology (USA)

PSD – Position Sensitive Diode

RGA – Residual Gas Analyzer (Mass Spectrometer)

SPM – Scanning Probe Microscopy

STM – Scanning Tunneling Microscopy

STS – Scanning Tunneling Spectroscopy

TDS – Thermal Desorption Spectroscopy

TPB – Triple Phase Boundary

TPD – Temperature Programmed Desorption

UPS - Ultraviolet Photoelectron Spectroscopy

XPS – X-ray Photoelectron Spectroscopy

YSZ – Yttria Stabilized Zirconia

Symbols

E_K - Electron kinetic energy

E_p - Pass energy of an electron analyzer

E - Energy

E_f - Fermi level (energy)

h - Planck Constant

d – Size (width) of tunneling gap in STM

v – Frequency

$h\nu$ – Photon energy

WF or Φ – Work function

Φ_b - Potential barrier between tip and sample in scanning tunneling microscopy

Φ_1 - Work function of STM tip

Φ_2 - Work function of sample

$\psi()$ - Quantum mechanical wave function

BE – Binding Energy

n- number of atoms or particles

I – Intensity or peak area

f – Photon flux

σ - Photoelectric cross section

θ - An angle dependent correction factor related to the geometry between the excitation photon path and that of the detected electrons

y - The efficiency of the photoexcitation process

λ_e - Electron mean free path

A - Sample area from which photoelectrons are detected

T or $T(E_K)$ - Transmission function of the electron analyzer

τ_{AM} - Response time of cantilever to surface forces in amplitude modulation mode

τ_{FM} - Response time of cantilever to surface forces in frequency modulation mode

Q – Q factor of an AFM cantilever

f_o – Resonance frequency of an AFM cantilever

φ - Phase shift between AFM drive signal and detection signal

k – Spring constant

a – Area of contact between the surface and an AFM tip

ε - Strain tensor

E^* - Reduced Young's modulus

S – Sticking coefficient

k_d – Desorption rate constant

z_{range} – Height scale of micrographs

v – Scanning probe (AFM/STM) scan speed in lines per second (l/s)

Abstract

Investigation of the Yttria Stabilized Zirconia (100) Surface by X-ray Photoelectron Spectroscopy and Scanning Probe Microscopy: Development of a Model Anode Support

Richard Gregory Green, Professor J.B. Giorgi, Advisor
University of Ottawa

Techniques and methodologies developed to reproducibly prepare and characterize yttria stabilized zirconia (YSZ) for use as a model catalyst support are presented. Analysis of a large number of YSZ(100) single crystals are examined by ambient atomic force microscopy (AFM), and x-ray photoelectron spectroscopy (XPS), in order to understand sources of variability and irreproducibility in the YSZ literature. The knowledge gained by ambient studies is then utilized to guide development of instrumentation and techniques to characterize YSZ under ultrahigh vacuum, and to prepare the (100) surface for self-consistent model catalyst studies.

In ambient conditions the complex interaction of impurities and defects are demonstrated to produce an inhomogeneous defect layer composed of stoichiometric and oxygen deficient regions. Introduction of oxygen vacancies modifies the lattice constant of YSZ, causing it to dewet and self organize at high temperature. Furthermore, stoichiometric and defective surface regions are shown to interact with metal deposited through e-beam evaporation in vastly different manners. Therefore variation in the defect layer can produce large dispersion in deposited metal location and dimension.

In-situ UHV scanning tunneling microscopy (STM) is used for the first time to study the surface of a bulk YSZ single crystal, images are presented in combination with XPS results. These techniques are used to characterize surface impurities and their interaction with YSZ. Cationic impurities are shown to accumulate at the upper surface region, but can be removed by heating to approximately 450 °C, whereas silicon requires heating to at least 900 °C. Carbon is found to react with YSZ(100) in complicated ways. Initial defect structure, in the form of oxygen vacancies and solubilized/surface carbon, can provide the conditions at elevated temperature to allow the reduction of zirconia to zirconium carbide. This carbide may be removed, along with the specific defect structure that provides the pathway for carbide formation, through thermal oxidation. STM shows that the clean and stoichiometric YSZ(100) surface may reconstruct under tip induced or thermally reductive conditions to form large clusters. With the removal of kinetic hindrance through heat, the clusters can self organize in a manner similar to that observed in ambient conditions.

Acknowledgments

I would like to thank Javier Giorgi for the opportunities he has provided, his helpful guidance, and long enduring patience. He has acted as the voice of experience, providing the right words, attitude and direction through my long and difficult growth into a surface scientist and UHV experimentalist.

I would like to thank Sander Mommers and the Mayer lab for their constant willingness to help with instrumentation and to lend parts to help me do the work.

I am grateful to the support staff at the University of Ottawa especially Ian Myers for his work with our electronics needs, from repair to building circuits, and for supplying the vast number of components I've required at one time or another. Ian has been extremely generous with his time and I have acquired a much better understanding of electronics as a result.

I would also like to thank my lab-mates especially Catherine Grgicak, and Shiliang Wang. Through discussions and work with Catherine I have escaped the vacuum from time to time and developed a good knowledge of the "real" solid oxide fuel cell world. Shiliang is patient and I've learned from example.

I would also like to thank my friends in Ottawa for letting me sleep in their basement, on their couch, or in their spare bedroom for extended periods when I couldn't make it home. The lab floor is a cold and unhealthy place at 3 am.

Finally, I would like to thank my brother Daniel C. Green for being excited enough about my thesis to want to be in the acknowledgments.

1. Introduction

1.1. Motivation: Solid Oxide Fuel Cell

Solid oxide fuel cells (SOFCs) [1-4] are electrochemical devices that convert chemical energy to electrical energy with high efficiency. Fuel cells in general are known for their applicability as clean energy devices since they may produce electricity through conversion of hydrogen to water, without any additional byproducts. SOFCs in particular have the added flexibility of operating with other fuels, such as hydrocarbons, with much higher efficiencies than conventional energy sources. SOFCs are therefore considered to be a bridging technology between the current oil based economy and one fueled by hydrogen.

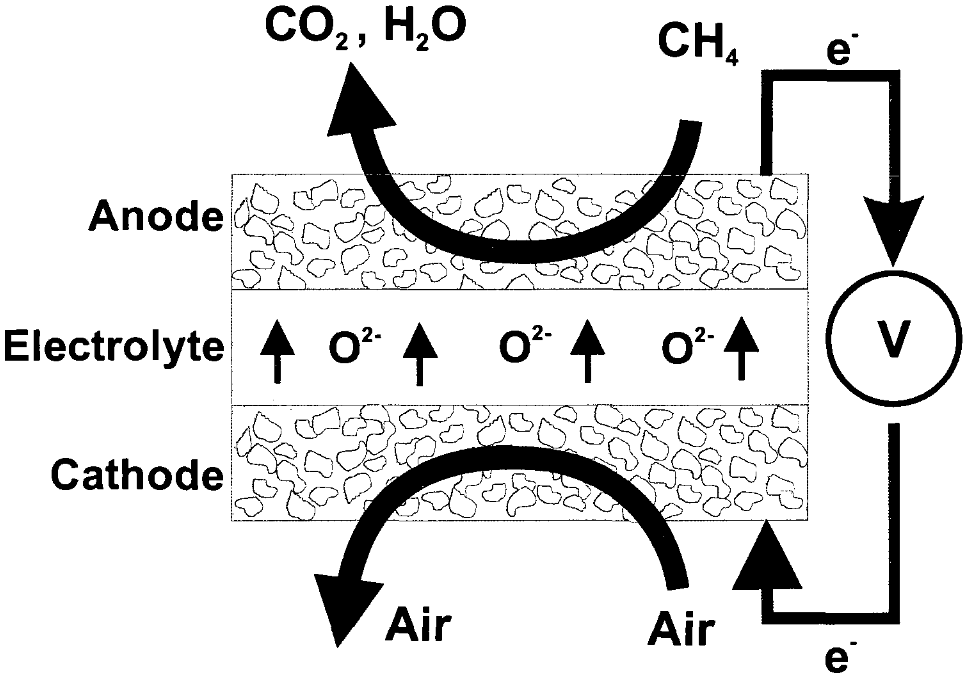

Figure 1-1 *Diagram of a solid oxide fuel cell. Oxygen is reduced to* O^{2-} *at the cathode which then diffuses across the ionically conductive electrolyte to the anode where fuel is oxidized by the ions, producing electricity and byproducts. Here the fuel is shown to be methane for which the byproducts are* CO_2 *and* H_2O*, instead* H_2 *may be used as fuel resulting in the formation of water only.*

A solid oxide fuel cell is made up of three main components; the anode, electrolyte, and cathode, as shown in Figure 1-1. Oxygen ions (O^{2-}) are produced at the cathode through the reduction of O_2. The ions are driven by their chemical potential across the dense electrolyte barrier to the anode where they oxidize the fuel, liberating electrons and producing a potential difference across the device. The electrons produced may be used to power a load as they return to the cathode. The cathodic half reaction is the reduction of O_2:

$$\frac{1}{2}O_2 + 2e^- \Leftrightarrow O^{2-}$$

For SOFCs converting hydrogen the anodic half reaction is:

$$H_2 + 2O^{2-} \Leftrightarrow H_2O + 2e^-$$

The overall reaction across the device is:

$$H_2 + \frac{1}{2}O_2 \Leftrightarrow H_2O$$

The electrolyte for which the solid oxide fuel cell is named, is a metal oxide that is capable of high ionic conductivity. The most common electrolyte used in commercial SOFCs is yttria stabilized zirconia, which is formed by doping ZrO_2 with Y_2O_3. For each yttria molecule substituted into the lattice one oxygen vacancy is produced. Doping to high levels provides a sufficient concentration of vacancies that oxygen ions may hop from one to another and conduct through the material. Even with the high level of vacancies, sufficient ionic conductivity for SOFC operation is only achieved at temperatures greater than approximately 800 °C. This places a major limitation on the types of materials which may be used to construct the fuel cell.

Both electrodes are normally composed of porous oxides interspersed with catalytically active particles which serve to both catalyze the reaction and to provide the necessary electrical conductivity. Conventional cathodes operate with strontium-doped lanthanum manganite (LSM),[5] while the anodes typically use nickel.[6] Both are supported within a porous YSZ matrix which provides thermal expansion matching to the electrolyte necessary for high temperature operation.

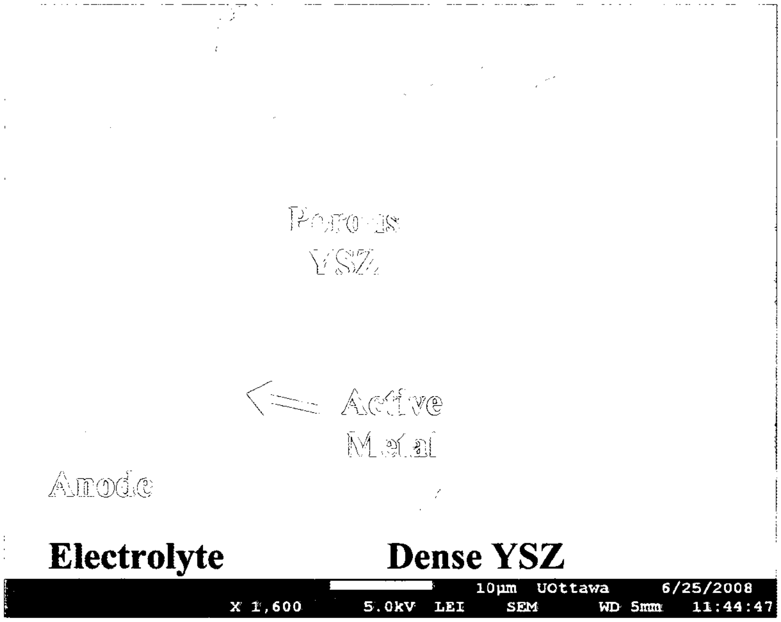

Figure 1-2 *A scanning electron micrograph of the anode-electrolyte interface. The porous YSZ supports catalytically active metal particles.*[*]

Figure 1-2 shows a micrograph of a porous anode sintered to a dense YSZ electrolyte. It is at the triple phase boundary (TPB) between the active metal particles, the YSZ support and the gas phase fuel that the anode reaction occurs. Techniques that may be used to study the reaction are hindered by its location buried within the anode material, and so investigations are often limited to electrochemical or post operation studies. Due to the

---

[*] SEM images acquired by Julie O'Brien, from materials based on synthesis by Catherine Grgicak; both are current or former members of the Giorgi lab.

complexity of the fuel cell system, in which electrical, catalytic, and micro-structural properties may all affect performance, it is difficult to deconvolute the action of many variables by these techniques alone. [6]

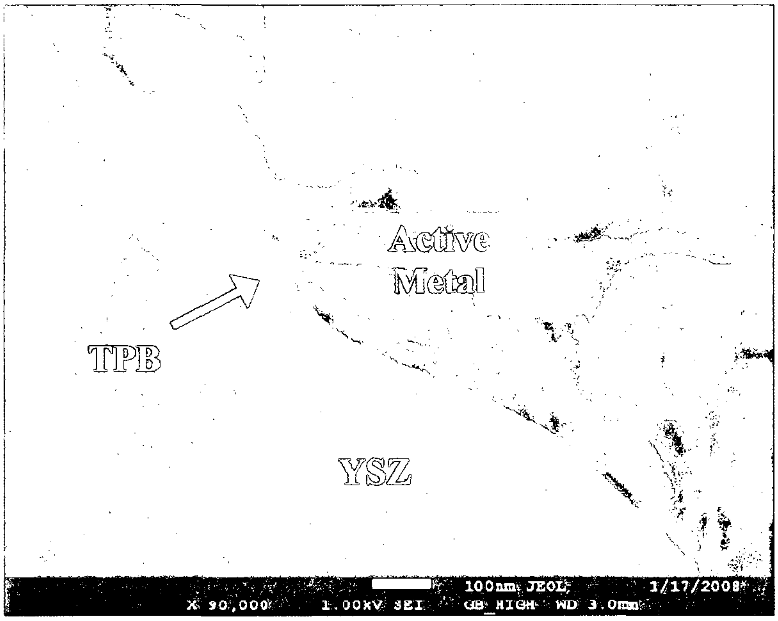

Figure 1-3 *Scanning electron micrograph of the anode of a solid oxide fuel cell. Both the YSZ and metal appear likely to be single crystals presenting morphological features of shaped steps and terraces indicative a thermodynamically stable state. The triple phase boundary (TPB) lies at the perimeter of the interface between the metal and YSZ.*[†]

While the fuel cell is complex it is not immune to reductionist methodologies. The chemical reactions which drive the fuel cell can be isolated from aggravating effects by reducing the system to the triple phase boundary uniquely. Figure 1-3 shows the TPB in a real fuel cell anode, it can be seen that at the most fundamental level it is composed of nano- or micro- particles of single-crystal YSZ and metal in contact. This interface can be recreated outside the fuel cell, by beginning with a YSZ single crystal support upon which is deposited an active metal to be studied. By this method a model catalyst is created which exposes the triple phase boundary to study by a vast array surface sensitive techniques.[7]

[†] SEM images acquired by Julie O'Brien, from materials based on synthesis by Catherine Grgicak; both are current or former members of the Giorgi lab.

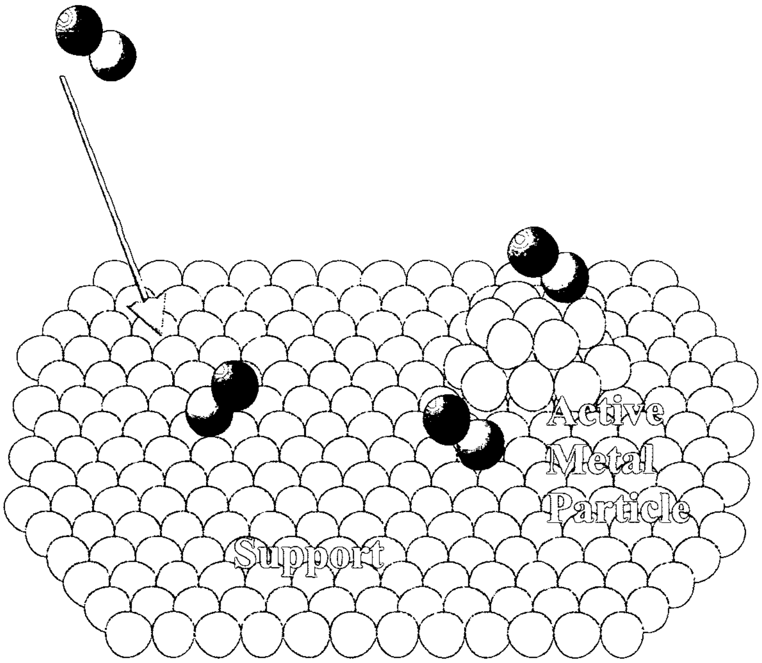

Figure 1-4 *Schematic of a model catalyst in which metallic clusters have been deposited on a single crystal substrate. Molecules from the gas phase are seen interacting with both the support and metal. The model catalyst recreates the triple phase boundary seen in real heterogeneous catalysts.*

G. Ertl has been credited with first applying surface science studies, previously reserved for the semiconductor industry, to investigations of catalysis.[8] For this transfer and his studies of the Haber cycle he was awarded the 2007 Nobel prize in chemistry.[9] Beginning in the 1960's, the focus of most research was on the investigations of catalysis on metal single crystals,[10-16] the field of model catalysts has since grown into more complicated systems including oxide single crystals or thin films grown on metal, as well as studies of metal particles deposited on oxides.[17-21]

Surface science techniques [7, 22, 23] rely upon relatively low energy probe ions, electrons, or photons that allow surface regions to be studied while being insensitive to the bulk. The particles derive their surface sensitivities from the fact that they are scattered very quickly as they penetrate into, or derive from depths of more than a few nano-metres within a solid. This low mean free path also forces studies be performed under vacuum, where the particles can move from source to sample to detector without being scattered by gas phase molecules. Though some techniques may be performed at pressures a few orders of magnitude higher, pressures are often on the level of ultra high vacuum (less than $1\text{x}10^{-9}$ mbar), where the surface under study can be cleaned of contaminant adsorbates. Such adsorbates, for example water or hydrocarbons, normally provide full coverages in ambient conditions and may interfere with characterization of sample properties. Once removed the low pressures prevent further adsorption of contaminant species for an extended time scale derived from the relationship:

$$\frac{d\theta_s}{dt} = \frac{SP}{\sqrt{2\pi m k_b T}} - k_d \theta_s$$

Where θ_s represents the coverage of adsorbates on the surface, S represents the sticking coefficient (probability that a molecule impinging on the surface will adsorb), k_d is the desorption rate and P and T are the gas phase pressure and temperature respectively. Therefore the rate of coverage formation decreases linearly with pressure so that depending on the identity of the gas, one monolayer will form at 1×10^{-6} mbar in a few seconds, while only a sub-monolayer will form over several hours at 1×10^{-10} mbar.[23] Moreover, because the ultra high vacuum chamber is equivalent to a sealed system, the gas phase environment can be modified and the sample exposed to only those gases which are intentionally allowed into the chamber.

The overarching advantage of studies in UHV is in theory total control, and characterization by techniques supplying fundamental information about the system under study. These techniques may include low energy electron diffraction (LEED), which provides surface crystal structure, X-ray/ultra violet photoelectron spectroscopy (XPS/UPS) which yields chemical and valence level information. Catalytic details such as adsorption sites and energies can obtained from methods utilizing mass spectrometry which measures mass to charge ratios of ionized gas phase molecules. Even high resolution imaging from scanning probe (AFM/STM) or electron microscopies can be performed to yield local topographical features down to the atomic scale.

By combining many surface sensitive techniques in one UHV chamber, a full gamut of complementary experiments can be performed on the same sample in an extremely controlled manner. For studies of model fuel cell catalysts such control initially entails production of an ideal support surface, in this case YSZ, which is free of contaminants and is atomically flat. Though all surfaces will contain a concentration of defects, their action should be well understood. Only when the support surface is fully characterized and reproducible should catalytically active metal be deposited since the support is well known in other systems to interact with the active metal. [19-21]

In this thesis the YSZ(100) single crystal is investigated for its use as a support in model fuel cell catalysts. With specific emphasis on development of a model anode, initial studies on the chemistry and topography of YSZ(100) outside of UHV provide insight into the parameters that are necessary for studies in UHV. Techniques and methodologies are developed from this information, which are exploited to study the segregation, reduction and oxidation behaviour of YSZ under the conditions required to reproducibly build the model anode catalyst.

1.2. Yttria Stabilized Zirconia (100)

The zirconium dioxide crystal structure at room temperature is monoclinic, at elevated temperatures the lattice undergoes a series of phase transitions changing geometries first to tetragonal, then to cubic above 2300 °C.[24] Beginning at concentrations near 4.5 atom %, doping zirconia with yttria (Y_2O_3) stabilizes the lattice in the cubic phase while at the same time introducing oxygen vacancies which increase its oxygen ionic conductivity. Commercial fuel cells typically use YSZ doped to concentrations between nine and ten percent, since it is within the range that ionic conductivity is maximized.[25]

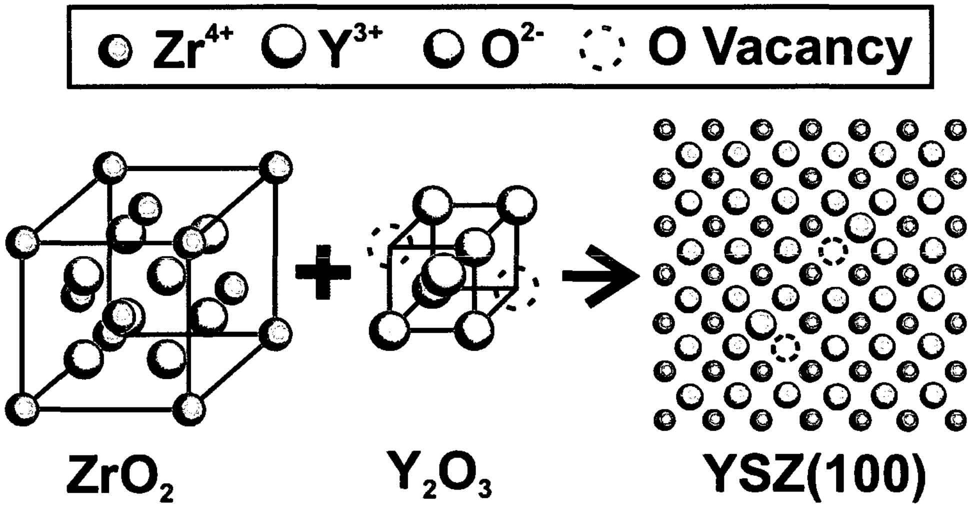

Figure 1-5 *The fluorite crystal structure of cubic zirconia and yttria. The direct substitution of the yttria in to the zirconia lattice results in the introduction of one oxygen vacancy per dopant. The YSZ(100) surface is shown, here the surface is terminated with oxygen.*

As shown in Figure 1-5, in the fully stabilized phase YSZ takes a fluorite structure which is comprised of a Zr^{4+} face centred cubic lattice in which oxygen ions are tetrahedrally coordinated with each zirconium ion. Yttria is also face centred cubic but it is not fully coordinated with oxygen, instead oxygen vacancies occupy the remaining lattice sites. Yttria directly substitutes into the zirconia lattice, with Y^{3+} occupying Zr^{4+} positions. In Figure 1-5 the (100) plane is shown with the oxygen vacancies still directly coordinated to yttrium; several modeling and experimental studies have shown that this is not necessarily so, with vacancies preferring to be 2nd nearest neighbor to yttrium.[26-29] Moreover the termination here is shown to be with a full layer of oxygen, however it remains controversial, with some models showing the surface layer to be oxygen deficient.[30] This makes some sense since the (100) surface, if fully oxygen or zirconium terminated, would be polar. Such surfaces are very prone to reconstruction since the energy cost associated with maintaining spatially separated charge is high.[31, 32]. While other surface terminations may be more stable, (110) for example, they are also more prone to segregation of yttrium.[30]

YSZ is by no means a simple system; aside from intentional doping, impurity atoms of several elements have been shown to be present. Depending on the study, various combinations of a few or many elements such as Ca, Na, Mg, Ti, Hf, Si amongst others may be present.[33-51] These impurities may segregate to the surface producing surface space charge that modifies the local properties of YSZ. Interaction with native YSZ elements are possible and co-segregation of YSZ with silicon has been reported.[41, 42] Aside from segregation, defects such as F-centres (oxygen vacancies), which may be neutral (2 electrons occupying a vacancy), doubly or singly ionized, can be produced by several methods. Thermal reduction [52-54], as well bombardment by ions [52, 55, 56], photons,[57] and electrons[52, 56, 58] can result in defect formation. Moreover at high enough concentration the interaction between these defects becomes important.[59, 60] Since it is often necessary to expose YSZ to some of these conditions during experimentation, efforts should be made to characterize their effects, and caution exercised in interpreting results.

The culmination of the complexity and dynamicity of the YSZ surface can be reflected in the sample history dependence of results in YSZ studies. Samples prepared in nominally different fashions can exhibit different properties. In a twelve part series by Nowotny *et. al.* on the YSZ biphase (interface with the gas phase in the absence of metal),[44, 61-71] the properties of YSZ have been extensively reviewed. One of the conclusions was:

> "Comparison of the data and models reported in different studies is problematic because there is a lack of uniformity in specimen properties, such as composition (including impurity level), microstructure, experimental procedure..."[62]

It is therefore of critical importance to produce a well characterized and reproducible surface, so that experimental results may transfer to different studies. Where the systems are dissimilar the factors which will be affected by these differences should be known. However Nowotny continues :

> "This issue, however, is very difficult to incorporate into a quantitative assessment of this aspect of a complete characterisation..."[62]

Currently, what comprises a well characterized sample is still unclear. It is within the scope of this work to determine some of the properties which are required to be controlled in order to produce a truly characterized surface for model catalyst studies. The goal of this thesis to understand which YSZ properties can modify its behaviour when used as a model catalyst support and to develop techniques to control these properties reproducibly.

1.3. Principles of Major Techniques

There are several extremely good books covering the instrumentation [7, 72], physics [23], and practical application of XPS [7, 23, 72-74], and therefore only a general description of the technique will be covered. The main focus of this section will be on the practical application of XPS especially as to how it will be used in studies of YSZ.

1.3.1. X-ray photoelectron spectroscopy

1.3.1.1. Introduction

X-ray photoelectron spectroscopy utilizes the photoelectric effect, first discovered by Heinrich Rudolf Hertz in 1887, to examine the kinetic energy distribution of photoelectrons emitted from core atomic levels of a material under study. The number of electrons detected (y-axis) at a specific kinetic energy (x-axis) make up a photoelectron spectrum. It was first brought into practical application by Kai Siegbahn (Nobel Prize 1981) beginning in 1954, when he developed the instrumentation to acquire high energy resolution spectra of NaCl. XPS enables identification of both atomic species as well as chemical bonding environments around these species.

An X-ray source producing photons with energies usually 1486.6 eV (Al anode) or less, are shone on the material to be studied[‡]. There is an element specific probability that an incident photon will be absorbed by an atom in the material, exciting a photoelectron whose energy can be detected. The energy analyzer (Figure 1-6) is comprised of a lens system, to electrostatically focus the electrons, a hemispherical analyzer to separate the electrons according to their energy, and a detector to count the number of photoelectrons of

---

[‡] The orientation of the source is optimally at a magic angle of $54^{\circ}44'$ relative to the entrance of the detection system.

that energy. This technique is surface sensitive since the inelastic mean free path of the photoelectron moving through a solid is typically on the order of nanometres. Therefore only electrons excited from atoms near the surface can be detected without collision. Since electrons will also interact with gas phase molecules, photoelectron spectroscopy must generally be performed at pressures of 1 x 10^{-5} mbar or lower§.

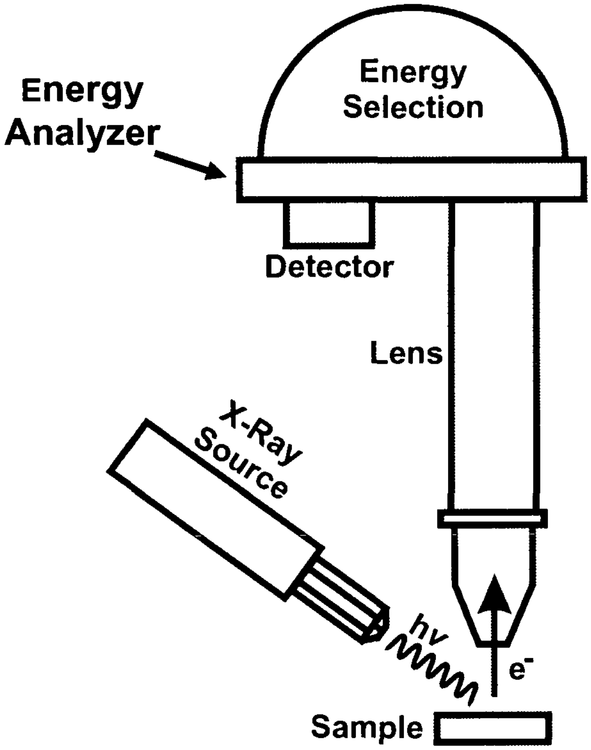

Figure 1-6 *Schematic of an x-ray photoelectron spectrometer. An x-ray source produces x-rays by bombarding an anode with high energy electrons. The anode emits x-rays of energy characteristic of the material from which it is made. The x-rays are directed towards a sample, which then emits electrons via the photoelectric effect. The electrons enter the lens system where they are focused to the entrance of the hemisphere which allows only electrons of a specific energy to pass to the detector. The energies which are allowed to pass may be scanned across a broad region so that a spectrum can be formed.*

---

§ A few synchrotron XPS end-stations allow higher pressures up to several mbar. The trick is to differentially pump the path of the photoelectrons such that they traverse the high pressure region for the shortest possible distance.

Nominally the kinetic energy of a photoelectron as derived from Koopman's theorem is given by:

$$KE = hv - BE - WF$$

Where KE is the emitted electron kinetic energy, hv is the energy of the incoming photon, BE is the binding energy or ionization energy of the given atomic orbital from which the photoelectron is emitted, and WF is the work function of the material. The equation above holds if the process is elastic, however there are many processes through which energy may be lost often resulting in broadening of characteristic electron energies, or production of separate "ghost" peaks [74]. Therefore some work is often needed for peak identification; fortunately many energy losses occur in a predictable manner for which there is precedence in the literature [74, 76]. An efficient introduction to peak identification is given by Moulder et al. [74], and amongst other phenomena, peak splitting due to spin-orbit coupling, mechanisms for electron energy losses (e.g. plasmon excitation), and satellite peaks resulting from incident photon energies off the main line, are discussed. This latter effect results in peaks shifted from the main chemical transitions by a value determined by the x-ray anode material in non-monochromated sources.

1.3.1.2. Information carried by electron energy: Chemical identification

When an electron is emitted elastically as a result of the photoelectric effect, the kinetic energy of the photoelectron is characteristic of the binding energy, or ionization energy of the atomic orbital from which the electron was excited. As is the case with *x-ray* photoelectron spectroscopy, the incident photon carries sufficient energy to excite core level electrons from one of several distinct orbitals of the atom. The electrons emitted from this set of orbitals therefore carry element specific information, that can be used to identify the atom from which they came. Moreover not only can elemental information be determined, but since valence bonding electrons can perturb the photoelectron energies, then characteristic elemental photoexcitation energies will be shifted from their elemental positions by an amount related to the bonding environment. As an example, electrons excited from the 3d orbital of zirconium in zirconia (ZrO_2) will have peak kinetic energies shifted approximately 3.7 eV lower than zirconium itself. This energy shift can be nominally related to the number of electrons that are more strongly correlated with the oxygen atom in the oxide, and less correlated with the zirconium, in this case four electrons.

A very simple expression of the binding energy shift is given by the charge potential model: [77]

$$\Delta BE = k(\Delta q) + \Delta V$$

Here the binding energy shift ΔBE at the core level of an atom varies linearly with the change in charge of that atom due to bonding, with the intercept given as the change in potential at the atom due to its neighbors. Both the Δq and ΔV terms show periodic trends (ΔV has atomic radius dependence), with equivalent compounds having decreasing binding energy shifts as one moves down a column. For ionic materials, ΔV is equivalent to the change in Madelung potentials between materials for which the shift is being determined.

1.3.1.3. Information carried by photoelectron flux: Quantification

Each atom within the measurement volume of XPS has some element specific probability of producing a photoelectron upon interaction with an x-ray. Therefore, the larger the number of atoms of that species the larger the number of characteristic electrons that will be produced. In XPS, spectra maxima are correlated to the elements from which they were produced based upon their positions in the binding energy scale. The maxima will have intensities related to the number of electrons detected and thus the number of atoms probed. For samples in which the analysis volume is homogeneous the number of atoms, n, can, in simplified from, be related to the detected signal according to: [74]

$$n = \frac{I}{f\sigma\theta y\lambda_e AT}$$

Here I is the number of photoelectrons detected per second for the given core line (peak area), f is the x-ray photon flux, σ is the photoelectric cross section of the core level orbital, θ is an angle dependent correction factor related to the geometry between the excitation photon path and that of the detected electrons (angle between source and analyzer), y is the efficiency of the photoexcitation process for the given transition, λ_e is the electron mean free path in the analyzed material, A is the sample area from which photoelectrons are detected and T is the transmission function of the analyzer, that is the efficiency with which the analyzer detects an electron of a specific energy.

Even if one were so inclined, the extreme difficulty in determining all the above parameters exactly is prohibitive, therefore perhaps more usefully, atomic ratios are determined instead. By this method, peak areas characteristic of an element in a compound are compared to peak areas of all other elements within the same compound. As a result the parameters *f*, *θ*, *A* fall off and the remaining factors can be incorporated into a single term called the relative sensitivity factor or RSF; a set of these factors for each element is often determined for each spectrometer. A more detailed discussion of relative sensitivity factors will be undertaken in chapter 2 but quantification in terms of atomic concentration *C* for the integrated intensities *I* of species *i* in a compound of *m* components can be given as:

$$C_i = \frac{n_i}{\sum_{j=1}^{m} n_j} = \frac{I_i / RSF_i}{\sum_{j=1}^{m} I_j / RSF_j}$$

This formula is used throughout this work to estimate atomic concentrations of the elemental components in YSZ.

1.3.1.4. Information carried by angular dependence of photoelectron spectrum: Depth profiling

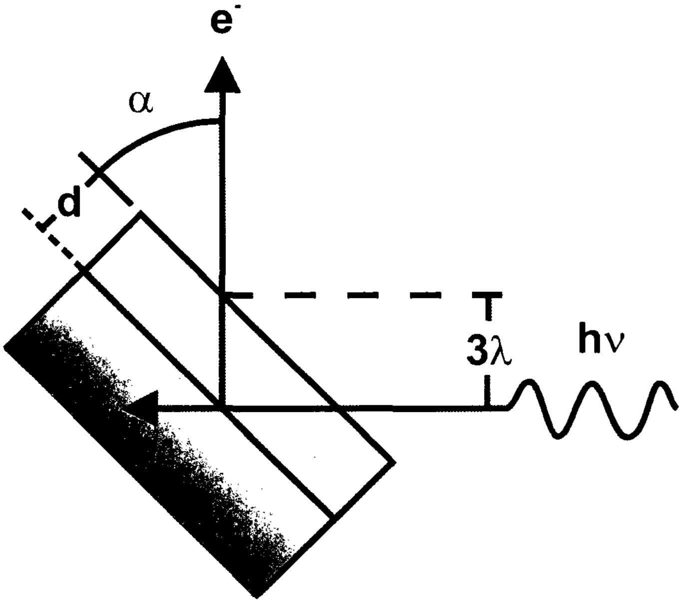

Figure 1-7 *Schematic of the enhanced surface sensitivity due to variation in the take off angle α. The smaller the angle the shorter the electron escape depth d as a result of an increase in the electron path length* $3\lambda_a$ *through the solid.[72]*

Since the mean free path of electrons in a material is finite, there is a higher probability that photoelectrons emitted from atoms closer to the surface will reach the detector before an inelastic collision with other atoms. Depending on the material this depth can be up to 10 nm. Briggs and Seah [72] have used the attenuation length λ_a of an electron in the material to be studied in the expression relating this depth *d* to the electron take off angle α:

$$d = 3\lambda_a \sin\alpha$$

From the Beer-Lambert law about 95% of the signal intensity originates from a distance $3\lambda_a$ within the material. For purely geometric reasons (Figure 1-7), increasing the sample angle, α, with respect to the analyzer, causes the depth (perpendicular to the surface) from which electrons are detected to decrease in proportion to sine of the angle (Figure 1-8)

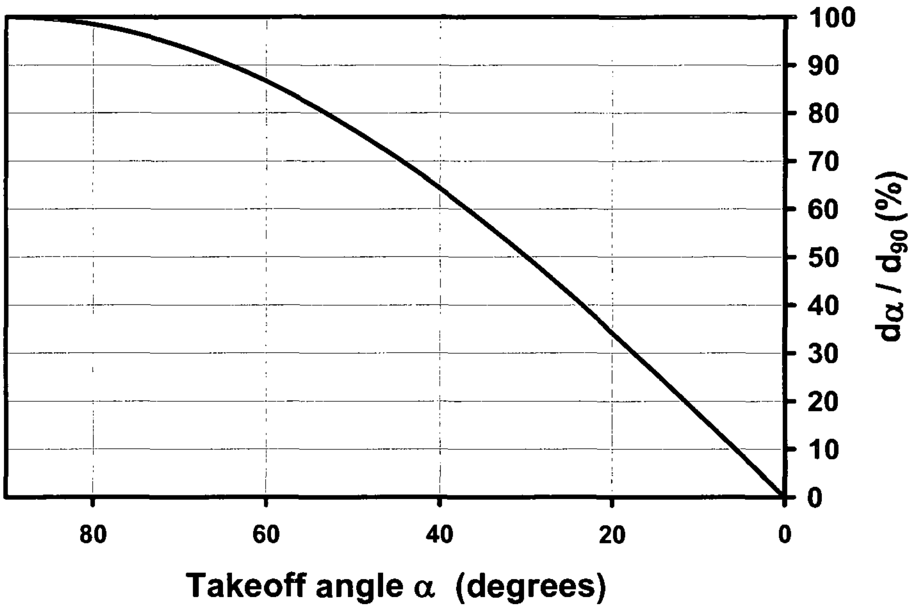

Figure 1-8 *Depth probed by XPS at a takeoff angle α as a percentage of the depth probed at a 90^o angle (electrons excited perpendicular to the surface). Ninety five percent of detected electrons originate from atoms within this depth.*

The attenuation length for photoelectrons has been found to be nearly equivalent to the inelastic mean free path (IMFP). Tanuma *et al.* showed that empirically measured attenuation lengths vary from calculated IMFPs by about 15%, probably within the systematic uncertainties of the attenuation length measurements.[78] This is extremely useful in practice since Powell and Jablonski have developed a database of experimental and calculated IMFPs [79], which can be acquired without charge from NIST upon request.[80] Less optimally there are a few other online resources which may be accessed which contain applets [81] or downloads [82] that can be used to determine IMFPs based upon equations from Seah [83, 84] or Powell [78, 85-90]. Figure 1-9 shows a partial screen shot of the applet from the former, in which the IMFP for ~13% YSZ is plotted as a function of electron kinetic energy .

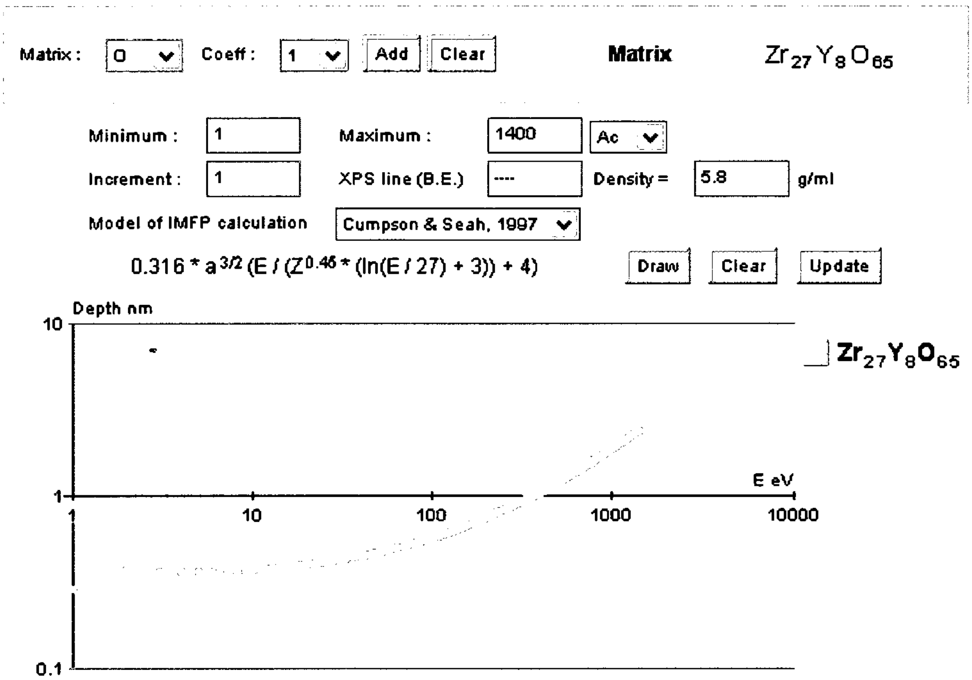

Matrix : 0
Coeff : 1
Matrix $Zr_{27}Y_8O_{65}$
Minimum : 1
Maximum : 1400 Ac
Increment : 1
XPS line (B.E.) ----
Density = 5.8 g/ml
Model of IMFP calculation Cumpson & Seah, 1997

$0.316 * a^{3/2} (E / (Z^{0.45} * (\ln(E / 27) + 3)) + 4)$

Figure 1-9 *Partial screen-shot of a plot of the electron inelastic mean free path in 13% YSZ as a function of electron kinetic energy.*

It can be seen that the inelastic mean free paths are strongly dependant upon the electron kinetic energy, with the IMFP decreasing with decreasing kinetic energy. It is for this reason that varying the excitation photon energy will also vary the probed sample depth, thus by decreasing this energy, surface sensitivity is increased.

Usually most XPS systems come equipped with an x-ray source containing a dual aluminum and magnesium anode which produces photons of 1486.6 and 1253.6 eV respectively. For analysis of the Zr $3d_{5/2}$ peak of YSZ (182.6 eV BE) this would produce kinetic energies for photoelectrons of 1304 eV for aluminum and 1071 eV for the magnesium sources. According to both Powel and Seah models, this results in a surface sensitivity improvement of 14% (100 x (1- d_{Mg}/d_{Al})).

Another method for depth profiling uses positive ion sputtering to etch the surface, and scans are performed at various etch depths. However under practical circumstances sputter yields for YSZ are not well known, and therefore etch depths can only be poorly estimated. Moreover ion bombardment is damaging and results in a non-equilibrium and non-stoichiometric surface due to preferential sputtering which may not well represent "true" YSZ. Understanding the effects of sputtering on the YSZ surface is a critical requirement for both depth profiling and for developing model catalysts, since it is often used to prepare "clean" samples. This has received some attention in this work and will be discussed in chapters 3 and 5 in more detail.

1.3.2. Scanning Tunneling Microscopy

Scanning tunneling microscopy (STM) is a type of scanning probe technique. It was first developed 1981 by Binnig and Rohrer [91] for which they won a Nobel prize in 1986. It exploits the quantum tunneling effect to measure the local density of states (LDOS) of a surface with high spatial resolution. In STM operation, a conductive tip and sample are brought in close proximity to each other so that when a voltage is applied between the two, electrons in the tip may tunnel across this small gap into the sample. If one then moves the tip to a new location this tunneling current will be found to change as a function of the sample's local electronic and topographical properties. By performing a raster scan across the sample the change in current can be mapped and an image formed. A more common implementation is to instead use the measured tunneling current to control the distance of the tip from the sample. As the tip is scanned laterally across the surface, a feedback circuit may adjust its height so that the measured tunneling current remains constant. Piezo-electric ceramics, which expand and contract by an amount related to the voltage difference applied across them, provide the highly precise movement required to scan and adjust the tip to sample height.

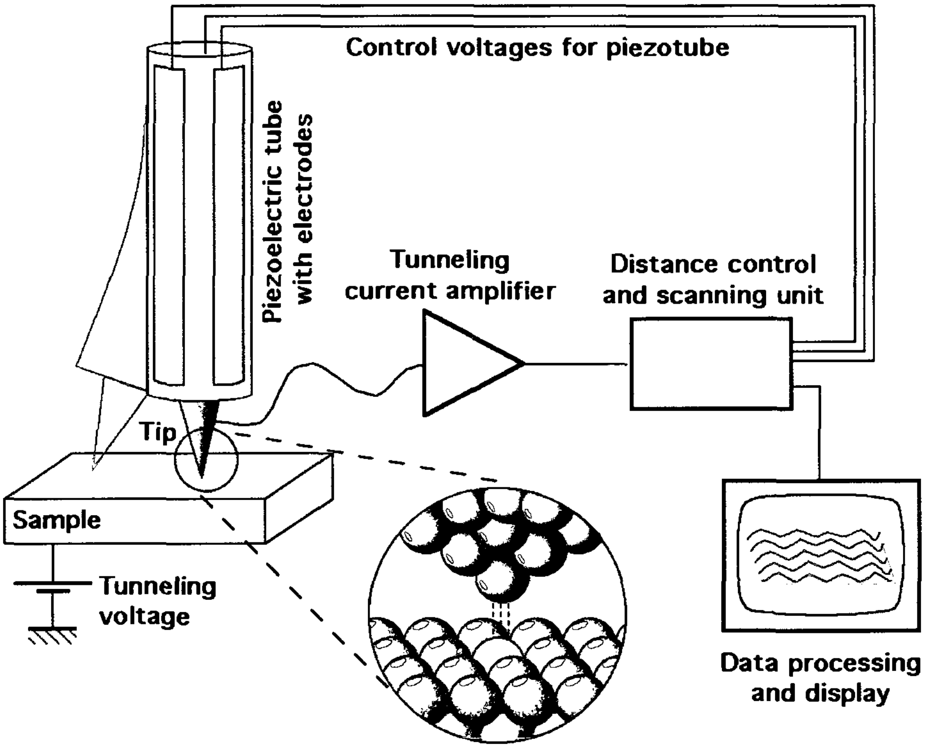

Figure 1-10 *Schematic demonstrating the general operation of a scanning tunneling microscope. The tunneling current between the tip and sample is amplified before being processed for imaging and to provide a feedback signal for height adjustment of the tip. The measured tunneling current is compared to a target value, above which the control system causes the piezo to contract and pull the tip away from the sample, below which it is moved forward. The height of the tip and/or the current can be mapped to spatial coordinates and an image produced.*[§§]

The experimental design of an STM is presented in Figure 1-10. The underlying principle that provides the exceptional angstrom lateral and sub-angstrom height resolution of STM, is the exponential dependence of tunneling current on the distance between the tip

---

[§§] Diagram created by Michael Schmid and used according to the permissions granted under Creative Commons Attribution ShareAlike 2.0 Austria License.

and sample. This gap space (less than 1 nm) may be modeled as a potential barrier, and quantum mechanics allows an electron of energy E in the tip to have some finite probability that its wave function, $\psi(d)$, can be found at a distance d into a barrier of potential Φ_b. That probability decreases exponentially with d and is given as the square of the relation:

$$\psi(d) = \psi(0)e^{-\kappa d}$$

$$where$$

$$\kappa = \sqrt{\frac{2m_e(\Phi_b - E)}{\hbar^2}}$$

If the sample is a distance d from the tip then the square of the wave function, $\psi(d)$, is the probability that an electron from the tip will tunnel to the sample.

The tunneling current is proportional to the number of electrons of sufficient energy to tunnel across the gap. This value is determined by the local density of electronic states in the tip and sample, for metals, all these states are occupied above the Fermi level, and empty below it. The tunneling mechanism in STM is illustrated in Figure 1-11. Here electrons from filled states in the tip (indicated by the darkened regions) are tunneling to empty states in the sample, through the barrier of potential Φ_b. The barrier is related to the effective workfunctions of the tip and the sample, Φ_1 and Φ_2 respectively. The magnitude of the tunneling current is not only given by the local density of states, but by how many filled states in the tip overlap in energy with empty states in the sample. The magnitude of this overlap can be modified by applying a potential difference between the tip and the sample (denoted eV in Figure 1-11.), thus shifting their Fermi levels with respect to each other and allowing a larger number of electrons to tunnel.

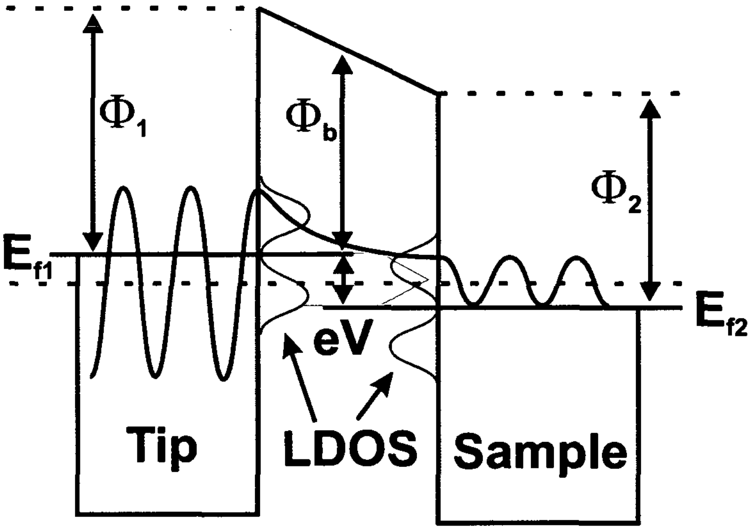

Figure 1-11 *Diagram of the tunneling mechanism in action in scanning tunneling microscopy. The tip is negatively biased by a value of* ***V*** *with respect to the sample, producing an energy overlap* ***eV*** *between filled stated in the tip and empty states in the sample. This applied potential effectively shifts their Fermi levels (E_f) with respect to one another. The probability that an electron will tunnel, and thus the current, exponentially decays with the distance separating the tip and sample. The potential barrier (Φ_b)through which the electron must tunnel is related to the work functions of the tip (Φ_1) and the sample (Φ_1).*

If the Fermi levels of the tip and sample are at the same energy, then no tunneling will occur. By applying a small voltage difference between the two then tunneling will begin, from the tip to the sample if the voltage is negative, and vice versa if it is positive. By scanning a range of voltages (V) and monitoring the resulting tunneling current (I), an I/V curve is formed in which the total local densities of states are probed as a function of bias potential. This is called scanning tunneling spectroscopy, and may provide the LDOS near the Fermi level.

Because STM relies on the continuous transfer of electrons, the current lost or gained to a material must be replaced or dissipated. Sufficiently conductive materials usually in the form of a metal or semi-conductor are therefore a limiting pre-requisite for the type of sample that can be measured by STM.

1.3.3. *Atomic Force Microscopy*

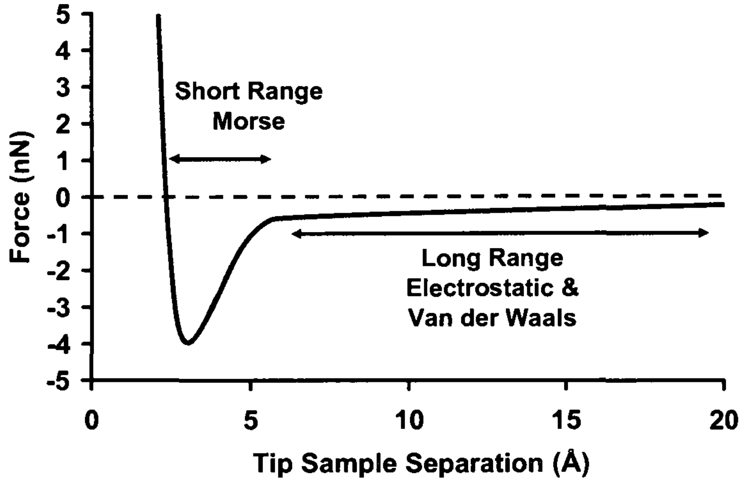

Figure 1-12 *The forces that will be felt by a tip as it approaches a surface.*

Atomic force microscopy is similar to scanning tunneling microscopy in experimental design, but the underlying physical quantity which is used for adjustment of the tip height is force rather than tunneling current. First developed by G Binnig and co-workers in 1986,[92] AFM allows virtually any solid to be studied regardless of electronic properties, sometimes with atomic resolution. No conduction is necessary since it is only the force of interaction between a sharp tip and a surface that is measured. The magnitude and direction of these forces vary with tip to sample distance. Electrostatic and van der Waals forces dominate over a fairly large extended range greater than approximately 5 Å. Below this, the sum of forces follow the Morse potential, first attractive then repulsive (Figure 1-12).

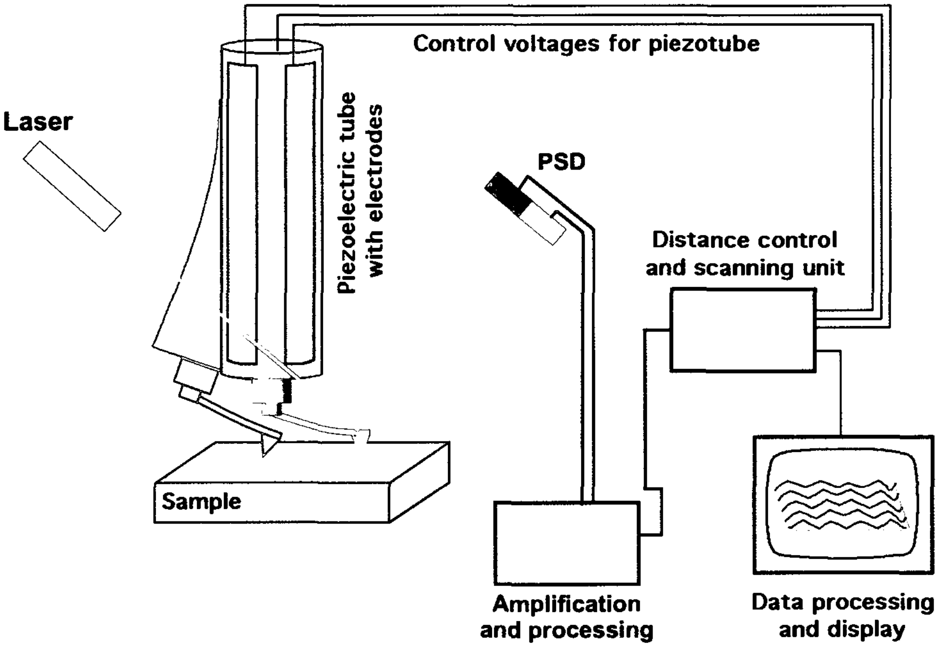

Figure 1-13 *Schematic of an atomic force microscope.*[***] *Similar to the STM (Figure 1-10) in operation, the AFM uses a cantilever probe which deforms in response to interaction forces with the surface. The deflection of the cantilever, reflects the height of the sample feature probed.*

In classic designs (Figure 1-13), the sharp tip is mounted on a thin silicon cantilever, and is brought into contact with the surface under study. In response to the force of interaction, the cantilever probe will bend. The magnitude of this deflection is used in the same manner as was tunneling current in STM: as feedback in the height adjustment of the tip. The cantilever deflection is measured by a laser beam that is reflected from it to be detected at a position sensitive diode (PSD). As the cantilever bends, the reflected path of the laser beam moves, so that it strikes the diode at a different position. The magnitude of the laser beam displacement is directly related to the magnitude of tip deflection and therefore the force of interaction between the tip and the sample. In this type of contact

---

[***] Diagram modified from an image created by Michael Schmid and used according to the permissions granted under Creative Commons Attribution ShareAlike 2.0 Austria License.

imaging mode, the topography image of the surface is built up from a series of height profiles. The height is controlled during a raster scan of the tip by maintaining a constant cantilever deflection.

In the pure contact mode of operation, the tip is simply dragged across the surface while measuring the beam deflection. In alternate, often non-contact modes, the tip may be oscillated while changes in amplitude or frequency are monitored.[93] Oscillation is often achieved by supplying a voltage sine wave to a shaker piezo upon which the cantilever is mounted. The frequency of this drive signal must match the natural resonant frequency of the cantilever. As the oscillating tip approaches the sample it experiences a variety of forces which cause a shift in its frequency, amplitude, and phase. Any of these shifts can be used as feedback for controlling tip height position and they each represent a different mode of operation.

In the frequency modulation mode (FM-AFM), the tip is initially oscillated at its resonant frequency far away from the surface. As the tip is brought closer, the frequency will shift higher or lower depending on the type of force (repulsive or attractive) it experiences. A frequency shift, or de-tuning value is selected as the target setpoint which the feedback circuitry attempts to maintain by adjusting tip height. The amplitude of the oscillations will change with interaction but in this mode the control circuit adds energy to the tip in order to maintain a constant vibrational amplitude. This type of technique is often used in UHV studies, where very small forces may result in large frequency changes. Resolution of subatomic features of silicon (111) have been reported under such conditions.[94]

In amplitude modulation mode (AM-AFM) the setpoint is an amplitude shift relative to the free oscillation of the cantilever. If operating in the attractive regime, that is, the region corresponding to the negative force of interaction as seen in Figure 1-12, the tip is often considered to be in the non-contact mode. If the tip is brought closer entering the repulsive region of the force curve, then the tip will initially be in intermittent contact with the surface. This is a so called tapping mode and the amplitude is in large part damped through hard contact with the surface, so that there is near one to one relationship between advancement of the tip, and a decrease in amplitude. This mode of operation is commonly used in air at ambient pressures.

In both FM- and AM- AFM the phase of the detected signal from the cantilever is shifted with respect to the drive signal due to interactions with the surface. In AM-AFM in which the phase is not corrected by the electronics, it is possible to collect the phase shift data and a phase image can be formed.

The origin of phase shifting can be broadly related to the quantity of energy that is lost by the tip through its interaction with the surface.[95] Therefore, significant effort has been performed in relating contrast to local changes in actual material properties such as adhesion and elasticity.[96-100] Magonov *et. al.* modeled the source of phase shifts and have developed a proportional relationship between the magnitude of the shift and the specimen's local Young's modulus of elasticity.[101] The relationship is generalized as :

$$\varphi \approx \frac{\pi}{2} - \varepsilon a E^{*} \frac{Q}{k}$$

Where φ is the phase shift, ε is the strain tensor in the interaction, a is the area of the tip in contact with the surface, E^{*} is the reduced Young's modulus, k is the cantilever force constant, and Q is Q-factor of the probe.

The value Q plays an important role in AFM studies. For AFM, it is defined as the resonance frequency of the cantilever divided by the width of that resonance peak at $\sqrt{2}$ of its maximum height. In a plot of oscillation amplitude against frequency a cantilever will be shown to resonate at only specific drive frequencies. The narrower the range of frequencies that will produce vibrations the better small changes in frequency or amplitude can be resolved. [102]

References:

1. Ormerod, R.M., *Solid oxide fuel cells.* Chemical Society Reviews, 2003. **32**(1): p. 17.

2. Badwal, S.P.S. and Foger, K., *Solid oxide electrolyte fuel cell review.* Ceramics International, 1996. **22**(3): p. 257.

3. Molenda, J., Swierczek, K. and Zajac, W., *High-temperature solid-oxide fuel cells (sofc) - materials and prospects.* Przemysl Chemiczny, 2005. **84**(11): p. 845.

4. Minh, N.Q., *Ceramic fuel-cells.* Journal of the American Ceramic Society, 1993. **76**(3): p. 563.

5. Jiang, S.P., *Development of lanthanum strontium manganite perovskite cathode materials of solid oxide fuel cells: A review.* Journal of Materials Science, 2008. **43**(21): p. 6799.

6. Jiang, S.P. and Chan, S.H., *A review of anode materials development in solid oxide fuel cells.* Journal of Materials Science, 2004. **39**(14): p. 4405.

7. Oura, K., Lifshits, V.G., Saranin, A.A., A.V., Z. and Katayama, M., *Surface science - an introduction.* Advanced texts in physics. 2003, Berlin: Springer-Verlag.

8. Freund, H.J. and Knozinger, H., *Foreword for the gerhard ertl festschrift.* Journal of Physical Chemistry B, 2004. **108**(38): p. 14183.

9. Freund, H., *Gerhard ertl: Congratulations!* Surface Science Reports, 2008. **63**(2): p. III.

10. Ertl, G. and Rau, P., *Chemisorption and catalytic reactions of oxygen and carbon monoxide on a palladium(110) surface.* Surface Science, 1969. **15**(3): p. 443.

11. Ertl, G., *Elementary processes in reactions on clean surfaces.* Chemie Ingenieur Technik, 1969. **41**(5-6): p. 289.

12. Ertl, G., *Structural properties of cleaved germanium surfaces.* Chemie Ingenieur Technik, 1969. **41**(5-6): p. 396.

13. Ertl, G., *Structure and reactions of pure solid state surfaces.* Chemie Ingenieur Technik, 1968. **40**(7): p. 361.

14. Ertl, G., *Study of surface reactions by diffraction of low-energy electrons.* Angewandte Chemie-International Edition, 1968. **7**(3): p. 234.

15. Ertl, G. and Giovanel.T, *Catalytic degradation of water on pure germanium surfaces.* Berichte Der Bunsen-Gesellschaft Fur Physikalische Chemie, 1968. **72**(1): p. 74.

16. Ertl, G. and Koch, J., *Interaction of CO and O_2 with aPd(100) surface.* Zeitschrift Fur Physikalische Chemie-Frankfurt, 1970. **69**(5-6): p. 323.

17. Asakura, K., Iwasawa, Y., Purnell, S.K., Watson, B.A., Barteau, M.A. and Gates, B.C., *Zirconium oxide supported on Pd(100): Characterization by scanning tunneling microscopy and tunneling spectroscopy.* Catalysis Letters, 1992. **15**(4): p. 317.

18. Campbell, C.T., Grant, A.W., Starr, D.E., Parker, S.C. and Bondzie, V.A., *Model oxide supported catalysts: Energetics, particles thickness, chemisorption and catalytic properties.* Topics Catal., 2001. **14**: p. 43.

19. Freund, H.-J., Ernst, N., Baeumer, M., Rupprechter, G., Libuda, J., Kuhlenbeck, H., Risse, T., Drachsel, W., Al-Shamery, K. and Hamann, H., *Model systems for heterogeneous catalysis: Quo vadis surface science?*, in *Surface chemistry and catalysis*, Carley, A.F., Editor. 2002, Kluwer Academic/Plenum Publishers: New York. p. 103.

20. Freund, H.-J., Baeumer, M. and Kuhlenbeck, H., *Catalysis and surface science: What do we learn from studies of oxide supported cluster model systems?* Adv. Catal., 2000. **45**: p. 333.

21. Goodman, D.W., *Model catalysts: From imagining to imaging a working surface.* Journal of Catalysis, 2003. **216**: p. 213.

22. Yates, J.T., *Experimental innovations in surface science.* 1998, New York: Springer-Verlag.

23. Woodruff, D.P. and Delchard, T.A., *Modern techniques of surface science.* 2 ed. Cambridge solid state science series, ed. Davis, E.A., I.M. Ward and C. D.R. 1994, Cambridge: Cambridge University Press.

24. Scott, H.G., *Phase relationships in zirconia-yttria system.* Journal of Materials Science, 1975. **10**(9): p. 1527.

25. Kilo, M., Argirusis, C., Borchardt, G. and Jackson, R.A., *Oxygen diffusion in yttria stabilised zirconia - experimental results and molecular dynamics calculations.* Physical Chemistry Chemical Physics, 2003. **5**(11): p. 2219.

26. Catlow, C.R.A., Chadwick, A.V., Greaves, G.N. and Moroney, L.M., *EXAFS study of yttria-stabilized zirconia.* Journal of the American Ceramic Society, 1986. **69**(3): p. 272.

27. Kawata, K., Maekawa, H., Nemoto, T. and Yamamura, T., *Local structure analysis of YSZ by Y-89 MAS-NMR.* Solid State Ionics, 2006. **177**(19-25): p. 1687.

28. Khan, M.S., Islam, M.S. and Bates, D.R., *Cation doping and oxygen diffusion in zirconia: A combined atomistic simulation and molecular dynamics study.* Journal of Materials Chemistry, 1998. **8**(10): p. 2299.

29. Komyoji, D., Yoshiasa, A., Moriga, T., Emura, S., Kanamaru, F. and Koto, K., *Exafs study of the fluorite-type compounds in the systems (1-x)ZrO_2-x$YbO_{1.5}$ ($0.18 \leq x \leq 0.5$) and $Zr_2Ln_2O_7$ (Ln = Tb, Dy, Ho, Er, and Yb).* Solid State Ionics, 1992. **50**(3-4): p. 291.

30. Eichler, A. and Kresse, G., *First-principles calculations for the surface termination of pure and yttria-doped zirconia surfaces.* Physical Review B, 2004. **69**(4).

31. Woll, C., *The chemistry and physics of zinc oxide surfaces.* Progress in Surface Science, 2007. **82**(2-3): p. 55.

32. Goniakowski, J., Finocchi, F. and Noguera, C., *Polarity of oxide surfaces and nanostructures.* Reports on Progress in Physics, 2008. **71**(1).

33. Anthony E. Hughes, *Segregation in single-crystal fully stabilized yttria-zirconia.* Journal of the American Ceramic Society, 1995. **78**(2): p. 369.

34. Ballabio, G., Bernasconi, M., Pietrucci, F. and Serra, S., *Ab initio study of yttria-stabilized cubic zirconia surfaces.* Physical Review B, 2004. **70**(7).

35. de Ridder, M., van Welzenis, R.G., van der Gon, A.W.D., Brongersma, H.H., Wulff, S., Chu, W.-F. and Weppner, W., *Subsurface segregation of yttria in yttria stabilized zirconia.* Journal of Applied Physics, 2002. **92**(6): p. 3056.

36. de Ridder, M., van Welzenis, R.G. and Brongersma, H.H., *Surface cleaning and characterization of yttria-stabilized zirconia.* Surface and Interface Analysis, 2002. **33**(4): p. 309.

37. Feliu, S. and Perez-Revenga, M.L., *Effect of the presence of alloying elements in interstitial-free and low-carbon steels on their surface composition after annealing in reducing atmospheres (dew point = -30 °C).* Metallurgical and Materials Transactions a-Physical Metallurgy and Materials Science, 2004. **35A**(7): p. 2039.

38. G.S.A.M. Theunissen, A.J.A.W., A.J. Burggraaf, *Surface and grain boundary analysis of doped zirconia ceramics studied by AES and XPS.* Journal of Materials Science, 1992. **27**: p. 5057.

39. Hauch, A., Jensen, S.H., Bilde-Sorensen, J.B. and Mogensen, M., *Silica segregation in the Ni/YSZ electrode.* Journal of the Electrochemical Society, 2007. **154**(7): p. A619.

40. Hansen, K.V., Norrman, K. and Mogensen, M., *TOF-SIMS studies of yttria-stabilised zirconia.* Surface and Interface Analysis, 2006. **38**(5): p. 911.

41. Hughes, A.E. and Badwal, S.P.S., *Impurity segregation study at the surface of yttria-zirconia electrolytes by xps.* Solid State Ionics, 1990. **40-1**: p. 312.

42. Hughes, A.E. and Badwal, S.P.S., *Impurity and yttrium segregation in yttria-tetragonal zirconia.* Solid State Ionics, 1991. **46**(3-4): p. 265.

43. Hughes, A.E., Stjohn, H., Kountouros, P. and Schubert, H., *Moisture sensitive degradation in* TiO_2-$Y_2O_3ZrO_2$. Journal of the European Ceramic Society, 1995. **15**(11): p. 1125.

44. Nowotny, J., Bak, T., Nowotny, M.K. and Sorrell, C.C., *Charge transfer at oxygen/zirconia interface at elevated temperatures - part 3: Segregation induced interface properties.* Advances in Applied Ceramics, 2005. **104**(4): p. 165.

45. Nowotny, J., Sorrell, C.C. and Bak, T., *Segregation in zirconia: Equilibrium versus non-equilibrium segregation.* Surface and Interface Analysis, 2005. **37**(3): p. 316.

46. Shibata, N., Oba, F., Yamamoto, T., Ikuhara, Y. and Sakuma, T., *Atomic structure and solute segregation of a sigma=3, 110 /{111} grain boundary in an yttria-stabilized cubic zirconia bicrystal.* Philosophical Magazine Letters, 2002. **82**(7): p. 393.

47. Stanek, C.R., Grimes, R.W., Rushton, M.J.D., McClellan, K.J. and Rawlings, R.D., *Surface dependent segregation of* Y_2O_3 *in t-*ZrO_2. Philosophical Magazine Letters, 2005. **85**(9): p. 445.

48. Theunissen, G., Winnubst, A.J.A. and Burggraaf, A.J., *Surface and grain-boundary analysis of doped zirconia ceramics studied by AES and XPS.* Journal of Materials Science, 1992. **27**(18): p. 5057.

49. Wang, X.-G., *Yttrium segregation and surface phases of yttria-stabilized zirconia(111) surface.* Surface Science, 2008. **602**(1): p. L5.

50. Zhang, Z.M., Nowotny, J., Pigram, P.J., Lamb, R.N., Nakamura, S. and Yamana, K., *Xps study of surface cation segregation in mullite/zirconia composites.* Surface and Interface Analysis, 1996. **24**(9): p. 647.

51. Zhu, J.J., van Ommen, J.G., Knoester, A. and Lefferts, L., *Effect of surface composition of yttrium-stabilized zirconia on partial oxidation of methane to synthesis gas.* Journal of Catalysis, 2005. **230**(2): p. 291.

52. Costantini, J.-M. and Beuneu, F.o., *Thermal recovery of colour centres induced in cubic yttria-stabilized zirconia by charged particle irradiations.* Journal of Physics: Condensed Matter, 2006(15): p. 3671.

53. Merino, R.I., Orera, V.M., Lomonova, E.E. and Batygov, S.K., *Paramagnetic electron traps in reduced stabilized zirconia.* Physical Review B, 1995. **52**(9): p. 6150 LP

54. Torres, D.I., Paje, S.E., Llopis, J., Morell, G. and Katiyar, R.S., *Spectroscopic study of CaSZ and YSZ thermochemically reduced crystals.* Journal of Luminescence, 1997. **72-4**: p. 724.

55. Iacona, F., Kelly, R. and Marletta, G., *X-ray photoelectron spectroscopy study of bombardment-induced compositional changes in ZrO_2, SiO_2, and $ZrSiO_4$.* Journal of Vacuum Science & Technology A, 1999. **17**(5): p. 2771.

56. Costantini, J.-M. and Beuneu, F., *Color center annealing and ageing in electron and ion-irradiated yttria-stabilized zirconia.* Nuclear Instruments and Methods in Physics Research Section B: Beam Interactions with Materials and Atoms, 2005. **230**(1-4): p. 251.

57. Simpson, W.C., Wang, W.K., Yarmoff, J.A. and Orlando, T.M., *Photon- and electron-stimulated desorption of O+ from zirconia.* Surface Science, 1999. **423**(2-3): p. 225.

58. Cotter, M. and Egdell, R.G., *Electron-beam reduction of cubic Y-doped $ZrO_2(100)$ - a study by x-ray photoelectron-spectroscopy.* Journal of Solid State Chemistry, 1987. **66**(2): p. 364.

59. Bogicevic, A. and Wolverton, C., *Nature and strength of defect interactions in cubic stabilized zirconia.* Physical Review B, 2003. **67**(2).

60. Pietrucci, F., Bernasconi, M., Laio, A. and Parrinello, M., *Vacancy-vacancy interaction and oxygen diffusion in stabilized cubic ZrO_2 from first principles.* Physical Review B, 2008. **78**(9).

61. Nowotny, J., Bak, T., Nowotny, M.K. and Sorrell, C.C., *Charge transfer at oxygen/zirconia interface at elevated temperatures - part 1: Basic properties and terms.* Advances in Applied Ceramics, 2005. **104**(4): p. 147.

62. Nowotny, J., Bak, T., Nowotny, M.K. and Sorrell, C.C., *Charge transfer at oxygen/zirconia interface at elevated temperatures - part 2: Oxidation of zirconia.* Advances in Applied Ceramics, 2005. **104**(4): p. 154.

63. Nowotny, J., Bak, T. and Sorrell, C.C., *Charge transfer at oxygen/zirconia interface at elevated temperatures - part 4: Work function v. Defect chemistry.* Advances in Applied Ceramics, 2005. **104**(4): p. 174.

64. Nowotny, J., Bak, T. and Sorrell, C.C., *Charge transfer at oxygen/zirconia interface at elevated temperatures - part 5: Reactivity models.* Advances in Applied Ceramics, 2005. **104**(4): p. 181.

65. Nowotny, J., Bak, T. and Sorrell, C.C., *Charge transfer at oxygen/zirconia interface at elevated temperatures - part 6 work function measurements.* Advances in Applied Ceramics, 2005. **104**(4): p. 188.

66. Nowotny, J., Bak, T. and Sorrell, C.C., *Charge transfer at oxygen/zirconia interface at elevated temperatures - part 7: Effect of surface processing.* Advances in Applied Ceramics, 2005. **104**(4): p. 195.

67. Nowotny, J., Bak, T. and Sorrell, C.C., *Charge transfer at oxygen/zirconia interface at elevated temperatures - part 8: Effect of temperature.* Advances in Applied Ceramics, 2005. **104**(4): p. 200.

68. Nowotny, J., Bak, T. and Sorrell, C.C., *Charge transfer at oxygen/zirconia interface at elevated temperatures - part 10: Effect of platinum.* Advances in Applied Ceramics, 2005. **104**(4): p. 214.

69. Nowotny, J., Bak, T. and Sorrell, C.C., *Charge transfer at oxygen/zirconia interface at elevated temperatures - part 11: Effect of surface doping with calcium.* Advances in Applied Ceramics, 2005. **104**(4): p. 223.

70. Nowotny, J., Bak, T. and Sorrell, C.C., *Charge transfer at oxygen/zirconia interface at elevated temperatures - part 12: Summary.* Advances in Applied Ceramics, 2005. **104**(4): p. 229.

71. Nowotny, M.K., Bak, T., Nowotny, J., Sorrell, C.C., Prince, K.E. and Kang, S.J.L., *Charge transfer at oxygen/zirconia interface at elevated temperatures - part 9: Room temperature.* Advances in Applied Ceramics, 2005. **104**(4): p. 206.

72. Briggs, D. and Seah, M.P., *Practical surface analysis -2nd ed. Volume 1, auger and x-ray photoelectron spectroscopy.* 2 ed. 1991: Wiley.

73. Fairley, N. and Carrick, A., *The casa cookbook - part 1: Recipes for XPS data processing.* 2005: Acolyte Science.

74. Moulder, J.F., Stickle, W.F., Sobol, P.E. and Bomben, K.D., *Handbook of x-ray photoelectron spectroscopy*, ed. Chastain, J. and R.C.J. King. 1995: Physical Electronics, Inc.

75. Fairley, N., *Transmission correction.* 2006, Casa Software Limited.

76. Crist, V.B., *Handbook of monochromated xps spectra - the elements and native oxides.* Vol. 1. 2000, Chichester: Whiley.

77. Seigbahn, K. and *al.*, *e.*, *Esca applied to free molecules.* 1969, Amsterdam: North Holland.

78. Tanuma, S., Powell, C.J. and Penn, D.R., *Proposed formula for electron inelastic mean free paths based on calculations for 31 materials.* Surface Science Letters, 1987. **192**: p. L849.

79. Powell, C.J. and Jablonski, A., *Nist electron inelastic-mean-free-path database-version 1.1.* 2000, Gaithersburg: National Institute of Standards and Technology.

80. National Institute of Standards and Technology, N., *Nist scientific and technical databases- nist electron-mean-free-path database version 1.1 - www.Nist.Gov/srd/nist71.Htm*. 2009.

81. Benoit, R., Durand, Y., Narjoux, B., Quintana, G. and Georges, Y., *XPS, AES, UPS and ESCA -www.Lasurface.Com*. 2008.

82. Tougaard, S., *Quases-tougaard inc. - www.Quases.Com*. 2009.

83. Seah, M.P. and Dench, W.A., *Quantitative electron spectroscopy of surfaces: A standard data base for electron inelastic mean free paths in solids.* Surface and Interface Analysis, 1979. **1**(1): p. 2.

84. Cumpson, P.J. and Seah, M.P., *Elastic scattering corrections in AES and XPS .2. Estimating attenuation lengths and conditions required for their valid use in overlayer/substrate experiments.* Surface and Interface Analysis, 1997. **25**(6): p. 430.

85. Tanuma, S., Powell, C.J. and Penn, D.R., *Calculations of electron inelastic mean free paths for 31 materials.* Surface and Interface Analysis, 1988. **11**(11): p. 577.

86. Tanuma, S., Powell, C.J. and Penn, D.R., *Calculations of electron inelastic mean free paths .2. Data for 27 elements over the 50-2000-eV range.* Surface and Interface Analysis, 1991. **17**(13): p. 911.

87. Tanuma, S., Powell, C.J. and Penn, D.R., *Calculations of electron inelastic mean free paths .3. Data for 15 inorganic-compounds over the 50-2000-eV range.* Surface and Interface Analysis, 1991. **17**(13): p. 927.

88. Tanuma, S., Powell, C.J. and Penn, D.R., *Calculations of electron inelastic mean free paths (IMFPS) .4. Evaluation of calculated IMFPS and of the predictive imfp formula tpp-2 for electron energies between 50 and 2000 eV.* Surface and Interface Analysis, 1993. **20**(1): p. 77.

89. Tanuma, S., Powell, C.J. and Penn, D.R., *Calculations of electron inelastic mean free paths .5. Data for 14 organic-compounds over the 50-2000 eV range.* Surface and Interface Analysis, 1994. **21**(3): p. 165.

90. Tanuma, S., Powell, C.J. and Penn, D.R., *Calculations of electron inelastic mean free paths (IMFPS) .6. Analysis of the Gries inelastic scattering model and predictive IMFP equation.* Surface and Interface Analysis, 1997. **25**(1): p. 25.

91. Binnig, G., Rohrer, H., Gerber, C. and Weibel, E., *Surface studies by scanning tunneling microscopy.* Physical Review Letters, 1982. **49**(1): p. 57.

92. Binnig, G., Quate, C.F. and Gerber, C., *Atomic force microscope.* Physical Review Letters, 1986. **56**(9): p. 930.

93. Garcia, R. and Perez, R., *Dynamic atomic force microscopy methods.* Surface Science Reports, 2002. **47**(6-8): p. 197.

94. Giessibl, F.J., Hembacher, S., Bielefeldt, H. and Mannhart, J., *Subatomic features on the silicon (111)-(7x7) surface observed by atomic force microscopy.* Science, 2000. **289**(5478): p. 422.

95. Tamayo, J. and Garcia, R., *Relationship between phase shift and energy dissipation in tapping-mode scanning force microscopy.* Applied Physics Letters, 1998. **73**(20): p. 2926.

96. Whangbo, M.H., Bar, G. and Brandsch, R., *Description of phase imaging in tapping mode atomic force microscopy by harmonic approximation.* Surface Science, 1998. **411**(1-2): p. L794.

97. Magonov, S.N., Elings, V. and Papkov, V.S., *AFM study of thermotropic structural transitions in poly(diethylsiloxane).* Polymer, 1997. **38**(2): p. 297.

98. Bar, G., Brandsch, R. and Whangbo, M.H., *Effect of viscoelastic properties of polymers on the phase shift in tapping mode atomic force microscopy.* Langmuir, 1998. **14**(26): p. 7343.

99. Bar, G., Thomann, Y. and Whangbo, M.H., *Characterization of the morphologies and nanostructures of blends of poly(styrene) block-poly(ethene-co-but-1-ene)-block-poly(styrene) with isotactic and atactic polypropylenes by tapping-mode atomic force microscopy.* Langmuir, 1998. **14**(5): p. 1219.

100. Noy, A., Sanders, C.H., Vezenov, D.V., Wong, S.S. and Lieber, C.M., *Chemically-sensitive imaging in tapping mode by chemical force microscopy: Relationship between phase lag and adhesion.* Langmuir, 1998. **14**(7): p. 1508.

101. Magonov, S.N., Elings, V. and Whangbo, M.H., *Phase imaging and stiffness in tapping-mode atomic force microscopy.* Surface Science, 1997. **375**(2-3): p. L385.

102. Yamanaka, K., Maruyama, Y., Tsuji, T. and Nakamoto, K., *Resonance frequency and q factor mapping by ultrasonic atomic force microscopy.* Applied Physics Letters, 2001. **78**(13): p. 1939.

2. Experimental

2.1. Ultra High Vacuum System

2.1.1. Description

The ultra high vacuum chamber is a custom designed system, integrating two separate chambers (Figure 2-1), one built by Specs GmbH of Berlin and the other by RHK Technology of Michigan. The Specs chamber houses x-ray and ultraviolet photoelectron spectroscopies (XPS/UPS), as well as low energy electron diffraction (LEED), ion bombardment and a metal evaporation source. The RHK chamber holds the atomic force and scanning tunneling microscopies (AFM/STM). Both chambers are separated by a gate valve and the sample may be transferred between the two on a UHV manipulator. The main manipulator is composed of a linear transfer arm (60 cm range in x), with nearly 360° rotational range about the axis of translation. The arm is mounted upon an xy-stage (yz according to the coordinate system used throughout this work) which allows the entire arm to be moved over a 20 mm range in the z and y directions (see coordinate system in Figure 2-1).

Samples may be transferred from ambient conditions into the Specs chamber via a load-lock, which is a small chamber separated from the main system by a gate valve. Attached to the load lock is a turbo pump, broad range vacuum pressure gauge (atmosphere to 1×10^{-9} mbar), and a secondary transfer arm. The load lock may be vented and a sample loaded on the arm, without breaking vacuum in the main system. Once the sample is loaded, the turbo pump may be started. Upon achieving sufficient vacuum ($\sim 1 \times 10^{-7}$ mbar), the gate valve may be opened and the sample transferred to the main manipulator in the Specs chamber. Since it is never exposed to ambient pressures, ultra high vacuum ($\sim 1^{-10}$ mbar)) in the main chamber is maintained. The time required to transfer a sample from ambient to UHV is usually about 1.5 to 2 hours.

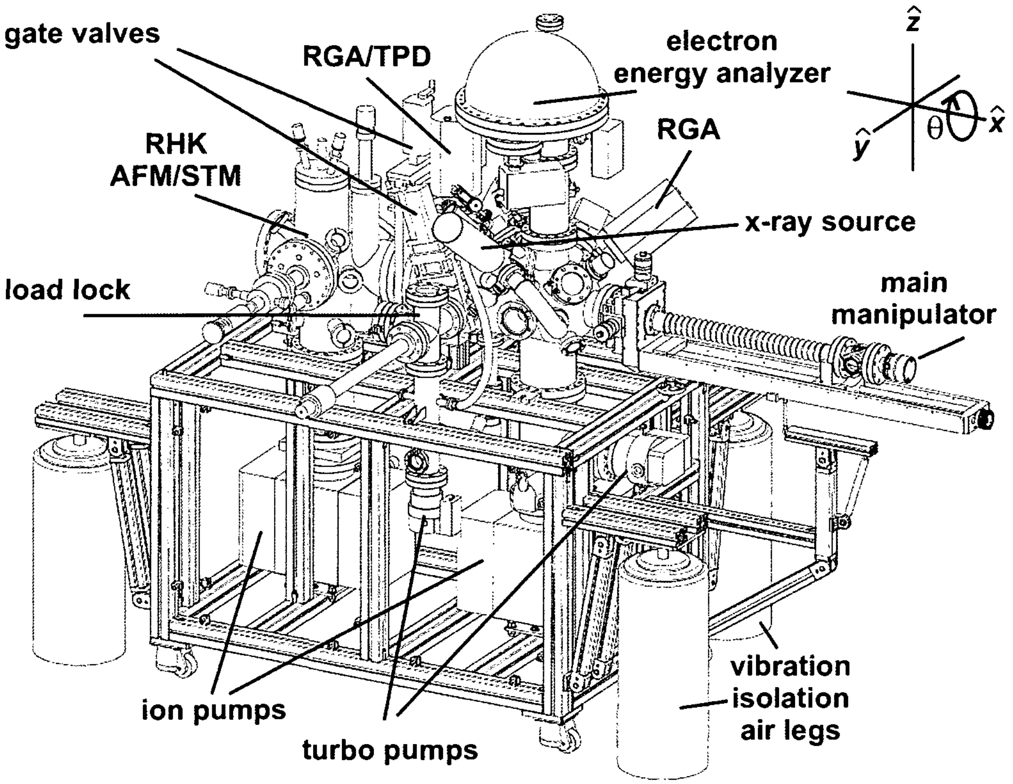

Figure 2-1 *Schematic view of the custom Specs/RHK ultra high vacuum system. It is divided into two main chambers separated by a gate valve. One side houses the scanning probe microscopes (AFM/STM), the other side holds techniques such as XPS/UPS, LEED, TPD, and ion bombardment. The coordinate system according to which sample positions are referenced is shown in the top right corner, the positive x-direction extends along the axis of the main manipulator, away from the chamber.*

The Specs chamber is composed entirely of mu-metal, a type of stainless steel with high magnetic permeability that acts as a magnetic shield, directing field lines around the shielded volume. Such fields might otherwise interact with information carrying electrons measured in XPS/UPS and LEED. This is not an issue for the microscopies and so the RHK chamber is simply made of a vacuum compatible stainless steel such as low carbon alloy 204.

Ultra high vacuum pressures are obtained with a combination of vacuum pumps each acting over a specific pressure range. Roughing pumps, in this case oil-less Varian scroll pumps, are used as backing to turbomolecular pumps. On their own a good roughing pump is capable of providing pumping action from atmosphere down to about 1×10^{-3} mbar. In combination with the large turbomolecular pump on the Specs chamber, less than 5×10^{-10} mbar has been achieved. Even lower pressures may be reached with ion pumps. They operate by ionizing gas phase molecules, that are then accelerated towards high surface area titanium plates, where they impact with high energy and are buried. There is a limit to how much material the titanium may hold and so the quantity of molecules ionized should be kept low in order to maintain the lifetime of the ion pumps. They are typically only turned on when pressures are already in the 1×10^{-9} mbar range, and may maintain vacuum pressures on the order of 1×10^{-11} mbar. The added benefit of the ion pumps is that they are quiet and contain no moving parts which could cause vibrations that interfere with scanning probe microscopy.

Even with all the pumping devices ultra high vacuum cannot be achieved unless the chamber is "baked", often for several days. Heating is performed by placing an aluminum frame around the system over which is draped temperature resistant insulating blankets. The thermal source is a set of fans incorporating heating elements similar to those found on kitchen stoves, they are placed on the frame and blow hot air into the system through holes in the blankets. Due to the thermal sensitivity of some of the components, the maximum chamber bake-out temperature is 115 °C. If the scanning probe microscope head is removed, this can be extended to 140 °C. Baking induces water and other high vapour pressure contaminants adsorbed on the chamber walls to desorb much more quickly than they would at room temperature. During baking the turbo pumps are operating so that desorbed species may be removed from the chamber. This reduces the overall vapour pressure of residual gases and UHV can be achieved. Figure 2-2 shows the chamber pressure as a function of baking time at 113 °C, the initial rise in pressure results from the chamber first becoming hot. After five hours the pressure slowly reduces as the concentration of adsorbed species lowers.

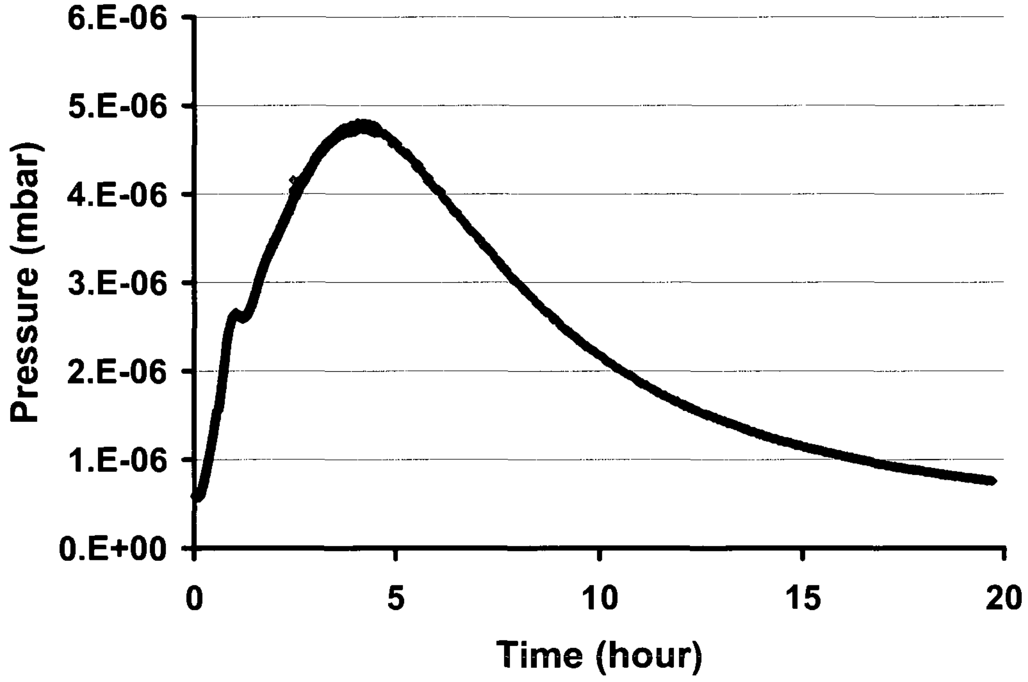

Figure 2-2 *Plot of the chamber pressure as a function of time during system bake-out at 113 °C.*

After baking, the vapour pressure of adsorbates not removed can be lowered through the use of titanium sublimation pumps. As the name suggests such pumps operate by sublimating titanium from a filament; the titanium diffuses through the chamber, sticking to the walls providing a reactive surface with which residual gases may react to form a solid product. After baking, the Ti sublimation pumps are usually run for one or two minutes every 4 hours, after a few days this is reduced to once every 32 hours.

For imaging to be performed, the turbo pumps, which cause high frequency vibrations, need to be turned off. Since turning them off means the pumps will be vented, the Specs chamber has a gate valve directly in front of its turbopump which may be closed. This allows UHV to be maintained by the ion pumps alone (the Specs and RHK chambers each hold an ion pump). Even with the turbopumps off, vibration isolation from external sources is necessary. The entire chamber is mounted on four pneumatic legs which when pressures of approximately 25-32 psi are provided to them, raise the entire chamber off the floor. A series of regulation valves act in opposition to chamber movement, providing more or less air to each leg when necessary. The legs are efficient at damping troublesome building vibrations with the exception of very low frequencies below 2 to 3 Hz. However, they do not sufficiently protect against acoustic noise, and oddly it has been found that my voice in particular, couples into the chamber vibrational modes and can be observed during imaging. It is essential that the lab remain quiet, and imaging is frequently performed at night or on weekends in order to take advantage of the lower traffic in the building as well as on the nearby autobus transit-way.

The sample to be studied is mounted in a special type of holder that is designed to be compatible with the RHK SPM. This holder, usually referred to as a sample "puck", is composed of two parts; a copper base which is machined to provide the necessary grooves for manipulation, and a titanium nitride coated molybdenum top. The coating provides chemical, mechanical, and thermal stability. A recess is machined into the molybdenum top, where the sample is held in place by screws and tungsten leaf clips.

For all techniques in the Specs chamber the puck is held at the end of the main manipulator on a sample stage. A schematic of the sample stage/holder, and the sample puck is shown in Figure 2-3.

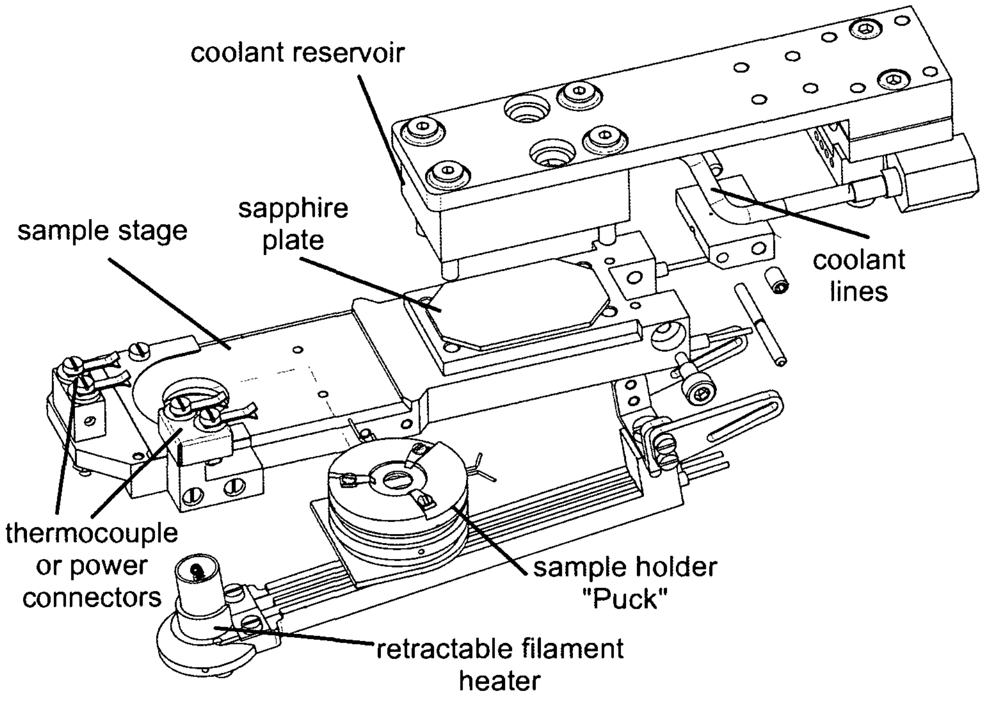

Figure 2-3 *A schematic of the sample holder that is held to the main manipulator. Coolant can be constantly flown through the reservoir which is in thermal but not electrical contact with the sample holder due to the sapphire plate. When in position, pins on the puck make contact with the clips mounted to the holder and can be used to measure temperature or carry power. A thoriated tungsten filament on a retractable lever can be used to heat the sample via electron bombardment. All necessary power and thermocouple lines travel down the length of the main manipulator arm to feedthroughs at its end.*

The stage itself is entirely composed of copper, however copper/beryllium springs and clips are used to hold the sample puck in place even when upside down. The clips also press the puck to the copper holder for good thermal contact, allowing the entire stage and sample to be cooled. Cooling is achieved by flowing a coolant such as liquid nitrogen to a reservoir that is in thermal contact with the copper stage through a sapphire plate. Sapphire is a good thermal conductor at low temperature, but poor at high temperature, and so, during sample heating thermal transfer to the manipulator is low, whereas during cooling heat may be extracted from the sample holder efficiently.

Heating is performed by a retractable filament heater that can be brought close to the back of the sample via holes in the stage and the bottom of sample puck. The heater can be moved out of the way during transfer to the load lock, or microscopy stage.

2.1.2. Sample position according to technique

In order to perform each technique the sample needs to be located at specific positions within the chamber. Because sample heating and cooling may modify the length of the transfer arm due to thermal expansion and contraction (~3 mm range), and micrometer screws may loosen over time, it has been much more useful to determine relative positions. For YSZ studies, the reference origin has been chosen to be the position required to provide maximum intensity of the zirconium 3d peak by XPS analysis. All other important positions are listed with respect to this position in the (x, y, z) reference frame. The angle zero is selected to be when the sample surface lies face up parallel to the floor, or more appropriately, when its lies perpendicular to the hemispherical analyzer lens axis. This provides a more internally consistent method for reproducing measurements, however in the case where the sample holder is bent, relative angles and positions may change, and so it is necessary to update the values intermittently or when deviations are suspected.

The relative positions are summarized in Table 2-1 , the nominal position at which to achieve maximum XPS signal intensity on the "absolute" scale (the system micrometers and measuring tape) is 69.1 cm, 11.18 mm, 11.60 mm, 0^{O} (x, y, z, θ). The ion sputtering position has been determined by measuring the maximum in the sputter current on a conductive sample. The LEED, doser, and TPD positions have been found using a clean palladium sample, for which a diffraction pattern was acquired and CO desorption studied.

Finally the evaporator position was initially estimated visually then the resulting deposition was confirmed by AFM and STM on both HOPG and YSZ.

Table 2-1 *The positions at which samples should be placed relative to the position required to achieve XPS signal maximum for the sample studied. The nominal position for XPS in the "absolute" system reference frame is nominally: 69.1 cm, 11.18 mm, 10.15 mm,* 0^O *(x, y, z,* θ*). The coordinate system is shown in Figure 2-1. The sample positions are given for each of the major techniques.*

Sample Positions

Process	*X (cm)*	*Y (mm)*	*Z (mm)*	θ (°)	Other
XPS/UPS	0.0	0.00	0.00	0	Source 10.7mm
Ion Sputter	-8.3	13.83	1.40	-60	
LEED (Nominal)	-18.1	-10.18	0.90	91	Optics full in
Metal Evaporator	-17.8	-7.40	-11.25	181	Shutter 235
Doser	-31.4	-9.56	12.40	49	
Mass Spectrometer	-29.0	0.67	7.40	0	RGA 0 mm

2.2. Instrumentation and Techniques

A brief summary on how to properly perform the given techniques are discussed, this is meant to be used as a supplement to the instruction manuals for each technique rather than a replacement.

2.2.1. X-Ray photoelectron spectroscopy

2.2.1.1. Considerations

X-ray photoelectron spectroscopy is probably the most dependable analysis technique on the system. That is not to say it is without issue. For example, in one common problem, the voltage supplied to the communication transceiver (EC10) falls below the 24 V required to maintain operation. In this instance the software freezes and the spectrum stops being recorded. The only way to correct this is by opening up the HSA 350 power supply to adjust one of the potentiometers. This needs to be performed approximately every 6 to 12 months. A second issue is that the cooling water to the x-ray source requires a constant flow of at least 2.7 litres per minute. Below this value the interlock will halt the x-ray source. Commonly, filters and connectors along the water lines will require cleaning, since they may become clogged with sediment, causing the flow to fall below its minimum value. From my experience the first thing to check is the filter in the water interlock case. If this does not solve the issue then some of the brass fittings, usually the elbows, in the same case need to be disassembled and the sediment removed. The filter needs to be cleaned every 4 to 8 months and the brass fittings every year or two.

If an experiment is underway and taking the time to check these filters and fitting would ruin the experiment, then the relief valve on the chiller may be tightened, increasing the flow (and pressure on the line). Normally this is not recommended and cleaning should be performed as soon as possible. We have only one chiller providing cooling water to the x-ray source as well as both turbo pumps and the evaporator. In order to achieve the necessary flow rate, the pressure limiting valve on the chiller pump has had to be set to about 95 PSI. This is already above the 80 PSI, that some of the evaporator tubing is rated for, and so increasing it much more than this, though possible, is asking for catastrophe.

Operating the XPS system and acquiring reproducible spectra between experiments requires very specific attention to sample position and angle, as well as the position of the retractable x-ray source. It is important that the sample be at the appropriate focal plane of the analyzer lens system (40 mm from entrance), or changes in sample mounting or puck position on the stage will be seen in the spectrum. It is a relatively time consuming task, but each time a spectrum is to be acquired after moving the sample, the position should be optimized. This is accomplished by acquiring a fixed energy scan (photoelectron intensity at constant binding energy measured in time) at a sample peak energy, while simultaneously adjusting the sample position. A maximum intensity should be found, and in this way spectra will be very reproducible. Most of the time only small corrections are required and it is often sufficient to optimize the sample position by examining the background during a spectrum acquisition, ensuring it is of consistent intensity.

2.2.1.2. Acquisition parameters

As mentioned the sample needs to be in the proper focal plane, however the x-ray source should also be as close to the sample as possible in order to maximize the number of excitation photons reaching the sample surface. A design flaw in the Specs/RHK system is that these are mutually exclusive. Ideally the source head could be advanced as close as possible to the sample as it rests in position at the focal plane of the analyzer. However because the source head is positioned too low, it will crash into the edge of the sample stage before converging on the sample. Only by moving the source away from the sample and thus lowering the x-ray flux can the sample be held at the focal plane. If the sample position is lowered with respect to the focal plane, the source may be moved closer, but counts are lost as a result of the poorer of focus. It turns out that there exists a balance between measured intensity gained by bringing the sample closer into focus, and signal lost by moving the source away. The appropriate nominal absolute positions are angle dependant since the sample and source can be moved closer to the focal plane at larger angles due to the geometry of the sample stage, this affects the z-position of the holder. The nominal absolute z-values are given for a range of angles in Table 2-2.

Table 2-2 *Ideal sample position in Z-direction (nominal absolute and relative) for angle resolved studies.*

θ	Z (mm)	ΔZ (mm)
0°	10.15	0
-10°	12.85	2.7
-20°	14.525	4.375
-30° <	15	4.85

There are several other parameters of importance for XPS and they are summarized in Table 2-3. The x-ray source requires specific anode voltages and emission current settings, the higher the total power the higher the x-ray flux, however there is a limit of 300 Watts, and 350 Watts for the magnesium and aluminum anodes respectively. Lens focus parameters and electron pass energies are input in the software, whereas iris, entrance and exit slit settings need to be adjusted manually with dials on the analyzer. The typical values used will result in measurement of photoelectrons emitted from a circular area on the sample of about 4 mm – 5 mm in diameter at a pass energy of 10 eV. Given that the other parameters remain the same, it seems that a larger pass energy accepts electrons from a wider detection angle, resulting in a spot size estimated to be between 5.5 mm and 6.5 mm at 30 eV. These values are measured by examining the signal intensity of an Al ring of known inner diameter as a function of x and y position.

In addition to hardware and software settings, parameters for the measurement scan itself such sampling time and energy resolution, are important. Typical scan values used for acquisition are also summarized in Table 2-3. A figure of merit plot compiled by V. Christ and available in the web [1] shows that the greatest return on investment in terms of improvement to signal to noise ratio (S/N) arrives when exactly 4 scans of the same region are performed consecutively then averaged. Though averaging a larger number of scans beyond this will of course improve the S/N, these improvements become increasingly more costly in terms of the amount of scan time required, so that 4 scans will give you a S/N ratio of 2 (as compared to a single scan) but 9 scans will only yield a ratio of 3. This is a result of the $\sqrt{n}$ dependency of the signal to noise ratio in spectroscopy in general, where n is the number of measurements. Whenever possible 4 consecutive scans were taken of each spectrum.

Table 2-3 *Typical XPS acquisition parameters.*

Source		
	Mg	Al
Voltage (kV)	14.26	12.51
Current (mA)	21	26
Analyzer		
Entrance Slit	7 mm x 20 mm	
Exit Slit	open	
Iris	32 mm	
Lens Mode	medium area	
Analysis Mode	fixed analyzer transmission	
Pass energy (eV)	10 or 30	
Scan		
	Survey	High Res.
Step Size (eV)	0.3-.5	0.1-0.25
Dwell Time (s)	0.1-0.4	0.2-4.0
# of Scans	1	1- 4

2.2.1.3. Calibration

The x-ray photoelectron system has a host of possible calibration requirements, extending from the power supplies which drive the lenses and necessary retarding voltages, to the binding energy and intensity scales.

The power supplies are generally not supposed to require calibration after they have been set by the manufacturer, however several issues have arisen at one point or another which have required that the output voltages be checked. In many cases poor power supply performance will exhibit symptoms in the measured spectra, often as errors in the binding energy positions of known peaks. Therefore both the power supply and binding scale calibration can be considered in unison.

Anthony and Seah of the National Physical Laboratory published a paper in 1983 [2] which has since become the de facto standard for binding energy scale calibration for XPS. They developed a metrological energy analyzer which they used to determine the absolute binding energy (BE) values for a series of photoelectron transitions in copper, silver, and gold. These positions span the normal XPS energy range, and therefore may act as reference peaks against which to calibrate binding energy scales.

The methodology involves measuring the XPS spectra of pure, Ar^+ sputter cleaned, foils of the reference metals and adjusting the system binding energy scale so that the experimental peak positions match those reported by Seah.[3, 4]. The type of x-ray source has been shown to modify the listed positions and so it is important to use an Al source to match the literature experimental conditions. In a completely uncalibrated system, BE differences between measured and literature values, will arise as a result of a combination of offset and gain errors in the relevant power supply, as well as an offset related to the work function of the analyzer. In the absence of power supply errors, the spectrum would solely be offset by the analyzer work function, that is, the minimum energy an electron must have in order to be detected. In this case every peak across the measured spectrum would be offset from their true value by the same amount. That quantity can be entered into the scan control software (Specs Lab 2) as the value for the analyzer workfunction, and a correction automatically made. If the peak positions are not offset by the same magnitude then there exists a gain error in the power supply, which can also be modified in the software. Any offset errors of the power supply itself will appear coupled with the analyzer workfunction measurement, and will be adjusted simultaneously.

The pass energy used in spectra acquisition by XPS can also modify the measured electron energies, with a shift from the true value being linearly proportional to pass energy. For our system the energy shift divided by pass energy was found to be 0.00257, this may be entered into Specs Lab 2 for automatic correction. In Figure 2-4 the Ag $3d_{5/2}$ peak is shown for a series of pass energies after all corrections and calibrations have been performed. It can be seen that all peaks lie within the reported value for the Ag $3d_{5/2}$ transition of 368.27 +/- 0.02 eV.[2]

Binding energy scales can be calibrated against a reference material and the appropriate values set in the acquisition software (Specs Lab 2), thereafter peak positions measured on conductive and grounded samples will be accurate. However this accuracy is not maintained when studying non-conductive samples, since in such systems electrons which leave the surface through the photoexcitation process cannot be replaced by conduction electrons. The sample therefore accumulates a (positive) surface charge which interacts with photoelectrons, causing them to slow down. The net result is an overall decrease in the electron's kinetic energy, and hence an apparent shift to higher binding energies.

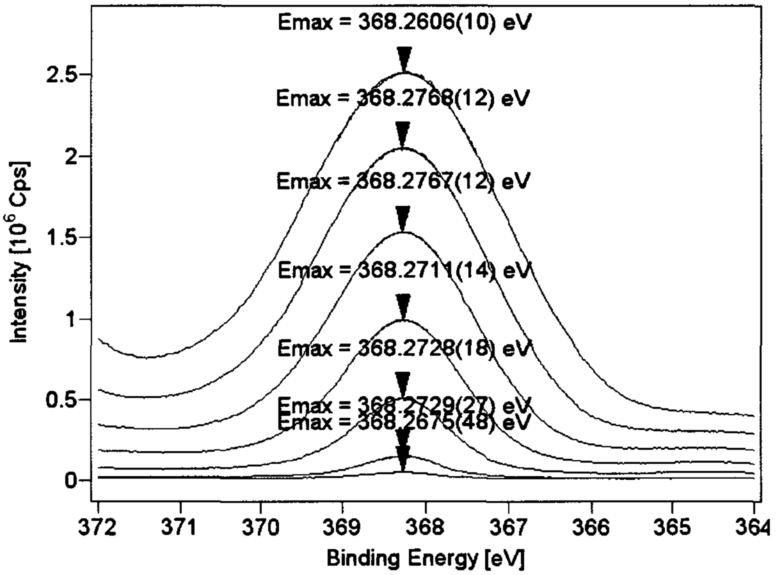

Figure 2-4 *XP-spectra of the Ag* $3d_{5/2}$ *transition measured at a series of pass energies (5,10,20,30,40,50,60) eV, with the binding energy scale corrected for each. The peak positions match the literature value (368.27 +/- 0.02 eV) within error.*

Methods to deal with such charging vary; compensation techniques may use an electron flood gun to neutralize the charge, or heating may cause the sample to become conductive. Most commonly used however, are internal standards, these are necessary even when neutralization or heating is implemented to confirm whether sufficient neutralization or conductivity has been achieved. In some instances, a metal such as gold is deposited on the surface, but more frequently the binding scale can be calibrated with adventitious carbon, that is, carbon based species which accumulate on any surface in air or even in vacuum (especially those which use oil pumps). An ASTM standard has been developed for charge compensation, used also by NIST, it sets the binding energy for adventitious carbon at 284.8 eV.[5] The drawback to this technique is that such carbon may exist in more than one state, graphite or hydrocarbon for example may be separated by 0.5 eV to over 1 eV and therefore this method is not always accurate. For studies of single crystal YSZ we have selected the Zr $3d_{5/2}$ peak for reference, and in common with other studies, have set it to 182.6 eV.[6, 7] No rigorous investigation of the binding energy of the Zr $3d_{5/2}$ transition has yet been performed, and there will be deviations between samples as a result of differences in yttria content. It is therefore estimated that systematic errors in peak positions could be as high as 0.2 eV. In this work, at the points where peak positions are reported, the errors mentioned alongside these values comprise the estimated random error and do not include the contribution from systematic errors.

Throughout this thesis we report surface compositions in terms of atomic percent values. As discussed in chapter 1, in deriving these values from the integrated peak intensities, the calculation depends upon knowing the relative sensitivity factors (RSFs) for each element of the system under study. For YSZ(100) this is not a trivial task since it is composed of three energy dependant components; the photoexcitation cross section, the inelastic mean free path, and the transmission function of the analyzer. These factors have been described in more detail in Chapter 1, some of which are not well understood for YSZ.

Scofield has published a list of theoretically determined cross section values[8] that are included with the CASA XPS [9] software used for spectrum analysis, and these have become well tested and accepted values. Some controversy arises with the IMFP for YSZ, from which some theoretical [10-18] and experimental [19] models provide lengths of less than 2.5 to 0.7 nm across the relevant energy range. Others however have proposed lengths as high as 7 nm.[20, 21]

The transmission function of the analyzer, which is the efficiency at which the analyzer detects charged particles of a specific energy, is usually determined by the manufacturer. For some reason this was not even nominally performed for our system, though in correspondence with the manufacturer, the function has been determined to take the form:

$$T(E_k) = A \times E_p \times \left(\frac{(E_k - wf)}{E_p} \right)^B$$

Where E_p, E_k, and wf are the pass energy, the particle (electron) kinetic energy, and the analyzer work function respectively. Parameters A and B are lens mode related parameters. Initial methods to perform calibration were based upon acquisition of individual spectra for clean gold, silver and copper samples. If the transmission coefficient is constant across the entire spectrum then each transmission peak in a single spectrum, can be integrated and divided by its corresponding cross section and IMFP to produce the same value. That is, since each transition represents 100 atom % of the homogeneous sample under study, each corrected peak area should yield the same value. The transmission function is not constant and has the form given above, however since the fully corrected values should be identical, then a least squares minimization can be performed to determine parameters A and B . This is achieved by minimizing the quantity:

$$\sum \left[\frac{T(E_i) I_j}{T(E_j) I_i} - 1 \right]^2 \textit{for all i and j}$$

Here $I_{i \text{ or } j}$ is the integrated intensity for photoelectron transition i or j, in the acquired spectra. The parameter A serves only to scale intensities for spectra taken at different pass energies, and will not affect calculations of atomic concentration from intensity ratios within the same spectrum. The resulting transmission function for the most frequently used set of lens and slit settings is plotted in Figure 2-5 for the relevant range of energies over which quantification of YSZ is performed.

There are many factors affecting quantification by XPS, from the transmission function, IMFP, to the necessary, yet inaccurate assumption (for YSZ) that the region probed is homogeneous. Practically speaking using XPS to determine absolute concentration is generally not worthwhile. Not only are there errors associated with the instrument itself but even in the way that spectra are fit. In fact NIST has attempted remedy this by creating an open trial in which they offer a set of spectra to be downloaded and fit according to an individual users techniques. The results may then be returned for comparison with other values, in this way fitting errors may be estimated. However since different samples will require different fitting techniques even this will not necessarily improve matters entirely.

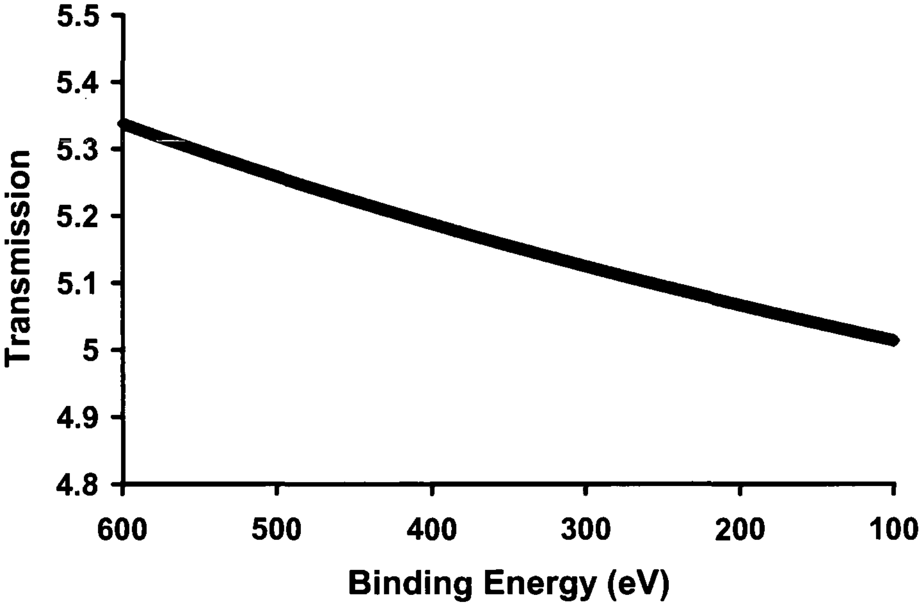

Figure 2-5 *Plot of the transmission function as determined from least squares minimization of integrated peak intensities for a series of spectra with transitions spanning the range of interest.. Parameters A and B were found to be 1 and -0.14 respectively. Acquisition conditions (Medium area lens mode, 7 mm x 20 mm entrance slit, full open exit slit, and 10 eV pass energy)*

It is much more accurate to view quantification reported in this thesis in terms of changes between scans, rather than as absolute compositions. The errors reported with each quantification are random errors derived from analysis of the background during peak fitting. These errors should be considered accurate when observing changes in the spectra, however in absolute terms an additional 5%-15% may be expected due to systematic errors.

That being said, it has been found that concentrations calculated using the Zr and Y 2p , or the Zr and Y 3d transitions are reproducible to within approximately 3 % - 5 % even though these peaks are separated by almost 200 eV. This indicates that energy dependant errors are quite small over this range. In addition, many of the concentration values measured are physically reasonable; for example, measured atomic concentrations of thermally oxidized YSZ have been found to be within 0.5 atom % to 1.5 atom % of bulk stoichiometric values. It is therefore reasonable to assume that absolute quantification values are far more accurate than can be guaranteed.

An additional important calibration that needs to be performed about once a month is the optimization of the detector voltage. That is the voltage which has to be applied to the single channel detector to produce an appropriate detection efficiency. In order to determine this optimal value, a voltage scan is performed in which the potential applied to the detector is varied while simultaneously monitoring the number of electrons detected. As seen in Figure 2-6 the plot increases to a plateau, according to the user manual the optimal voltage should be set just beyond this point. This is somewhat arbitrary and so a quantitative value based upon the point at which the slope of the tangent is equal to -25 Counts per Second Volt (C/Vs) has been selected to improve repeatability. If a working voltage is selected beyond this point the lifetime of the detector will be reduced.

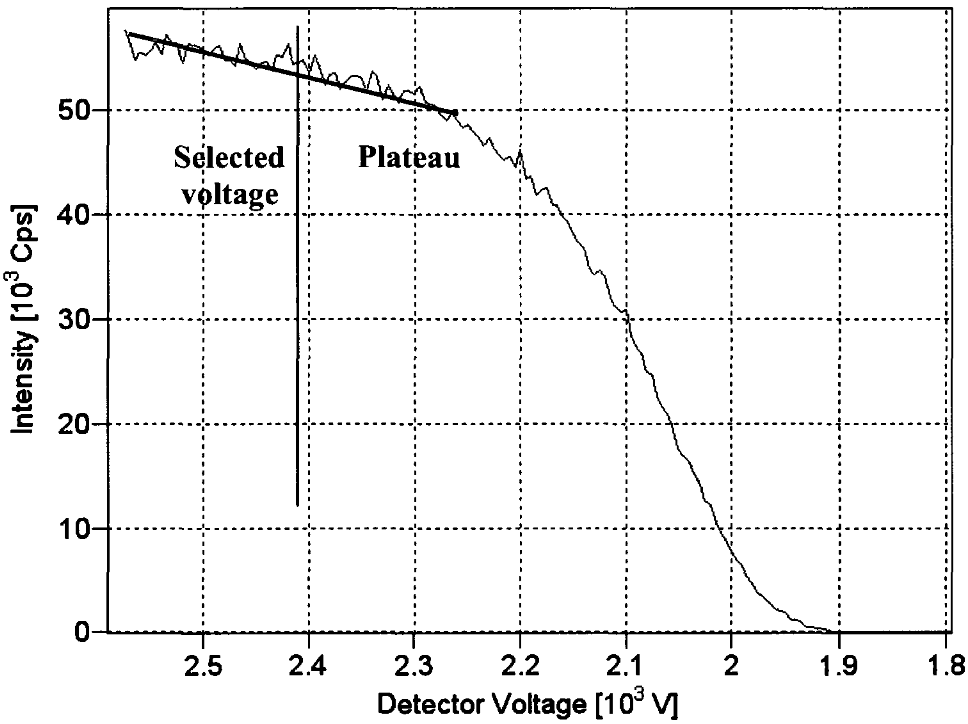

Figure 2-6 *Detector voltage scan demonstrating the shape of the curve and the working point of the detector selected based upon the voltage value at which the slope of the tangent becomes* $-25\ CV^{-1}s^{-1}$.

As a final note, calibration of intensity and binding energy scales are dependent upon lens, slit, and pass energy settings, and therefore calibration should be performed under the same acquisition conditions as experimentation. Without knowing exactly which conditions might be required for experiments beforehand, and because standard sample preparation can be time consuming, calibration data has been collected for several lens and slit combinations. As an example set, calibration values for the pass energy dependence of binding energy is shown for a variety of lens/slit combinations in Table 2-4.

Table 2-4 *Slope values in the linear relationship between binding energy shift and pass energy for a series of lens and slit combinations.*

Slit	Lens			
	Medium Area	**High Magnification**	**Medium Magnification**	**Large Area**
5/Open	0.00641	-0.00171	0.00157	0.00574
6/Open	0.00028	-0.00251		
7/Open	0.00257	-0.00154		
8/Open	0.00375	-0.00135	0.0018	

2.2.1.4. XPS peak fitting

Proper fitting of acquired YSZ spectra is not a trivial task, especially when several complicated transitions may be occurring simultaneously. In some cases up to a hundred spectra have been considered in detail and so the current fitting technique has actually been determined as an average set of parameters over these spectra, and they are therefore likely quite accurate.

In order to develop a proper fitting procedure[22] first an understanding of the resolution of the spectrometer must be obtained. This allows one to estimate the maximum width that should be assigned to an individual peak, beyond this width a second peak will have to be fit. One of the standards for characterizing the resolution of the spectrometer, is the full width at half maximum of the Ag $3d_{5/2}$ peak on a sputter cleaned sample. This has been measured to be approximately 1.14 eV as seen in Figure 2-7 for the conditions at which high resolution spectra of YSZ are normally acquired.

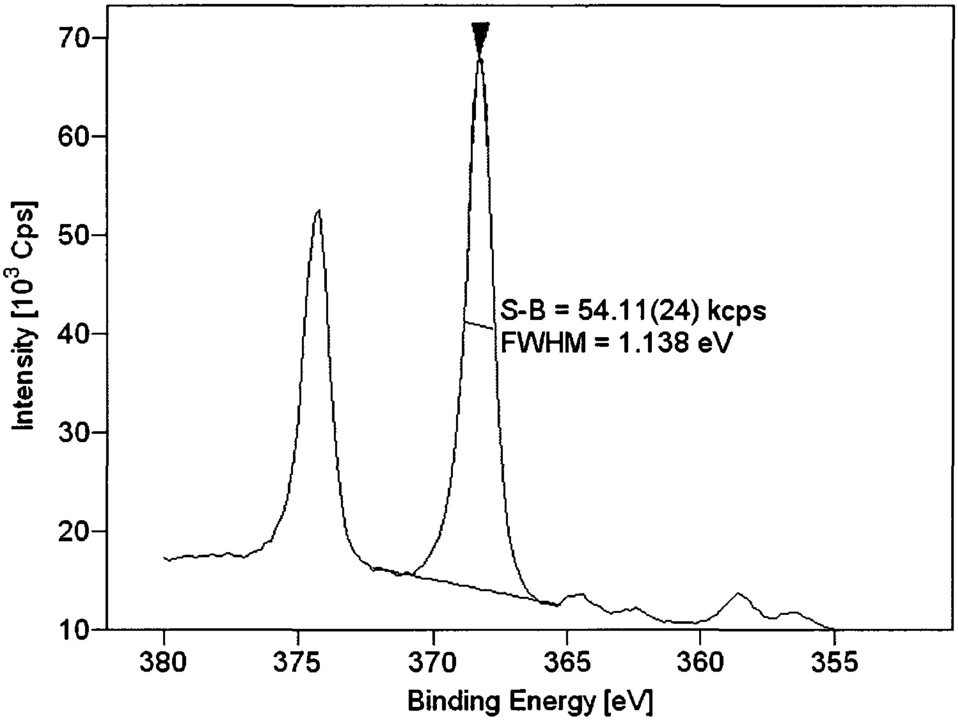

Figure 2-7 *Full width at half maximum of a sputter cleaned high purity Ag foil (99.999 %) demonstrating the expected resolution for the medium area, and medium magnification mode, acquired with a pass energy of 10 eV. Ag 3d envelope with the 5/2 peak FWHM indicated.*

Because the natural line width of the Ag $3d_{5/2}$ transition is very small it is useful for determining the spectrometer resolution, however if a natural line width is actually greater than the spectrometer resolution, then fitting more than one peak to the transition would be an error. Literature values for the natural full width at half maximum have been sought for relevant YSZ peaks in order to determine whether measured peak widths are broadened due to the spectrometer or are actually natural line widths.[23-25] As well, the catalysis centre at the University of Ottawa has acquired, during my studies, a Kratos Axis XPS equipped with a monochromated source. This system has a better resolution than the Specs spectrometer and therefore measurement of YSZ spectra of the same sample in both machines should offer a way to determine which peaks are natural or are spectrometer broadened. If they are measured to be the same, then a natural line width is concluded.

Table 2-5 *Peak fitting parameters for a YSZ(100) single crystal. The peak shape is written as a mixed Gaussian/Lorentzian product, with the form GL(n) where n=0 represents a pure Gaussian and n=100 a pure Lorentzian. The Zr 3d and Y 3d envelopes are composed of doublets with the 3/2 spin peak being fully defined by the 5/2 spin. The binding energy scales are calibrated by setting the Zr* $3d_{5/2}$ *4+ state to 182.6 eV.*

Parameter	O 1s	C 1s	Zr 3d $_{5/2}$	Zr 3d $_{3/2}$	Y 3d $_{5/2}$	Y 3d $_{3/2}$
Max FWHM (eV)	1.5-1.6	1.5-2.5	1.4	1.4	1.45	1.45
Background	Shirley					
Shape	GL(30)	GL(50)				
Doublet Separation (eV)	n/a		2.39		2.05	
Area Constraint				3d5/2 x 0.6886		3d5/2 x 0.6889
Nominal Position	530.5	284.8-286.0	182.6	3d5/2 + 2.39	157.5	3d5/2 + 2.05
Scofield RSF	2.85	1	4.33	2.97	3.7	2.54

Measurement has shown that, with the exception of carbon, all line widths decrease when measured with the Kratos spectrometer as compared to the Specs system. Using this information, a set of parameters for peak fitting have been developed. Fitting is performed using CASA XPS software written by Neal Fairley [9], and the parameters used throughout this work are summarized in Table 2-5.

The fitting procedure for a YSZ(100) sample which has not undergone significant reduction is as follows:

- Identify, label and fit Shirley type background to each transition envelope which requires quantification. These are usually the O 1s, C 1s, Zr 3d and Y 3d regions.
- Fit separate background to shake-up peaks corresponding to the regions in the previous step. A shake-up peak arises from photoelectrons that originate from an

atom that is left in an excited state. O 1s , Zr and Y 3d envelopes each have a shake-up peak in YSZ.

- Perform satellite subtraction from the raw data.
- Insert and fit components according to the parameters listed in Table 2-5.
- Calculate random error.

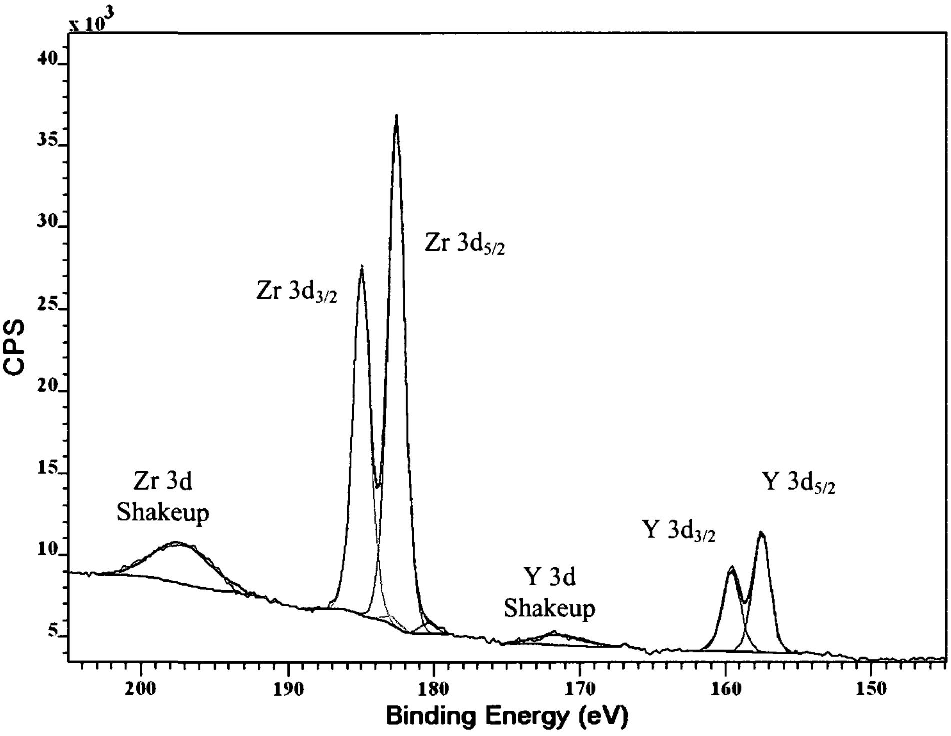

Figure 2-8 *Fit XP-spectrum of the Zr and Y 3d region. Peaks are fit according to the parameters listed in Table 2-5, the shape of the Shirley background is most visible under the Zr envelope.*

If the sample has undergone significant reduction as can occur for zirconia, then additional peaks of the same form listed in Table 2-5 should be added accordingly. For the reduction of Zr^{4+} (ZrO_2) to carbide or Zr^0, a series of intermediate peaks will also be present which represent the Zr^{3+} (Zr_2O_3) and Zr^{2+} (ZrO), (any Zr^{+} overlaps with the ZrC) peak. Each of these is down-shifted consecutively from the other by 0.9 eV to 1.2 eV.[26]

Often only elemental quantification is necessary, and there is no regard to state specific concentrations. In this case the error is only increased slightly by fitting a background without component peaks, quantification will then be calculated based upon any area above the background in the selected region. This is less time consuming than fitting individual peaks when there is no scientific merit to do so. The random quantification errors are calculated in CASA XPS by a Monte Carlo technique based upon the expected form XPS noise should follow.

2.2.2. Ambient atomic force microscopy

Ambient atomic force microscopy is performed on an Agilent 5500 microscope normally in intermittent contact (tapping) mode with tips oscillating at a nominal resonance frequency of 160 kHz. The highly doped silicon cantilever tips are sometimes coated on the back side with an aluminum reflex coating in order to improve the magnitude of light reflected from the tracking laser, and therefore improve the signal to noise ratio in the detection signal.

In imaging a new material for the first time and important step is to determine which AFM probe tips work best for the sample under study. Usually this is related to how hard the sample is and the size of the expected features. Of the 10-20 different types of tips tried (Budget sensors, Olympus, MikroMasch, AppNano, Vista), the most consistent imaging has been achieved with Nanosensor brand, model NCL tips or their very sharp (and expensive) SS-NCL probes. The NCL cantilevers have a reported nominal tip diameter of less than 7 nm, while the SS-NCL tips are less the 2 nm. The SS probes are almost $100 USD each and therefore should only be used on samples when the added resolution might be worth while. Because they are so sharp and the sample so hard, the tip may only last for a few hours of imaging before blunting.

Since YSZ(100) single crystals is very hard, damage to the tip is possible when tapping against the surface during imaging. In order to minimize the tapping force, it has been found useful to retract the tip slightly after approach and reduce the setpoint (amplitude offset) until images just become clear. Below this value the tip will interact too strongly with carbon overlayer and imaging will be unstable, above this point the tip dulls too quickly.

The Agilent 5500 AFM is what is called an open loop system, in which the dimensional scales measured are calibrated based upon the relationship between the length of the scanning piezos and the voltage supplied to them. Calibration of this scale is based upon sample standards of known dimension. The microscope had just been delivered when it was used for quantitative measurement of surface features and therefore had been recently calibrated by the manufacturer. However, the z-calibration (heights normal to the surface) have been double checked by measuring the step heights of annealed gold on mica and have proven to be accurate to within approximately 20 pm.

2.2.3. Ultra high vacuum frequency modulated atomic force microscopy

Non-contact AFM is performed with the RHK model UHV 350 scan head capable of both AFM and STM by simply changing the probe type (cantilever or sharp wire). Though scanning and data conversion is performed with RHK's SPM 1000 control electronics, Nanosurf easy PLL FM control and FM sensor electronics are used to drive the cantilever oscillations and detect the feedback signal. Non-contact AFM is performed in frequency modulation mode (FM-AFM) in which the measured feedback is the shift in the probe cantilever's resonant frequency. This shift increases with larger forces of interaction between the tip and the sample. The change in frequency is measured with respect to the free resonance frequency measured far away from the sample. Cantilever oscillations are driven by the Nanosurf electronics in self oscillation mode, in which the detection signal (from the cantilever) is fed into the drive signal (to the piezo which excites the cantilever). The electronics in this case simply maintain a constant amplitude by controlling the amplification of the detection signal. Simultaneously, a constant phase shift (between drive and detection signals) is produced, and as a result, the tip self-oscillates.

The setpoint corresponding to the frequency shift is entered in the associated Nanosurf software which is run in conjunction with the RHK imaging software. The Nanosurf electronics convert deviations from this setpoint to a proportional -10 V to +10 V DC signal which is fed into the RHK scan controller and is used as the feedback signal during imaging.

The cantilever tip used in experiments is cemented with conductive UHV compatible silver epoxy on a tip holder outside the chamber. The mounting of the tip on its holder is critical, so that once inside the chamber it may be appropriately aligned with the laser and detector. The RHK system comes with an alignment jig which recreates the same geometry between the tip, laser and detector which exists inside the chamber. Only a thin amount of epoxy should be used when mounting the tip since the glue requires curing at 140 °C for 20 to 30 minutes, and curing often causes the position of the tip to shift out of alignment. Using the thinnest layer of glue possible helps reduce the possibility of the tip shifting too far. In practice one to two tips out of three come out of alignment after curing and need to be discarded, as a result usually two to three tips are mounted at once to increase the probability that at least one will be good. In addition to the alignment of the cantilever it is also important that the height to which it extends from the end of the tip holder be about 1.3 mm. If it is too short the approach range of the scan head will not be sufficient to come into feedback range of the surface, if it is too long then the tip will crash before the scan head can come to rest on the sample puck.

Tips used in vacuum should not have a reflex coating, especially for variable temperature studies, since any thermal gradients across the tip will result in strain due to differences in thermal expansion between the tip and its coating. A shift in the resonance frequency will result. The tips used with the most success have been Budget sensor brand tips model FM. These have a nominal resonance of 50 Hz, with an added benefit of having a sufficiently small spring constant to be used for contact mode AFM if desired. Nanosensors uncoated NCL tips have also been used with some success.

The best imaging results are obtained when the Q factor for the cantilever is high. This requires determination of the best resonance peak for the tip in vacuum. Since a cantilever in vacuum has several resonant modes, a scan of the frequency response of the cantilever in vacuum allows some rough determination of the best resonance peak. This can then be fine tuned by shifting the drive frequency while simultaneously monitoring the detected signal for an amplitude maximum. Both the input and output channels are monitored on an oscilloscope during tip optimization and imaging.

2.2.4. Ultra high vacuum scanning tunneling microscopy

Scanning tunneling microscopy has been used with very good success and has become the microscopy of choice in UHV over FM-AFM. A detailed description of its setup and performance will be discussed in chapter 4, however supplemental information is provided here.

STM is performed at elevated temperatures using the RHK UHV 350 AFM/STM scan head. Unlike FM-AFM, all necessary electronics for scanning and feedback detection are housed in RHK's SPM 1000 control system. The only external electronics are the amplification circuits. These are the RHK IVP 300 pre-amplifier which attaches directly to a feedthrough on the chamber, and a secondary stage multigain amplifier. The short distance between the tunneling junction and the first amplifier, minimizes the noise pickup before amplification, hence improving the signal to noise ratio. As well as an amplifier, the IVP 300 acts as a current to voltage converter providing one volt DC for every nano-Amp of tunneling current.

Calibration of the dimensional scales was initially performed by the manufacturer using pitch gratings and by achieving atomic resolution of known materials such as Si(111). Since the atomic spacing of Si(111) is well known measurement of the spacing by STM can be used to calibrate the XY scales of the scan head. In the z-direction single atomic steps of Si(111) or of highly ordered pyrolytic graphite may be used.

Because temperature will affect the calibration of the scan piezos, calibration should be performed at the same temperature measurement will take place. For YSZ(100) this temperature is 275 °C to 300 °C. Atomic resolution imaging of Si(111) under the same conditions were attempted for calibration purposes. This turned out to be very difficult, since for creating similar heat transfer conditions, Si(111) had to be mounted in the same manner as YSZ(100). Unfortunately the method for cleaning and annealing Si(111) in order to create the conditions for achieving atomic resolution, is not entirely compatible with the fashion in which YSZ(100) is mounted. After more than a week of trying unsuccessfully, it was decided that height scales could simply be referenced to a YSZ(100) atomic step, and XY scales would not be calibrated. However measurements of the same YSZ (100) sample by both the calibrated Agilent AFM and by UHV STM indicate that that step widths are reasonably well matched. It is therefore estimated the X/Y scales to have an error of approximately 10 % - 20% in the 100 nm to 1.5 um range.

2.2.4.1. STM tip preparation

One of the main criteria for achieving high resolution images in STM is having a sharp tip. Ideally it should be terminated by a single atom, in which case the vast majority of tunneling current will then be achieved between this atom and the nearest surface atom. However, as the tip becomes more blunt the number of atoms which terminates the wire increases and the point on the tip through which tunneling occurs delocalizes accordingly. Each atom on the tip at the same distance to the surface will contribute to the tunneling current equally, in effect the viewed image will be a convolution of images obtained from each tip atom through which there is significant tunneling. The maximum resolution in an image will therefore be determined by the area covered by this group of tip atoms. As a result it is critical to make the tip as sharp as possible, limiting the area through which tunneling occurs.

The most common technique to produce a sharp tip is by simply cutting a wire on an oblique angle while simultaneously pulling the cutters and wire away from each other. This causes a messy tear-off that can result in an atomically sharp tip. Though obviously very quick, the draw-back to this technique is that it is not very controlled and the probability of obtaining a sharp tip is not very high.

For more controlled and reproducibly sharp tips electrochemical etching is usually the technique of choice. [27-29] The underlying principle is that a metallic wire can be placed in an electrolyte solution along with a counter electrode, when a sufficient potential difference is placed between the metallic wire and the counter electrode an electrochemical reaction will proceed which causes metal wire to etch away. Because etching will occur preferentially at the surface of the solution, eventually the weight of the wire in the solution will be too great to be held by the portion of the wire at the interface, and the wire will pull apart. If etching is immediately halted at this point the wire should reproducibly come to a very sharp point sufficient for atomic resolution of many materials.

Etching needs to be immediately stopped after breaking, otherwise tip blunting will occur, therefore etching requires a type of trigger circuit which monitors the reaction and turns off the driving voltage at the appropriate point. Several types of circuits exist and they are generally based upon detection of the point at which break-off occurs by monitoring the etch current and immediately halting the bias voltage.

We have designed a tip etch circuit based partly upon a design from the Möller group at the University of Essen and found in a dissertation.[30] The schematic is shown in Figure 2-9. The circuit basically acts as a triggered voltage supply which monitors the etch current and turns off the etch voltage when a sharp change occurs (e.g. when the wire breaks apart). The voltage associated with this change must be larger than a threshold voltage set by the user via a potentiometer otherwise the etch voltage will be maintained. The threshold voltage ensures that noise or small changes in the tip that do not correspond to a drop off, do not cause etching to halt.

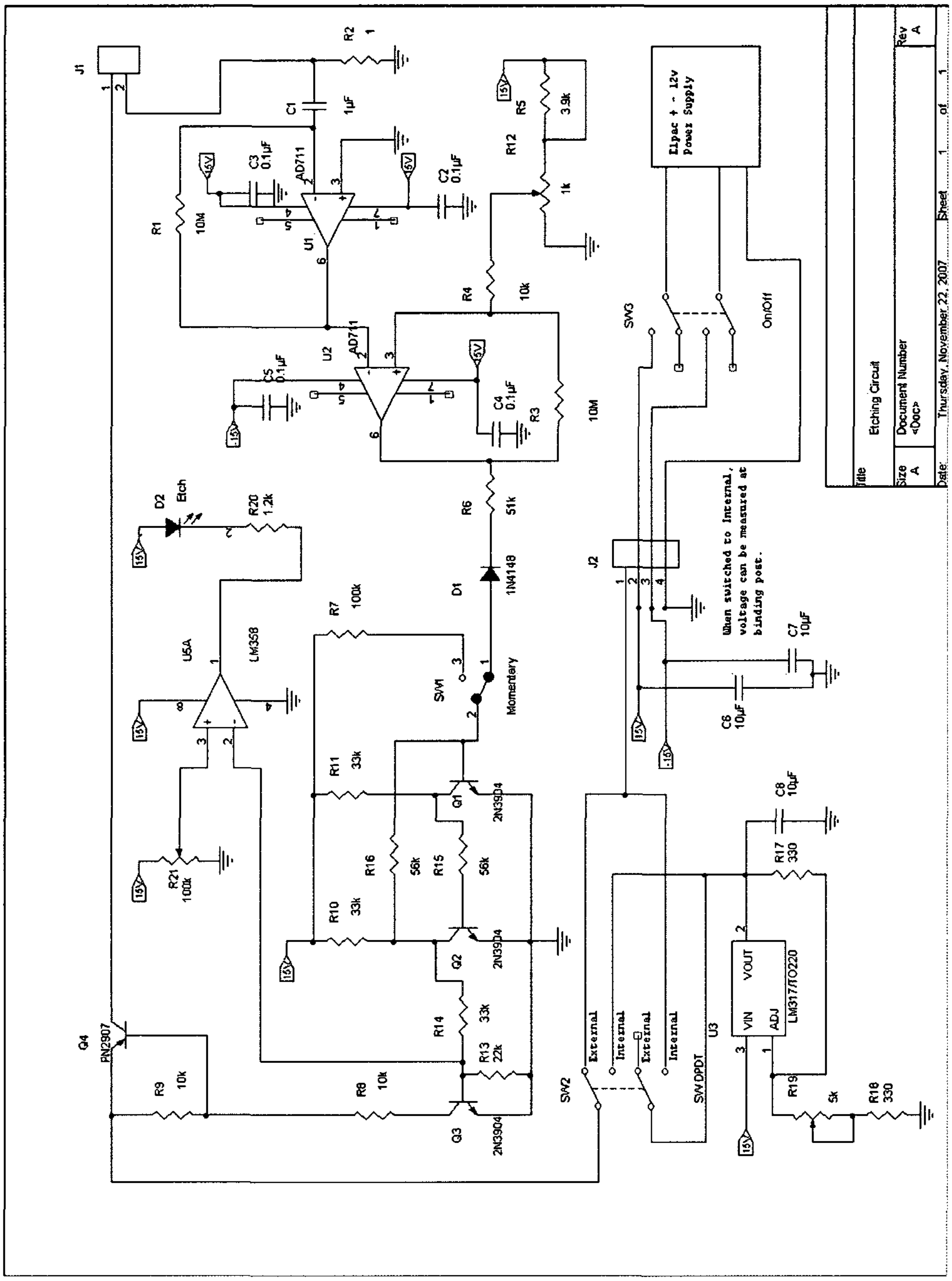

Figure 2-9 *Tip etch circuit which is used to apply the etch voltage and halt it immediately after etching is complete.*

The device supplies a DC voltage which can only etch specific metals; throughout this thesis either tungsten or platinum iridium alloy wire (0.25 mm diameter) is used to make tips. Of these only tungsten can be etched by a DC voltage, with Pt-Ir tips required to be cut in the manner described above.

The tip etch setup is shown in Figure 2-10. The etch circuit is mounted in an aluminum enclosure that has a common ground to the power supply. Coax cables connect the circuit to the tungsten wire and the counter electrode. Proper shielding is necessary since the etch current becomes very low near the drop off point and noise may cause the circuit to trigger arbitrarily. The tip wire (W 99.98 %) purchased from ESPI metals is mounted inside a small gauge needle, which is itself insulated with Teflon tape and mounted inside a coax cable with the core removed. The needle and coax shield are soldered and crimped to a male RG 58 connector allowing easy removal from the support frame which holds a female RG 58 connector.

Attempts were made with immersing part of tip wire into a beaker of solution (3 M KOH) for etching using a graphite rod as a counter electrode. However the immersed portion of the tip would crumble somewhat erratically as it was etched, causing the circuit to trigger arbitrarily. Instead a platinum wire formed into a loop is used as the counter electrode, the tip wire is placed within the centre of the loop, then they are both dipped momentarily into the KOH solution. Capillary forces hold a thin film of solution in place within the loop, and this is sufficient to etch the tip. An added benefit is that when drop-off occurs, the portion of the wire which has broken off can be caught and used as a sharp tip as well. In this way two tips may be formed for each etch cycle.

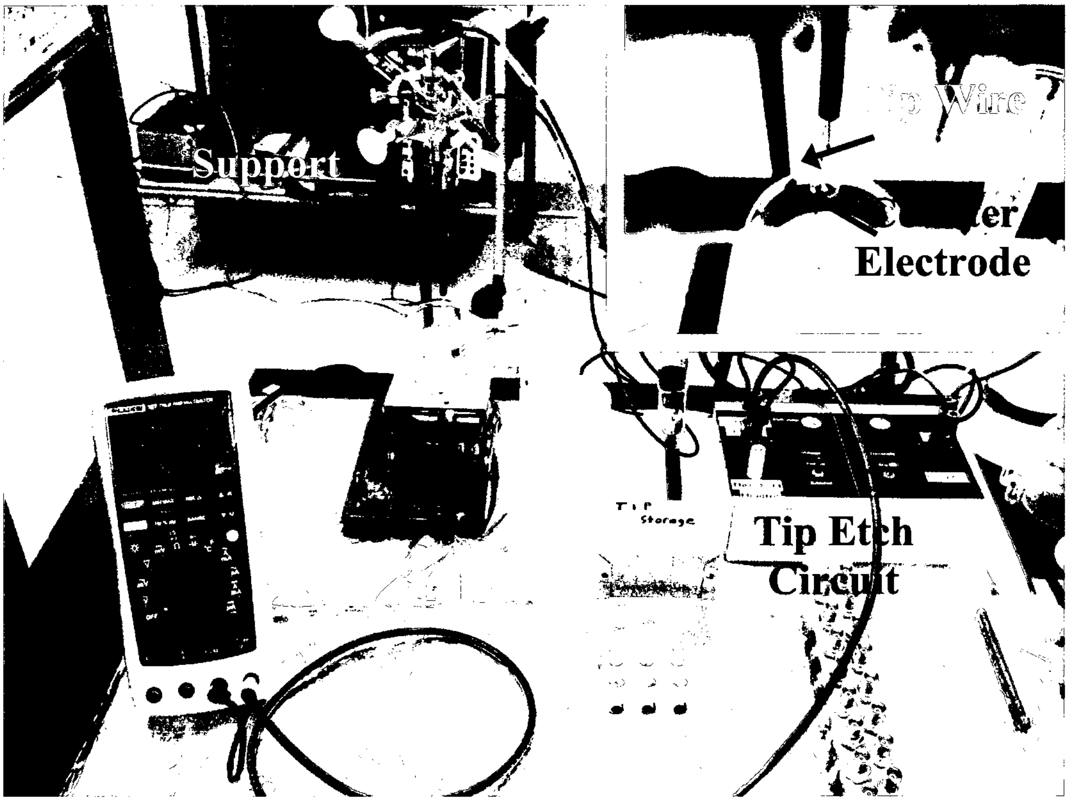

Figure 2-10 *Experimental setup to electrochemically etch tungsten STM tips. The etch trigger circuit applies a voltage across the tip wire (+) and the platinum loop which acts as a counter electrode (-).*

As a product of the electrochemical reaction, the etched tips have a thick oxide layer formed on the surface which acts as an insulator. Removal of this oxide can be achieved by heating the tip in vacuum to approximately 600 °C - 700 °C; beyond this temperature recrystallization may occur, dulling the tip.

Heating in vacuum is performed by spot welding the etched tips to a tantalum ribbon which is itself spot welded between two copper electrodes. The electrodes are held in place within a ceramic screw-down terminal block as shown in Figure 2-11. A two prong power feedthrough mounted on the load-lock chamber is connected to two Kapton coated power cables (UHV compatible). These cables can be connected to the ceramic terminal to provide resistance heating current across the tantalum ribbon (Figure 2-12). Once in the load-lock and under vacuum (~1 x 10^{-7} mbar), a current of approximately 4 A - 6 A is required for the tips to glow slightly orange (viewed through a window) indicating the appropriate temperature has been reached. Heating is maintained for about 30 seconds to 1 minute. The ceramic block can be disconnected and the power wires moved aside when not in use.

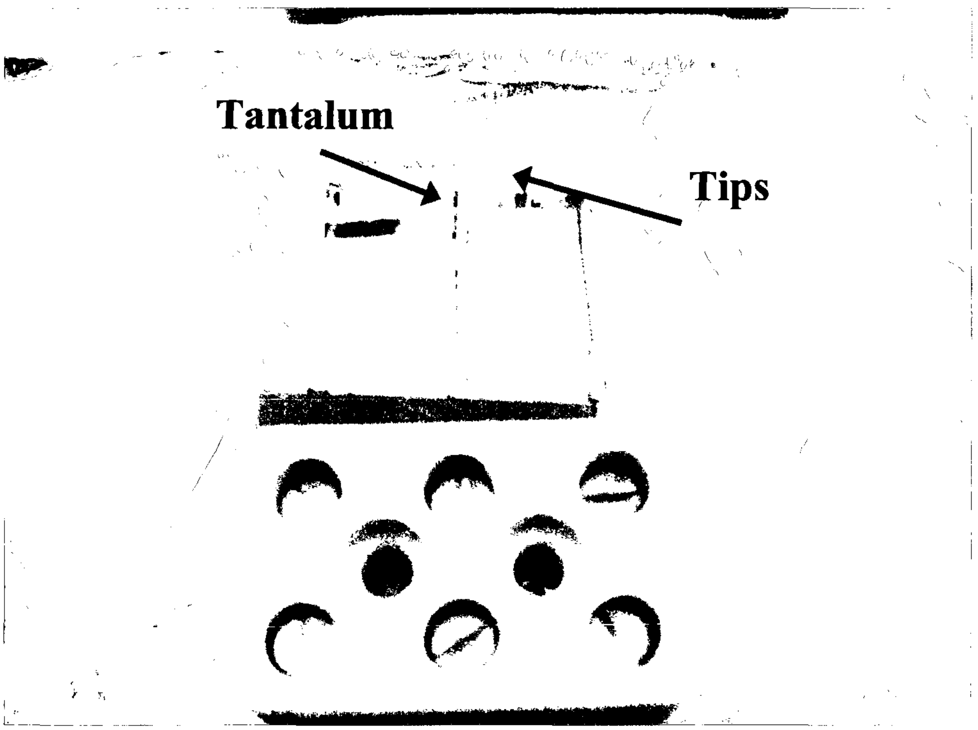

Figure 2-11 *The ceramics screw-down terminal which holds the copper electrodes between which tantalum ribbon is spot welded. The etched but oxidized tungsten tips are spot welded to the ribbon and heated to 600 °C – 700 °C in vacuum by passing current across the tantalum foil.*

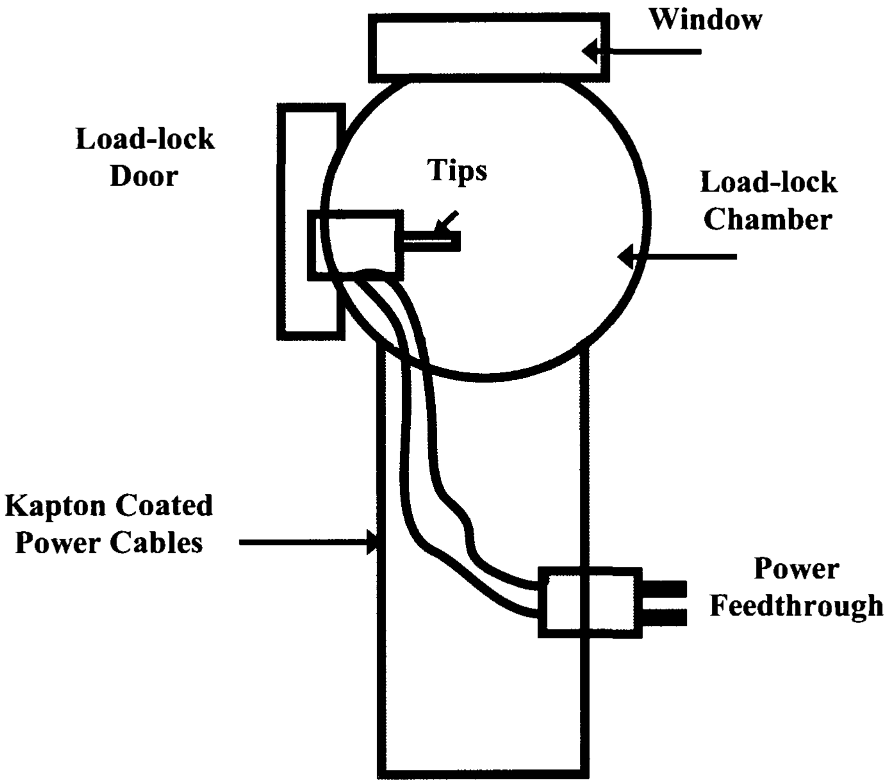

Figure 2-12 *Schematic demonstrating the resistive heating of etched tip under vacuum in the load-lock chamber.*

The sharpness and profile of the etched tips have been confirmed by scanning electron microscopy. Figure 2-13c shows an etched and thermally reduced tip at 500 000 times magnification, the observed diameter is better than 10 nm. The tip is likely even smaller at the end since it cannot be clearly resolved due to vibrations.

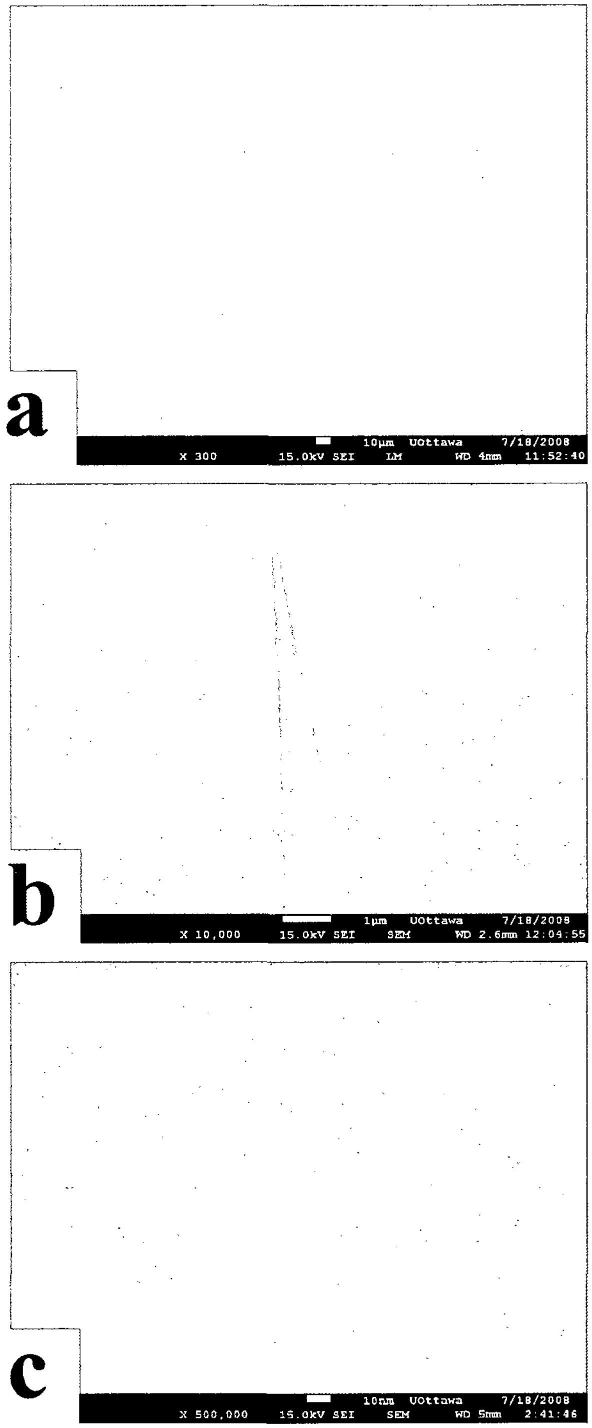

Figure 2-13 *Scanning electron micrographs of an electrochemically etched and thermally vacuum reduced STM tip. (a)* X *300 magnification showing the entire etch profile. (b)* X *10 k magnification demonstrating the high aspect ratio near the end of the tip. (c)* X *500 k magnification showing the tip apex..*

2.2.5. *Ar+ Sputtering*

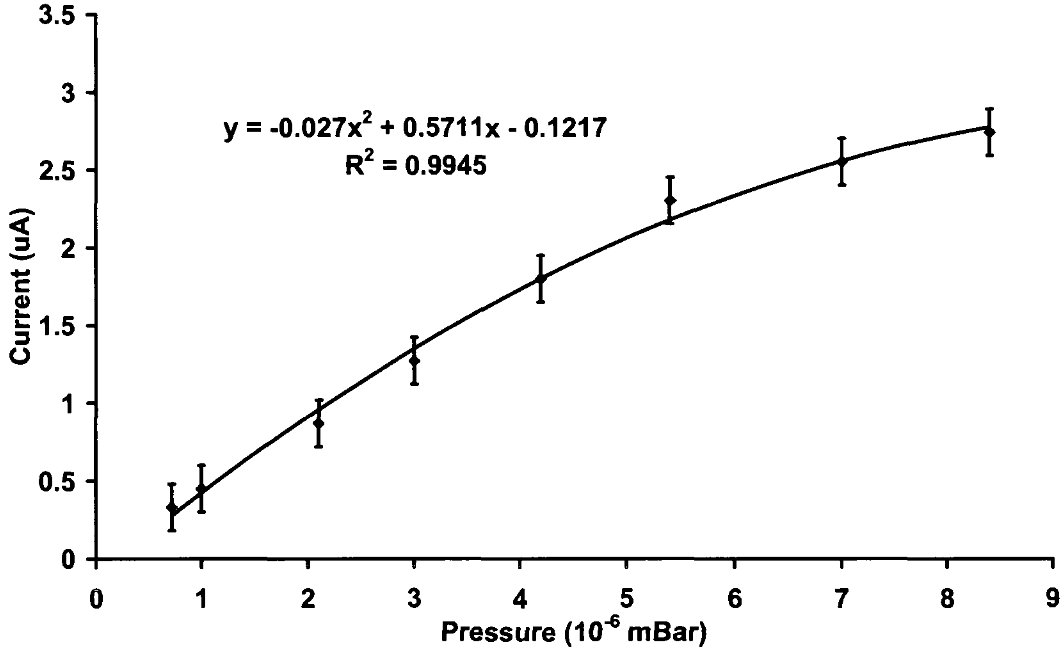

Figure 2-14 *Sputter current on a 6 mm diameter area of HOPG as a function of argon pressure (N_2 calibration of the ion gauge) at 600 eV ion energy.*

Ion sputtering is used to clean samples by bombarding the surface with argon ions at energies up to 3 keV. The ion beam in all experiments is incident normal to the surface. Because the ions are positively charged, electrons from the sample may neutralize the charge if the sample is sufficiently conductive. Measurement of the conduction current between the sample and ground will then be related to the number of sputtering events. For YSZ(100) studies it is not always possible to measure the current since it is an insulator. However, the Ar+ fluence can be estimated by calibrating the sputter current on a conductive sample as a function of back pressures of Ar in the chamber. Figure 2-14 presents a plot of the sputter current on a sample of HOPG as a function of argon partial pressure in the chamber. The data can be fit to a 2nd order polynomial and used for an approximate calculation of sputter fluence. The sputter cross section for YSZ will be different than for HOPG. Zirconium itself has a sputter yield almost twice as large as carbon, 0.6 atoms/ion compared to 0.35 atoms/ion. Very little data exists on the sputter yield of YSZ itself,[24] however it is estimated that the after a nominal correction (multiply by 0.6/0.35) the accuracy is better than 100 % of the listed value.

2.3. Heating and Cooling

YSZ single crystal samples are purchased from MTI corporation, pre-polished and cut into circular disks 0.5 mm or 0.25 mm thick with an outer diameter of 8 mm. The samples are doped with either 13 mol % or 9 mol % yttria. In house preparation of the YSZ(100) single crystal both in ambient and in UHV conditions requires sample heating. In vacuum, heating of the sample needs to be performed in unison with cooling of the sample holder, otherwise degassing will be too great and the sample will accumulate residual gasses. In addition to the need to heat to a specific temperature, in order to maintain reproducibility, the rate at which that point is reached should be consistent between experiments. Normally it is assumed that if refractory materials such as YSZ are cooled quickly enough their properties after heating will be similar to those at high temperature[31-33] since the material will not have had sufficient time to equilibrate. While this is likely true in the bulk it is not necessarily so at the surface region [34], moreover heating at uncontrolled rates will result in changes in the overall length of time at which the sample spends at elevated temperatures. This may have unpredictable results, and is not consistent with controlled studies of a very complex material such as YSZ.

2.3.1. Ambient heating

Ambient heating of YSZ (100) single crystals to 1000 °C is performed in a tube furnace. The furnace is controlled by a home built system which includes an Omega Engineering [35] CN8200 series temperature controller which reads temperature from a K-type thermocouple to offer feedback to a silicon controlled rectifier (SCR) based power controller. This type of controller produces a current that is proportional to the feedback, rather than by using a solid state relay which is either fully on or fully off. In the "full on/full off" mode the power to the furnace is varied by the amount of time the current flows, and therefore if it is used for producing linear temperature ramps, the result is often an oscillation about the ramp rate sought. Using the proportional SCR, current may always flow but in controlled quantities so that the linear ramp rate is more stable. The present design has an RS 232 interface and may be computer controlled as well, temperatures may be recorded during heating and cooling. Figure 2-15 demonstrates controlled cooling of the furnace from 1000 °C. The thermal inertia of the furnace prevents cooling at the set rate (8 °C/min) below ~500 °C, this lower region is instead fit to a rate of -4.7 °C/min.

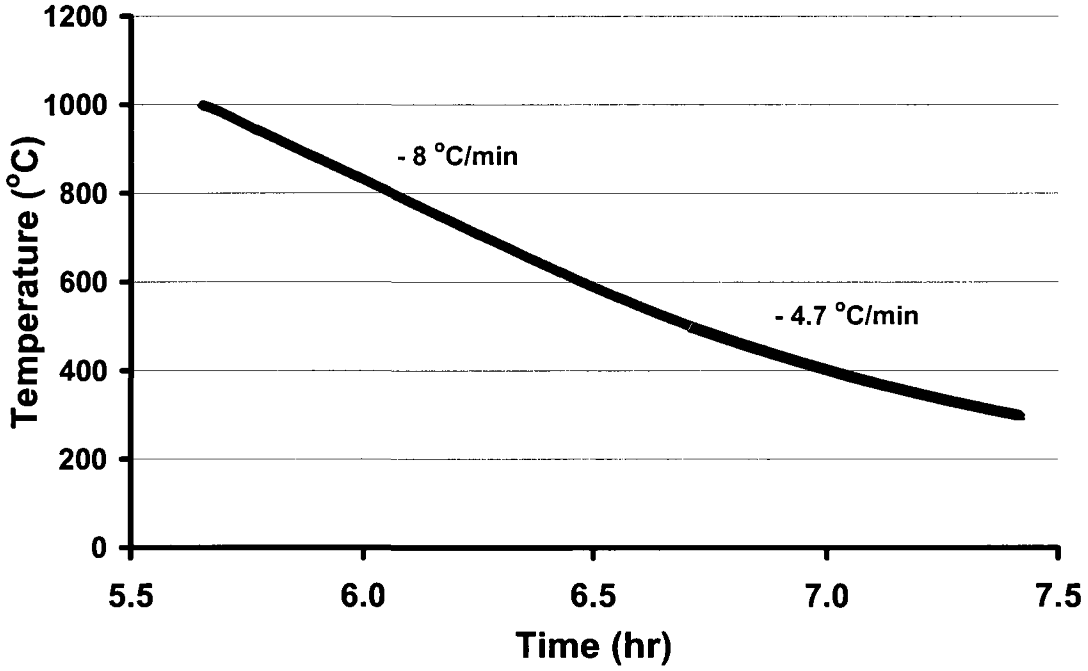

Figure 2-15 *Cooling curve set to cool at a rate of 8 °C/ min, at approximately 500 °C the thermal inertia of the furnace prevents cooling at that rate, and cooling slows. Between 500 °C and 300 °C the cooling rate is approximated to be -4.7 °C/min.*

2.3.2. UHV heating and cooling

2.3.2.1. Main manipulator

Heating in UHV to temperatures and times sufficient to anneal YSZ(100) has provided one of the most unexpected, critical, and challenging problems which has had to be solved before consistent studies could be preformed. The problem is derived from a design flaw in the system, or perhaps from a different perspective, the system is not designed for the temperatures necessary to study YSZ. Either way the main challenge is the inefficient cooling of the sample holder (Figure 2-3).

Cooling is performed by continuously flowing liquid nitrogen under pressure, from the end of the main manipulator arm to a reservoir in thermal contact with the sample holder. One of the first design flaws is the narrow internal diameter (<1 mm) of the stainless steel tubing which carries the liquid nitrogen to the reservoir. Because of this narrow diameter, the pressure of the liquid nitrogen has to be held very high in order to produce sufficient flow through the tubing to cool the sample holder. However, if the pressure inside the dewar is held too high then gaseous nitrogen will increasingly dissolve in the liquid, lowering the cooling efficiency. It has been determined experimentally that a pressure of 40 PSI in the liquid N_2 dewar will provide the best cooling rate at the holder.

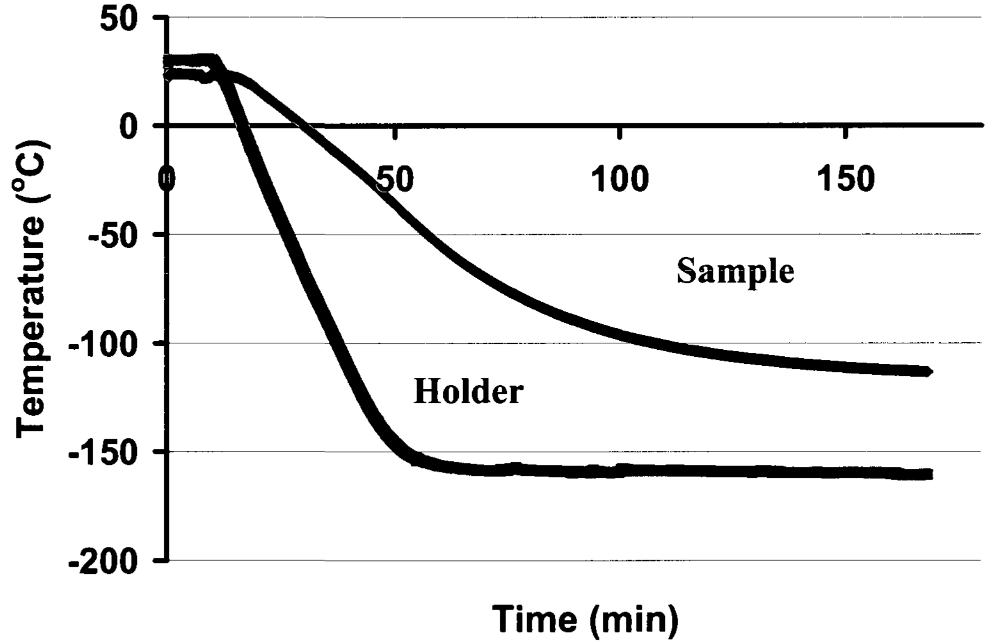

Figure 2-16 *Cooling curves for the sample holder and the sample itself.*

Figure 2-16 shows the cooling curve of the holder and sample as liquid nitrogen is constantly flown through the reservoir. It takes approximately 50 minutes for the holder to reach -160 °C. The base sample temperature will vary depending on thickness of crystal and mounting technique but here the sample reaches approximately -115 °C after over two hours of cooling. The lowest sample temperatures achieved have been -155 °C with a 0.25 mm YSZ crystal, but normally with a 0.5 mm thick crystal mounted in the manner required for STM imaging, approximately -130 °C can be expected.

Figure 2-17 *Photograph of the sample while it is being heated through electron bombardment. The puck surface is glowing hot as a result of thermal transfer from the sample and from stray heating electrons.*

Once the holder has reached a base temperature, sample heating via electron bombardment can be performed. This is typically done by applying a negative voltage as low as -1 kV to the heating filament (1 % thoriated tungsten) which will accelerate electrons thermionically emitted from it towards the back of the sample. Currents of about 1.6 A are required to heat the filament to the point where electrons are emitted. Inefficient holder cooling allows the sample to be heated to 1000 °C for only about 5 minutes before the holder reaches approximately 200 °C. In Chapter 3 it is shown that at 1000 °C annealing only occurs very slowly, times on the order of hours may be needed, so that it has not been possible to use the main manipulator for full sample preparation. Most experiments are now performed while the sample is held at 300 °C; this temperature (Chapter 4) has been found to increase the conductivity of YSZ sufficiently to prevent charging during XPS, STM, and ion sputtering. With constant liquid nitrogen cooling, the holder heats up but stabilizes at temperatures around -90 °C to -30 °C, so that a sample temperature of 300 °C can be held indefinitely. The main draw back to operating under this condition is the vast quantity of liquid nitrogen that is used. A 300 litre dewar will last 9-12 hours, and a second tank must always be kept on hand since most experiments require more time. Extending sample temperatures much above 350 °C – 450 °C, results in the holder temperature rising above its maximum operating value of 200 °C.

2.3.2.2. Preparation chamber

After much effort to improve heating and cooling on the main manipulator without sufficient success, it became clear that an alternative heating method would be required. The most reasonable course has been to design a new side chamber into which is incorporated an efficiently cooled sample holder. Simultaneously, a side chamber provides an ability to dose the sample in high partial pressures of oxygen without affecting the main chamber. Because of its high residence time, exposing the sample to back pressures of O_2 ($> 1 \times 10^{-5}$ mbar) in the main chamber will result in poor vacuum. After a few hours of dosing it has been found to take several days of pumping to achieve pressures just less than 1×10^{-9} mbar, and despite the time lost to heating and cooling, it is often faster to bake the chamber overnight.

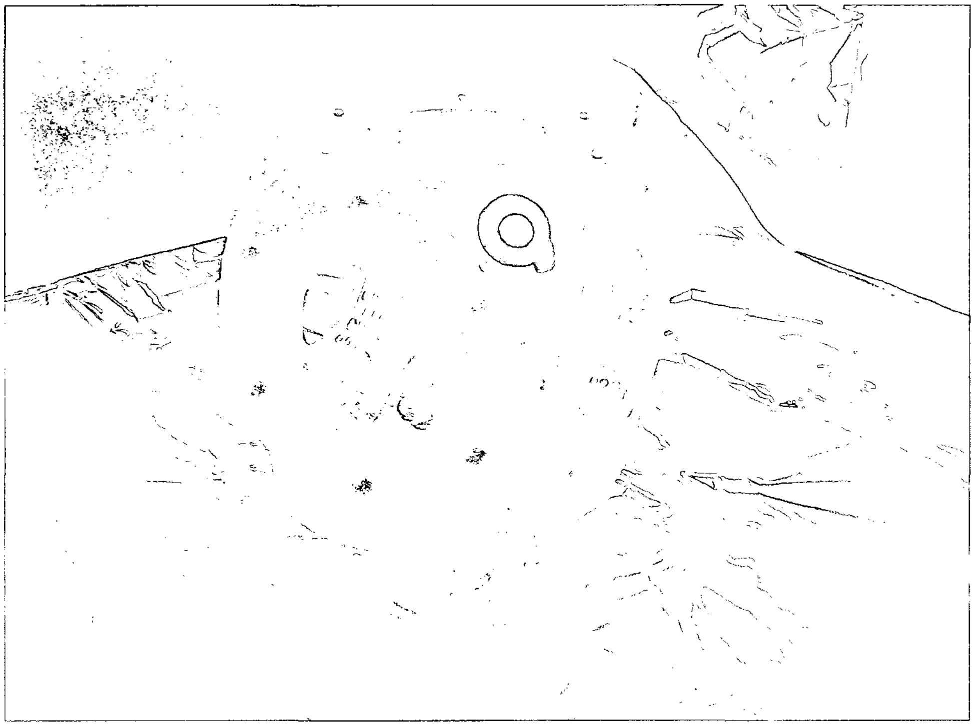

Figure 2-18 *Photograph of the multi-port cube upon which the preparation chamber is based.*

The preparation chamber is designed around a multi-flange cube purchased from Kimbal Physics [36] and shown in Figure 2-18. It holds five 2.75" openings as well as five 1.33" openings. A heating coil is mounted in a machined alumina holder which is itself attached to the end of a linear manipulator (2.25 cm range). The heater (Figure 2-19) may be moved in to heat and retracted to transfer the sample puck between chambers. The alumina filament holder is designed to be mechanically strong so that in an advanced position it may hold the puck in place with enough force to allow the transfer fork to grab it.

Figure 2-19 *Photograph of the interior of the preparation chamber, visible are the alumina support rods which thermally isolate the holder from the chamber, the heating filament in its alumina mount, and the gold plated copper sample holder. The holder is cooled by flowing liquid nitrogen through channels machined into it.*

The sample holder was initially designed of low oxygen copper, gold plated to minimize the sticking coefficient of gases. Unfortunately the cooling flow-through reservoir and tubing required silver soldering which chronically leaked, even after several iterations by the machine shop. The current version is composed of low carbon 204 stainless steel which can be welded. The holder is held by six 1/8" diameter sintered alumina rods as shown in Figure 2-19, these are poor conductors of heat and so it is largely thermally isolated. Electron bombardment may be performed by placing a negative voltage on the filament and ground or positive voltage on a metallic backing plate under the sample (Chapter 4). This plate is electronically connected to a pin extending from the puck which will make electronic contact with a clip on the holder when the puck is brought into position. The clip is isolated from the chamber and may be held at high voltage via an electronic feedthrough. The holder itself is not electronically isolated from the chamber and is therefore always at ground potential. This is a result of contact at the feedthrough with the stainless steel tubing which delivers the coolant to the holder.

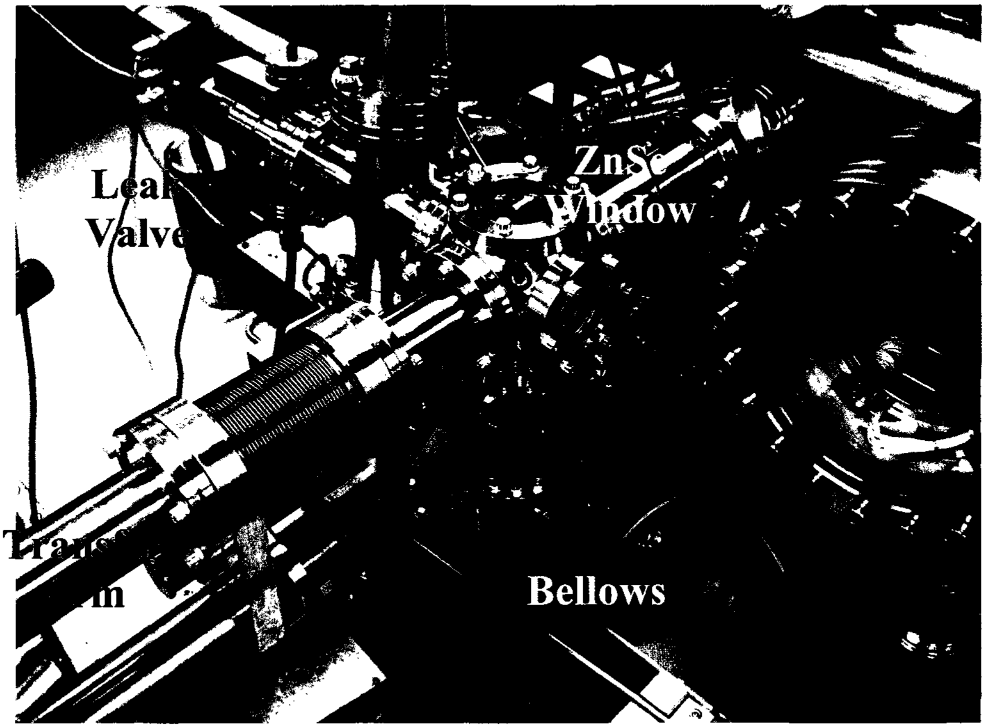

Figure 2-20 *Photograph of the assembled preparation chamber. The ZnSe window through which pyrometric temperature measurement of the sample is made is mounted on the top of multi-port cube. Liquid nitrogen is fed through stainless steel tubing to the sample holder with the resulting thermal contraction compensated by the contraction of bellows (covered by support tubing in this image). The heater is moved up or down in the holder via the linear transfer feedthrough attached under the cube. A leak valve, pressure gauge and turbo pump are connected to the cube through a 2.75" cross shown here on the left side of the cube.*

As coolant flows through the tubing and the holder, thermal contraction begins, which, because the holder is anchored in position, places a great deal of strain at the feedthroughs. Normally this could be relieved by coiling the tubing allowing it to expand and contract like a spring, however due to space limitations, this could not be done. Instead the feedthroughs themselves are connected to the main cube via flexible bellows which can expand and contract as necessary. All connections between the tubing, holder and feedthroughs are NPT fittings using stainless steel gaskets.

The necessary orientation of the preparation chamber with respect to the main chamber prevents thermocouple pins attached to the sample from making contact with any clips on the preparation holder. As a result, temperature is measured by pyrometry through a zinc selenide window. The window has the required transparency over the infrared range read by the pyrometer to produce accurate temperature measurements. Calibration for the emissivity of YSZ(100) is performed by measuring the crystal temperature as read by the pyrometer (through the ZnSe window), against that measured by a pre-calibrated K-type thermocouple to which the sample is attached. The crystal is heated under ambient conditions inside a tube furnace. At 1000 °C the emissivity setting on the pyrometer should be 0.82, and is within 7 °C of the thermocouple measurement across the range (100 °C - 1000 °C). The pyrometer must be held approximately 60 cm from the sample for good focus, and a measurement spot size 6 mm in diameter.

Attached to the preparation chamber is a turbo pump, large range vacuum pressure gauge (1×10^3 mbar to 1×10^{-9} mbar), and a leak valve for gas dosing. It is separated from the main chamber by a 2.75“ gate valve. Sample transfer occurs via a linear, rotatable translation arm onto which an aluminum fork is mounted to hold the puck. A screw is used to mechanically press a K-type thermocouple to the holder in order to measure its temperature.

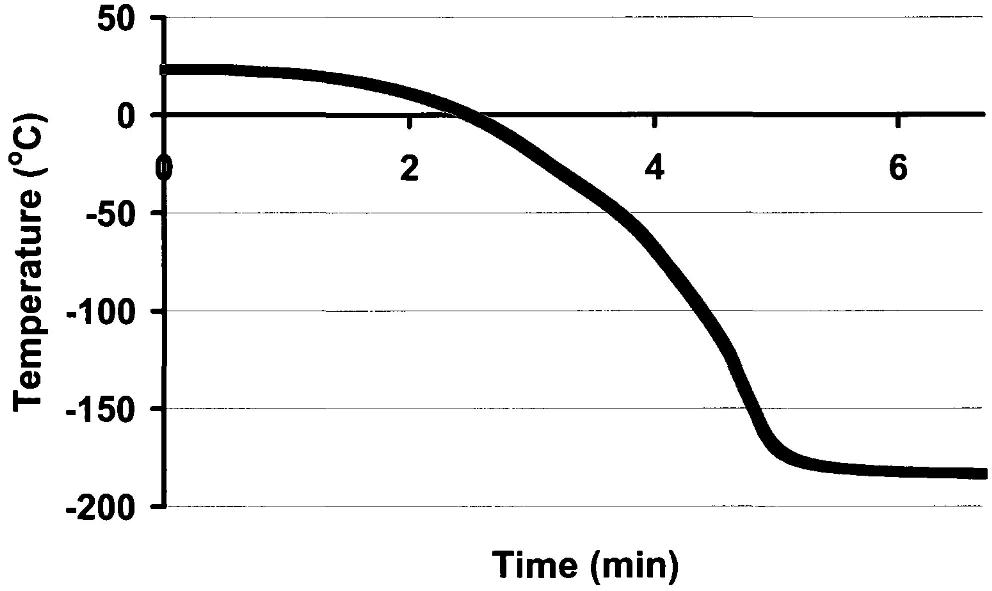

Figure 2-21 *Cooling curve of the preparation chamber holder showing a ten fold improvement on cooling speed compared to the sample holder on the main manipulator (Figure 2-16).*

The cooling efficiency of the preparation holder is at least an order of magnitude better than that of the main manipulator (Figure 2-16). As shown in Figure 2-21 upon flow of liquid nitrogen to the holder it only requires approximately 5 minutes to cool to -183 °C. Sample heating to 1000 °C by electron bombardment only causes the holder to temperature to rise by 6 °C or 7 °C. Sample heating can therefore be performed indefinitely.

2.3.2.3. Temperature measurement and control

Control and accurate measurement is critical for studies of a dynamic system like YSZ. As mentioned earlier since the segregation dynamics are as yet unclear for YSZ, in order to improve reproducibility in experiments involving heating (most studies in this work), a method has had to be devised to tightly control heating rates and record sample temperature at all points of an experiment. Moreover the ability to heat in a linear fashion makes accessible temperature programmed desorption spectroscopy, a technique which may provide adsorption/desorption energies, and is therefore extremely useful for catalysis studies.

Sample temperature is measured by a K-type thermocouple which is mechanically pressed to the surface of the YSZ single crystal. The differential signal produced by the thermocouple is amplified by an instrumental amplifier mounted close to the UHV feedthrough from which the signal is transferred. The amplified signal is read by custom software written in Labview (National Instruments), via a National Instruments M-series analog to digital (A/D) converter. The software filters and processes the voltage, transforming it into a cold junction compensated temperature signal. The reference temperature from which compensation is determined is derived from a calibrated linear thermistor purchased from Omega. The thermistor is in thermal contact with the differential junction between K-type and copper material at the screw down terminal of the instrument amplifier.

The heating and control method is diagrammed in Figure 2-22. The measured temperature is used for feedback by the software which has been written to produce both linear heating and cooling ramps. The A/D board has eight differential inputs as well as two -10 V to +10 V analog outputs. One of these outputs is used to control an SH100 power supply built by Specs. The control voltage can be selected at the SH100 to vary either the current flowing through the heating filament (0 A to 3 A) or the acceleration voltage applied to it (0 to -1000 V). Of these two quantities only current is controlled by the software since sample temperature is found to be much more responsive to it than to acceleration voltage.

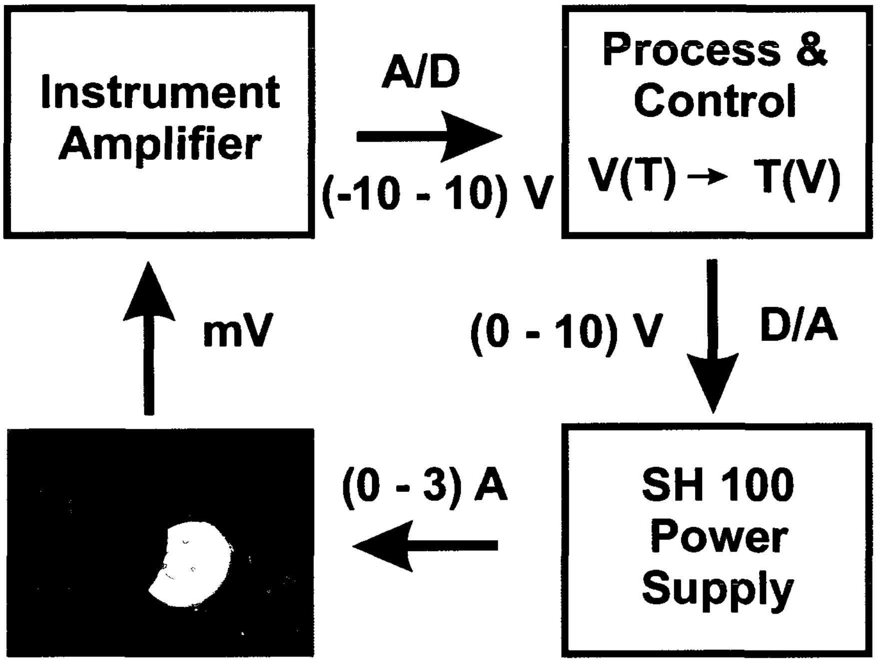

Figure 2-22 *A diagram of the temperature and control technique. Clockwise from bottom left, the temperature of the sample is measured via a K-type thermocouple, the thermo-voltage is amplified at the instrument amplifier to a -10 V to +10 V range. This voltage is converted to a digital signal by an A/D converter and read and processed by custom Labview software. The software converts the thermo-voltage to a temperature value which is used for a feedback to control an SH 100 power supply. The power supply produces up to 3 A of current proportional to the 0 V to 10 V signal it receives from the control software. The current provides power to the heating filament.*

The instrument amplifier (Figure 2-23) is based around a commercial four channel preamplifier with adjustable gains and offsets, purchased from Audon of the UK. This amplifier is mounted in an aluminum enclosure into which is also integrated the reference thermistor (Omega 44204) with its necessary supply voltage circuitry.

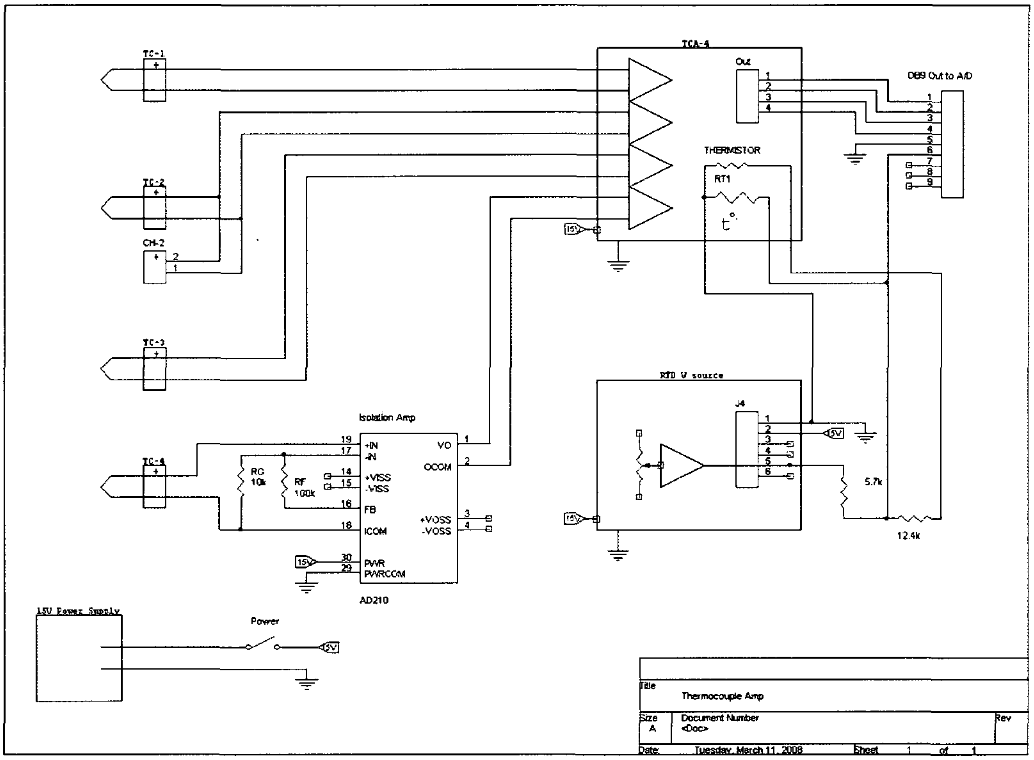

Figure 2-23 *Basic schematic of the instrument amplifier setup, including the high voltage isolation amp, and added temperature measurement at the terminal block of the preamp for cold junction compensation of the measured thermo-voltages. The output runs to an A/D board with low pass filtering added to its breakout box to reduce pickup as the signal travels across the lab from the instrument amplifier.*

An isolation amplifier (AD210) is added on input channel four of the pre-amp allowing measurement of points held at a high voltage, which could otherwise cause damage to the pre-amp or A/D board. This is of great usefulness when the sample holder is biased to a high negative voltage for the purpose of repelling bombardment electrons from the heating filament.

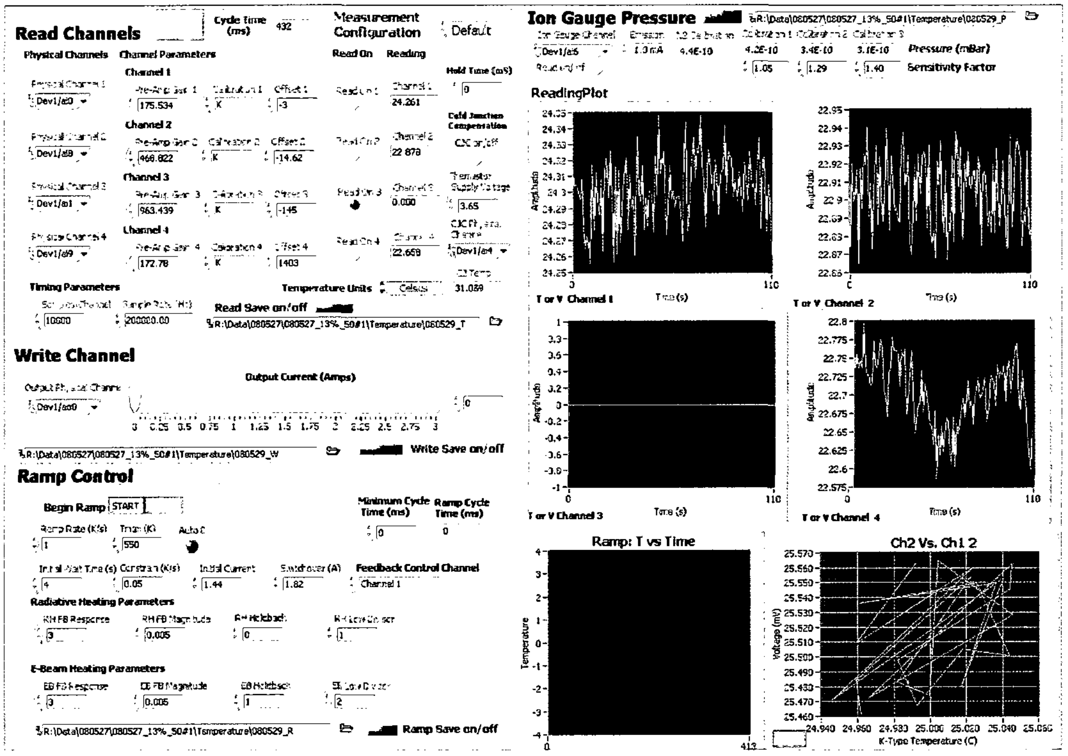

Figure 2-24 *Screen shot of the temperature measurement and control software written in Labview.*

The software (Figure 2-24), written in the Labview programming language, acts as a control and observation centre during experimentation and provides temperature monitoring, recording, and control. It is divided into three main components: Read Channels, Write Channel, and Ramp Control.

In the first component, up to four channels from the A/D board can be read nearly simultaneously, from user defined channels with pre-selectable sampling rates and times, which are then averaged. The signals read can be maintained as voltages or converted according to some transformation function, the software currently offers voltage to temperature conversion for most thermocouple types. These temperatures can be cold junction compensated based upon the temperature derived from the thermistor and read into the software on a fifth and selectable channel. Toggle switches allow only certain channels to be read minimizing the time between individual measurements. Each channel is plotted in its own window as a function of time in order to observe trends.

The second component is the Write Channel, which allows manual control of the output voltage channel. It is currently set to provide 0 V to 10 V DC to the SH 100, controlling the power supply to produce a proportional 0 A to 3 A of current. By changing cabling the provided current can be used to heat filaments in the main manipulator, the microscopy chamber, or the preparation chamber. All these filaments have been prepared of the same gauge 1 % thoriated tungsten wire (0.1 mm diameter) by wrapping 10-11 turns over a 0-80 screw, and therefore provide similar heating power for the same current.

The final main component is the Ramp Control, with which linear temperature ramps can be performed. The temperature used for control and feedback can be selected from amongst the four read channels discussed previously and the ramp rate can be set either positive for heating, zero for stable temperature, or negative for linear cooling ramp. For stable linear heating, two sets of parameters must be set, one set is for the regime in which radiant heating from the filament dominates (low temperature), and the other set is when electron bombardment dominates. The switch points between these regimes is input based upon an experimentally determined filament current value, typically between 1.60 A and 1.85 A. The other parameters are similar to proportional and integral gain values, and generally one or two ramps might be required to determine the appropriate parameters for a given sample.

The underlying principle for control is very simple; an initial filament current is set which starts the sample heating, the temperature is recorded in time and the rate at which it changes is calculated. If this value is outside the set rate by more than a selected magnitude, then the filament current is increased or decreased according to a pre-set amount. The simple technique produces extraordinarily good results as shown in Figure 2-25, the only qualification is that the temperature read from the sample must actually be representative of its temperature. If the sample is not mounted properly or there are ground loops or shorts, then the software will try to feedback on a physically inaccurate signal resulting in a nonsense, possibly damaging response. Because the sample is thin and somewhat fragile, ramp rates should not be too quick to prevent cracking due to thermal expansion strains. Up to 2 °C/s - 3 °C/s may be possible, but 0.5 °C/s - 1.5 °C/s are most commonly implemented.

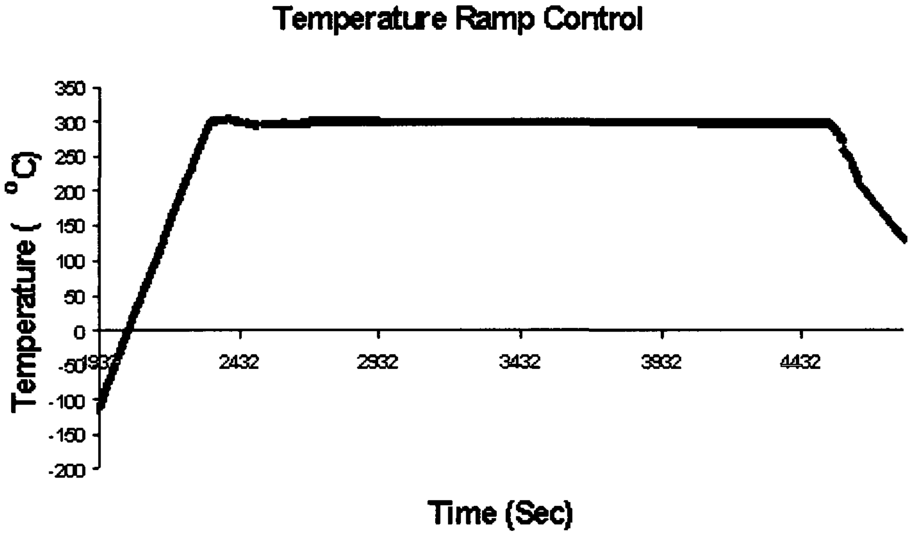

Figure 2-25 *A software controlled, linear temperature ramp of the sample from below -100 °C. At 300 °C the rate is held constant for experimentation before cooling at a controlled rate. The thermal inertia of the holder prevents the sample cooling rate from being maintained at lower temperatures.*

All values read or written in the software can be recorded into text files, with each measurement time stamped. Pressure from the ion gauge in the main chamber can also be monitored and recorded in time, and can later be compared to sample temperature to determine if their was excessive degassing during heating, or some other event.

2.3.3. Temperature Programmed Desorption

The temperature control software discussed above may produce linear ramps recorded in time, these values may be correlated to mass spectrometry signals since they are also recorded with respect to time. During most experiments the residual gas analyzer is left on, so that the most important conditions relevant to sample properties (temperature, time, gas phase environment) can be constantly monitored and recorded. If specific samples exhibit normally uncharacteristic properties, it has often been possible to look back at the recorded data to determine if some uncontrolled event had taken place.

An ability to produce linear temperature ramps as well as to simultaneously record mass spectrometry signals permits temperature programmed desorption spectrometry (TPD) to be performed. In this technique the sample is initially cooled to some low temperature at which chemisorption of some probe or catalytically relevant gas phase molecule occurs. Linearly increasing the sample temperature causes the desorption of the chemisorbed molecules which are then detected by the mass spectrometer. To ensure that the molecules originate from the sample surface, a dedicated mass spectrometer is aimed directly at the sample. Its quadrupole is incased in a quartz bulb with a small aperture at its apex. The bulb is differentially pumped so that high pressure gases desorbed from the sample will be detected with low background at the spectrometer.

The temperature at which a peak in the mass spec. signal of the desorbed species occurs, has been related by Redhead to the activation energy of desorption for the specific binding site from which the species originated.[37] This yields catalytically relevant information, since if adsorption is reversible, the energy of desorption is its equivalent.

Heats of adsorption can often be related to the performance of a catalyst as stated in Sabatier's principle.

A piece of software has been written in Excel visual basic which extracts and correlates saved temperature and RGA data, plotting the mass spectrometry signal against the temperature at which the corresponding species was desorbed. A resulting TPD spectrum is shown in Figure 2-26, this spectrum is derived from a linear ramp of a YSZ(100) sample.

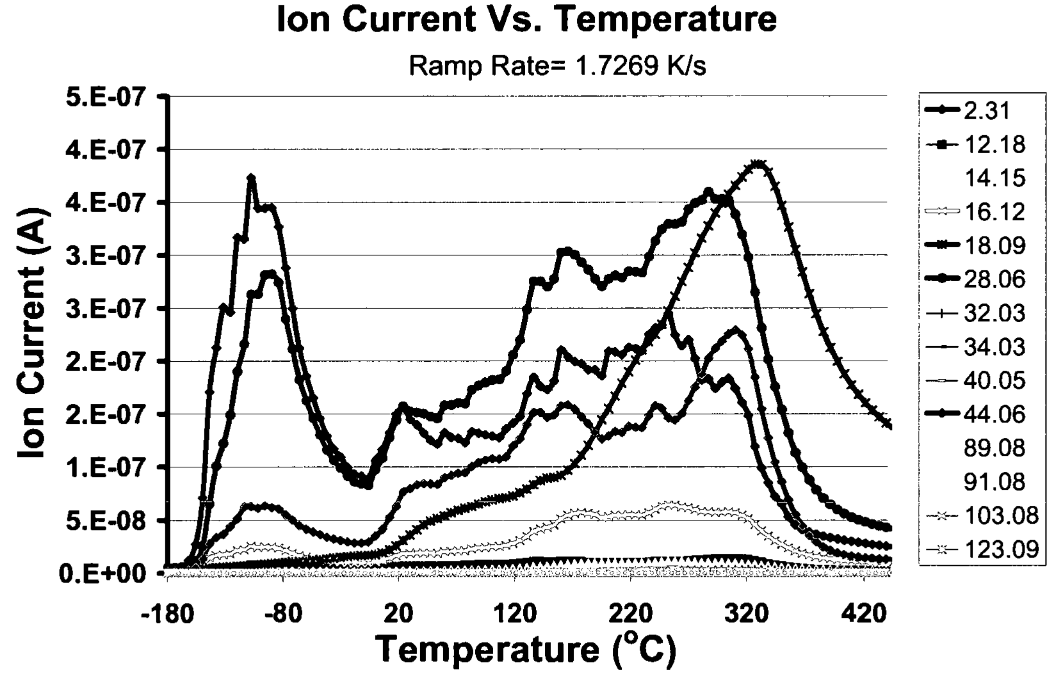

Figure 2-26 *A plot of a temperature programmed desorption spectrum produced by an Excel visual basic program which combines independently but simultaneously acquired temperature and mass spectrometry data. Each curve corresponds to a desorbed species of different mass to charge ratio.*

2.4. Sample Mounting

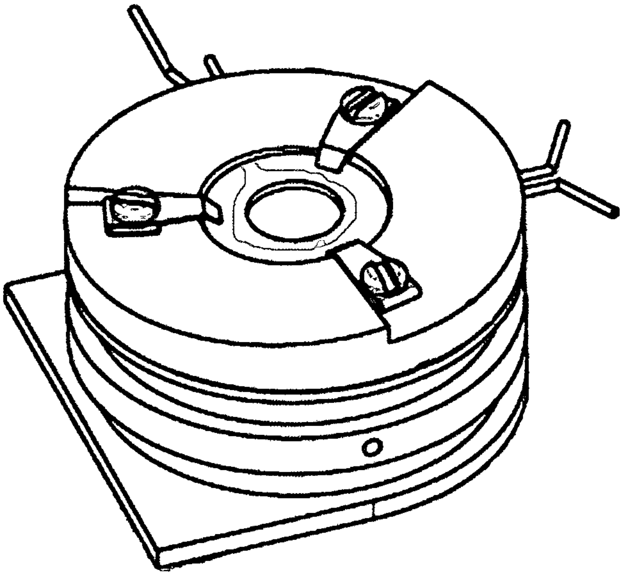

Figure 2-27 *RHK sample puck into which the YSZ(100) single crystal is mounted.*

The sample puck into which the YSZ(100) single crystal (MTI corporation, 8 mm OD, 0.25 mm or 0.5 mm thick) is mounted is shown in Figure 2-27. The puck is made up of two main components, the copper base, and a molybdenum top. Into the copper base two grooves are machined which are used to transfer the puck from one holder to another. The top part has three ramps on its surface which are necessary for scanning probe microscopy. The recess in the top is approximately 10 mm in internal diameter and 2 mm deep, as measured from the base of the ramps. The sample should be mounted so that it is 2.4 mm in height from the bottom of the recess, this ensures the sample will be at the appropriate height for SPM. Temperature is measured via a K-type thermocouple, which is composed of a dissimilar metal junction that produces a temperature dependent voltage when in the presence of a temperature gradient. The metals which make up the junction at the sample are composed of 0.13 mm diameter chromel-alumel wires spot welded at one end. The wires should form a circle around the top edge of the sample so that when the thermocouple is compressed to it via a sapphire washer and tungsten leaf clips, the holding force will be distributed evenly. This will help reduce the probability of cracking the sample during thermal cycling. Alternatively, if the circle is not formed, a small groove can be machined into the bottom of the sapphire washer in which the thermocouple junction is placed, this will also help prevent cracking. Though caution should be exercised to make the groove of proper size so that the junction is still pressed to the sample. The thin thermocouple wires are spot welded to thicker (0.5 mm OD), more rigid, K-type pins that extend from the puck and make electrical contact with a set of clips mounted holder when the puck is in position. The manufacturer (SPECS) initially made these clips out of copper beryllium alloy which produce no magnetic field to interact with information carrying electrons during experimentation. After extreme difficulties in measuring temperatures greater than 800 °C, however, these clips were found to be inadequate. The problem results from the clips themselves acting as dissimilar junctions with the thermocouple wire. A thermoelectric voltage is produced which acts in opposition to the true sample thermocouple voltage. Normally this would not be an issue if the clips are uniformly heated, however this is not the case, especially at high sample temperatures. As a solution to the problem the clips have been modified by spot welding the appropriate k-type wire between the clips. Currently the pins extending from the puck that carry the sample thermoelectric voltage, make contact with this wire, rather than the copper beryllium alloy.

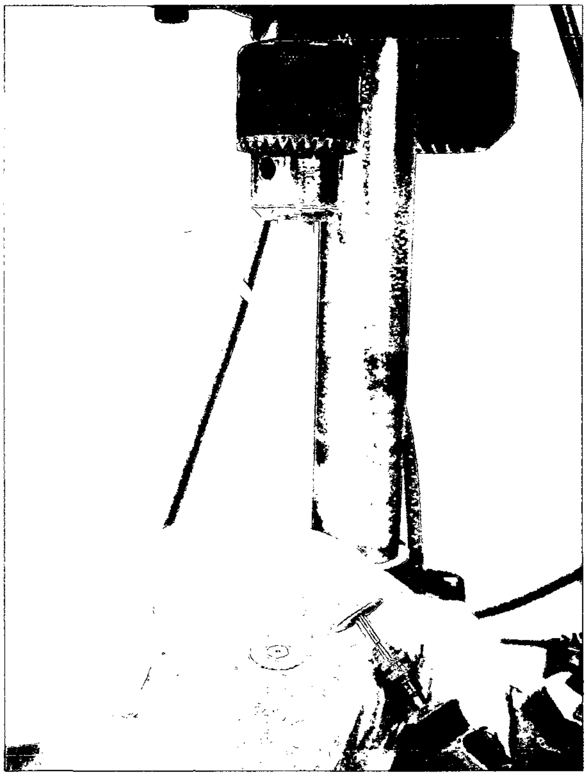

Figure 2-28 *Photograph of the makeshift lathe used to machine an alumina tube into a sleeve used in sample mounting.*

Alumina (Al_2O_3) in either highly sintered or single crystal sapphire form, is commonly used for the studies discussed in the present work. It is used to mount the sample within its holder or electronically isolate other components such as heating filaments or contacts. Both sapphire and sintered alumina are extremely hard and the machine shop at the university of Ottawa does not have the ability to work with them. A technique has therefore had to be developed in order to machine the materials within the lab and build the necessary components. One of the components that is required for mounting the YSZ sample within the puck is an alumina sleeve. The sleeve is placed around the sample and the various sapphire rings or disks upon which it sits (see Chapter 4). The sleeve laterally isolates the sample and metal plates from the puck allowing a high differential voltage to exist between them without arcing. Holes in the sleeve also guide the thermocouple wires which at one time commonly came out of place, shorting to the puck.

Due to its hardness, sintered alumina must be machined with diamond tools. Various cutting wheels and mandrels impregnated with diamond powder can be commonly purchased at quite a reasonable price for use in rotary tools (Lee Valley). The best way to produce the sleeve (10 mm OD x 8 mm ID x 3 mm thick) is by beginning with a half inch alumina tube

(Cotronics Corporation), and machining the outer diameter of the tube to the appropriate size. Machining can be performed by tightening the tube into place within the chuck of a drill press, then using a rotary hand tool turning a diamond cut-off wheel to manually grind the tube down while it is spinning in the drill press. The drill acts like a lathe and the tube OD can be carefully worn down to the appropriate size under a near continuous stream of cooling water. Holes can be carefully drilled into the sleeve with very fine mandrels after it has been formed. The process takes time and practice, but the sample stability it provides is necessary for long experiments and multiple heating cycles, and Macor or other machinable ceramics may not possess the temperature stability, or may act as sinks for contaminant gases that may desorb during experimentation.

References

1. Crist, B.V., *www.XPSdata.Com*. 2006, XPS International, Inc.

2. Anthony, M.T. and Seah, M.P., *XPS - energy calibration of electron spectrometers .1. An absolute, traceable energy calibration and the provision of atomic reference line energies.* Surface and Interface Analysis, 1984. **6**(3): p. 95.

3. Seah, M.P., Gilmore, I.S. and Spencer, S.J., *XPS: Binding energy calibration of electron spectrometers 4 - assessment of effects for different x-ray sources, analyser resolutions, angles of emission and overall uncertainties.* Surface and Interface Analysis, 1998. **26**(9): p. 617.

4. Seah, M.P., Gilmore, L.S. and Beamson, G., *XPS: Binding energy calibration of electron spectrometers 5 - re-evaluation of the reference energies.* Surface and Interface Analysis, 1998. **26**(9): p. 642.

5. ASTM, *Designation e 1523-03: Standard guide to charge control and referencing techniques in x-ray photoelectron spectroscopy*, in *ASTM International, E 1523-03.* 2003.

6. Sygellou, L. and Ladas, S., *Interfacial effects in ultra-thin nickel deposits on yttria stabilized zirconia.* Surface Science, 2004. **566-568**: p. 698.

7. Sygellou, L., Zafeiratos, S., Tsud, N., Matolin, V., Kennou, S. and Ladas, S., *Interaction of ultrathin nickel oxide films with single-crystal zirconia and alumina surfaces.* Surface and Interface Analysis, 2002. **34**(1): p. 545.

8. Scofield, J.H., *Hartree-slater subshell photoionization cross-sections at 1254 and 1487 eV.* Journal of Electron Spectroscopy and Related Phenomena, 1976. **8**(2): p. 129.

9. Fairley, N. and Carrick, A., *The casa cookbook - part 1: Recipes for XPS data processing.* 2005, Acolyte Science. p. 94.

10. Cumpson, P.J. and Seah, M.P., *Elastic scattering corrections in AES and XPS .2. Estimating attenuation lengths and conditions required for their valid use in overlayer/substrate experiments.* Surface and Interface Analysis, 1997. **25**(6): p. 430.

11. Seah, M.P. and Dench, W.A., *Quantitative electron spectroscopy of surfaces: A standard data base for electron inelastic mean free paths in solids.* Surface and Interface Analysis, 1979. **1**(1): p. 2.

12. Tanuma, S., Powell, C.J. and Penn, D.R., *Proposed formula for electron inelastic mean free paths based on calculations for 31 materials.* Surface Science Letters, 1987. **192**: p. L849.

13. Tanuma, S., Powell, C.J. and Penn, D.R., *Calculations of electron inelastic mean free paths for 31 materials.* Surface and Interface Analysis, 1988. **11**(11): p. 577.

14. Tanuma, S., Powell, C.J. and Penn, D.R., *Calculations of electron inelastic mean free paths .2. Data for 27 elements over the 50-2000-eV range.* Surface and Interface Analysis, 1991. **17**(13): p. 911.

15. Tanuma, S., Powell, C.J. and Penn, D.R., *Calculations of electron inelastic mean free paths .3. Data for 15 inorganic-compounds over the 50-2000-eV range.* Surface and Interface Analysis, 1991. **17**(13): p. 927.

16. Tanuma, S., Powell, C.J. and Penn, D.R., *Calculations of electron inelastic mean free paths (IMFPs) .4. Evaluation of calculated IMFPs and of the predictive IMFP formula tpp-2 for electron energies between 50 and 2000 eV.* Surface and Interface Analysis, 1993. **20**(1): p. 77.

17. Tanuma, S., Powell, C.J. and Penn, D.R., *Calculations of electron inelastic mean free paths .5. Data for 14 organic-compounds over the 50-2000 eV range.* Surface and Interface Analysis, 1994. **21**(3): p. 165.

18. Tanuma, S., Powell, C.J. and Penn, D.R., *Calculations of electron inelastic mean free paths (IMFPS) .6. Analysis of the gries inelastic scattering model and predictive imfp equation.* Surface and Interface Analysis, 1997. **25**(1): p. 25.

19. Yubero, F., Espinos, J.P. and Gonzalez-Elipe, A.R., *Optical properties of zirconia-yttria single crystal compounds by reflection electron energy loss spectroscopy.* Journal of Vacuum Science & Technology a-Vacuum Surfaces and Films, 1998. **16**(4): p. 2287.

20. Nowotny, J., Bak, T., Nowotny, M.K. and Sorrell, C.C., *Charge transfer at oxygen/zirconia interface at elevated temperatures - part 3: Segregation induced interface properties.* Advances in Applied Ceramics, 2005. **104**(4): p. 165.

21. Anthony E. Hughes, *Segregation in single-crystal fully stabilized yttria-zirconia.* Journal of the American Ceramic Society, 1995. **78**(2): p. 369.

22. Hughes, A.E. and Sexton, B.A., *Curve fitting XPS spectra.* Journal of Electron Spectroscopy and Related Phenomena, 1988. **46**(1): p. 31.

23. Hughes, A.E., Stjohn, H., Kountouros, P. and Schubert, H., *Moisture sensitive degradation in* TiO_2-$Y_2O_3ZrO_2$. Journal of the European Ceramic Society, 1995. **15**(11): p. 1125.

24. Theunissen, G., Winnubst, A.J.A. and Burggraaf, A.J., *Surface and grain-boundary analysis of doped zirconia ceramics studied by AES and XPS.* Journal of Materials Science, 1992. **27**(18): p. 5057.

25. Parmigiani, F., Depero, L.E., Sangaletti, L. and Samoggia, G., *An XPS study of yttria stabilized zirconia single crystals.* Journal of Electron Spectroscopy and Related Phenomena, 1993. **63**: p. 1.

26. Song, Z., Bao, X., Wild, U., Muhler, M. and Ertl, G., *Oxidation of amorphous ni-zr alloys studied by XPS, UPS, ISS and XRD.* Applied Surface Science, 1998. **134**(1-4): p. 31.

27. Guise, O.L., Ahner, J.W., Jung, M.C., Goughnour, P.C. and Yates, J.T., *Reproducible electrochemical etching of tungsten probe tips.* Nano Letters, 2002. **2**(3): p. 191.

28. Kerfriden, S., Nahle, A.H., Campbell, S.A., Walsh, F.C. and Smith, J.R., *The electrochemical etching of tungsten stm tips.* Electrochimica Acta, 1998. **43**(12-13): p. 1939.

29. Melmed, A.J., *The art and science and other aspects of making sharp tips.* Journal of Vacuum Science & Technology B, 1991. **9**(2): p. 601.

30. Schwendemann, T.C., *Atomic scale investigations of the thermal and electron induced chemistry of small molecules on Pt(111) as revealed by scanning tunneling microscopy*, in *Department of Chemistry.* 2006, University of Virginia.

31. Thome, T., Pham Van, L. and Cousty, J., *Evolution of yttria stabilized zirconia (100) surface morphology with temperature.* J. Eur. Ceram. Soc., 2004. **24**: p. 841.

32. Kurnosikov, O., Van, L.P. and Cousty, J., *High-temperature transformation of vicinal (0001) Al_2O_3-alpha surfaces: An afm study.* Surface and Interface Analysis, 2000. **29**(9): p. 608.

33. Van, L.P., Kurnosikov, O. and Cousty, J., *Evolution of steps on vicinal (0001) surfaces of alpha-alumina.* Surface Science, 1998. **411**(3): p. 263.

34. Nowotny, J., Sorrell, C.C. and Bak, T., *Segregation in zirconia: Equilibrium versus non-equilibrium segregation.* Surface and Interface Analysis, 2005. **37**(3): p. 316.

35. www.Omega.com, *Omega engineering.*

36. www.kimballphysics.com, *Kimball physics inc.*

37. Redhead, P.A., *Thermal desorption of gases.* Vacuum, 1962. **12**: p. 203.

3. Ambient Studies

3.1. Introduction

In order to study normally complicated heterogeneous catalysts in which the action of several variables may make the system difficult or impossible to decipher, model catalyst and even thin film studies are performed under ultrahigh vacuum (UHV). In such an environment the complexity of the system may be reduced to its most basic components and studied in an environment free of contaminants such as water and hydrocarbons as adsorbates. Furthermore the UHV environment permits the use of very powerful spectroscopic techniques such as XPS or UPS which are not generally available in ambient systems due to the short electron inelastic mean free path (Chapter 1 and 2). As is the case with all initial studies of model catalysts, SOFC studies first require production of well characterized and preferably very simple surfaces; ideally an atomically flat single crystal free of extrinsic defects such as surface contaminants, point defects etc. [1-6] Techniques to obtain such a surface vary depending on the identity of the crystal and the type of study, but for oxides in UHV, this usually involves positive ion sputtering to clean the surface as well as thermal annealing to form an atomically flat construction.[7, 8] For YSZ, a common cleaning procedure involves cycles of ion sputtering and annealing in vacuum or in back pressures of O_2.[9-16] While this procedure can provide a clean YSZ surface free of hydrocarbons, it is not known if it leads to the same stoichiometry or surface topography from sample to sample. In fact we and others have found that characteristics tend to vary depending on the history of the sample.[9, 11, 17, 18]

Compounding the complexity of the situation, is the use in this work of a new and untested UHV system. Normally one would perform tests first on a known standard sample in order to be assured of the proper functioning of the instrument, and to learn how it is used. For our system testing was in fact performed with success on common samples such as highly ordered pyrolytic graphite (HOPG), and Si(111) however these are conductive and are in general relatively simple surfaces. Transfer of instrumentation knowledge toward YSZ studies was only nominal and had to be performed with caution. Experiments performed on insulators especially highly defective and possibly polar oxide surfaces such as YSZ(100), are subject to a host of complications. Sample charging, differential charging, and impurity segregation are examples of measurement induced phenomena that may affect the observed spectrum or image, without being a reflection of the material property supposedly being probed. Separating instrumental and measurement induced effects from material properties ideally requires either complete characterization of instrument behavior under all conditions, or complete knowledge of the material. Neither of these options is reasonable and so a median should be found in which some sample information can be combined with some instrumentation knowledge. As an example, if sample imaging may be performed and reproduced by two different techniques, then much greater confidence can be placed on the result. If two techniques cannot be used, one must count on reproducing results over several experiments and between samples in order to be assured of the results. This may be prohibitive for very long and difficult UHV experiments.

In developing a clean and flat surface for YSZ, Ar+ sputtering followed by annealing is often performed. One can expect that sputtering will destroy the stoichiometry by preferentially removing or redistributing oxygen or yttria, perhaps producing/increasing surface roughening.[19, 20] In order to restore stoichiometry, heating in back pressures of

O_2 is performed and if the temperature is sufficiently high then surface annealing will also occur and a thermodynamically stable surface composed of steps and terraces is expected to result. Very few studies have been performed on YSZ [21] surface annealing and it is not well known what the rate of defect annealing is, and therefore at what temperature and for what length of time is heating required in order to develop a flat stoichiometric surface. Moreover this time will be modified by the initial surface morphology, with rougher surfaces requiring longer annealing times at a given temperature. Further, how the partial pressure of oxygen may affect the surface is not clear for YSZ. It is an oxygen conductor and therefore a more complicated relationship between, topography, stoichiometry and temperature may exist since YSZ has the capacity to both eject oxygen or incorporate it in the lattice depending on the ambient partial pressure and temperature.[16,22]

One would be tempted to sputter the surface and assume some equilibrium surface structure is reached, however no studies have been performed to confirm this nor is there any information regarding the appropriate sputtering parameters to reach such an equilibrium. Generally sputtering is performed until no surface contaminants are detected by some chemically sensitive spectroscopy such as XPS, Auger, or LEIS. These techniques say nothing of topography and surface defects, and LEED, which is often used for other materials to characterize surface crystal structure, is not entirely convincing in the case of YSZ, since surface charging and surface roughening may both result in diffuse diffraction spots.[13] Without alternate confirmation instrumental and material effects cannot be separated.

In this chapter we examine the YSZ(100) surface using a combination of ambient and UHV techniques. In UHV, both non-contact FM-AFM imaging and heating to high temperatures for extended periods of time have proven to be extremely difficult with the as-received system. The former being due to sample charging, and the latter a result of machine design issues which make maintaining a cool sample holder impossible above a certain sample temperature. If the holder temperature rises much above 250 °C soldering at the coolant reservoir will become unstable and catastrophic venting of the chamber will ensue.

For these reasons, imaging and heating have been transferred out of the UHV environment. Intermittent contact (tapping mode) AFM under ambient conditions has been performed to study surface topography on a large number of YSZ(100) single crystals in order to determine the possible variation between samples. How this variation may affect such factors as annealing, sputtering, and metal deposition is examined with the goal of developing sufficient material knowledge so as to separate out instrumental effects, and to guide experiments and instrumentation development upon transfer to UHV.

The following subsections describe a study of the surface variability in a large number (n=20) of YSZ(100) single crystals. The source of this variability, its modification through high temperature annealing, and the influence such disperse surfaces may have on palladium deposition and in-situ cleaning is discussed. Some of the images in this chapter correspond to phase or topography scans and are labeled to reflect which channels they represent. Black letters on a white background signify topography images, while white on black indicate phase (dissipation in Chapter 4). Black letters on a grey background represents more highly magnified scans within regions of images that are also presented. Different panels within a figure may be labeled with the same letter though of different colouring, this indicates that several channels (or magnifications) of the same image are being presented. Unless otherwise indicated the imaging scan speed (v) is one line per second.

3.2. Surface Variability and Annealing

Previous studies in air of the YSZ(100) surface after treatment to 1200 °C have shown terraces separated by steps.[9-11] The step heights were determined to be approximately half unit cell (2.5Å). The authors observed, in some samples, the presence of pits 20 nm -30 nm in diameter and 0.51 nm or 0.25 nm in depth, distributed homogenously on the surface with high density. However, Thome *et al.* [21] observed the evolution of parallel terraces without the presence of pits. In this case the step height increases from 0.5 nm at 1000 °C to 1 nm at 1200 °C, and 2 nm after annealing to 1400 °C.

The discrepancies related to sample history dependence, and pitted vs. non-pitted surfaces, lead to the question of whether or not the disparity is entirely the result of different surface treatments, or in part, is a result of the initial variation between samples. It is important to emphasize that the presence of surface features dramatically affects the growth of metal particles on the surface, which in turn determines the relevance of the model catalyst studies to real systems.[1, 3-6, 23, 24] Therefore, as an initial step, it would be of great value to observe the variation in surface morphology between samples of YSZ single crystals, and the evolution of the steps and defects as a function of preparation conditions.

Studies using atomic force microscopy have been performed recently to view the initial surface structure of wide bandgap insulators [25-30] prepared by cleavage. Various topographies such as pointed directional steps are formed from the cleavage, and annealing causes surface diffusion and interaction of defects such as steps, evaporation pits and dislocations. To our knowledge no detailed work has been performed on YSZ. In order to obtain a nominally flat YSZ(100) surface, crystal manufacturers commonly use chemical and mechanical polishing, but crystals prepared in this manner are often found to contain defects such as etch pits, and therefore characterization of such surfaces remains important. Previous studies have shown that YSZ begins to form terraces of 1 or more atomic steps in air at temperatures between (800-1000) °C.[21, 31] However in these cases the studies were performed on single samples at low resolution. We will therefore use temperature treatments of a large set of samples to study the surface structure and defects of YSZ(100) at the nanometer scale after air anneal to 1000 °C. Furthermore the evolution of selected surfaces and nano-structures with time and higher temperatures are examined.

3.2.1. Experimental

Flux grown YSZ(100)$^{\pm 30'}$single crystals (ZrO_2:Y_2O_3 = 87:13) of 8 mm diameter and 0.5 mm thick were purchased from MTI Corporation with a nominal roughness of less than 5 Å obtained after a proprietary chemical and mechanical polishing technique (CMP). This technique, common to many YSZ(100) suppliers,[32-34] involves multiple polishing steps with solutions of nanoparticles of silica and alumina. MTI Corporation also adds a heat treatment to 1000 °C.

Approximately 20 samples in total were analyzed. Of these, 5 samples were randomly selected to be both imaged with AFM and characterized by x-ray photoelectron spectroscopy (XPS) prior to heating to determine the initial topographic and chemical variability in the as-received samples. All 20 crystal samples were placed in a covered alumina boat, and heated without pretreatment to 1000 °C in a clean quartz tube furnace for the allotted time. Upon cooling, topographic imaging was performed in air on several areas of each sample using a Molecular Imaging PicoPlus atomic force microscope in intermittent contact mode. The cantilevers used for imaging had a nominal resonance frequency of 190 kHz and were manufactured by Nanosensors (PPP NCL or SSS NCL). Upon annealing we found that the 20 surfaces showed a wide array of topographies, which could fit into one of 3 qualitative categories.

XP-spectra were acquired after the heat treatment in order to view surface chemical changes due to the annealing process. XPS and in-situ cleaning were performed in our multi-technique ultra-high vacuum chamber with a base pressure of 1 x 10^{-10} mbar. Shifts in the binding energy spectra due to charging effects were observed and corrected using the Zr $3d_{5/2}$ peak (set at 182.6 eV for Zr in YSZ).[15, 35]

Time evolution of the surface morphology was performed by heating samples of each type to 1000 °C for (1, 3, 5 and 11) hrs. A temperature evolution of the samples was also performed by heating to 1150 °C and 1300 °C for 1 hr each in a high temperature muffle furnace.

Palladium was e-beam evaporated onto the YSZ surface at room temperature from a high purity rod (ACI Alloys 99.98%). Sintering was performed at 135 °C in air for 30 minutes with AFM micrographs acquired both pre- and post-sintering.

Root mean square (RMS) roughness values and feature heights measured from line profiles were obtained with the commercial control software for our AFM (Pico Scan 5). Unless otherwise stated, RMS values were calculated based upon 2 μm x 2 μm images, which taken at a resolution of 512 x 512 points, resulted in a lateral step size between height elements of approximately 4 nm. Statistical image analysis in 2-D was carried out using "UTHSCA Image Tool" freeware available online. Due to our pendulum style AFM, images in some cases required flattening before analysis or presentation. We used the minimum order possible, which was determined by the image size.

3.2.2. Initial variability

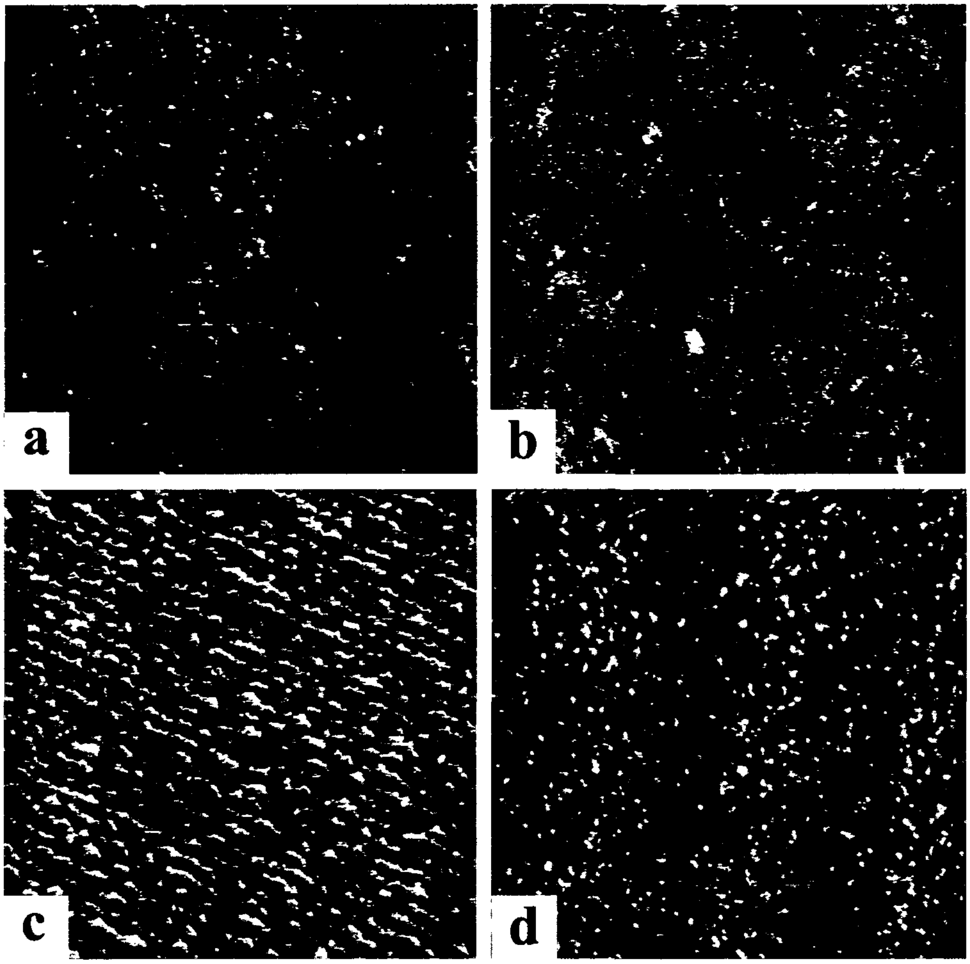

Figure 3-1: *2000^2 nm^2 AFM images of YSZ(100). (a)(z_{range}=5 Å) and (b)(z_{range}=4 Å) As received single crystals. (c)(z_{range}=7 Å) and (d)(z_{range}=10 Å) Samples a and b treated to 1000 °C for 1 hr. Heating in air causes the concentration of contaminant carbon to decrease and the surface to anneal. The resulting images present more finely resolved features with the removal of carbon improving image quality.*

For samples imaged "as-received", the chemical and mechanical polishing of the surface by the manufacturer resulted in an image with an root mean square roughness (RMS) of 0.8 Å, well below the maximum corrugation reported by the supplier (<10 Å guaranteed, <5 Å typical). Figures 3-1a and 3-1b represent two different samples of as-received YSZ(100), both with parallel terraces. These terraces are not normally seen by other authors at room temperature in the as-received samples,[21, 31] and are probably the result of annealing by the supplier during surface preparation. A large quantity of horizontal streaks in the fast scan direction is common to all the images viewed before annealing, and is attributed to adsorbate interactions with the cantilever tip.

Figure 3-2 shows XP-Spectra of the Zr 3d, O 1s and C 1s peaks before and after temperature treatment (1000°C, 1 hr). The corresponding carbon concentration of the as-received samples was calculated to be approximately 14 atom percent, and a small Si peak was sometimes observed. A second C peak was often seen and attributed to a reduced carbon species such as a carbide (BE = 282.1eV).[36, 37] From peak intensities and their relative sensitivity factors available from the Scofield library, we found the oxygen to metal ratio ($O/(Y+Zr)=1.7\pm0.1$) to be below the stoichiometric value of 1.9.

3.2.3. Thermal anneal to 1000 °C

Each sample was imaged after annealing to 1000 °C for 1 hr and a wide range of surface morphologies was observed by AFM; we have qualitatively divided them into 3 categories which are discussed in more detail below. Figure 3-3 shows example images of each type, as well as line profiles of significant features from each. The Type 1 surface is most common, observed in 50% of the samples studied; Type 2 and 3 constitute 25% each. XPS of the post anneal crystals show a large decrease in the C 1s peak accompanied by the formation of some reduced zirconium species (Figure 3-2). Both ZrC or SiC could be present,[36] but their overall concentration in the probed surface volume is small (<3%). For all measurements we see an increase in the oxygen to metal ratio upon heating, near to its stoichiometric value. This process could be viewed as the filling of oxygen vacancies during annealing.

Figures 3-1c and 3-1d show changes due to annealing of the samples seen in Figures 3-1a, and 3-1b, respectively. For all images the quantity of horizontal streaks has been dramatically reduced upon heating, allowing resolution of finer defect structure not clearly visible in the as-received samples. Major features such as steps and terraces remain the same, though the RMS roughness values increase from an average of 0.8 to 1.8 Å. Therefore, the observed surface features are not solely due to surface carbon, which has been reduced dramatically.

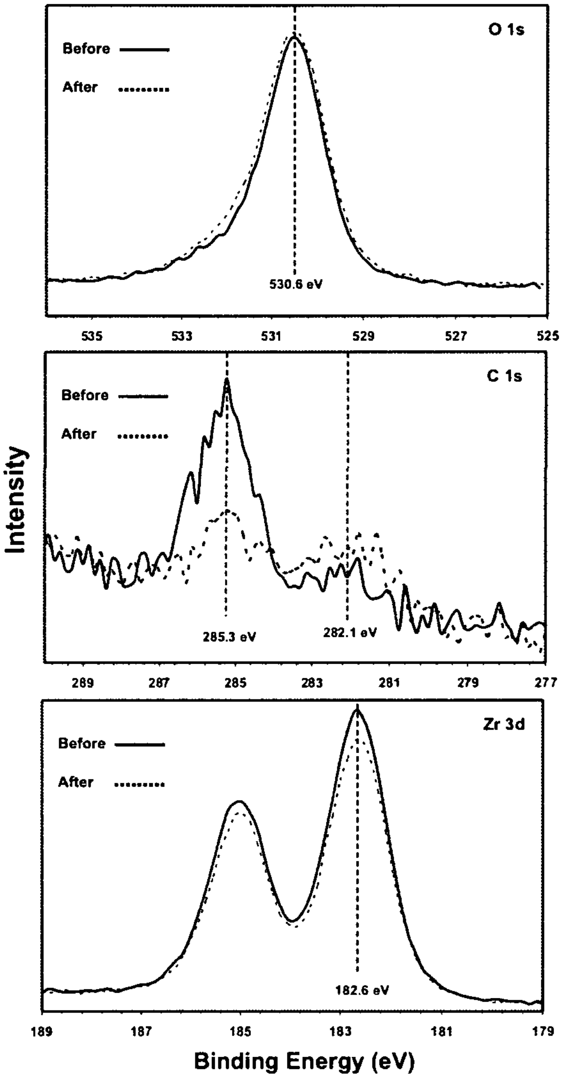

Figure 3-2: *XP Spectra of the as-received sample (solid line labeled "Before") and after treatment to 1000°C for 1 hr ("After"). The panels show the O 1s, C 1s and Zr 3d peak regions. Binding energy was calibrated using the Zr 3d peak at 182.6 eV. Results show an increase in oxygen to metal stoichiometry, and a decrease in carbon concentration.*

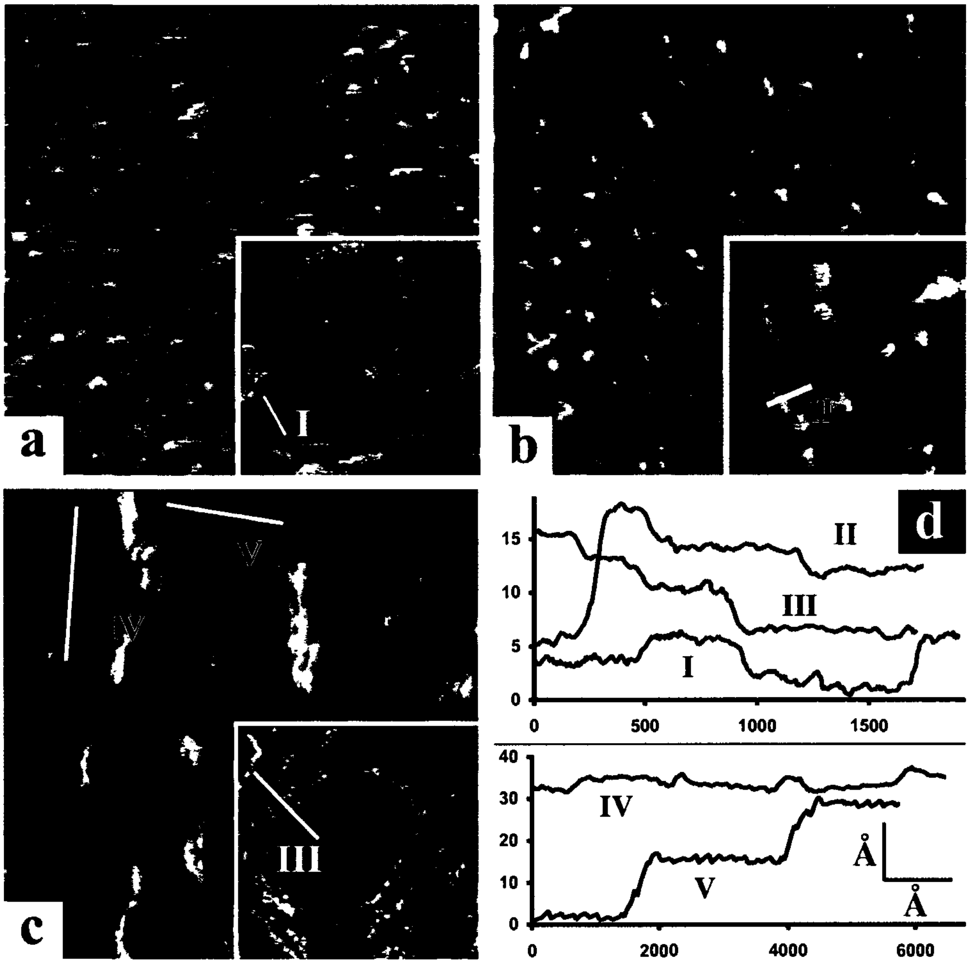

Figure 3-3 *2000^2 nm^2 AFM images of YSZ(100) after treatment to 1000 °C for 1 hr. Insets show higher magnification 500^2 nm^2 images. (a)(z_{range}=9 Å, inset z_{range}=10 Å) Type 1 surface (b)(z_{range}=10 Å, inset z_{range}=17 Å) Type 2 (c)(z_{range}=19 Å, inset z_{range}=10 Å,* v=*1.8 l/s) Type 3. (d) Line profiles corresponding to all three images as labeled by roman numerals.*

A large number of surface nanostructures and defects were resolved by AFM. We have used some of these features to qualitatively categorize all the surfaces into 3 Types. Importantly, all the surfaces measured contained a large number of defects, generally not reported in previous YSZ(100) studies.[9-11, 21, 31]

Type 1 surfaces (Figure 3-3a) are characterized by a high density of parallel steps and terraces. The step edges show a variable number of defects, and the terraces themselves often contain pits or clusters of ad-atoms. The sizes of the terraces vary from sample to sample, ranging from ~50 nm (Figure 3-1c) to ~600 nm (Figure 3-1d). However, within each sample, the terrace sizes were relatively constant with a low standard deviation (mean σ=15%). The pits also varied in size, but as a rule for this surface type no pits exceeded 1 unit cell in height (reported bulk value **a**=5.124 [33]), and were most often 0.5**a**. The pits sometimes intersect with a step edge, distorting the edge shape. In fact for many surfaces of this type most of the contour at the edges is the result of pitting. Even with the pitting at step edges, terraces for Type 1 surfaces are clearly resolved with step heights being uniquely half unit cell. Type 1 images exhibited the lowest RMS roughness with an average of 1.5 Å.

Type 2 surfaces (Figure 3-3b) have a more complicated defect structure as compared to Type 1. These surfaces contain a larger concentration of surface pits some of which extend to a depth greater than 1 unit cell (0.5**a** to 3**a**.). These pits have distorted the surface structure to such an extent that no parallel terraces or steps can be clearly defined. For some of the Type 2 samples we were able to resolve square shaped pits with the edges along two crystallographic directions. The average RMS roughness for these images is intermediate at 2.2 Å.

Type 3 surfaces (Figure 3-3c) show rectangular holes distributed on the surface. The holes range in size from (80 to 330) nm along the major axis length and show atomically flat bottoms (corrugation < 1Å). The image is dominated by these holes, but ridges can be observed in the areas between them. Due to the small sizes between ridges, it is difficult to determine from the line profile whether a single or double step is measured. However, in general the smallest and by far the most common ridges have a step height of 0.5**a**. The holes themselves are typically 0.5**a** in depth with respect to the next lowest ridge, though in some cases we observe larger depths. These larger heights are possibly due to an arrangement of steps along terraces whose edges are not regular. In Figure 3-3c, holes which lie next to each other in the y-direction (IV in Figure 3-3c) are frequently separated from one another by a thin boundary line of half unit cell height, but lie at the same height with respect to one another. On the other hand holes adjacent to each other in the x-direction (V in Figure 3-3c) are almost always separated in height from each other by higher multiples of the half unit cell, up to a maximum of 12.5 Å. This indicates that irregular terraces are generally running along the y-direction in this image. The RMS roughness of this sample type is larger than the others due to the high ridge and hole features; they have an average RMS of 3.0 Å.

All samples exhibit a large number of defects that cannot be explained solely by the thermal production and agglomeration of point defects. The most unexpected features are the large rectangular holes with flat bottoms that were sometimes found in Type 2 surfaces but were the defining characteristic of the Type 3 surface. The origin of this feature cannot be determined unequivocally, however, there is a precedent for the growth of geometric pits reflecting the surface plane when a mechanism allows for the removal or diffusion of surface atoms, a comparison with other surfaces can aid in understanding.

Dynamic force microscopy of KBr(100) surfaces have shown that electron irradiation causes the formation of rectangular pits with atomically flat bottoms and atomically straight steps.[30, 39] The mechanism involves the formation of defects (f- and h-centers) by the electron beam, which eventually result in preferential desorption of atoms from step edges. Such a mechanism is not operational in our case since we do not use an electron source, however the preferential desorption (or diffusion) from existing defect sites seems relevant. This mechanism may be initiated thermally if the nature of the defects makes them sufficiently reactive as was the case reported by Engelhardt *et al.* [39, 40] for the growth of evaporation pits in which the combination of electron bombardment and heat caused the formation of hexagonal pits in $CaF_2(111)$. Evaporation is an unlikely mechanism for surface pitting in YSZ due to its high melting point (2680 °C), however this example illustrates how the initial production of defects by some mechanism may alter the energetics of the surface allowing pit formation through movement of atoms. This movement may simply be diffusion across the surface, since the energy barrier for this process is much lower. More recently, Gritschneder *et al.* observed the presence of small shallow pits on the terraces of $CeO_2(111)$.[41] That surface is characterized by its hexagonal geometry, which is evident in the formation of hexagonal terraces as well as hexagonally shaped pits. Pit sizes were small (3 nm - 10 nm) and appear with low density, homogenously dispersed on the surface.

The ceria, CaF_2 and KBr studies seem to explain the observation of the rectangular holes in YSZ(100), namely that the presence of defects on the surface provides sites from which the holes can grow. The shape of the holes are given by the symmetry of the surface, namely the sides of the rectangle follow crystallographic directions. On YSZ(100), the corners of the rectangular holes are sometimes rounded, suggesting the presence of kink-atoms and subsequent growth of the edges in a different direction may not have such a high energetic penalty. However the question remains as to how the defects are initially produced.

In these experiments, the surfaces were not irradiated or otherwise altered prior to heat treatment, suggesting that the samples are received with a variable defect structure (bulk and/or surface) due to the manufacturing process. As mentioned in the experimental section, the process involves flux growth and subsequent chemical and mechanical polishing, as well as heat treatment to 1000 °C. It is likely that the combination of CMP, which is well known to produce etch pits and other defects in crystals,[42] and heat, results in the variety and structure of observed features. The high density of defects in our case, as well as their growth with temperature (see following section) suggests that the mechanism for growth of the surfaces and nano-structures seen is partly the result of interaction between defects formed during polishing. That is the defects' interaction cannot be neglected, and at 1000 °C when surface diffusion is active due to the removal of kinetic hindrance, these interactions may dominate the energetics.[39, 43-45]

Alternatively, etching can occur not only via the CMP cleaning of the surface, but possibly through chemical reaction during the annealing process to 1000 °C, a process which has already been performed by the supplier before delivery. We cannot rule out such a mechanism completely, but any reaction of the surface with carbon (which is the most common contaminant) would either result in a loss of oxygen, which by XPS was in fact found to increase, or by formation of carbides by reaction with Zr or Y. The small amount of carbide we see cannot account for all the surface features. Furthermore, all samples contained a similar quantity of carbon at the surface in the as-received state, and all were prepared in the same manner, yet only a fraction developed pits. An initial variation in the samples themselves must still be the largest contributor to the observed features.

3.2.4. Annealing: Evolution of Type 3 surfaces in time and with temperature

In order to elucidate the annealing and defect growth mechanism for our YSZ surfaces we examine the topography of a Type 3 sample as a function of annealing time. Imaging was performed at room temperature for the same crystal annealed for 1, 3, 5, and 11 hours at 1000 °C. Figure 3-4c shows the surface at 1 hour, while Figures 3-4a, and 3-4b were taken at 5 and 11 hours respectively. From image analysis we find that the holes cover a linearly increasing percentage of the surface with time, 38 % at 1 hour to 58 % at 11 hours. This increase is initially a result of the holes growing in size from an average area of

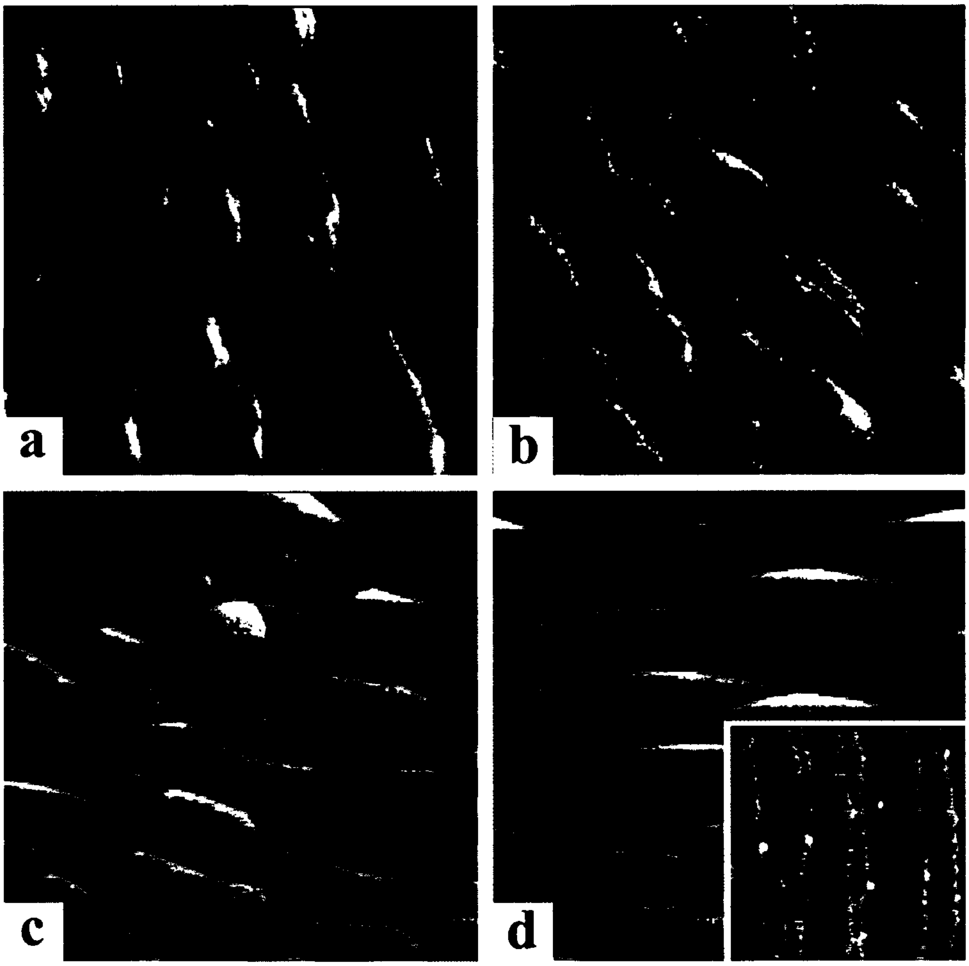

Figure 3-4 *2000^2 nm^2 images of a YSZ(100) Type 3 surface. (a)(z_{range}=18 Å) Time evolution, after 5 hrs at 1000 °C. (b)(z_{range}=22 Å) Time evolution, after 11 hrs at 1000 °C. (c)(z_{range}=21 Å) Temperature evolution, after 1 hr at 1150 °C. (d) (z_{range}=15 Å) Temperature evolution, after 1 hr at 1300 °C. Inset in d (z_{range}=10 Å) shows a 1000 nm x 1000 nm Type 1 surface treated to 1300 °C.*

2.9 x 10^4 nm^2 at 1 hour to 4.4 x 10^4 nm^2 at 5 hours, with the number of holes per unit area remaining relatively constant at approximately 13 μm^{-2}. At 11 hours we find that the number concentration of holes has increased significantly to about 17 μm^{-2}, but the average size has decreased to 3.9 x 10^4 nm^2. Initially the holes grow at the expense of the contoured areas, but since the underlying structure is made up of irregular steps and terraces, the holes can only grow as large as the terraces supporting them. Furthermore, once one side of the square-like holes is restricted, the adjacent side only elongates along the terrace to a fixed extent, until the energetics prefer the formation of, or division into, another hole. This view is supported by the existence of the narrow boundaries of 0.5**a** height between holes. The growth of the holes in time supports the contention that the initial defect structure from the CMP surface preparation, either in the form of etch pits or high concentrations of smaller point defects, seeds the surface for the growth of larger structures upon heating.[42, 45]

It is clear that the annealing kinetics at 1000 °C for a Type 3 sample are relatively slow. If one were to use the rate of hole growth (percent coverage) as an estimate of the overall surface annealing rate for YSZ at 1000 °C, then it can be written simply:

$$Ridge \xrightarrow{k_a} Hole$$

$$\frac{d[A_{hole}]}{dt} = -\frac{d[A_{ridge}]}{dt}$$

$$\frac{d[A_{hole}]}{dt} = -k_a[A_{ridge}]^{v} = -k_a[1 - A_{hole}]^{v}$$

Assuming $\nu = 1$, if one considers annealing as a diffusive process in which each unit is independently moving, similar to a first order reaction. Then the integrated rate law is:

$$[A_{ridge}] = [A_{ridge}]_o e^{-kt}$$

$$or$$

$$[1 - A_{hole}] = [1 - A_{hole}]_o e^{-kt}$$

Here $[A_{hole}]$ is the surface concentration of the species located in a hole and can be written as the ratio of the total surface area covered by holes upon the total area examined.

Plotting the natural logarithm of [1-A_{hole}] versus anneal time in Figure 3-5 yields a rate constant from the slope of the fitted line:

$$k_a = (0.057 \pm .013) \text{ hours}^{-1}$$

In practical terms the amount of time required to cover half the surface in holes from a completely un-annealed sample is:

$$\tau_{½} = (18.5 \pm 4.0) \text{ hours}$$

In this case the error is derived from the image analysis procedure* which provides a measurement of area coverage with an estimated uncertainty of 5 %.

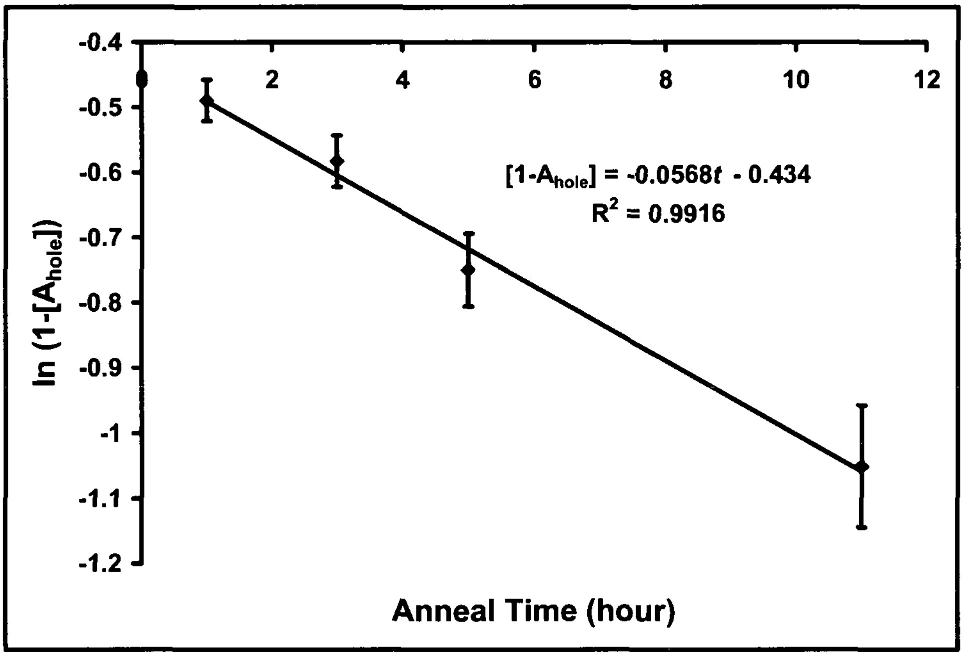

Figure 3-5 *Plot of the surface fraction not annealed (ridged area) as a function of air anneal time at 1000 °C. Assuming first-order kinetics the slope of the line yields the rate constant for the hole growth, and consequently a rough estimate for the annealing kinetics of the YSZ (100) surface in air at 1000 °C.*

---

[*] Image analysis was performed by printing the topographic AFM images to be analyzed in a large enough format to just fit an entire letter page i.e. 8" x 8". A transparency was placed over the image and the areas to be quantified were traced along with the corresponding scale bar. The transparencies were then scanned and analyzed using the aforementioned software. Alternatively the phase channels of the AFM images considered showed sufficient contrast between holes and ridges and could have been analyzed directly by integrating the intensity distribution.

The determined rate constant can only be considered a rough estimate of the actual surface annealing process since it will surely vary depending on the initial structure at the surface and the type of defects. For this estimate we used a relatively macroscopic entity, the holes, as a higher order manifestation of an atomic diffusion process. Obviously pits which are very large in depth will take longer to anneal, however using the holes as an estimate is scientifically relevant since it is the production of atomically flat areas we seek. The holes are literally areas that are atomically flat.

Though the holes themselves are atomically flat, the overall surface roughness is seen to increase in time. Over the first 5 hours the RMS roughness remains constant at 4.0 Å, but becomes larger at 11 hours to a value of 4.7 Å. This increase in roughness is accompanied by the loss of the ridge structures to a hole-and-step height increase, reaching 3.5**a**. Upon heating the same sample to 1150 °C for 1hour (Figure 3-4c), we find that the holes have largely healed save for smaller circular pits 0.5 or 1**a** in height with diameters between 20-80 nm. The ridged structures have also smoothed and the irregular terraces are now clearly visible with maximum step heights of 3.5**a**. RMS roughness has reduced to approximately 4.3 Å due to the hole and ridge smoothing. Figure 3-4d shows the same YSZ surface annealed for 1hr at 1300 °C, the surface is now entirely free of surface pits, and has further flattened (RMS roughness ~2.7Å). The image shows the formation of wavy terraces, similar to those seen by Cho *et al.* for $SrTiO_3(100)$ surface annealed to 1000 °C.[47] Such terraces are sometimes considered to be the result of crystal miscuts along both directions of the surface, with a miscut in only one direction resulting in parallel terraces. This wavy structure can be compared to the parallel step and terraces of a Type 1 surface annealed to 1300 °C (inset of Figure 3-4d). The difference implies that initial surface defects determine the morphology of the annealed structure even up to 1300 °C. Complicated structures result as a combination of crystal miscut and defects introduced during crystal preparation by the manufacturer.

3.3. Defect Layer

It has been shown that the there may exist a variety of initial defect surfaces on YSZ, and that they are mobile, though slowly annealing, at 1000 °C. In the Type 3 surface AFM topography images show areas composed of large ridges and atomically flat holes, though the surface is attributed generally to the presence of defects, the types are not clear, nor is the mechanism for orienting into squares.

For surfaces to self-organize as they do in Type 3 samples, there must be some net energy being lowered as a result of this organization. YSZ(100), if bulk terminated, is polar. Polar surfaces are well known to undergo major reconstruction, as the energy cost associated with maintaining separated opposing charges is high. When kinetically permitted, atoms can rearrange towards a neutral surface, sometimes resulting in an extreme variety of complex nano-structures.[48, 49] Alternatively if a heterogeneous surface region exists in which one species has a lattice mismatch with another, then surface reconstruction may occur in such a manner as to minimize the strain induced by such a mismatch.[47, 50, 51]

In the previous calculations of the annealing kinetics of a Type 3 surface, it was shown that annealing occurs relatively slowly. However, the rate cannot be attributed strictly to atomic diffusion, if simultaneously a chemical process such as reaction or even segregation is underway. These processes may be required for the formation of the flat bottomed holes, and may be rate limiting. Some additional insight can be gained by examining the XP-spectra taken of the sample shown in Figure 3-4 after the corresponding anneal times.

Quantification of the XPS signals of the Type 3 surface as a function of annealing time (Figure 3-6) show that oxygen content in the examined volume increases with anneal time so that the defect layer is apparently becoming more stoichiometric. When examined in unison with their corresponding AFM topography images some of which are presented in Figures 3-3c and 3-4b, this would suggest that flat holes are actually more stoichiometric than the ridged portions, since it is these areas covered by the flat portions that increase in time.

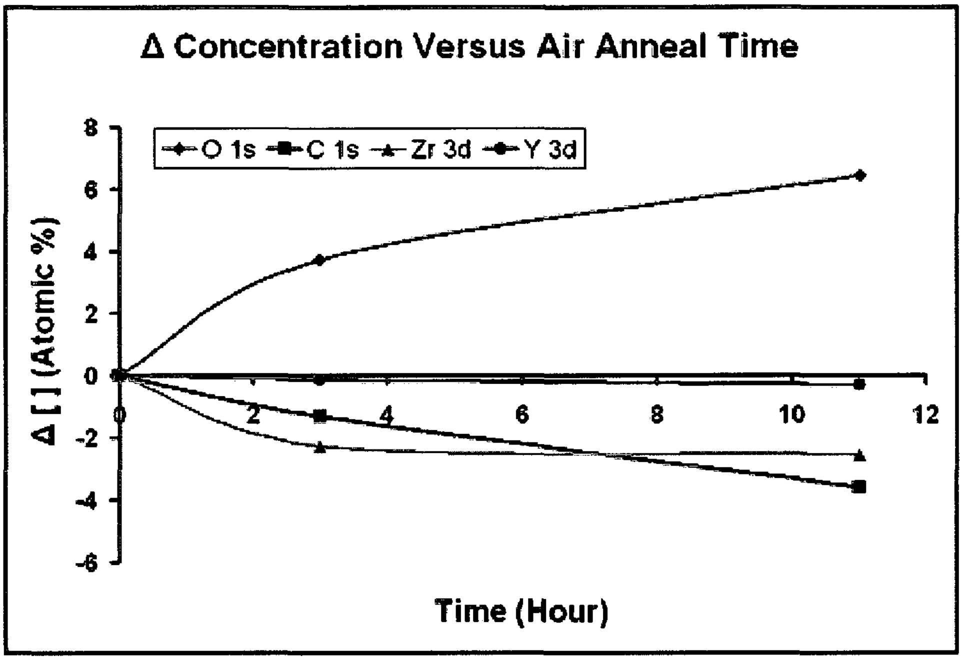

Figure 3-6 *Change in atomic concentration by element as a function of ambient anneal time at 1000°C. Oxygen concentration is shown to increase with anneal time, indicating the surface becomes more stoichiometric in time. Lines are guides to the eye only.*

The possibility of having two species on the surface which interact to minimize lattice mismatch is strengthened upon examining AFM phase image channels. Phase image contrast is derived from differences in the elastic modulus of the material being probed and therefore contains chemical sensitivity.[52-54] In Figure 3-7a phase imaging shows a nearly bimodal intensity distribution (Figure 3-7c) with the holes being dark and the ridges being bright. One interpretation of the combined XPS and AFM data is that there exists a non-stoichiometric defect layer on the surface (the ridged areas) as a result of oxygen vacancies

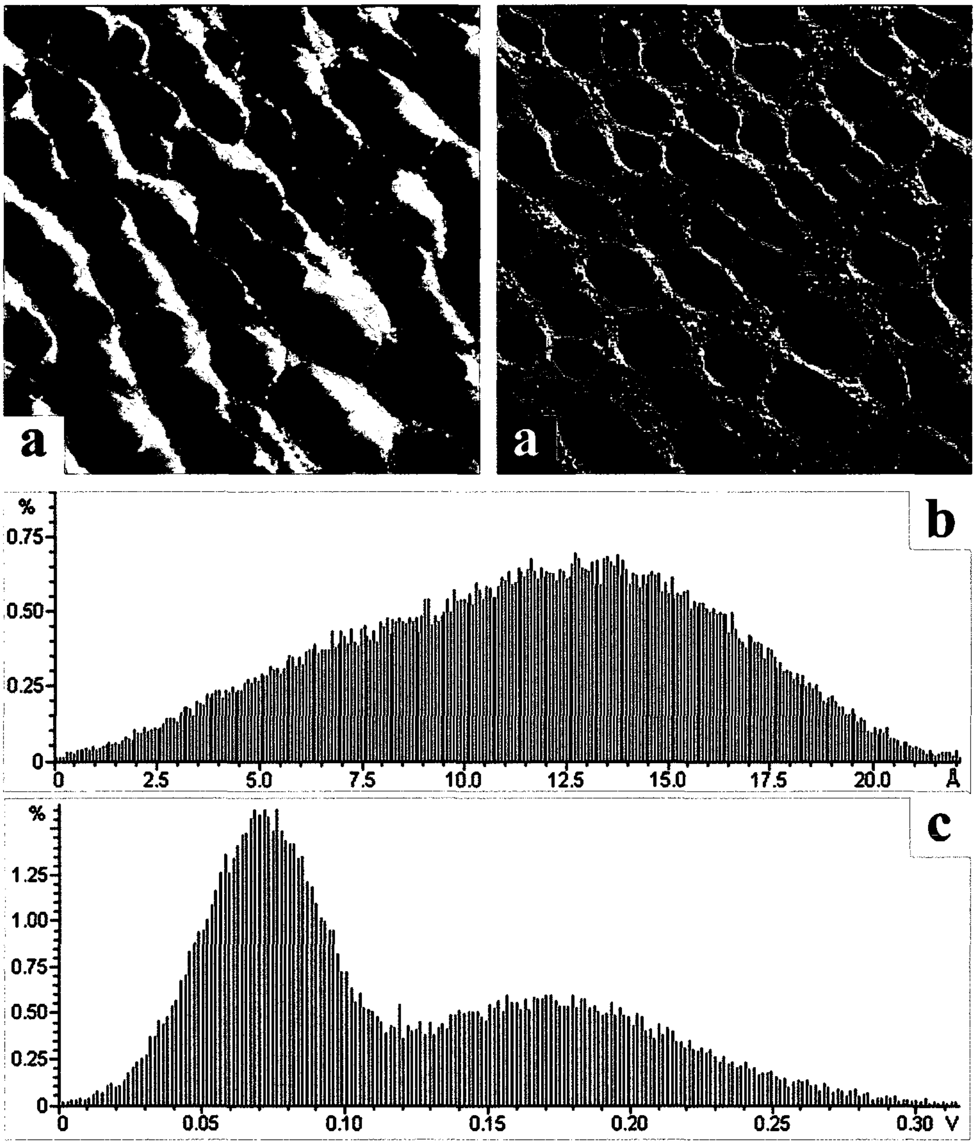

Figure 3-7 *(2000^2 nm^2) (a) Topography (left)(z_{range}=22 Å) and phase image (right)(z_{range}=2.9°) of the YSZ (100) surface after heating in air to 1000 °C for 11 hours. The phase image clearly shows the contrast between the flat holes and the ridged areas of the surface. Phase contrast results from changes in elastic modulus and therefore has chemical sensitivity, indicating the surface is composed of at least two different species. Panels (b) and (c) show the intensity distributions for topography and phase imaging respectively, the bimodal distribution is apparent in (c) with the peaks representing the hole and the ridged areas separated by a phase difference of 0.9 ° (0.1 V x 9 °/V).*

produced during the CMP process. These vacancies, in sufficient concentration, may modify the lattice mismatch to such an extent that self organization over the underlying stoichiometric surface (flat holes) is possible. At sufficiently high temperatures such as 1000 °C, oxygen is reincorporated into the matrix which attains it's stoichiometric lattice spacing value and may recombine with the underlying surface (the holes).

Polar surfaces like YSZ(100) may be also stabilized by the adsorption of hydroxyl groups.[55] In this way the increasing trend in oxygen concentration with corresponding expansion of the flat areas could be explained by regions becoming hydroxylated during the annealing process. Morterra *et al.* have presented a complicated interaction of annealing temperature with surface hydroxyl groups on tetragonal-YSZ.[56] This is likely not a dominant effect since it is shown in chapter 5 that major topographical surface modifications occur upon reduction of a cleaned YSZ surface rather than through hydroxyl removal.

Though surface hydroxylation may account for the increase in oxygen observed, the existence of a near surface suboxide layer has been reported elsewhere for defective YSZ.[20] Here the suboxide is proposed to exist in layers of varying stoichiometry with the most reduced layer near the surface, eventually reaching full stoichiometry at depths greater than approximately 1.2 nm. Calculations of the bond geometry of YSZ [57] show modification of the bond length around oxygen vacancies in YSZ and therefore modification of the lattice constant would occur for the suboxide.[58] Moreover, Wang *et. al.* showed by nano-indentation measurements that modification of the elastic modulus in cubic fluorite oxides will occur with the introduction of oxygen vacancies, this could account for the observed phase image contrast.[59]

Phase contrast is not observable for all sample images; in these cases the surface could be completely covered in a defect layer, or no defect layer at all. However the absence of phase contrast does not necessarily guarantee that material properties which would normally produce it are not present on the surface. That is, conclusions can be drawn from the presence of phase contrast, but not necessarily from its absence. Phase imaging generally requires specific scanning parameters, typically high tip oscillation amplitudes in conjunction with low (i.e. close to the surface) setpoints.[52, 60, 61] These scan parameters could not necessarily be maintained while concurrently acquiring high quality topography images whose optimal scanning parameters could be different. Fortunately in many cases both imaging channels optimized simultaneously, and in Figure 3-8 samples with surface Types 1 (a and b) and Type 2 (c) exhibit phase contrast indicating the that the heterogeneous defect layer can be found on all surface types.

Normally phase contrast can be well correlated with specific topographic features such as pits and terraces as seen in Figures 3-8b and 3-8c, however in Figure 3-8a such a correlation does not exist. Instead contrast exists between areas near the step edges, and areas just after the steps. Point defects such as vacancies are well known to accumulate at step edges since binding energies may be lower due to the abrupt termination of the lattice. The formation of a suboxide would therefore more likely begin at the step edge as seen in Figure 3-8.

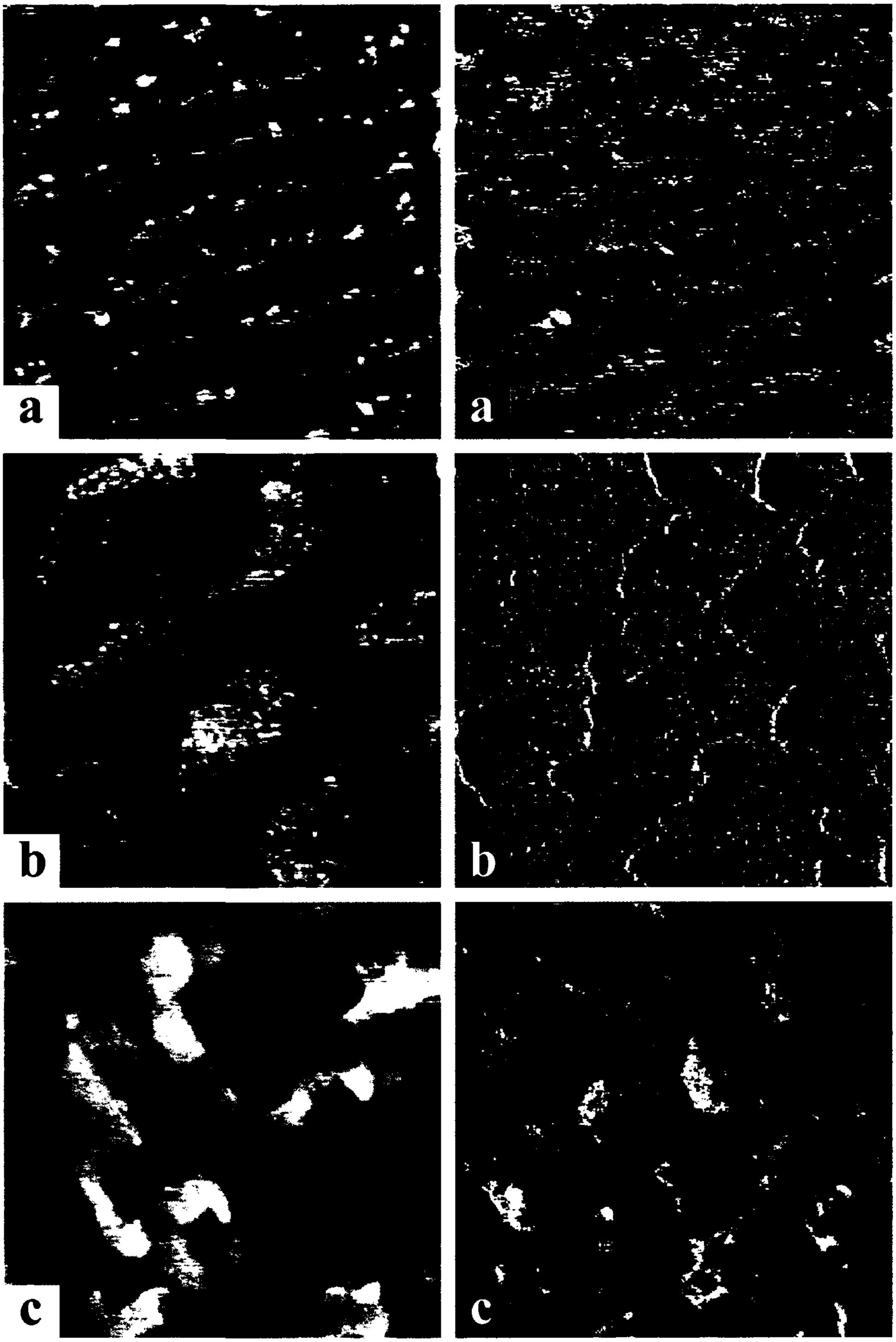

Figure 3-8 *Left panels: topography, right panels: phase. Image set (a)(1500^2 nm^2, 5hr, z_{range}=4 Å, 0.5°) Type 1 surface with no pits, observed phase contrast does not correspond to any discernable topographic feature. Image set (b)(450^2 nm^2, 1hr, z_{range}=7 Å, 0.5°) of Type 1 surface, pitting in topography corresponds with phase contrast, initial defect structure from CMP has not yet had sufficient time to organize. Image set (c)(500^2 nm^2, 1hr, z_{range}=17 Å, 1.6°,* v=*0.8 l/s) Type 2 surface with phase contrast corresponding to square pits.*

3.3.1. 1-D nano-structures on a Type 1 surface

Figure 3-9 shows high resolution images obtained with an ultra-sharp tip (SSS-NCL), of a Type 1 surface annealed to 1000 °C for various lengths of time. We have been able to resolve the growth of linear structures at step edges running in 2 perpendicular crystallographic directions. The widths of the lines are ~8 nm (~5 nm after elementary tip deconvolution) with line heights typically in units of 0.5**a** thus appearing to grow in a layer by layer fashion. The terraces are delineated by steps uniquely 0.5**a** in height.

The origin of the lines is not certain, and we have been unable to find reports of similar nano-structures on oxides. However, there are a few possibilities to explain these features. Firstly, a mechanism similar to the organization of overlayers during epitaxial growth may be possible if the impurity defects are sufficiently mobile. In the case of a system in which one species is deposited on a substrate of different identity, the mechanism involves self organization of deposited molecules or atoms oriented so that the excess energy arising from crystal lattice mismatch with the underlying substrate is minimized.[50, 51] As an example, Cimalla *et al.* have shown the growth of geometric structures of SiC on Si.[62] It is conceivable that the same sort of mechanism is at play here with the accumulation and growth of impurities or other defects such as ZrC, SiC, segregation of Y_2O_3, co-segregation of Si and Y.[63, 64] Further, the growth could result from small amounts of partially reduced YSZ suboxide identical to the proposed mechanism for the formation of the thicker defect layers discussed in the previous section. From XPS measurement of the shifted C 1s peak attributed to carbides, we find the surface coverage of carbide to be less than 3 %. This value seems too small to account for the observed features, however carbon may still play a role, perhaps in stabilizing other defects; this will be discussed further in Chapter 5.

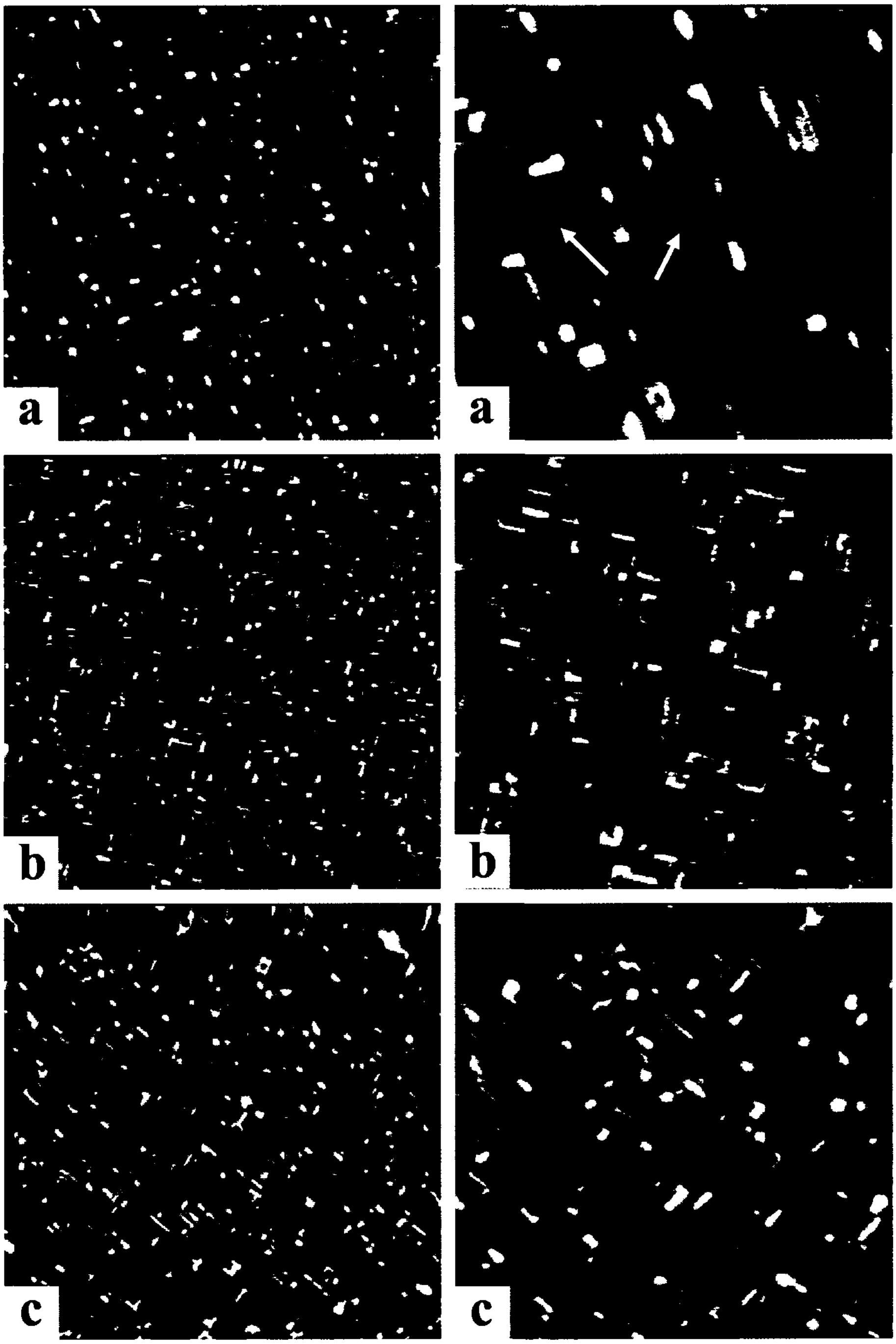

Figure 3-9 *Topographic AFM micrographs (left column 1000^2 nm^2, on right column (a) 340^2 nm^2 (b) and (c) 500^2 nm^2). YSZ annealed at 1000°C for: (a)(left z_{range}=12 Å, right z_{range}=12 Å) 1 hour, shows the initial formation of line defects by a preferential dewetting at the step edge. (b)(left z_{range}=16 Å, right z_{range}=15 Å) 5 hours, shows a higher concentration of line defects and terrace roughening due to diffusion of material from terraces to step edges. (c)(left z_{range}=14 Å, right z_{range}=13 Å) 11 hours, the concentration of line defects has lowered and the terraces have smoothed as a result of oxidation and subsequent recombination of line defects with the surface.*

Figures 3-9a to 3-9c show the growth of the line defects in time corresponding to air anneal times at 1000 °C of 1, 5 and 11 hours respectively. At 1 hour (Figure 3-9a) the step edges seem to first organize such that linear "trenches" are formed. The arrows indicate examples of positions where material in the step diffuses from the terrace to sites on top of it, thus a "trench" is formed with raised areas lining it, in one case on a single side and in the other case, both sides. It appears that the surface at this stage is undergoing a dewetting-like process, with diffusion occurring in preferential directions. Esch *et al.* have demonstrated in atomically resolved FM-AFM images that thermally induced oxygen vacancies in $CeO_2(111)$ (a cubic fluorite structure) tend to accumulate in linear chains along the surface.[65] This process may act as the initial source of the linearization, acting as nucleation points or dewetting points for subsequent formation of larger linear structures. Alternatively, if the energies of diffusion are larger in one crystallographic direction than another then this type of linear structure could be formed.

After annealing for 5 hours (Figure 3-9b), the step edges are covered with greater density of higher and more clearly defined linear structures. Dewetting has occurred further and several layers of line defects have grown on top of each other, up to step heights of 18 Å or 3.5**a**. At 11 hours of annealing (Figure 3-9c) the line defects have reduced in number though the overall height of the features has increased. Those remaining are composed of a larger number of layers, some as high as 23 Å (4.5**a**).

The process for the growth of these line defects can be more clearly determined by considering the images themselves (Figure 3-9) in combination with the corresponding statistical analysis of several images taken at the specified anneal time. The statistical analysis results are summarized in Table 3-1 and are taken over a set of 4 to 7 images for each of the given anneal times. The metric "max peak to valley" or MPV is defined as the height difference between the highest and lowest pixel on the image, and bounds the maximum feature size. The mean height is the average height of all pixels above the background minimum and can be related to the average volume of defects. The "terrace RMS roughness" metric is simply the RMS roughness on the terraces, no line defects or steps were included in these calculations.

Table 3-1 *AFM micrograph image analysis results summarizing the annealing of 1-D line defects on the surface of YSZ(100) in time. Statistics related to the terrace roughness are also presented. The results suggest that roughening initially occurs due to dewetting of a defect layer from the terraces, over time these defects are healed and the line defects rewet the surface. These measurements were taken over several images of the same sample.*

Anneal Time (hrs)	RMS Roughness (Å)	Mean Height (Å)	Max Peak to Valley (Å)	Terrace RMS Roughness (Å)
1	2.31 ± 0.08	4.67 ± 0.13	22.17 ± 1.27	0.23 ± 0.05
5	3.12 ± 0.06	5.91 ± 0.12	28.26 ± 1.08	0.57 ±0.06
11	2.80 ± 0.11	5.50 ± 0.17	35.95 ± 1.04	0.25 ± 0.04

The growth of the defects can be explained if we assume that initially the sample near surface region is defective as a result of the polishing process. If the nature of these defects alters the YSZ lattice to such an extent that the line defects may arise as result of strain minimization, they do so only when the temperature is raised and the diffusion is no longer limiting. At 1 hour of annealing time the diffusion and self organization has just begun with material at the step edges the first to mobilize. At this point the overall surface roughness, the maximum feature height, and the terrace roughness is the lowest of the three measurements. This indicates that higher layers of growth have yet to form. The low value of the terrace RMS suggests that the formation of the line defects is largely from the movement of atoms at the step edges rather than diffusion from locations further onto the terrace.

At 5 hours, as can be seen from image 3-9b, the line defects have accumulated and cover a larger portion of the overall image. The jump in the MPV is due to higher growth structures composed of a larger number of layers. Interestingly, the terraces themselves have become much rougher with the terrace RMS roughness more than doubling. This can be well explained by the diffusion of defective material from the terrace proper, to the step edges, where the growth of lines originally began and which now act as nucleation sites.

At 11 hours the area covered by the line defects has decreased significantly but the maximum feature height has increased. The continued growth, layer upon layer, minimizes the lattice strain by minimizing the interface "footprint" between mismatched lattices. The overall and terrace RMS roughness have both decreased suggesting two possible mechanisms: either the total volume of defective material has completely dewet from the terraces and accumulated into the few but high line defects seen in image 3-9c; or the defective material has become less defective, lowering the lattice mismatch allowing recombination with the pristine YSZ. This latter option is favoured since the overall volume above the terrace, roughly related to the mean height parameter, has actually decreased.

If in fact the defective layer is composed of oxygen vacancies as proposed in the previous section, this would explain the growth of line defects and subsequent recombination with the surface as the vacancies become filled upon thermal oxidation. For this to be possible the annealing kinetics allowing organization of defects must be at least on the same order or faster than the oxidation kinetics. If oxidation occurs quickly compared to surface diffusion then it would be expected that the surface would remain flat, with suboxide becoming stoichiometric before having a chance to organize. One would be tempted to examine the oxidation kinetics from Figure 3-6, to compare with the annealing kinetics estimated in Section 3.2.4. However, for annealing to a flat stoichiometric oxide to occur, oxidation must first take place and therefore, oxidation may very well be a rate limiting step before a true atomically flat surface can be achieved.

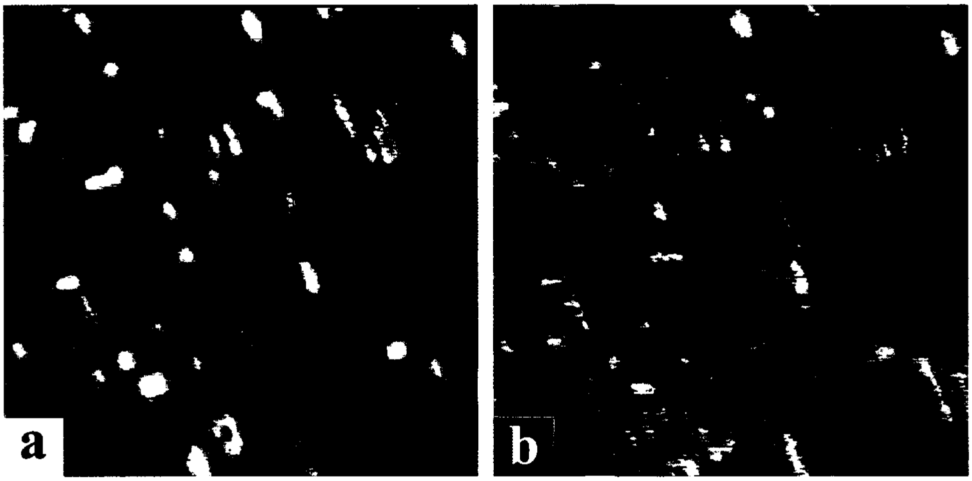

Figure 3-10 *(340^2 nm^2, z_{range}=12 Å, 2.7°) Left panel: topography, right panel: phase. YSZ (100) annealed for 1 hour at 1000 °C. Phase image shows some contrast at line defects.*

Figure 3-10 demonstrates the topography (identical to Figure 3-9a) and phase image taken at 1 hour of annealing to 1000°C. Phase contrast is clearly visible indicating a difference in elastic modulus between the line defects and the terraces. This is consistent with a defective overlayer that has not yet dewet, though the defects which alter the modulus of elasticity are present. As the defective material does dewet, thicker defect structures are formed, which act more like a bulk material rather than a thin film of the wetted layer, thus the modulus could be expected to change and the higher contrast for higher features could be expected. Moreover, the line defects can be considered to be a preferential organization of the most reduced areas of the sample since these would have the greatest lattice mismatch and the largest driving force to dewet. Since we see dewetting possibly as a result of an increase in oxygen vacancies, then areas of higher reduction should appear rougher than those that are less reduced. This is in fact true with the terrace RMS for the current sample (see Table 3-1), higher than the bottoms of the holes in the Type 3 surface which have an average RMS roughness of 0.17 Å ± 0.01 Å.

Whether the self organized defect layer discussed is the result of a high concentration of oxygen vacancies, or is composed of segregants such as yttria, the self organization due to defect interactions underlies the mechanism. Few studies[21] into the defect types on surfaces of YSZ have been performed, however Kolodziej *et al.* have reported the growth of large interconnecting rectangular terraces on KBr as a result of the complex interaction of defects caused by the combination of e-beam induced desorption with higher temperatures (197 °C).[66] In that case, electron bombardment can produce a large number of point defects, which modify the surface allowing for preferential desorption. A similar example of strong defect interactions is the phenomenon of surface melting observed for vicinal metal surfaces, which involves the general roughening of a surface when the defect concentration becomes sufficiently high.[67, 68] In such cases the energy of defect formation decreases as a result of interactions with each other, leading to the roughening or melting of the surface well below the melting point of the bulk crystal. In the present case, the observed structures are not due to melting or e-beam desorption, but the coupling of a high concentration of defects with the sufficient mobility induced by elevated temperatures can lead to interesting, and potentially useful organized structures, pointing to an attractive area for future study.

3.4. Palladium Deposition

The use of metal nanoparticles deposited on an oxide single crystal as a model for heterogeneous catalysts is well established.[1, 3-6, 23, 24] Typically these models rely on the metal substrate interaction to create a relatively narrow distribution of particle properties (size and shape), and these properties depend directly on the morphology of the surface. Due to the wide variety of possible defects topographies observed for YSZ(100), it is important to determine how this variability may effect the deposition, growth and sintering behaviour of metal particles.

3.4.1. Palladium deposition on Type 3 surface

The effect of YSZ(100) surface morphology on metal particle growth is exemplified here by the deposition of a sub-monolayer coverage of palladium on a Type 3 surface. Figure 3-11 shows a YSZ(100) type 3 surface before deposition (a), the same surface after deposition of a sub-monolayer amount of palladium at room temperature (b), and after sintering in air to 135 °C for 35 minutes (c). Figure 3-11b shows the 3-dimensional growth of palladium at nucleation points outside of the holes, forming small particles about 6 Å in height in the area of the ridge edges (Pd particles prevent resolution of the ridges). The small amount of Pd deposited and the peak overlap with other species made difficult the exact quantification of Pd on the surface by XPS. Further, quantification by AFM was limited by errors in image analysis so that comparing the observable quantity of Pd before sintering, to that after is inconclusive. Overall, the determination of whether Pd is present inside the holes is not possible by XPS and AFM under the given conditions.. Therefore possibility of an atomic wetting layer of Pd inside the holes cannot be excluded, even though their bottoms remain atomically flat and no larger particles are visible. Upon heating the surface in air, the palladium particles grow to 15 Å in height. Interestingly, the Pd mobility takes the particles to the bottom of the holes, and we can no longer resolve any particles on the ridge edges, which once again become visible.

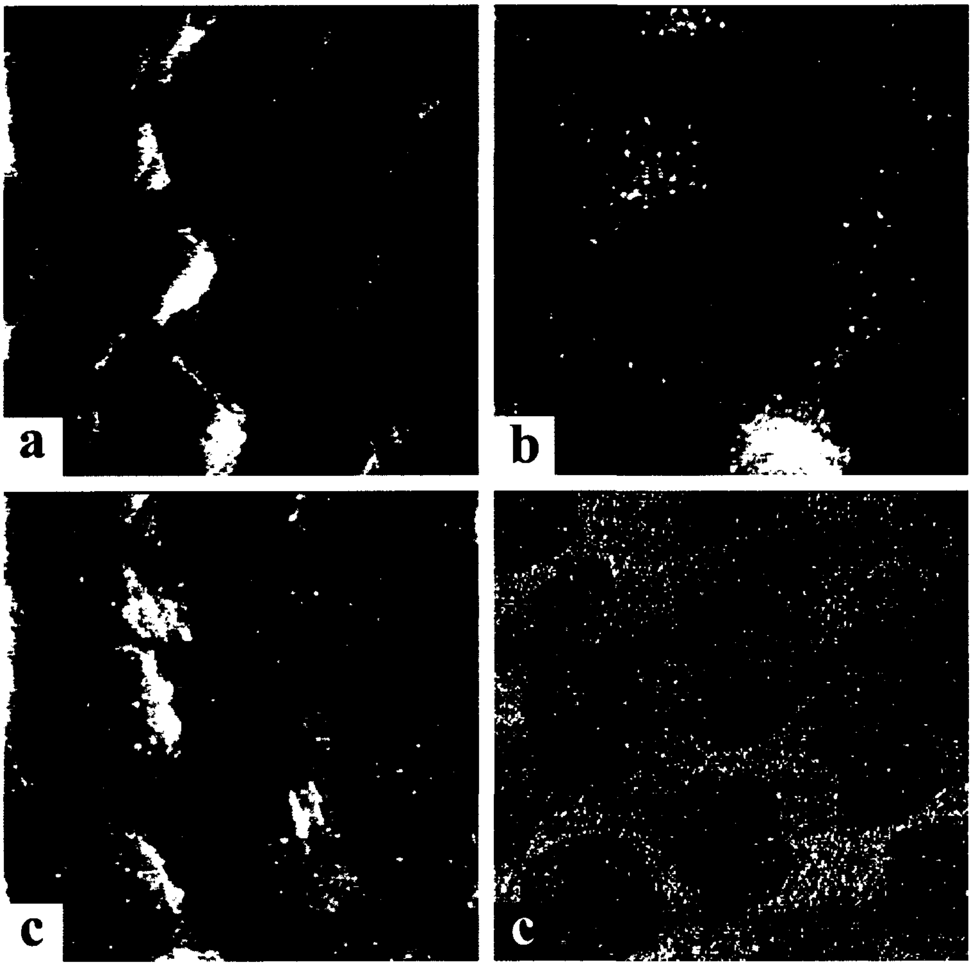

Figure 3-11 *YSZ (100) Type 3 surface. (a) (1385^2 nm^2, z_{range}=12 Å) Before palladium deposition. (b) (1000^2 nm^2, z_{range}=20 Å) After sub-monolayer quantity of Pd deposited in UHV at room temperature. Particles appear on ridged areas, with little or none in the holes. (c) (1000^2 nm^2, z_{range}=16 Å, 0.9°) After sintering (b) to 135 °C for 30 minutes. The particles sinter and are trapped in the holes, few particles are visible on ridged areas. The corresponding phase image on the right shows the particles to be localized in the holes only.*

Thin film formation of metal on oxides is unusual, however Asakura *et al.* have studied the growth of zirconia on Pd(100) by STM.[69] Their results showed that when ZrO_2 was treated at high temperatures with oxygen it tended to wet the surface as a thin film. However, when treated with hydrogen at high temperatures, thus reducing the ZrO_2, non-wetting particles tended to form. Therefore in the present study of the Type 3 surface, the deposition of Pd may in fact probe the surface for stoichiometric and reduced regions. With the holes previously argued to be stoichiometric and the ridged areas reduced, the possible wetting of the holes and clear particle formation on the ridged areas reinforce this contention further.

Since the Pd is in effect "trapped" in the holes at the sintering temperature, one could envision using the hole formation as a method to template the surface and limit particle size due to sintering at higher temperatures. The size of the holes and therefore the maximum quantity of material able to sinter together for any given metal loading (monolayer or less), could be controlled to some extent by the size of the crystal miscut. Lower miscuts would result in larger terraces, and therefore larger holes and larger particles size due to the interaction between hole growth and terrace size discussed in section 3.2.4. This assumes of course that particles would not cross the 0.5**a** barriers and that metal within a hole would sinter completely. Further a method for seeding the crystal for growth of the Type 3 surface would have to be developed, otherwise one would have to count on a 25% probability of obtaining such a surface from the particular manufacturer used in this study. Since the manufacturer may change its processing or quality control at any time without notice this would not be an optimal course.

3.4.2. Palladium deposition on a Type 2 surface

In contrast to the Type 3 surface, Figure 3-12 shows the growth of Pd on a Type 2 sample. We were unable to resolve any initial growth of particles on the surface with the same coverage as deposited on the previous Type 3 sample. However upon further deposition of a larger amount of metal at room temperature, large clusters of particles are found in what were the square pits on the surface. Sintering at 135 °C produced no observable effect.

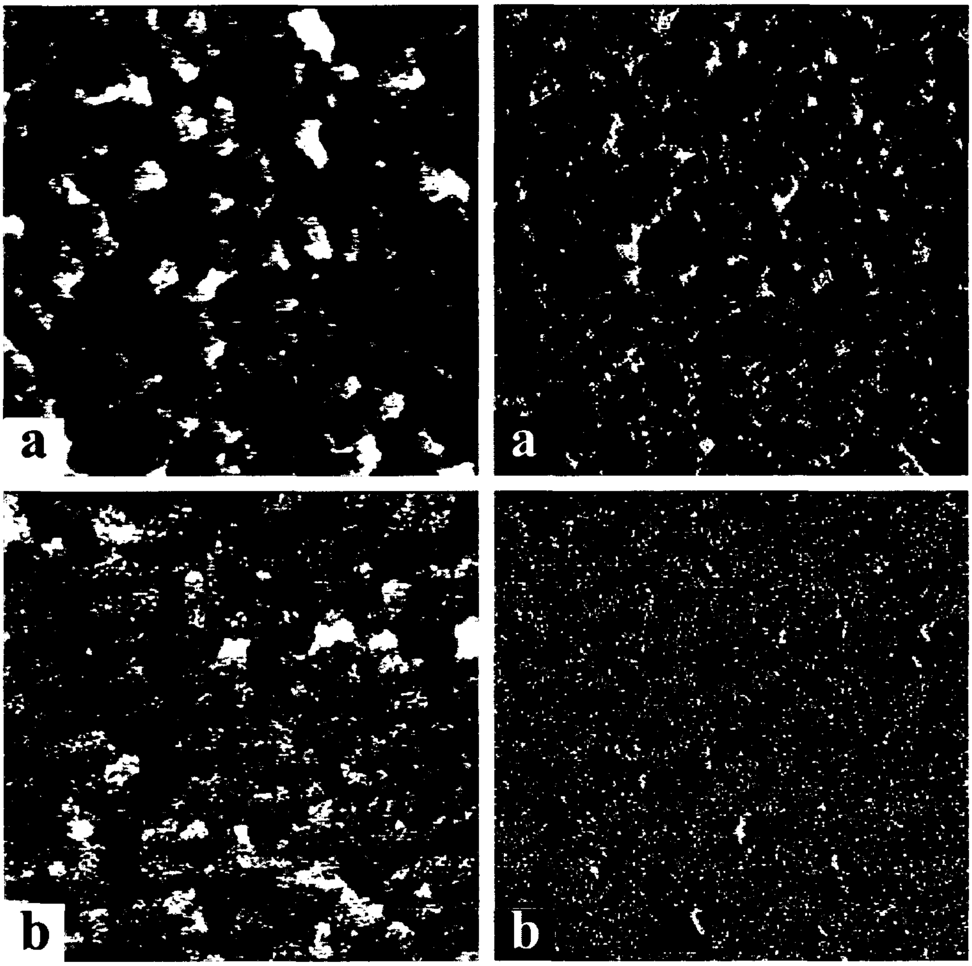

Figure 3-12 *(1000^2 nm^2)(a and b) YSZ (100) Type 2 surface. (a) Topography (left)(z_{range}=11 Å) and phase channels (right)(z_{range}=1.8°) of post annealed samples. Square pits similar to those found in a Type 3 surface are observed. (b) (z_{range}=10 Å, 0.5°) Metal is found to be sufficiently mobile at room temperature to locate in the hole bottoms, where it grows according to the Stranski-Krastanov mechanism. The difference in mobility of palladium at room temperature between the Type 2 and Type 3 surfaces is attributed to morphology differences.*

The initial formation of particles on the areas outside the dark regions (phase image Figure 3-12a) does not occur indicating two possible dominant effects: differences in chemical composition or differences in morphological structure. These defective regions may be different chemically from those of the ridged areas in the Type 3 sample, and lack the point defects which would provide nucleation points for metal accumulation. However the initial nucleation in the Type 3 sample may be a result of its surface morphology rather any particular chemistry, therefore in the absence of the small ridges with which Pd particles were found to coordinate in the Type 3 surfaces, nucleation will not occur. In Type 2 surfaces, the rough areas outside the square pits (bright regions in phase panel of Figure 3-12a) are not ridged. These two effects may also be combined, but the net result is that nucleation does not occur.

At higher metal loadings seen in Figure 3-12b, palladium appears to cover areas which correspond to the square pits. Where there was phase contrast at these pits in Figure 3-12a , the contrast is no longer visible in Figure 3-12b. Interestingly the metal forms clusters of particles. The possible thin film growth in the holes of the Type 3 sample for a sub-monolayer deposition was again observed for this Type 2 sample at similar metal loading. Whereas at higher metal loading, particles are observed to form 3-dimensional clusters, overall demonstrating a Stranski-Krastanov Type growth. In such a mechanism, the first or first few layers form a thin film, but subsequent layers grow as three dimensional islands. The observed features, both the flat bottoms at low deposition volumes, and particle formation at high volumes could be explained by such a mechanism. The high mobility of Pd at higher temperature and preference for localization in the stoichiometric holes is clearly demonstrated in Type 3 samples. It is therefore not surprising that in the absence of the ridges on the Type 2 surface, metal is not observed in these still rough and defective areas. Even at room temperature, with no ridges to trap palladium, the metal is sufficiently mobile to move to its preferred location, at the bottom of the square, stoichiometric pits.

The difference in nucleation and growth of Pd on the two surface types highlight the importance of the support morphology in the growth, mobility and sintering behaviour of the supported metal. For example, as discussed above, a change in the size and coverage of hole structures on the surface, in combination with the observed mechanism of metal growth and sintering for the Type 3 surface, provide a range of Pd/YSZ morphologies and interactions for further study.

Clearly, the surface morphology plays a fundamental role in the growth of particles or films on the surface. In fact, the presence of surface pits on YSZ(100) has been shown to have a direct impact in the formation of $La_2Zr_2O_7$ thin films.[9-11] Here we have shown that both chemistry and morphology have an effect on growth, sintering and localization of Pd clusters. The variability in the surface defect structure will therefore drastically impact reproducibility in experiments involving deposition of metal. Surfaces, depending on the type will have disperse relative proportions of the surface containing holes, ridged areas, and rough areas with no ridges, that will interact with the metal differently.

3.5. UHV Cleaning

For UHV studies, the sample is typically cleaned in-situ to produce a contaminant free surface that can be recovered, even after successive experimental processes, by a second cleaning. Procedures for YSZ involve cycles of Ar^+ sputtering at energies between 0.5 and 3 keV and annealing in vacuum or back pressures of O_2 until XPS or AES yield no contaminant peaks.{Simpson, 1999 #16} No studies have been performed which have examined how sputtering and subsequent annealing affects the surface topography of YSZ(100). In this section we examine how sputtering may modify the surface of a Type 1 and Type 2 surface.

3.5.1. UHV cleaning and air annealing a Type 2 surface

Figure 3-13 demonstrates how the surface topography of a Type 2 sample is modified by successive UHV cleanings and air anneal cycles. The UHV cleaning is comprised of Ar^+ sputtering cycles at 600 eV or 2.5 keV for 30 minutes or 1 hour all while the sample is heated to 300 °C. The sputtering is performed in 3.5e-6 mbar back pressures of argon gas producing approximately 1 $\mu A/mm^2$ of sputter current. Each sputter cycle is followed by in-situ oxidation in back pressures of 1.0×10^{-5} mbar of molecular oxygen for 10 minutes at 400 °C, plus a flash to 600 °C. This is a common technique reported by Simpson *et. al.*[16] Longer anneal cycles at 1000 °C were performed in air for approximately 2.5 hours each. After each set of cleaning cycles the sample is imaged by AFM.

Figure 3-13a is the YSZ(100) Type 2 sample which has been heated to 1000 °C for 2.5 hours in air (baseline). Image 3-13b corresponds to the same sample after undergoing two UHV cleaning cycles, each comprised of 30 minutes of ion sputtering (600 eV) followed by thermal oxidation as described previously. The results show that major features remain, deep pitting and square etch pits at the step edges are apparent though the surface has been flattened slightly. Elemental concentrations by XPS and image analysis results of AFM micrographs are summarized in Table 3-2 , and a decrease in RMS roughness from 4.22 Å in the annealed sample (Figure 3-13a) to 3.57 Å in the sputtered sample (Figure 3-13b) is seen. Overall the carbon content has decreased significantly but the oxygen content has not increased, this is likely due to preferential sputtering of oxygen. The metal content is correspondingly high relative to stoichiometric concentrations.

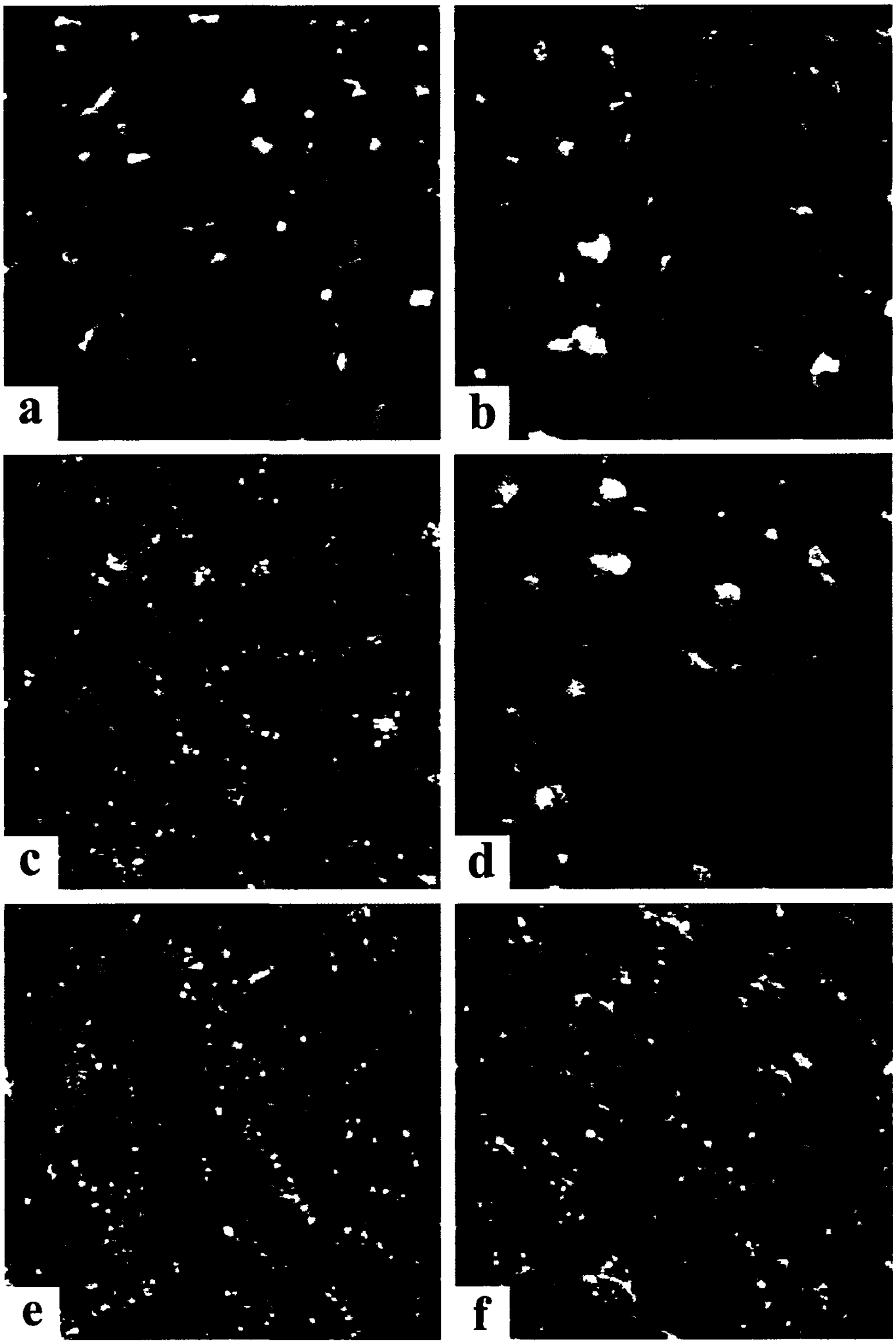

Figure 3-13 *(All images 2000^2 nm^2) (a)(z_{range}=21 Å) Air annealed sample (1000 °C) showing Type 2 surface features. (b)(z_{range}=21 Å) Sample seen in (a) after Ar$^+$ sputtering for 30 minutes at 600 eV. (c)(z_{range}=20 Å) Sample (b) after Ar$^+$ sputtering for 60 minutes at 2500 eV. (d)(z_{range}=13 Å) Sample (c) annealed in air for 2.5 hours at 1000 °C. (e)(z_{range}=12 Å) Sample (d) after second Ar$^+$ sputtering cycle for 60 minutes at 2500 eV. (f)(z_{range}=11 Å) Sample (e) after annealing in air to 1000 °C for 2.5 hours, sample is approaching Type 1 surface, with parallel terraces emerging.*

Figure 3-13c presents the sample after a second cleaning cycle, this time with ion energies of 2.5 keV. The square pits have smoothed completely though the deeper pits remain. The RMS roughness has increased to 3.85 Å as a result of uniform roughening across the surface due to sputter damage. The carbon has almost been removed completely; this may have improved the oxidation kinetics during the thermal oxidation cycle resulting in a higher oxygen content. The surface remains equivalently metal enriched. Annealing the sample in air for 2.5 hours at 1000 °C lowers the RMS roughness significantly, Figure 3-13d shows that the roughening due to sputter damage has been healed though the larger scale contours of the pits remain. XPS shows an approach to stoichiometry with the oxygen content increasing and a decrease in metal concentration. This result may be caused by a combination of actual chemical changes in the lattice composition, and adsorption of water and hydrocarbons (carbon concentration 2.6 %) on the surface due to ambient exposure. The magnitude of each contribution is unknown though a larger asymmetry in the oxygen 1s peak, weighted at high binding energies is noted. This indicates the presence of adsorbed oxygen surface species.

A third sputtering (1 hour at 2.5 keV) followed by an in-situ thermal oxidation cycle results again in a roughening due to sputter damage (Figure 3-13e), though smoothing of the large scale contours including the surface pits has occurred. This combination has resulted in an overall RMS roughness (2.39 Å) that has remained constant within experimental error. The chemical composition is very similar to the sample after the previous sputter-oxidize cycle indicating that perhaps a sputter induced equilibrium chemical concentration is reached. That is, sputtering will alter the elemental concentrations at the surface due to preferential sputtering. At some point however, under long enough exposures, the chemical makeup should reach some sputter induced "pseudo-equilibrium" that is different from the chemical makeup at thermodynamic equilibrium. This result shows that under these conditions, it requires an hour or less of sputtering to reach such a "pseudo-equilibrium".

Table 3-2 *Summary of XPS elemental concentrations and image analysis of AFM micrographs for a Type 2 sample undergoing a series of* Ar^+ *sputtering and air anneal cycles to* 1000^oC*. A fully stoichiometric sample will have a O:Zr:Y atomic ratio of 65.3:26.7:8.0.*

Process	Figure	O 1s (Atom %)	C 1s (Atom %)	Zr 3d (Atom %)	Y3d (Atom %)	RMS Roughness (Å)
As Received	n/a	57.1 ± 1.0	11.7 ± 1.4	23.9 ± 0.5	7.2 ± 0.2	n/a
Anneal 2.5 hrs	4-13a	59.3 ± 0.9	7.1 ± 1.3	25.5 ± 0.5	8.1 ± 0.3	4.22 ± 0.07
Sputter 600 eV	4-13b	59.3 ± 0.7	3.0 ± 1.0	28.6 ± 0.4	9.0 +/ -0.2	3.57 ± 0.18
Sputter 2.5 keV	4-13c	61.1 ± 0.6	1.1 ± 0.5	27.3 ± 0.4	10.4 ± 0.3	3.85 ± 0.05
Anneal 2.5 hrs	4-13d	63.0 ± 0.7	2.6 ± 0.9	25.0 ± 0.4	9.4 ± 0.2	2.37 ± 0.11
Sputter 2.5 keV	4-13e	61.0 ± 0.6	0.0 ± 1.0	27.6 ± 0.4	11.4 ± 0.3	2.39 ± 0.12
Anneal 2.5 hrs	4-13f	n/a	n/a	n/a	n/a	1.39 ± 0.08

A second and final air anneal cycle for 2.5 hours at 1000 °C, again produces a significant smoothing of the surface, now 1.39Å. Figure 3-13f shows that the parallel terraces characteristic if a Type 1 sample have begun to form, though some of the major contours reminiscent of the deep terraces on the initially air annealed sample (Figure 3-13a) remain. A step and terrace structure of a Type 1 surface is the thermodynamically preferred structure, and given a sufficient number of cleaning cycles, one would expect to obtain this surface type. The length of anneal time and number of sputtering cycles however will be dependent on the initial surface structure.

Though we were unable to perform the long thermal annealing cycles in vacuum it seems that surface may be cleaned with several cycles of ion sputtering and annealing in oxygen. The difficulty in beginning with an unknown topography is that though clean and stoichiometric surfaces may be achieved by the cleaning methods discussed, this state is not necessarily indicative of a flat surface. Using this solely as a criteria for preparing samples between experiments could result in high irreproducibility and inaccurate conclusions.

3.5.2. UHV cleaning and air annealing a Type 1 surface

For vacuum studies it seems that it would be very inefficient to begin with a Type 2 or 3 sample which have a large defect volume at the surface. Unless the surface is of interest for its unique morphology, beginning with a Type 1 sample would require many fewer cleaning cycles. Moreover since the step and terrace structure is the thermodynamically stable surface, modifications during experiments could always be cleaned and annealed, recovering the initial surface. Types 2 or 3 surfaces, in contrast would always be unrecoverable by this cleaning procedure.

It seems reasonable therefore to begin with a Type 1 surface and clean it while causing as little damage as possible, since long annealing cycles are required to smooth the surface after sputtering damage. In Figure 3-13b we saw that sputtering at 0.6 keV smoothed the sample and removed carbon, without causing extensive high frequency roughening due to sputter damage of a 2.5 keV ion beam seen in Figures 3-13c and 3-13e. In this section a Type 1 sample is selected (Figure 3-14), palladium is deposited and sintered, then sputtering using less damaging 0.6 keV ions is performed. In this way it is possible to determine if and how quickly a surface free of both carbon and palladium may be obtained by this cleaning procedure.

Figure 3-14c presents the result of 2 cleaning cycles in which the sample seen in 3-14b was subject to two cycles of Ar ion sputtering at 0.6 keV for 30 min at 300 °C followed by annealing to 600 °C in 1 x 10^{-5} mbar back pressures of O_2. XP-spectra, whose results are summarized in Table 3-3 show the sample to be completely free of contaminants including carbon. As can be seen, the major features such as pits and terraces remain, while the RMS roughness has decreased even compared to the as-annealed surface of Figure 3-14b, from 2.01 Å to 1.24 Å. This decrease shows that the Pd has been removed and the surface flattened further. Figure 3-14c shows that the sputtering is not completely undamaging and some higher frequency roughening is observed. However the magnitude of the roughening is small compared to what would have been caused by a 2.5 keV beam, and is even lower than the RMS roughness of the Type 2 sample after many cycles of cleaning and air annealing (1.39Å). Moreover, this cleaning procedure on the Type 1 sample produces a near stoichiometric surface as seen in Table 3-3.

Though the cleaning cycle on a Type 1 surface using 600 eV argon ions produces less damage, it roughens the surface none the less, and a longer period of thermal oxidation is required to heal this roughening. Figure 3-14d shows the results of air annealing to 1000 °C for 2.5 hours, the surface has not recovered entirely to the surface seen if Figure 3-14a. This is somewhat to be expected since as shown in section reaching an equilibrium surface requires very long anneal times at 1000 °C and initial defect structures will modify the annealing process. By cleaning the surface the defect structure has been modified and a second air anneal should result in a somewhat different surface, in this case Figures 3-14d

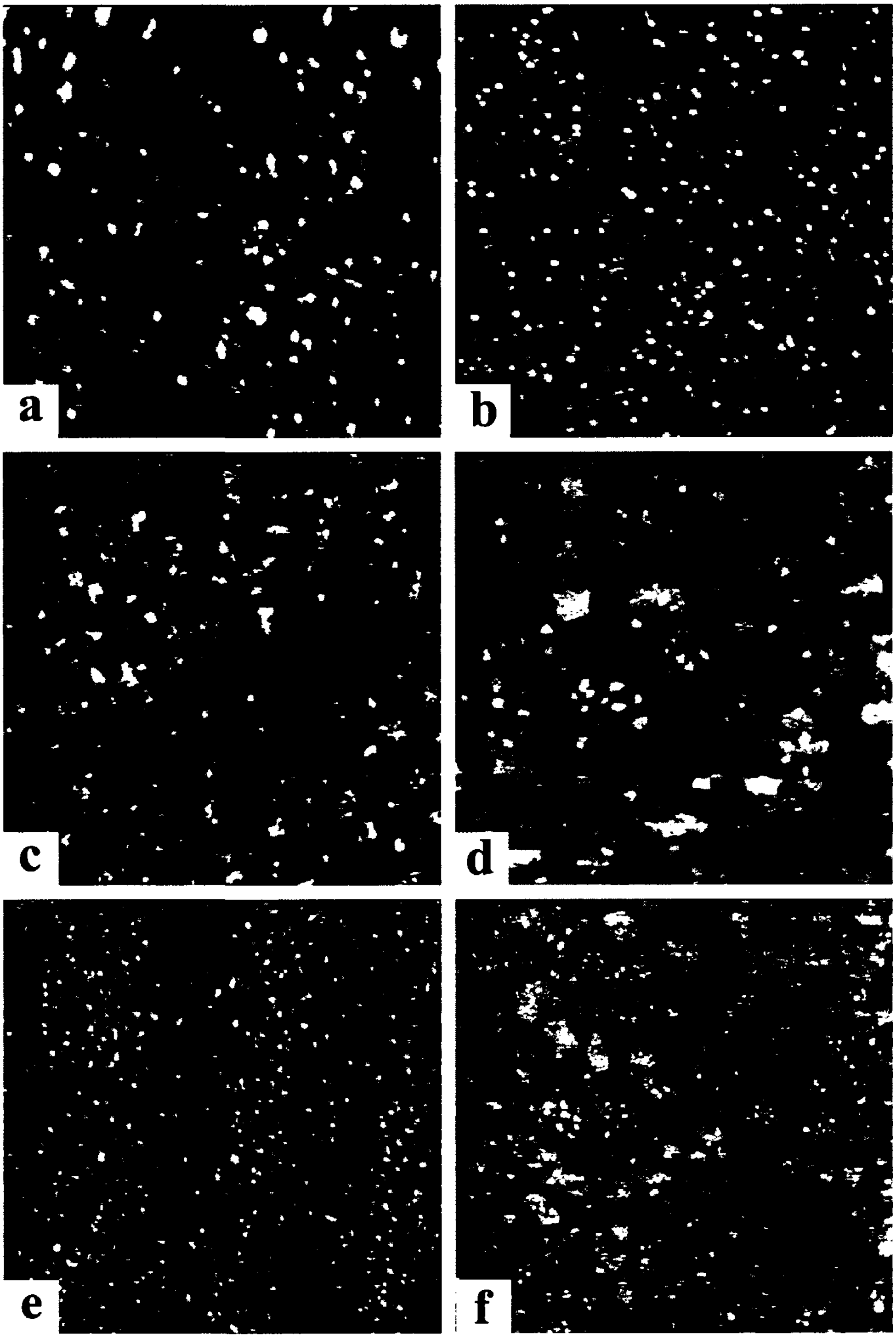

Figure 3-14 *AFM micrographs ((a-d)* 1000^2 *nm*^{2}*) (a)(*z_{range}*=10 Å) Type 1 sample after 1000 °C air anneal. (b)(*z_{range}*=15 Å) After deposition and sintering (30 min at 135 °C) of sub-monolayer amounts of Pd. (c)(*z_{range}*=7 Å) After cleaning cycles involving sputtering with 0.6 keV Ar ions. (d) (*z_{range}*=11 Å) After second air anneal. (e) and (f) (*2000^2 *nm*^{2}*), (e)(*z_{range}*=10 Å) Larger image of uncleaned surface after initial anneal. (f)(*z_{range}*=11 Å) Larger image after several cleaning cycles and second air anneal.*

and 3-14f show extensive island growth. This growth appears not to be self-organized, and is likely only a result of incomplete sintering of particles that had been initially separated from the step edge, rather than making up a reduced defect layer. Though certainly not conclusive, phase imaging shows no contrast (not shown) indicating the surface may be entirely stoichiometric.

Table 3-3 *Summary of XPS elemental concentrations and image analysis of AFM micrographs for a Type 1 surface after undergoing a series of processes. Beginning with the as-received sample the processes in order from top to bottom continue as air anneal at 1000 °C for 2.6 hours, deposition of a sub-monolayer coverage of Pd by e-beam evaporation, in-situ cleaning cycle of 0.6 keV Ar^+, sputtering and thermal oxidation, lastly annealing in air again for 2.5 hours. The results show that an in-situ cleaning on a Type 1 surface may remove deposited Pd and impurity carbon to produce a clean and stoichiometric surface, if not completely flat.*

Process	**Figure**	**O 1s (Atom %)**	**C 1s (Atom %)**	**Zr 3d (Atom %)**	**Y3d (Atom %)**	**RMS Roughness (Å)**
As Received	4-1b	57.8 ± 0.9	9.7 ± 1.3	25.1 ± 0.5	7.5 ± 0.2	0.70 ± 0.04
Anneal 2.5 hrs	4-14a,e	64.1 ± 0.6	2.3 ± 0.7	26.1 ± 0.3	7.5 ± 0.2	2.01 ± 0.02
Deposit Pd	4-14b	63.0 ± 1.2	2.3 ± 1.2	26.9 ± 0.9	7.8 ± 0.7	3.22 ± 0.59
Sputter 0.6 keV	4-14c	64.0 ± 0.5	0 ± 1.0	27.9 ± 0.4	8.1 +/ -0.2	1.24 ± 0.05
Anneal 2.5 hrs	4-14d,f	n/a	n/a	n/a	n/a	1.88 ± 0.03

The decrease in RMS roughness as a result of cleaning, suggests that further sputter/anneal cycles will continue to flatten the surface; presumably a flat surface will eventually be achieved. However, whereas a large number of cycles are needed to flatten a surface only a small number are needed to clean it. Imaging, therefore, is important to ensure a well characterized surface since variations between samples before sputtering will remain after sputtering. If, as we suggest, defect interactions are a contributing effect determining the sample surface evolution during annealing to 1000 °C, then it follows that the addition or modification of defects through sputtering will alter such evolution, resulting in a different topography upon annealing. This effect is demonstrated in Figures 3-14f, in which it can be seen that the surface in Figure 3-14a or 3-14e is not recovered.

3.6. Low Energy Electrons and Surface Topography

Literature involving YSZ(100) has relied on low energy electron diffraction (LEED) to assess some measure of flatness of the surface.[13] LEED is really a technique used to examine the long range order of the surface crystal structure. In this technique, electrons produced by an electron gun are directed towards the sample typically at a normal angle of incidence to the surface under study. Electrons interact elastically with the surface and diffract to form a series of spots on a phosphorescent screen. The spots may be related back to the surface crystal structure since the incident electron, reciprocal lattice and diffraction spot positions must satisfy the Laue condition.[70]

It is important to note that because LEED is an electron based technique, it is most suitable for conducting samples. In insulators, charging effects will be observed, typically destroying completely the diffraction pattern. In the case of YSZ(100), other authors have used the partial conductivity of YSZ at elevated temperatures to obtain LEED patterns of the surface. However, at elevated temperatures, there is increased atom mobility with the corresponding increase in the uncertainty of the atomic positions. The net result is a broadening of the diffraction spots, that is, a diffuse LEED patterns.

LEED has been used to determine both surface cleanliness and surface ordering, since impurity overlayers will generally be seen to modify the lattice of the substrate, and a lack in ordering will result in no or diffuse diffraction spots. Using LEED instead of a scanning probe technique such as AFM or STM is often acceptable, however in the case of YSZ(100) since LEED is an averaging technique in which measurements are preformed over hundreds or thousands of microns, one could expect a variety of results which do not fully describe the surface topography at the local level.

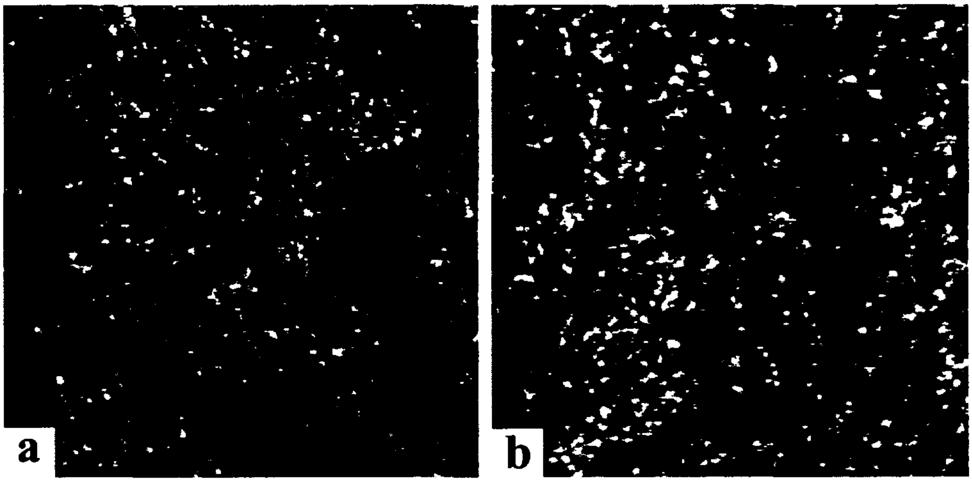

Figure 3-15 *AFM micrographs of YSZ(100). (a) (1700^2 nm^2, $z_{range}=5$ Å) as received sample b) (1000^2 nm^2, $z_{range}=4$ Å) after exposure to 125 eV electrons from a LEED electron gun for 30 minutes.*

Moreover the probe electrons themselves may alter the surface, with electrons stimulating the production of defects.[16] Figure 3-15 shows the damaging effects of LEED electrons on the topography of YSZ(100) crystals. Before bombardment the surface clearly shows parallel terraces characteristic of a Type 1 surface. After exposing the sample to 125 eV electrons from a LEED electron gun for 30 minutes, the sample was found to visibly darken in the area exposed to the beam. Upon AFM imaging of the darkened region the surface was found to be damaged, with steps and terraces being flattened and the overall surface roughened with coarse particle-like features.

Using LEED for topographic identification of YSZ is therefore very much less useful than scanning probe techniques since LEED itself damages and modifies the surface. It will therefore be difficult to determine if previous conclusions based on LEED data should be considered reliable. SPM techniques must therefore be used to confirm results and to acquire meaningful information.

3.7. Conclusion and Transfer to UHV

Studies of the YSZ(100) surface by atomic force microscopy have shown that variability in surface topography between different samples prepared in the same manner can be large. Surfaces ranging from high densities of parallel steps and terraces, to surfaces dominated by large square pits are observed, as well as finer nano-structures of self-organized arrays of intersecting 1-dimensional lines. This variability has been shown to depend on the initial defect structure in the as-received samples due to surface preparation by the supplier. Even after sintering to 1300 °C the surface topography is dependant on its structure at lower temperatures. Observations of the evolution of a Type 3 surface in time not only exhibits slow annealing kinetics, but shows that this history dependence is the result of defect interactions which can modify the annealing process. In fact, we propose that it is the combination of a high concentration of defects with heat that allow the defects to mobilize and interact producing a pathway for the growth of organized nano-structures. The defect structures or defect layers observed have been proposed to be composed of regions containing a large number of oxygen vacancies which modify the lattice constants. This sub-oxide layer having lattice mismatch to the underlying stoichiometric surface self organizes to minimize the strain induced by such a mismatch.

The observed variability in YSZ(100) topography has a direct impact on metal growth at the surface, since stoichiometric and non-stoichiometric regions interact very differently with Pd. This dispersion may be strictly a result of chemistry or as a combined result of chemistry and morphology. Whereas stoichiometric surfaces exhibit Stranski-Krastanov growth, non stoichiometric regions seem to result in three dimensional or island growth if the morphology provides nucleation points such as the ridges seen in Type 3 surfaces. The morphology of these sub-oxide regions may allow metal particles to be trapped at room temperature, however at higher temperatures these particles become mobile, ultimately preferring to be coordinated at the bottom of square pits, which are believed to be near stoichiometric surfaces. In the absence of this morphology, palladium is sufficiently mobile even at room temperature to preferentially accumulate in the square pits.

The surface variability will also impact the type and number of cleaning cycles required to produce a clean, flat, and stoichiometric surface. Beginning with a Type 2 sample will require far more cleaning cycles, to produce a clean and flat surface, though ultimately a Type 1 surface is acquired. Whereas beginning with a Type 1 surface will require only one or two cleaning cycles to achieve near stoichiometry, and much shorter annealing cycles to become flat. Using ion energies of 0.6 eV were shown to be capable of cleaning the surface of both impurity carbon and deposited palladium, though thermal annealing is still required to heal some minimal sputter damage. Sputtering under 2.5 keV energies is much more effective in modifying extremely defective surfaces containing etch pits etc. such as a Type 2 surfaces, however the high energies of the ions produces extremely rough surfaces with higher frequency corrugation.

Defects in the as-received samples, whose manufacturing may vary from batch to batch offer different surface morphologies to the active metal. This has tremendous implications for catalysis and thin film studies. AFM has proven to be extremely useful in identifying the surface topography, annealing kinetics and interaction of the surface with sub-monolayer depositions of palladium. Moreover the phase imaging mode of AFM has provided an ability to detect chemical differences at the nanometre scale, via the detection of elastic modulus differences. These differences are believed to be brought about by changes in oxygen vacancy content between nanoscale regions at the YSZ(100) surface. Low energy electron diffraction, though commonly used for other substrates, was found in the case of YSZ(100) to be damaging, resulting in modification of surface topography. Without additional studies it is not useable for YSZ(100) model catalyst studies in which strict control and characterization of the surface is required.

The overall results from this chapter provide some insight into methodologies which can be transferred to ultrahigh vacuum studies. Since Type 1 surfaces have been found to be the equilibrium topography of YSZ(100), beginning with such surfaces at the start of UHV experiments would save a great deal of effort in producing a flat sample. Therefore annealing samples in air and pre-selecting Type 1 samples based on ambient AFM measurements will be of benefit.

Regardless of the initial quality of the selected sample, annealing is required to produce a flat and stoichiometric surface, especially after ion sputtering. We have shown that the annealing kinetics are very slow, and therefore a capability to heat samples to at least 1000 °C for up to several hours in vacuum and higher partial pressures of oxygen must be developed. This heating procedure must also be compatible with all other techniques used in UHV, specifically SPM since it has been shown that imaging the surface at the nanoscale is critical in confirming surface structure and therefore reproducibility between experiments.

References

1. Campbell, C.T., *Ultrathin metal films and particles on oxide surfaces: Structural, electronic and chemisorptive properties.* Surface Science Reports, 1997. **27**: p. 1.

2. Goodman, D.W., *Model catalysts: From imagining to imaging a working surface.* Journal of Catalysis, 2003. **216**: p. 213.

3. Freund, H.-J., Ernst, N., Baeumer, M., Rupprechter, G., Libuda, J., Kuhlenbeck, H., Risse, T., Drachsel, W., Al-Shamery, K. and Hamann, H., *Model systems for heterogeneous catalysis: Quo vadis surface science?*, in *Surface chemistry and catalysis*, Carley, A.F., Editor. 2002, Kluwer Academic/Plenum Publishers: New York. p. 103.

4. Freund, H.-J., Baeumer, M. and Kuhlenbeck, H., *Catalysis and surface science: What do we learn from studies of oxide supported cluster model systems?* Advances in Catalysis., 2000. **45**: p. 333.

5. Campbell, C.T., Grant, A.W., Starr, D.E., Parker, S.C. and Bondzie, V.A., *Model oxide supported catalysts: Energetics, particles thickness, chemisorption and catalytic properties.* Topics in Catalysis, 2001. **14**: p. 43.

6. Goodman, D.W., *Model oxide supported catalysts: Energetics, particles thickness, chemisorption and catalytic properties.* Topics in Catalysis, 2001. **14**: p. 43.

7. Fukui, K.-i., Takakusagi, S., Tero, R., Aizawa, M., Namai, Y. and Iwasawa, Y., *Dynamic aspects and associated structures of $TiO_2(110)$ and $CeO_2(111)$ surfaces relevant to oxide catalyses.* Physical Chemistry Chemical Physics, 2003. **5**: p. 5346.

8. Joshi, A.B. and Norton, M.G., *The influence of annealing on the surface morphology of MgO.* Applied Surface Science, 1997. **115**: p. 307.

9. Lu, C.J., Senz, S. and Hesse, D., *The influence of yttria stabilized zirconia surface pits on the initial stage of reactive $La_2Zr_2O_7$ formation from La_2O_3 vapours and yttria stablized zirconia (001) substrates.* Philosophical Magagazine A, 2001. **81**: p. 2705.

10. Lu, C.J., Senz, S. and Hesse, D., *The impact of YSZ surface steps on structure and morphology of $La_2Zr_2O_7$ islands growing on YSZ(100) surfaces by vapour-solid reaction.* Surface Science, 2002. **515**(2-3): p. 507.

11. Lu, C.J., Senz, S. and Hesse, D., *Formation and structure of misfit dislocations at the $La_2Zr_2O_7$-Y_2O_3 stabilized ZrO_2 (001) reaction front during vapor solid reaction.* Phil. Mag. Lett., 2002. **82**: p. 167.

12. Dilara, P.A. and Vohs, J.M., *TPD and HREELS investigation of the reaction of formic acid on ZrO_2(100).* Journal of Physical Chemistry, 1993. **97**: p. 12919.

13. Neergaard Waltenburg, H. and Moller, P.J., *A study of Pd growth on an yttria stabilized ZrO_2(100) surface.* Applied Surface Science, 1999. **142**: p. 305.

14. Zafeiratos, S. and Kennou, S., *The interaction of ultrathin nickel films with yttria stabilized zirconia (100).* Surface Science, 2003. **532-535**: p. 402.

15. Zafeiratos, S. and Kennou, S., *Gold/nickel ultrathin bimetallic overlayers on yttria stabilized ZrO_2(100).* Journal of Physical Chemistry B, 2002. **106**: p. 41.

16. Simpson, W.C., Wang, W.K., Yarmoff, J.A. and Orlando, T.M., *Photon and electron stimulated desorption of O+ from zirconia.* Surface Science., 1999. **423**: p. 225.

17. Sygellou, L. and Ladas, S., *Interfacial effects in ultra-thin nickel deposits on yttria stabilized zirconia.* Surface Science., 2004. **566-568**: p. 698.

18. Green, R.G., Barre, L. and Giorgi, J.B., *Nano-structures in YSZ(100) surfaces: Implications for metal deposition experiments.* Surface Science, 2007. **601**(3): p. 792.

19. Miteva, V.A., Stanchev, A., Marashev, Y., Kelly, R. and Licciardello, A., *On the mechanism of bombardment-induced oxygen redistribution at ZrO_2 surfaces.* Vacuum, 1996. **47**(10): p. 1235.

20. Morant, C., Sanz, J.M. and Galan, L., *Ar-ion bombardment effects on ZrO_2 surfaces.* Physical Review B, 1992. **45**(3): p. 1391.

21. Thome, T., Pham Van, L. and Cousty, J., *Evolution of yttria stabilized zirconia (100) surface morphology with temperature.* Journal of the European Ceramic Society, 2004. **24**: p. 841.

22. Sasaki, K. and Maier, J., *Chemical surface exchange of oxygen on Y_2O_3-stabilized ZrO_2.* Solid State Ionics, 2003. **161**(1-2): p. 145.

23. Henry, C.R., *Morphology of supported nanoparticles.* Progress in Surface Science, 2005. **80**: p. 92.

24. Santra, A.K. and Goodman, D.W., *Oxide supported metal clusters: Models for heterogeneous catalysts.* Journal of Physics: Condensed. Matter, 2003. **14**: p. R31.

25. Giessibl, F.J. and Reichling, M., *Investigating atomic details of the $CaF_2(111)$ surface with a Q-plus sensor.* Nanotechnology, 2005. **16**: p. S118.

26. Filleter, T., Maier, S. and Bennewitz, R., *Atomic scale yield and dislocation nucleation in KBr.* Physical Review B, 2006. **73**: p. 155433/1.

27. Bennewitz, R., *Structured surfaces of wide band gap insulators as templates for overgrowth of adsorbates.* Journal of Physics-Condensed Matter, 2006. **18**(26): p. R417.

28. Reichling, M. and Barth, C., *Scanning force imaging of atomic size defects on the $CaF_2(111)$ surface.* Phys. Rev. Lett., 1999. **83**: p. 768.

29. Knoppik, D. and Penningsfeld, F.P., *Quantitative-evaluation of evaporation structures of 100 NaCl, 110 NaCl, and 111 NaCl surfaces annealed in a vacuum between 400 °C and 800 °C.* Journal of Crystal Growth, 1977. **37**(1): p. 69.

30. Such, B., Kolodzej, J., Czuba, P., Piatkowski, P., Struski, P., Krok, F. and Szymonski, M., *Surface topography dependent desorption of alkali halides.* Physics Review Letters, 2000. **85**: p. 2621.

31. Fan, Y.C., Fitzgerald, A.G., Xu, H.C., Storey, B.E. and Tooke, A.O., *Atomic force microscopy studies of the surface morphology of annealed single crystal substrates and substrate annealing effects on the $YBa_2Cu_3O_7$-x thin film growth.* Institute of Physics Conference Series, 1997. **153**.

32. NEYCO, France, 2004.

33. CrysTec GmbH, Germany, 2005.

34. North Crystals, USA, 2006.

35. Parmigiani, F., Depero, L.E., Sangaletti, L. and Samoggia, G., *An XPS study of yttria stabilized zirconia single crystals.* Journal of Electron Spectroscopy and Related Phenomena, 1993. **63**: p. 1.

36. Hakansson, K.L., Johansson, H.I.P. and Johansson, L.I., *High resolution core level study of ZrC(100) and its reaction with oxygen.* Phys. Rev. B, 1993. **48**: p. 2623.

37. Song, Z., Bao, X., Wild, U., Muhler, M. and Ertl, G., *Oxidation of amorphous Ni-Zr alloys studied by XPS, UPS, ISS and XRD.* Applied Surface Science, 1998. **134**(1-4): p. 31.

38. Bennewitz, R., Schar, S., Barwich, V., Pfeiffer, O., Meyer, E., Krok, F., Such, B., Kolodzej, J. and Szymonski, M., *Atomic resolution images of radiation damage in KBr.* Surface Science, 2001. **474**: p. L197.

39. Engelhardt, J.B., Dabringhaus, H. and Wandelt, K., *Atomic force microscopy study of the* CaF_2*(111) surface: From cleavage via island to evaporation topographies.* Surface Science, 2000. **448**(2-3): p. 187.

40. Engelhardt, J.B., Dabringhaus, H. and Wandelt, K., *Atomic force microscopy study of the* CaF_2*(111) surface: From cleavage via island to evaporation topographies (vol 448, pg 187, 2000).* Surface Science, 2002. **516**(1-2): p. 216.

41. Gritschneder, S., Namai, Y., Iwasawa, Y. and Reichling, M., *Structural features of* CeO_2*(111) revealed by dynamic SFM.* Nanotechnology, 2005. **16**: p. S41.

42. Shikida, M., Kawasaki, K., Sato, K., Ishihara, Y., Tanaka, H. and Matsumuro, A., *Nano-mechanical method for seeding circular-shaped etch pits on (100) silicon surface.* Sensors and Materials, 2003. **15**(1): p. 21.

43. Kurnosikov, O., Van, L.P. and Cousty, J., *High-temperature transformation of vicinal (0001)* Al_2O_3*-alpha surfaces: An AFM study.* Surface and Interface Analysis, 2000. **29**(9): p. 608.

44. Williams, F.J., Aldao, C.M. and Weaver, J.H., *Surface morphologies for Br etched Si(100) 2x1: Kinetics of pit growth and step retreat.* Journal of Vacuum Science & Technology B, 1996. **14**: p. 2519.

45. Tracz, A., Wegner, G. and Rabe, J.P., *Kinetics of surface roughening via pit growth during the oxidation of the basal plane of graphite. 1. Experiments.* Langmuir, 1993. **9**: p. 3033.

46. Heffelfinger, J.R. and Carter, C.B., *Mechanisms of surface faceting and coarsening.* Surface Science, 1997. **389**: p. 188.

47. Cho, G.-B., Yamamoto, M. and Endo, Y., *Surface features of self organized $SrTiO_3(001)$ substrates inclined in [100] and [110] directions.* Thin Solid Films, 2004. **464-465**: p. 80.

48. Woll, C., *The chemistry and physics of zinc oxide surfaces.* Progress in Surface Science, 2007. **82**(2-3): p. 55.

49. Goniakowski, J., Finocchi, F. and Noguera, C., *Polarity of oxide surfaces and nanostructures.* Reports on Progress in Physics, 2008. **71**(1).

50. Mano, T., Notzel, R., Hamhuis, G.J., Eijkemans, T.J. and Wolter, J.H., *Direct imaging of self organized anisotropic strain engineering for improved one dimensional ordering of (In,Ga)as quantum dots.* Journal of Applied Physics, 2004. **95**: p. 109.

51. Brunner, K., Zhu, J., Miesner, C., Abstreiter, G., Kienzle, O. and Ernst, F., *Self organized periodic arrays of SiGe wires and Ge islands on vicinal Si substrates.* Physica E, 2000. **7**: p. 881.

52. Garcia, R. and Perez, R., *Dynamic atomic force microscopy methods.* Surface Science Reports, 2002. **47**(6-8): p. 197.

53. Stark, R.W., Drobek, T. and Heckl, W.M., *Tapping-mode atomic force microscopy and phase-imaging in higher eigenmodes.* Applied Physics Letters, 1999. **74**(22): p. 3296.

54. Tan, S.S., Sherman, R.L., Qin, D.Q. and Ford, W.T., *Surface heterogeneity of polystyrene latex particles determined by dynamic force microscopy.* Langmuir, 2005. **21**(1): p. 43.

55. Cappus, D., Hassel, M., Neuhaus, E., Heber, M., Rohr, F. and Freund, H.J., *Polar surfaces of oxides - reactivity and reconstruction.* Surface Science, 1995. **337**(3): p. 268.

56. Morterra, C., Cerrato, G., Ferroni, L. and Montanaro, L., *Surface characterization of yttria-stabilized tetragonal* ZrO_2 *.1. Structural, morphological, and surface hydration features.* Materials Chemistry and Physics, 1994. **37**(3): p. 243.

57. Khan, M.S., Islam, M.S. and Bates, D.R., *Cation doping and oxygen diffusion in zirconia: A combined atomistic simulation and molecular dynamics study.* Journal of Materials Chemistry, 1998. **8**(10): p. 2299.

58. Goff, J.P., Hayes, W., Hull, S., Hutchings, M.T. and Clausen, K.N., *Defect structure of yttria-stabilized zirconia and its influence on the ionic conductivity at elevated temperatures.* Physical Review B, 1999. **59**(22): p. 14202.

59. Wang, Y.L., Duncan, K., Wachsman, E.D. and Ebrahimi, F., *The effect of oxygen vacancy concentration on the elastic modulus of fluorite-structured oxides.* Solid State Ionics, 2007. **178**(1-2): p. 53.

60. Magonov, S.N., Elings, V. and Whangbo, M.H., *Phase imaging and stiffness in tapping-mode atomic force microscopy.* Surface Science, 1997. **375**(2-3): p. L385.

61. Crittenden, S., Raman, A. and Reifenberger, R., *Probing attractive forces at the nanoscale using higher-harmonic dynamic force microscopy.* Physical Review B, 2005. **72**(23).

62. Cimalla, V., A.A., S., Foerster, C., Zekentes, K., Ambacher, O. and Pezoldt, J., *Self organized SiC nanostructures on silicon.* Superlattices and Microstructures, 2004. **36**: p. 345.

63. Hughes, A.E. and Badwal, S.P.S., *Impurity segregation study at the surface of yttria-zirconia electrolytes by XPS.* Solid State Ionics, 1990. **40-1**: p. 312.

64. Hughes, A.E. and Badwal, S.P.S., *Impurity and yttrium segregation in yttria-tetragonal zirconia.* Solid State Ionics, 1991. **46**(3-4): p. 265.

65. Esch, F., Fabris, S., Zhou, L., Montini, T., Africh, C., Fornasiero, P., Comelli, G. and Rosei, R., *Electron localization determines defect formation on ceria substrates.* Science, 2005. **309**(5735): p. 752.

66. Kolodziej, J.J., Such, B., Czuba, P., Krok, F., Piatkowski, P., Struski, P., Szymonski, M., Bennewitz, R. and Schar, S., *Frenkel defect interactions at surfaces of irradiated alkali halides studied by non-contact atomic-force microscopy.* Surface Science, 2001. **482**: p. 903.

67. Feenstra, R.M., Slavin, A.J., Held, G.A. and Lutz, M.A., *Edge melting of the Ge(111) surface studied by scanning tunneling microscopy.* Ultramicroscopy, 1992. **42**: p. 33.

68. Conrad, E.H., Aten, R.M., Kaufman, D.S., Allen, L.R., Engel, T., den Nijs, M. and Riedel, E.K., *Observation of surface roughening on Ni (115).* Journal of Chemical Physics, 1986. **84**: p. 1015.

69. Asakura, K., Iwasawa, Y., Purnell, S.K., Watson, B.A., Barteau, M.A. and Gates, B.C., *Zirconium oxide supported on Pd(100): Characterization by scanning tunneling microscopy and tunneling spectroscopy.* Catalysis Letters, 1992. **15**(4): p. 317.

70. Wikipedia, *LEED.* www.wikipedia.org, 2008.

4. Ultra High Vacuum Imaging

4.1. Statement of the problem

In the previous chapter, YSZ(100) was studied by ambient AFM, demonstrating both the power and necessity of surface imaging. Initial variations between samples, changes in surface morphology with heating, and the effect this variability could have on metal growth and nucleation from the vapour phase was shown. Studies in ultra high vacuum require the same careful characterization of the surface, from the start, and throughout each experiment.

Amplitude modulated, tapping mode AFM of the type used in the ambient measurements is poorly transferred to studies in UHV since in vacuum cantilever probes react very slowly to surface interactions. The reason for this, is that response time is directly dependent upon the Q–factor of the cantilever according to $\tau_{AM} \sim 2Q/f_o$,[1] where τ_{AM} is the response time of cantilever to surface forces in amplitude modulation mode, f_o is the resonance frequency of the AFM cantilever, and Q is its Q-factor (Chapter 1). In vacuum, where Q's may be orders of magnitude higher than in air, the response time becomes very slow and resolution decreases.

A second mode of operation is true contact mode (CM-AFM), in which the cantilever is dragged across the surface, and its deflection provides a feedback signal. This mode, though useful for hard surfaces like YSZ, would be inappropriate after deposition of metal, since the cantilever is more likely to interact with the metal, dragging it around, rather than imaging it. For this reason, we have seldom used CM-AFM.

An alternative to either amplitude modulated or contact AFM, is frequency modulated AFM (FM-AFM). In this mode, the feedback signal is determined by the resonance frequency shift of an oscillating probe. Repulsive, or attractive interactions of the probe with the surface will cause its resonance frequency to increase or decrease respectively. This Δf settles on a timescale $\tau_{FM} \sim 1/f_o$ rather than being Q–factor dependent.[1] High Q's in this instance are therefore useful since in general higher Q's provide a better signal to noise ratio.

We have put a great deal of effort into imaging YSZ by FM-AFM in UHV and it has been possible to image successfully on several occasions. Figure 4-1 shows an AFM micrograph of a Type 3 YSZ(100) surface, the same surface seen in Figure 3-11a. The left hand image represents the topography, while the right is the dissipation image. Dissipation is related to the amount of energy the AFM control electronics needs to supply to the cantilever in order to maintain a constant oscillation amplitude, or more simply the amount of energy lost by the cantilever through non-conservative interaction with the surface. Like phase imaging, contrast in the dissipation channel can indicate differences in elastic modulus of the surface. The image was acquired by applying a bias voltage on the cantilever probe of 8.75 V. This type of voltage is required to counteract surface charging, and minimize the electrostatic interaction between surface and probe which can degrade the quality of the image, or even prevent imaging altogether. In air this is not generally a problem since adsorbates from the environment, mostly water and hydrocarbons, are usually sufficient to dissipate charge. In UHV the surface concentration of the adsorbates is often insufficient, and sample charge must be counterbalanced with tip voltage, in this way the net electrostatic force acting between sample and tip is zero.

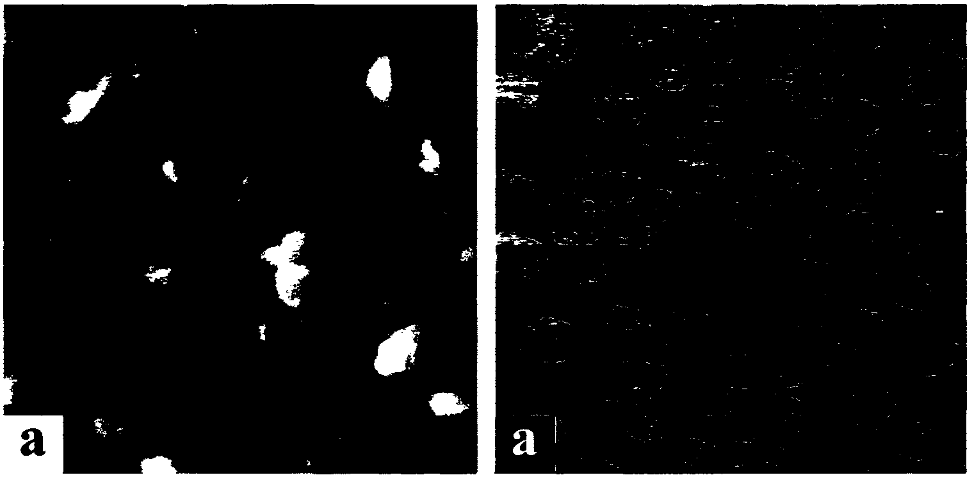

Figure 4-1 *AFM micrograph (2000^2 nm^2, z_{range}= 16 Å, 20 mV, v= 2.5 l/s) of YSZ(100) single crystal after a one hour anneal at 1000 °C. Image acquired in UHV in frequency modulation mode, the left panel corresponds to topography and the right to the dissipation channel. Even in true non-contact mode, contrast between hole bottoms and surrounding areas is obvious, indicating chemical differences. Tip bias was set at 8.75 V during imaging.*

Difficulties may arise when the surface is differentially charged. In this case, the tip voltage would have to be modulated during imaging, with a response time scale faster than the scan speed. This is similar to the way Kelvin probe force imaging is performed,[2] and though this is a useful technique, it is more difficult in practical terms, requires an additional set of electronics, and is not guaranteed to satisfy the problem in a consistent basis. We have found DC voltages required to counterbalance the charge on some YSZ(100) samples to be as small as zero or as large as ten Volts depending on the sample, and one can find in the literature some *in-vacuo* cleaved crystals reported to require much higher values.[3, 4] The voltage ramping required to minimize the electrostatic interaction at each imaging point might therefore need to be performed over a broad range, and with sufficient resolution, requiring prohibitive amounts of time.

More frequently than not, despite our best efforts, imaging YSZ(100) has been unsuccessful by FM-AFM. This has been especially true for experiments in which metal was deposited on the YSZ surface through e-beam evaporation. For such systems we have never been able to acquire FM-AFM images. We believe this is largely a result of charge localization around deposited metal particles or through trapping of stray electrons from the evaporation source. Both of these mechanisms would serve to increase differential charging and destabilize imaging.

Other techniques reportedly used for charge dissipation such as radioactive sources, hot filaments to provide stray electrons, partial pressures of some gas, or heating, remain untested for YSZ(100). Even if they prove viable techniques to neutralize surface charge, it is unknown what side-effects the sample may experience as a result.

Solutions to surface charging do exist, and under most circumstance it is our belief that YSZ could be imaged with FM-AFM. The overarching concern however, is the cost in time and effort of finding such a solution. Undoubtedly parameters used in one experiment would need, at the minimum, modification for subsequent experiments. Perhaps different approaches altogether would be required. In some rare instances we have been able to acquire images after only an hour or two of effort, while often imaging success was only attained after upwards of 10 to 12 hours, if it was attained at all. Since total probabilities are multiplicative, experiments in which sample cleaning, spectroscopic analysis (XPS/UPS, TDS), and metal deposition are to be combined with imaging, each technique must have a sufficiently high probability of success. Moreover the time required to perform combined experiments must be smaller than the time required for impurities from the vacuum to accumulate on the sample surface, otherwise multiple cleaning cycles would be required, in many instances destroying the system under study.

The likelihood of successfully imaging YSZ(100) in a reasonable time with our FM-AFM system is estimated to be approximately 1/5. Given that for most useful experiments, more than one imaging session is required, the probability of performing a successful experiment becomes unreasonably small ($(1/5)^n$). Clearly this probability needs to be improved.

4.1.1. Scanning tunneling microscopy

A more commonly used technique in UHV for imaging relatively flat surfaces is scanning tunneling microscopy. It has extremely high z-resolution due to the exponential dependence of the tunneling current on tip-sample separation. It is non-contact, and the electronic structure can be examined through the use of current/voltage spectroscopies, providing some chemical sensitivity. STM has been used with great success to study many other metal oxides such as TiO_2, Al_2O_3, MgO [5, 6]. However, these oxides are either made reasonably conductive through reduction (TiO_2), or frequently studied as thin films over a conductor, in order to dissipate charging. True insulating single crystals are generally not subject to this technique at room temperature.

M. Filal and co-authors have reported the electrical conductivity of a YSZ single crystal as a function of temperature.[7] Within the 327 °C to 527 °C range the bulk electrical conductivity increases by approximately 5 orders of magnitude, which, given the dimensions of our sample would result in resistances of hundreds of mega-Ohms to kilo-Ohms. How this resistance range translates into a target temperature for performing STM is not obvious.

First indications of an appropriate temperature range sufficient to perform STM measurements comes from studying YSZ with XPS at elevated temperatures. Figure 4-2 demonstrates consecutive scans of the Zr 3d doublet taken while ramping the sample temperature from room temperature to above 300 °C. The first scans taken from room temperature overlap on the left hand side of the Figure, shifted to high binding energies as a result of surface charging produced by electrons as they are excited from the sample. At approximately 150 °C to 175 °C the doublet begins to shift to lower binding energies, indicating that surface charging is beginning to be neutralized by conduction electrons. Finally in the range 225 °C to 275 °C shifting is complete, with photoelectrons ejected from the surface being completely replaced with conduction electrons.

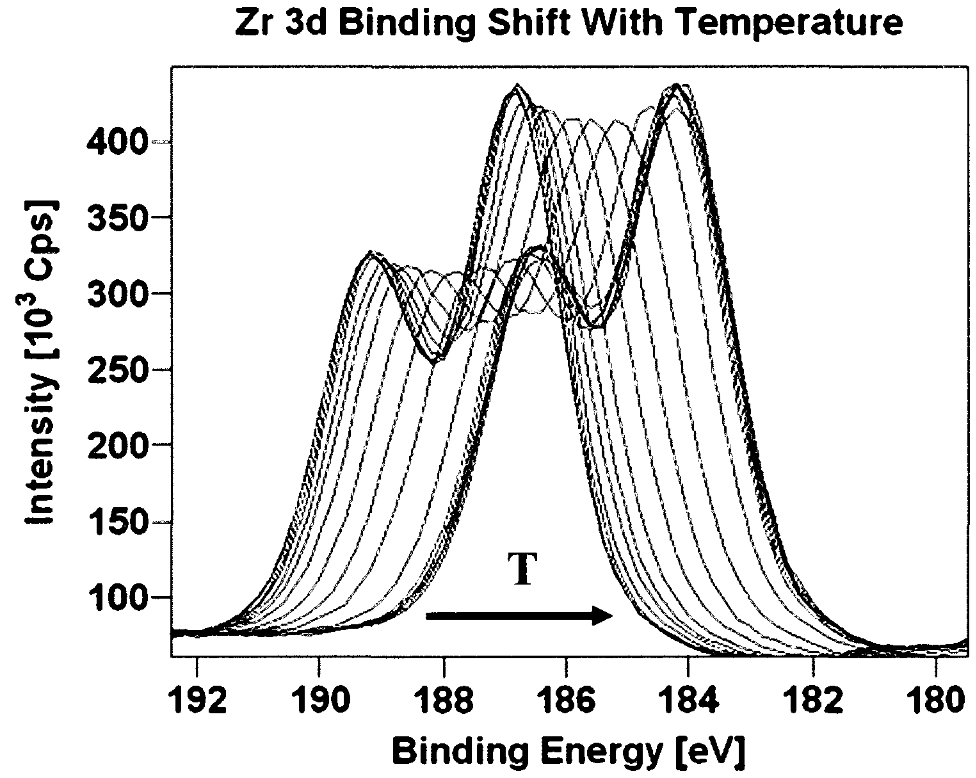

Figure 4-2 *Series of overlaid XP-spectra of the Zr 3d region taken at regular intervals during sample temperature ramp from 23 °C to 300 °C. The left most doublet taken at 23 °C is shifted to high binding energies due to sample charging, at approximately 150 °C to 175 °C charging begins to dissipate and the doublet begins to shift to lower binding energies as a result. The shift to lower binding energies ceases at sample temperatures between 225 °C and 275 °C. The lowering in peak height at intermediate temperatures is caused by peak broadening.*

The value of 275 °C therefore provides a target value at which to attempt scanning tunneling microscopy. The low value is extremely fortuitous, since in our system, heating to sample temperatures much higher than 300 °C requires electron bombardment. The difficulty with this heating method is that it requires that a high magnitude voltage be applied to either the sample or the filament in order to accelerate the heating electrons. For sample preparation and ramping, this is not a problem, however for STM, the power supply needs to provide a high voltage that is extremely clean and stable. Otherwise temperature fluctuations at the sample and scan head will result in volatile imaging due to thermal expansion effects. None of the supplies available to us could provide such stability, and either our equipment would have to be customized or new (expensive) supplies purchased. SPECS GMbH, who manufactured our chamber, are in the process of developing such a power supply for their high speed STM, and it should be available shortly.

Herein we discuss the experimental design and preliminary results of imaging YSZ(100) single crystal at elevated temperature with STM.

4.2. Experimental

Scanning tunneling microscopy is performed on an RHK combined STM/AFM microscope at elevated temperatures generally between 260 °C and 300 °C using a cut platinum/iridium tip or a chemically etched tungsten tip. The temperatures are reached primarily through radiant heating from a filament at the back of the sample stack (Section 4.3). A gravitational flow of chilled water through a cryostat attached to the sample stage is used to cool the sample holder during imaging. The stage is never allowed to exceed 150 °C, with the microscope chamber pressure limited to a maximum of 1.5×10^{-9} mbar. To minimize drift, before tip approach the sample temperature is allowed to equilibrate for approximately 1 hour.

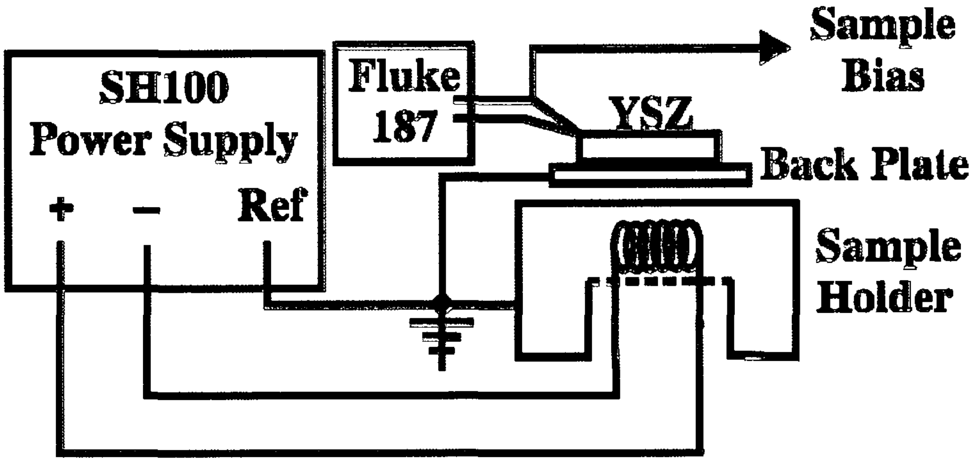

Figure 4-3 *Wiring diagram for performing scanning tunneling microscopy on YSZ at elevated temperature. Heating power supply (Specs SH100), sample holder, and back plate are all referenced to ground at a common point to prevent ground loops. Temperature is measured with a high impedance multimeter using a K-type thermocouple mechanically connected to the sample. This thermocouple is also used to bias the sample for imaging and is connected to the RHK controller to complete the tunneling circuit.*

Figure 4-3 demonstrates a rough wiring diagram for STM imaging of YSZ. The electrical connections though which the sample is heated, biased, and temperature measured, are of critical importance. Ground loops need to be carefully eliminated, and measurement of temperature needs to be performed using a passive device to prevent the introduction of electronic noise. In the present study, temperature is measured with a high impedance multimeter (Fluke 187). A metallic back plate is placed between the sample and the heating filament in order to sink any emitted thermionic electrons. Bias voltages reported subsequently refer to the potential applied to the sample, with the tip considered to be at ground potential.

4.3. Sample mounting

The RHK microscope used in these studies relies on a Johnny Walker beetle for coarse approach of the tip toward the sample. In this design, three piezo tubes acting like legs on a tripod carrying the STM tip "walk" down in unison; on three ramps machined to the surface of the sample holder. The requirement for these surface ramps constrain the type of holder which may be used. When developing a method to perform STM in conjunction with other techniques such as spectroscopy and in-situ annealing of YSZ(100), the setup must allow for the following :

1) High sample temperatures of 900 °C or 1000 °C for sample preparation.
2) Stable sample heating to 300 °C during STM imaging.
3) Measurement of tunneling current isolated from heating electrons.
4) Large exposed sample area, providing improved spectroscopy statistics.
5) Johnny Walker beetle compatibility.

Figure 4-4 shows an exploded view of the resulting sample mounting design. Here, a series of 8 mm diameter disks composed of materials selected for their electrical or thermal properties are used to satisfy the above conditions. The thoriated tungsten filament (not shown) heats the tantalum plate (0.1 mm thick) which may be raised to a high potential for e-beam heating or grounded during imaging. A sapphire ring (MTI Corporation) which is electrically and thermally insulating at high temperatures, but thermally conductive at cryogenic temperatures isolates the tantalum plate from the holder[8]. Sapphire allows efficient cooling at low temperatures for desorption experiments, but reduces heat transfer to the holder during annealing. Heat from the tantalum plate conducts across a dense beryllia disk (Brush ceramics [9]) to the sample. Beryllia is both an extremely good thermal conductor and an electrical insulator over a wide temperature range[10] and therefore serves to allow heat transfer to the sample while isolating it electronically. A K-type thermocouple, used to measure temperature and act as a connection for sample biasing, is mechanically pressed between the sample and a second sapphire ring. This ring has a 6 mm internal diameter allowing a large exposed sample area for spectroscopy. A thin, highly sintered alumina tube is placed around the sample stack, isolating the disks laterally and providing stability during thermal cycling.

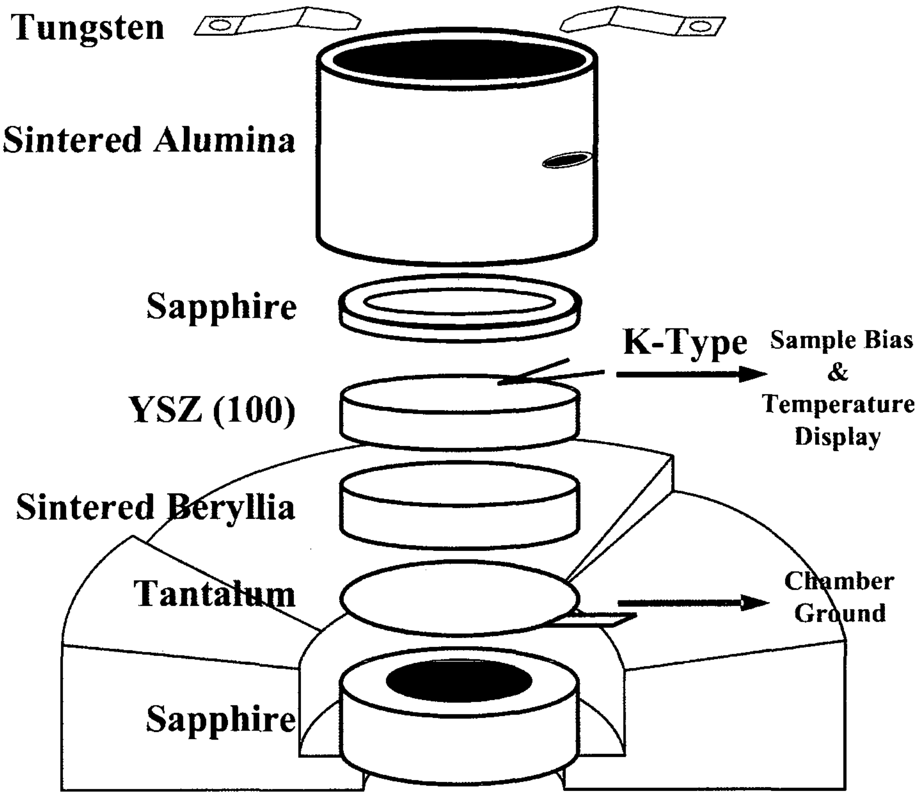

Figure 4-4 *Exploded view of the sample mounting stack including a cross section of the sample holder. From bottom to top: Sapphire ring thermally and electrically isolates the sample from the holder. A tantalum plate sinks the thermionic electrons emitted from the heating filament to ground. A beryllia disk conducts heat to the sample and isolates it electronically. The sample is biased, and the tunneling current and temperature are read through the K-type thermocouple which is mechanically pressed to the sample by a sapphire ring held in place by tungsten clips screwed to the holder. A thin sintered alumina tube surrounds the stack providing lateral isolation from the sample holder and stability during heating.*

The entire stack including the alumina tube is held in the sample holder within a ~10 mm ID recess using tungsten leaf clips. The clips run over the edges of the alumina tube and press down on the second sapphire ring, holding the whole stack in place. The clips are screwed to the holder but remain isolated electronically from the sample.

4.4. Comparison with ambient AFM

Though not sufficient at room temperature to support a tunneling current, the conductivity of YSZ increases significantly with temperature[7]. At values of 260 °C to 300 °C tunneling may be achieved, we have found this variability to depend largely on the state of oxidation of the surface, with stoichiometric samples requiring higher temperatures for tunneling than partially reduced samples.

In order to compare major topographical features, imaging of a YSZ single crystal is performed in air by AFM after annealing to 1000 °C for 90 minutes. It is then examined by XPS and STM under UHV conditions. Figure 4-5a presents the topographical atomic force micrograph of a Type 1 sample in which the expected steps, terraces, and etch pits are apparent.[11] The streaks, visible along the x-direction are attributed to surface adsorbates interacting with the tip. These adsorbates, remaining on the surface from ambient conditions, become clearer upon imaging by STM. In Figure 4-5b the scanning tunneling micrograph, now in UHV, shows 3-D particles 5 Å -20 Å in height. These particles are not visible in the intermittent contact AFM image since the oscillating cantilever pushes through the soft overlayer, making contact with the underlying structure. Under the imaging conditions for STM, tunneling occurs at least partially into the overlayer, resulting in a feedback signal which tracks to some extent the topography of the adsorbates. The 3-D particles (5 Å - 20 Å in height) are stable on the surface at the imaging temperature and over the imaging timescale (several hours). No preference of adsorption sites is observed as the coverage is homogeneous.

XPS indicates that the C 1s envelope is largely composed of C-O and/or C-H bonded carbon (spectra not shown). The inset of Figure 4-5b shows the tendency of the adsorbates to be oriented along the fast scan direction (in this case to the right), indicating some interaction between tip and adsorbates occurs. The slight downward orientation is likely a result of remnant thermal drift.

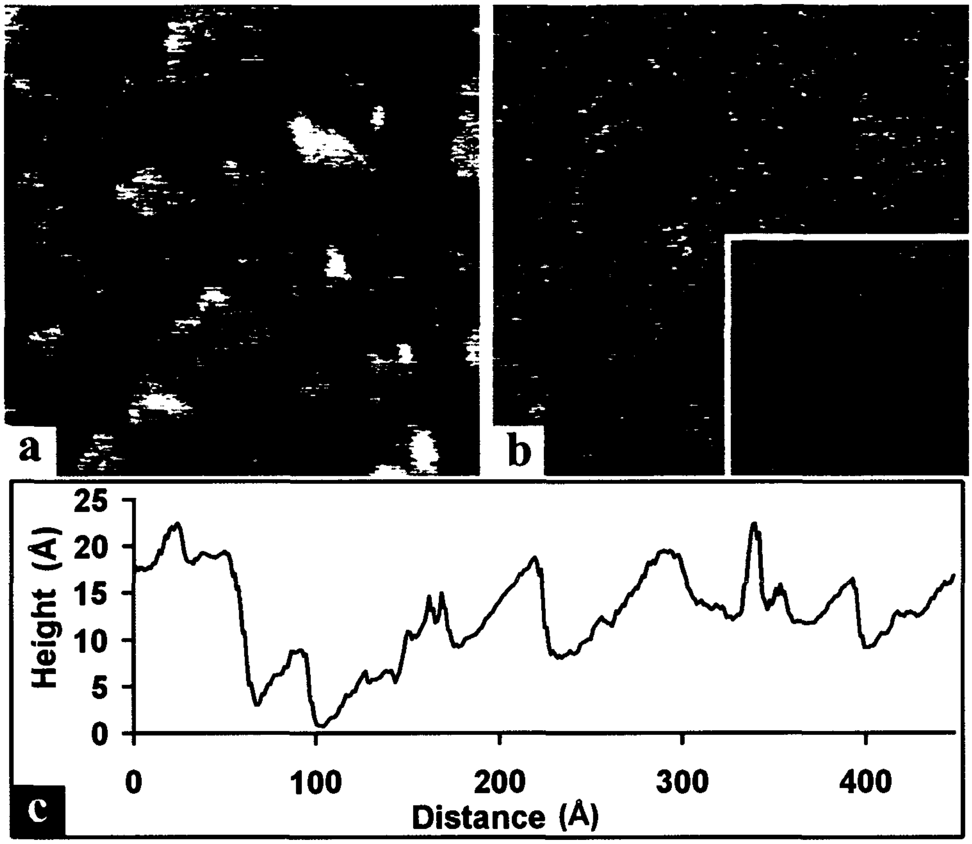

Figure 4-5 *(a) (500^2 nm^2, z_{range}= 3 Å, v= 1 l/s) YSZ (100) imaged by intermittent contact AFM in ambient conditions.(b) (500^2 nm^2) the same sample imaged in vacuum by STM at 280 °C (6V, 500 pA , z_{range}= 30 Å, v= 2.5 l/s). Inset of (b)(z_{range}= 25 Å, v= 2.5 l/s) shows a 100^2 nm^2 STM micrograph. The images show that the "macro"-scopic features such steps and terraces are reproduced by both techniques, but only STM detects the contaminant overlayer. (c) 45 nm line scan from a 50^2 nm^2 STM image demonstrating the high signal to noise ratio. The peak to peak noise is estimated to be less than 0.5 Å..*

STM imaging is performed at approximately 280 °C; at this temperature undissociated water should be absent from the surface, however hydroxyls and hydrocarbons may remain up to 800 °C [12]. Post imaging XPS shows the surface region contains approximately 13.5 ± 1.1 atom % of carbon with a binding energy of 285.4 ± 0.1 eV (FWHM of envelope = 1.8 eV). Carbon 1s transitions above 284.8 eV are often attributed to C-O, or C-N bonds. Although nitrogen is not believed to be on the surface, the main N 1s peak may have partial overlap with the Y 3s peak, making absolute confirmation difficult. The wide full width at half maximum of 1.8 eV of the C 1s peak suggest C-H bonds associated with free carbon are also likely large components of the carbon envelope[13] (fitting of C 1s envelope is discussed in more detail in Chapter 5).

Clearly surface cleaning is required to view smaller features, however, as one would expect, major features such as steps and terraces are reproduced in both scanning probe techniques.

The line scan shown in Figure 4-5c is taken from a (50 x 50) nm^2 image, the coarse features seen are derived from profiles of the adsorbates. The fine, high frequency contour overlaying the profile, is the noise floor. In this image we have measured this peak to peak noise to be under 0.5 Å, much better than the 1 Å to 1.5 Å observed in ambient AFM images.

4.5. STM tip induced surface reconstruction

In Chapter 3 it has been proposed that many of the observed defect structures at the surface of YSZ(100) can be ascribed to a lattice mismatch between highly defective and less defective regions. The resulting mismatch produces a dewetting and self organization pathway at temperatures sufficient to allow surface mobility. The strongest indications suggest that the defect layer contains a higher concentration of oxygen vacancies, that modify the lattice constant. This reduced sub-oxide layer is believed to exist as a result of the chemical and mechanical polishing which damages the surface, introducing defects such as oxygen vacancies. Other methods such as vacuum annealing may reduce the surface of YSZ, but also STM tip induced reduction and/or reconstruction may occur, as has been reported for other metal oxides. [14, 15]

Susceptibility of oxides surfaces toward reduction may be probed by monitoring the effect of the tunneling current on surface morphology. In some circumstances, by applying a sufficient voltage difference between tip and sample, the surface may undergo a reconstruction and/or reduction. These processes will depend on several factors, including the potential difference between tip and sample, the tunneling current, and the length of time tunneling occurs into (or out of) the scan area of interest (scan speed, number of scans). Figure 4-6 demonstrates this same effect for a clean and approximately stoichiometric YSZ(100) surface which has been prepared by a cleaning procedure that includes cycles of in-situ thermal oxidation to 900 °C – 1000 °C (Chapter 5). Figure 4-6a shows an imaged area, including a step a half unit cell in height, that has only been scanned twice. It is quite flat though some texture has begun to appear in the form of what appear to be clusters (bright spots in the image). After scanning the same area several more times, higher clusters begin to appear. We have then zoomed out, and scanned a larger area surrounding the same region. In figure 4-6b, the former scan region can be delineated. Reconstructed particles appear over the entire area, with some particles being up to 15 Å in height. The square scan region is slightly skewed as a result of drift over the time required to perform multiple scans, but clearly STM is able to modify the surface of YSZ(100) simply by imaging it.

While reconstruction and particle growth appear to be operative, it is not possible to determine if the observed particles in the STM images are formed at the surface or in the subsurface region of the YSZ crystal. Moreover, the STM images shown were acquired in constant current mode, in which the feedback loop moves the tip up and down in response to the surface so as to maintain a constant tunneling current. Often this movement corresponds to actual topography, however areas which provide higher current density (in this case a larger number of empty electronic states) will also produce movement in the z-direction. It is not clear if the particles seen are the result of actual clustering and height increase, or if they are simply areas providing higher current density as would be expected for reduced oxide within the YSZ crystal. This effect was observed by Antonov *et. al.*, who deliberately implanted Zr clusters in a YSZ film and observed the resulting tunneling via STM.[16]

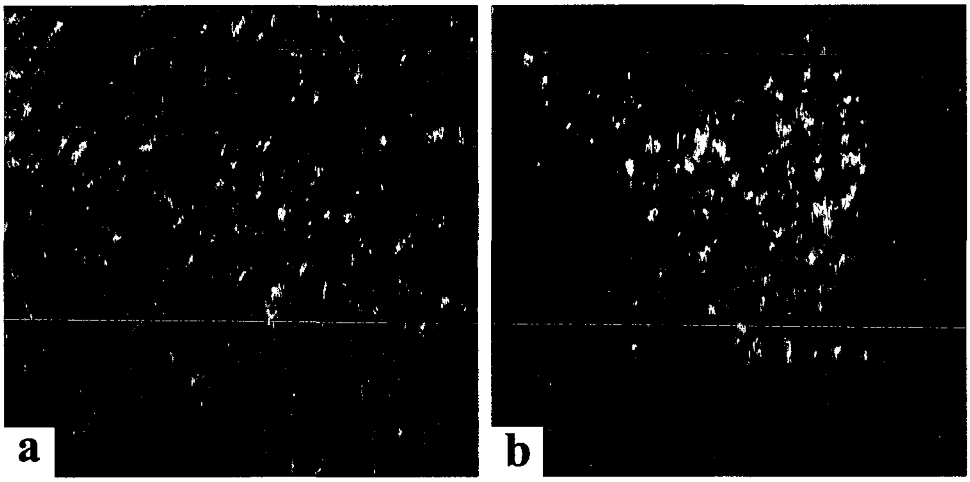

Figure 4-6 *(a) 120^2 nm^2 (5.74 V, 392 pA, 290°C, , z_{range}= 15 Å,* v= *2.5 l/s) Small scan region after only 2 scans of same area. (b) 240^2 nm^2 (5.74 V, 392 pA, 290°C, z_{range}= 20 Å,* v= *2.5 l/s) larger area scan after having scanned area of image a) several times. Deviation from a square scan area in (b) is a result of thermal drift over the numerous scans.*

We expect that the present features will be a combination of the two effects, with by far the largest contribution being a result of clustering. Due to the exponential dependence of current on distance from the tip to the surface feature, if the features were due to reduced sites without height increase, the observed particles would have to provide densities of empty electronic states, approximately 15 orders of magnitude greater than the full oxide. In metals, for each Angstrom in tip-sample separation, the tunneling current approximately decreases by an order of magnitude.[1]

In Figure 4-6, the surface though reasonably flat, is not atomically flat, and corrugation of 1 to 1.5 Å is measured. The origin of this "texture" is not clear, however since clustering seems to be due to tip induced reduction and/or reconstruction, a single scan may be sufficient to begin reconstruction. Alternatively this contouring may be an innate surface characteristic, with reconstruction driven thermodynamically. Especially in ultra high vacuum, in the absence of hydroxyls or hydrocarbons to stabilize the surface, and no oxygen to maintain stoichiometry, cluster formation may easily occur.

4.6. Conclusion

Atomic force microscopy is a very useful tool in characterizing local surface topography, and has been used to examine YSZ in ambient conditions. Of more difficulty is transfer of AFM studies into vacuum for multi-technique experiments. This is particularly true for non-contact methods such as FM-AFM, in which sample charging makes imaging difficult.

Scanning tunneling microscopy has been used for the first time to visualize the surface of a bulk YSZ material taking advantage of the (minimal) electronic conductivity that the material offers at temperatures of 260 °C - 300 °C. A sample mounting technique has been demonstrated that provides high temperature stability at 300 °C, as well as efficient thermal conduction to the sample for high temperature sample preparation.

The equivalence of AFM and STM images has been shown in the observation of the "macro" features of the YSZ (100) surface, but only STM offers the enhanced resolution in UHV to observe clustering likely due to partial reduction of the surface layer. Reduction and reconstruction can be induced by interaction of the STM tip with the sample, and consequently, scan parameters must be selected to minimize such an effect. Since this reconstruction was shown to be dependent on scan time, one could, for example, select and test scan parameters outside the target imaging area. Once the parameters are optimized, one would move to the target area and perform a scan. In this way tip-sample interaction time is minimized, providing less opportunity for surface modification.

References

1. Morita, S., Wiesendanger, R. and Meyer, E., *Noncontact atomic force microscopy.* Nanoscience and technology. 2002, Berlin: Springer.

2. Wikipedia, *Kelvin probe force microscope*, in www.wikipedia.org. 2008.

3. Engelhardt, J.B., Dabringhaus, H. and Wandelt, K., *Atomic force microscopy study of the CaF_2(111) surface: From cleavage via island to evaporation topographies.* Surface Science, 2000. **448**(2-3): p. 187.

4. Engelhardt, J.B., Dabringhaus, H. and Wandelt, K., *Atomic force microscopy study of the CaF_2(111) surface: From cleavage via island to evaporation topographies (vol 448, pg 187, 2000).* Surface Science, 2002. **516**(1-2): p. 216.

5. Diebold, U., *Structure and properties of TiO_2 surfaces: A brief review.* Applied Physics a-Materials Science & Processing, 2003. **76**(5): p. 681.

6. Woll, C., *The chemistry and physics of zinc oxide surfaces.* Progress in Surface Science, 2007. **82**(2-3): p. 55.

7. Filal, M., Petot, C., Mokchah, M., Chateau, C. and Carpentier, J.L., *Ionic conductivity of yttrium-doped zirconia and the "composite effect".* Solid State Ionics, 1995. **80**(1-2): p. 27.

8. Yates, J.T., *Experimental innovations in surface science.* 1998, New York: Springer-Verlag.

9. Brush Ceramics, S.T.B., Tucson, AZ 85706 USA. www.brushceramics.com.

10. Slack, G.A. and Austerman, S.B., *Thermal conductivity of beo single crystals.* Journal of Applied Physics, 1971. **42**(12): p. 4713.

11. Green, R.G., Barre, L. and Giorgi, J.B., *Nano-structures in YSZ(100) surfaces: Implications for metal deposition experiments.* Surface Science, 2007. **601**(3): p. 792.

12. de Ridder, M., van Welzenis, R.G. and Brongersma, H.H., *Surface cleaning and characterization of yttria-stabilized zirconia.* Surface and Interface Analysis, 2002. **33**(4): p. 309.

13. Moulder, J.F., Stickle, W.F., Sobol, P.E. and Bomben, K.D., *Handbook of x-ray photoelectron spectroscopy*, ed. Chastain, J. and R.C.J. King. 1995: Physical Electronics, Inc.

14. Klusek, Z., Busiakiewicz, A., Datta, P.K., Schmidt, R., Kozlowski, W., Kowalczyk, P., Dabrowski, P. and Olejniczak, W., *Room and high-temperature scanning tunneling microscopy and spectroscopy (HT-STM/STS) investigations of surface nanomodifications created on the* TiO_2*(110) surface.* Surface Science, 2007. **601**(6): p. 1513.

15. Yan, J.W., Xie, Z.X., Cao, Z.X., Zhou, C.J., Kang, J.Y. and Mao, B.W., *Formation and STM tip-induced reduction of ultra thin sno film on au(111).* Chemical Physics Letters, 2003. **373**(5-6): p. 575.

16. Antonov, D.A., Gorshkov, O.N., Kasatkin, A.P., Maximov, G.A., Saveliev, D.A. and Filatov, D.O., *Investigation of the electronic properties of the Zr nanoclusters in the YSZ films by combined STM/AFM.* SPM Proceedings, 2004.

5. Ultra High Vacuum Studies

In this chapter the impurity profile of YSZ(100) is discussed, how these impurities interact with the YSZ(100) surface and how they may be removed is examined in detail. XPS, STM and STS are used in combination to examine the YSZ surface at different stages of processing, and reaction. Ultimately methods of cleaning and flattening the surface are offered towards the creation of an ideal YSZ(100) surface. The importance of these investigations is derived from the necessity to reproducibly control and characterize the factors which may modify the YSZ surface at all stages of a model catalyst experiment. Moreover, because all real catalysts contain impurities, in order to partially bridge the complexity gap between real catalysts and model catalysts it is important to understand the role of these impurities and defects even on single crystal YSZ(100).[1-3]

5.1. Segregation and surface impurities studied by XPS and AR-XPS

5.1.1. Introduction

Several studies have examined impurities in stabilized zirconia systems and their segregation behaviour. The most commonly reported contributors have been Hf, Mg, Na, Ca, Fe, Ti and Si, originating from the zircon sands from which ZrO_2 is purified.[3-11] Aside from impurity segregation, yttria is well known to diffuse to the surface in YSZ as a result of heating in air. The literature in this regard is controversial, with some reports showing surface yttria concentrations as high as 30 mol% in a 10 mol% bulk YSZ sample that has been heated above 1000 °C.[12] This report, by de Ridder *et. al.* demonstrated that yttria accumulates in the subsurface region, with Ca, Na, and Si covering the topmost surface. In contradiction to this, Burgraaf et al. have shown in studies by XPS and AES, that with sufficient annealing times, yttria will segregate to the surface or grain boundaries to an equilibrium concentration of 15 to 16 mol %. This surface concentration is reported to be independent of bulk concentration, so that in effect, all sufficiently annealed YSZ surfaces will have similar compositions. Nowotny *et. al* have argued that the incongruity in the studies by de Ridder and Burgraaf arise from differences in sample preparation and characterization techniques.[1] They consider that the de Ridder study less accurately represents true YSZ properties since the analysis technique used, low energy ion scattering (LEIS), relies on detection of backscattered ions from the YSZ surface. The incident ions used both for cleaning and LEIS are in the 3 keV to 5 keV energy range, and as such, modify the surface producing a non-equilibrium system that does not truly represent YSZ under normal use.

Our own results somewhat confirm this idea. As shown in Chapter 3, the damaging effects, both by ions and electrons, were demonstrated to modify the surface topography of YSZ. Furthermore, studies of ion-bombarded YSZ(100) by XPS show chemical modification in the surface as well. Y/Zr metal ratios changing as a function of sputter time at 600 eV are shown in Figure 5-1. This sample, previously annealed in air for several hours, presents a surface Y/Zr ratio within 1% of the bulk value at time zero. After initial bombardment, the Y/Zr ratio drops significantly with a maximum decrease of about 0.06 between 0 and 10 minutes. After ten minutes the Y/Zr ratio increases steadily, reaching a "sputter equilibrium" at about 50 minutes. This ratio is greater than the start, as-annealed, value by 0.02, indicating a new "sputter equilibrium", different from the as annealed ratio.

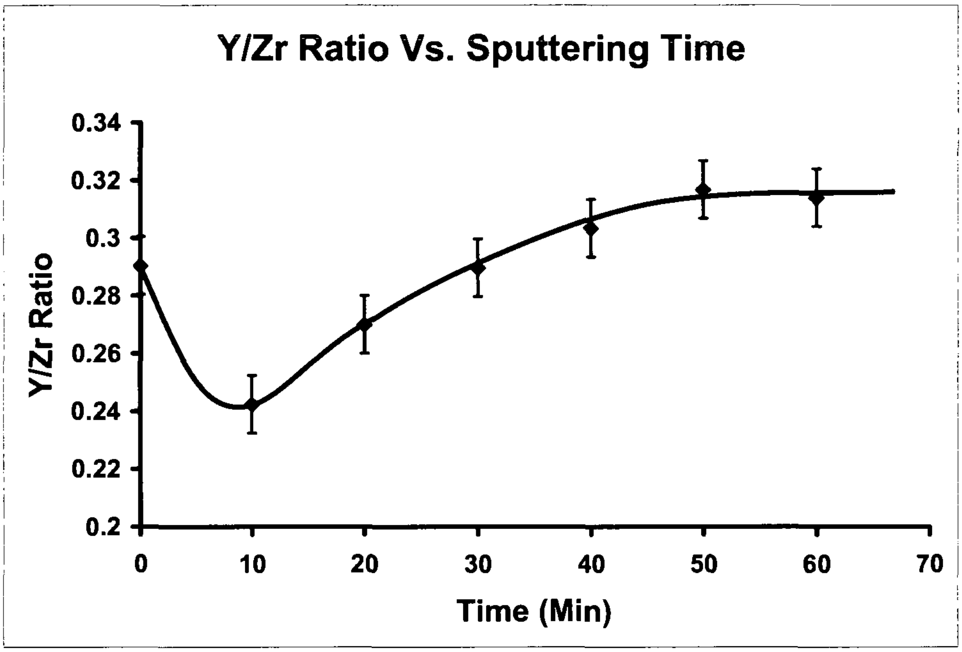

Figure 5-1 *X-ray photoemission quantification results of the Y/Zr metal ratios plotted as a function of sputter time under 600 eV argon ions (3.5 x 10^{-6} mbar). The curve demonstrates modification of the surface chemistry through ion bombardment. The Y/Zr ratios dips through a minimum at 10 minutes before rising to an equilibrium ratio. This "sputter equilibrium" ratio is different from the air annealed ratio at time 0, and therefore describes a system different from what one could expect in air annealed systems.*

In order to maintain a surface which, as accurately as possible, reflects a real YSZ system, we have chosen for study single crystals which have bulk concentrations near the segregation equilibrium concentrations reported by Burgraaf. Our selected crystals (13 mol% Y_2O_3), are closer to that equilibrium value (15%-16%) and should therefore be subject to less segregation induced changes. Normally one would be tempted to use a 9.5% Y_2O_3 – YSZ sample; this ratio is most often employed in SOFC studies since within the 9 to 10 mol% range, oxygen ion mobilities are maximized. However, since we are concerned with accurately recreating the triple phase boundary in the absence of conduction O^{2-}, ion mobilities are less important than appropriate surface composition.

XPS measurements of air annealed YSZ single crystals on our system yield surface Y/Zr metal ratios between 0.29 ± 0.01 and 0.31 ± 0.01 for both 9.5 and 13 Y_2O_3 mol% single crystals, confirming the results of Burgraaf. However 13 mol % crystals, according to their bulk concentrations, also correspond to Y/Zr ratios within this range (0.299). In this regard, 13 % Y_2O_3 corresponds to an equilibrium composition value, this value is different than the (15-16) % reported by Burgraaf. This discrepancy may be due to sample, and/or XPS calibration differences in the Burgraaf study. In that investigation, the samples examined were poly-crystalline powders. Since the (101) surface has been reported to be more thermodynamically stable than the (100) surface, one would expect the crystals composing the powders would more often be (101) terminated.[13] Moreover Eichler *et. al.* have shown that the (101) orientation is better stabilized by yttrium surface segregation than the (100) orientation.[13, 14] It is therefore not surprising that the results of Burgraaf show slightly higher yttrium surface concentrations after segregation equilibrium has been achieved.

5.1.2. *Impurities in the surface region of air-annealed YSZ(100): XPS analysis using dual anode x-ray source*

In Chapter 3 surface impurities were reported to be largely composed of carbon with perhaps small amounts of Si, and Na. Higher resolution XPS of the surface of a post air annealed sample (5 hours, 1000 °C) exhibits several possible impurities in small amounts. Figure 5-2 shows XP-Spectra acquired with excitation x-rays from an aluminum (bottom spectra) and a magnesium anode. The lower excitation energies characteristic of the magnesium anode provides higher surface sensitivity than the aluminum anode.

Peak identification can be made by examining position, relative intensity, as well as changes in peak position when spectra are acquired using x-ray sources of different energy.

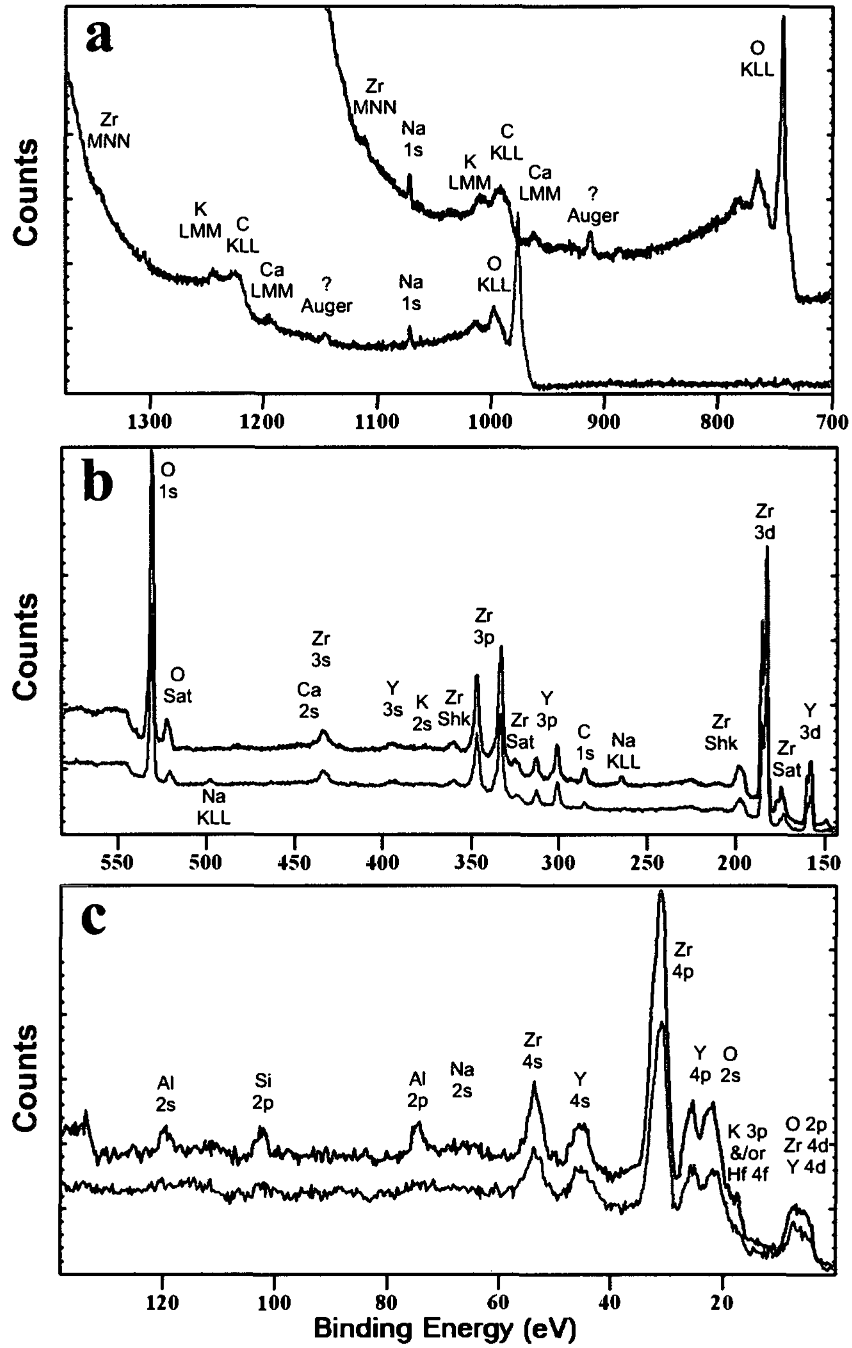

Figure 5-2 *(30 eV pass energy, 0.2 eV step, 0.1 s dwell) XP-spectra of air annealed YSZ(100) acquired using both an aluminum (bottom) and a magnesium Kα x-ray excitation source. Peak identification indicates the presence of cationic impurities such as Na, K, Ca, as well as Si, and C. Other impurities such as Hf, Mg, Cl may be present in small quantities. Al is an artifact of the* Al_2O_3 *ring used in sample mounting, it can be eliminated by optimizing the detector focus.*

In XPS, electrons excited as a result of an auger mechanism will shift in binding energy with changes in the energy of the x-ray source, while peaks due to an inelastic photoelectron transition will remain at the same binding energy. In this way, using two different sources allows Auger peaks to be distinguished from photoelectron peaks as a result of their movement.

Figure 5-2a shows the high binding energy/low kinetic energy section of the YSZ(100) XP-spectrum, this region most clearly exhibits the cationic impurities, separated from any overlapping peaks. Though small, the elements Na, Ca, and K can be clearly resolved. The Na 1s peak remains in the same position between scans while all other elements shift, indicating that they are Auger peaks. The sole unidentified transition (labeled with a question mark) shifts in a similar manner, and may possibly correspond to a Ag or Pd Auger transition. However, the peak is observed even after surface cleaning and is therefore likely to be an artifact, perhaps associated with electron sources within the chamber such as an ion gauge or ion pumps. Such sources would be constant in kinetic energy and would, like Auger peaks, appear to shift in binding energy with different x-ray sources.

Figure 5-2b shows the mid-energy-range spectrum, the transitions in this range are most frequently used for quantification (O 1s, C 1s, Zr 3d, Y 3d). It has been difficult to separate out possible contaminant peaks which overlap with the main elemental transitions of YSZ. Hafnium is reported to be one of the largest contaminants of YSZ in the bulk,[3, 6] however due to peak overlap it is not clear if it is found at this surface. Though Hf may be seen by bulk analytical techniques, because it is almost equivalent in size to zirconium, it may not segregate to the surface to a detectable extent (energies of segregation are, amongst other factors, exponentially dependent upon atomic radius differences). As such it will not be seen by our XPS which at photoelectron takeoff angles of 90° (perpendicular to surface) probes up to approximately 2.5 nm or 5 unit cells into the bulk. In Figure 5-2a Hf overlaps with Ca 2s, Zr 3s and K 2s, both of these elements were identified to be present by their Auger peaks in panel a.

Figure 5-2c shows the valence region of YSZ(100), here two contaminants are clearly visible, Al and Si. Though Al has been reported previously to be a surface contaminant it is believed that the observed peaks in this case are mainly a consequence of the Al_2O_3 ring used for surface mounting. In most samples studied, these peaks can be eliminated by optimizing the sample position, focus conditions, or by lowering the pass energies. Silicon is a very commonly reported segregant and appears to a greater or lesser degree on all as annealed samples. The large differences in peak size between scans using Mg and Al x-ray sources are attributed to the enhanced surface sensitivity and signal to noise ratio in scans using the Mg source.

5.1.3. Angle resolved XPS

Previously the largest contribution of surface impurities was shown to be made by C, Na, K, Si. As seen in Chapter 1, angle resolved XPS allows some depth information to be acquired by adjusting the angle between the sample and detector, and therefore modifying the path length of detected electrons through the sample. At a 90° takeoff angle 95% of photoelectrons originate from depths within the sample of 0.5 nm to 2.5 nm depending on their kinetic energy.[15-21] At angles of 55° and 25°, this corresponds to ranges of 0.4 nm - 2.0 nm and 0.2 nm – 1.1 nm respectively.

Angle resolved XP-spectra of the same sample studied in Figure 5-2 have been performed (10 eV pass energy, 0.25 eV step, 0.2 s dwell) over takeoff angles 90°, 55° and 25°. From these spectra the intrinsic elements as well as the main segregants were quantified as a function of angle, the results are summarized in Table 5-1. While all elements intrinsic to YSZ decrease with an increase in surface sensitivity (lower takeoff angle), all impurities increase. Consequently, the segregants are more strongly localized at the surface. This is particularly true of carbon, which more than doubles (156 % increase) in concentration between 90° and 25°, indicating that surface localization is even stronger for carbon. This is not surprising since much of the carbon is absorbed from ambient conditions, rather than diffusing from the bulk. The impurity segregants Si, Na, and K increase by approximately the same value, indicating they may be localized at the same depth.

Table 5-1 *Calculated elemental quantification summary of angle resolved XP-spectra taken of air annealed YSZ(100). Change is calculated between 25° and 90° with the largest changes representing the strongest localization of the element near the surface.*

Element	Concentration (atom %) at Takeoff Angle			
	90°	55°	25°	Change (%)
0 1s	56.1 ± 0.9	53.5 ± 1.0	51.8 ± 1.0	-8
C 1s	6.4 ± 1.3	13.3 ± 1.3	16.4 ± 1.3	156
Zr 3d	24.8 ± 0.4	20.7 ± 0.4	17.6 ± 0.4	-29
Y 3d	7.4 ± 0.2	6.0 ± 0.2	5.3 ± 0.2	-28
Si 2p	1.4 ± 0.5	1.9 ± 0.5	2.4 ± 0.6	71
Na KLL	3.6 ± 0.6	4.2 ± 0.7	5.9 ± 0.9	64
K $2p_{3/2}$	0.4 ± 0.2	0.5 ± 0.3	0.7 ± 0.2	75
Y/Zr	0.298 ± 0.012	0.286 ± 0.013	0.296 ± 0.015	-0.002

Both Zr and Y decrease by similar amounts indicating they are generally well correlated in location, however oxygen decreases by much less. As the takeoff angle declines less of the bulk is probed, and therefore less lattice oxygen will be measured. Due to the YSZ stoichiometry ([O]/{[Zr]+[Y]} = 1.88), the probed quantity of lattice oxygen should decrease by 1.88 times the sum of the changes in zirconium and yttrium concentration. This should result in an overall oxygen decrease of 15.6 atom %. As can be seen, the decrease is shown to be only approximately 4.3 atom %. Obviously the oxygen measured is not only located in the lattice, and much of the reduction in measured lattice oxygen is compensated for by an increase in measured oxygen content at the surface layer. The surface oxygen is present in the form of hydrocarbons, undissociated water and hydroxyls.[22]

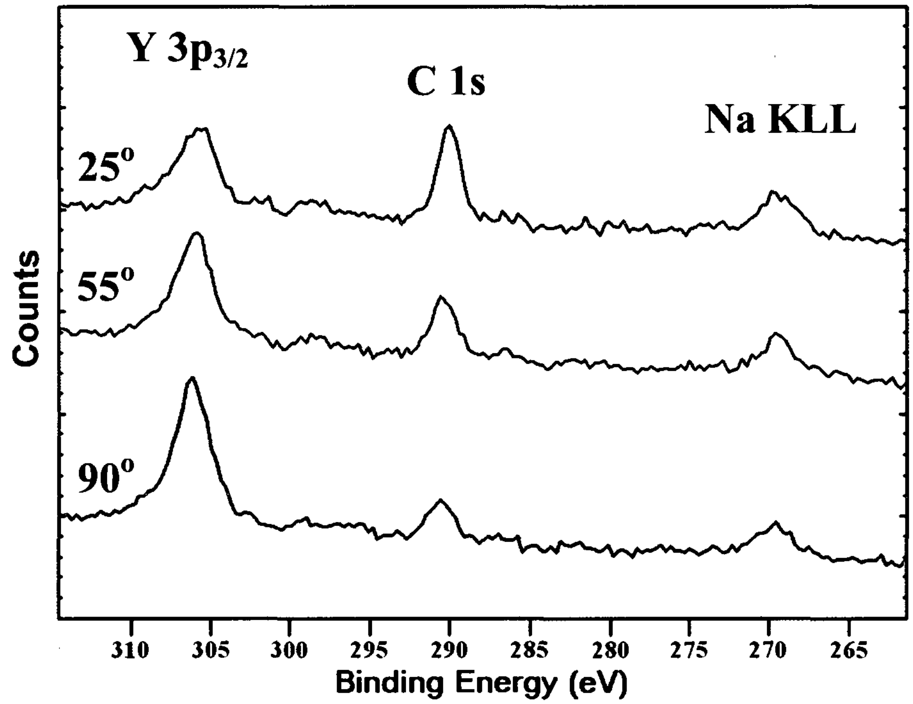

Figure 5-3 *Angle resolved XP spectra demonstrating the strong surface localization of carbon, and the significant but less pronounced surface localization of Na. Yttrium is clearly localized further from the surface. Note: binding energy scales are not corrected.*

5.1.4. Chemical stability at elevated temperatures in vacuum

In Chapter 4 a method for imaging YSZ(100) by STM at elevated temperatures was presented. The increase in electrical conductivity with temperature for YSZ allows tunneling current to be dissipated, and in XPS allows sample charging due to loss of electrons through photoexcitation, to be neutralized with conduction electrons. High temperatures are also required for thermal desorption and catalysis studies. The effect of heat on impurities in vacuum is therefore important.

Table 5-2 *Calculated atomic concentrations derived from XP-spectra acquired at a series of elevated temperatures.*

Element	Concentration (atom %) at 55° Takeoff Angle			
	23 °C	150 °C	300 °C	450 °C
0 1s	54.8 ± 1.0	55.5 ± 1.2	55.4 ± 1.2	57.1 ± 1.0
C 1s	12.5 ± 1.6	9.9 ± 1.1	8.7 ± 1.4	9.7 ± 1.2
Zr 3d	21.9 ± 0.6	21.9 ± 0.5	22.9 ± 0.5	22.3 ± 0.4
Y 3d	6.0 ± 0.2	6.3 ± 0.2	6.6 ± 0.2	6.0 ± 0.2
Si 2p	1.7 ± 0.6	1.8 ± 0.9	1.6 ± 0.6	2.3 ± 0.7
Na KLL	3.2 ± 1.2	4.7 ± 1.2	4.7 ± 1.1	2.6 ± 0.7
Y/Zr	0.274 ± 0.017	0.287 ± 0.014	0.290 ± 0.015	0.270 ± 0.013

Table 5-2 shows the changes in the surface chemical composition of the sample studied in Table 5-1 at elevated temperatures under UHV conditions. Since the K $2p_{3/2}$ could not be conclusively identified at higher temperatures, and represents under a 1% surface composition, it is not included in these quantification values.

From 23 °C, linear temperature ramps were performed consecutively to 150 °C, 300 °C, and 450 °C at a ramp rate of 0.5 °C/s. The temperature was held at each target for approximately 30 minutes in order to acquire the XP-spectra before the next ramp was begun. Table 5-2 presents a quantification summary of the XPS data, and it can be seen that only a few elements are modified significantly over the temperature range. One of these elements is carbon, which decreases significantly between room temperature and 300 °C.

The decrease over this range is largely attributed to carbon seen at binding energies above the free carbon value of 284.8 eV, these are often associated with O-C bonds or a conjugated carbon species.[23] A nominal increase in carbon is seen between 300 °C and 450 °C, and though the change is not significant within the listed errors, this trend has been repeated several times with various samples and is believed to be real. The interaction of surface carbon with YSZ(100) turns out to result in complicated effects that will be discussed in detail in Section 5.3, and it will be shown that at temperatures above 300 °C, dissolved carbon may diffuse to the surface accounting for this apparent increase.

In Section 5.1.3 oxygen was shown to be located in higher concentration at greater depths within the sample. In spite of the loss of oxygen in the form of hydrocarbons, the removal of carbon from the surface layer should allow greater sample depths to be probed and an increase in oxygen concentration should be observed. In Table 5-2 an increase in oxygen concentration between room temperature and 450 °C is observed, but it is interesting to note the greatest apparent increase in oxygen occurs between 300 °C and 450 °C, even though the lowest carbon concentration is seen at 300 °C. This perhaps indicates that after carbon leaves the surface it may be replaced by oxygen diffusing from the bulk or subsurface region.

A small increase in Y and Zr is seen between room temperature and 300 °C, this is expected to result from the removal of carbon from the surface. At 450 °C, both these values decrease slightly, corresponding with the increase in carbon and oxygen, indicating again a diffusion of oxygen and carbon to the surface.

Finally the Na concentration decreases between 300 °C and 450 °C, while that of silicon remains relatively constant across the full range of temperatures studied. The melting point of sodium is approximately 97.72 °C at STP, and its vapour pressure is greater than

100 Pascal at 450 °C.[24] Due to this relatively large vapour pressure, evaporation is the likely mechanism for Na loss.

5.2. Surface cleaning

Surface cleaning methods in UHV vary, one common process for YSZ(100) by Simpson *et al.* indicates ion sputter at energies between 0.5 and 3 keV, followed by annealing to 627 °C in vacuum or back pressures of 1.0×10^{-5} Torr oxygen.[25] Both the sputter energy and oxygen partial pressure range is troublingly large, since there is a dramatic difference between the magnitude of sputter damage from a 2.5 keV beam than one 600 eV in energy. Furthermore, at a 627 °C anneal temperature, topographical sputter damage would not be healed in a reasonable length of time due to the very slow annealing kinetics at this temperature.[26]

In Chapter 3 the effect of Ar+ sputtering on surface topography and chemistry was studied by AFM and XPS. The Type 1 surface was shown to be the equilibrium topography and sputtering such a surface for 30 minutes at 600 eV could remove contaminants without altering the surface type. After subsequent annealing in air to 1000 °C, the surface type was still maintained though formation of larger islands and pits, likely through the coalescence of smaller defects, was observed. Since in that study, high temperature annealing was performed in air, possible effects of partial pressures of nitrogen, CO, CO_2, water and other molecules which can be found in air, could not be accounted for. In vacuum studies this is not the case and control of the gaseous phase is possible, examination of the surface topography after sputtering, and annealing in vacuum or partial pressures of oxygen remains important.

5.2.1. Argon sputtering in time

In the absence of preferential sputtering, argon bombardment in combination with XPS can provide depth information. Sputtering will remove subsequent layers of material in time, and by acquiring XP-spectra at specific intervals, depth information can be provided. In the presence of preferential sputtering, however, deconvolution of sputtered induced chemistries from intrinsic depth profiles may be difficult.

Table 5-3 presents quantification results of XP-spectra taken at 300 °C and a takeoff angle of 55°, at sputter time intervals of 10 minutes, from 0 to 50 minutes. Sputtering was performed at 300 °C with Ar ions at a back pressure of 3.5 x 10^{-6} mbar with the sputter beam directed parallel to the surface normal.

Table 5-3 *Calculated elemental composition of a Type 1 YSZ(100) sample after sputtering for the indicated time at 600 eV, 3.5 x 10^{-6} mbar Ar, at a sample temperature of 300 °C. Equilibrium reached between 30 or 40 minutes of sputter time, surface impurities are eliminated after 10 minutes.*

Element	Concentration (atom %) at Sputter Times (min), 55°					
	0	10	20	30	40	50
0 1s	51.6 ± 1.0	63.8 ± 0.4	63.6 ± 0.4	63.0 ± 0.4	62.4 ± 0.4	62.5 ± 0.4
C 1s	16.5 ± 1.3	< 1.5	< 1.5	< 1.5	< 1.5	< 1.5
Zr 3d	20.9 ± 0.4	29.1 ± 0.3	28.5 ± 0.3	28.7 ± 0.3	28.6 ± 0.3	29.0 ± 0.3
Y 3d	5.8 ± 0.2	7.1 ± 0.1	7.9 ± 0.2	8.3 ± 0.2	9.0 ± 0.2	8.5 ± 0.2
Si 2p	2.3 ± 0.8	< 1	< 1	< 1	< 1	< 1
Na KLL	2.9 ± 0.6	< 1	< 1	< 1	< 1	< 1

Over the first ten minutes all defect impurities, which were found to be highly surface localized from previous angle resolved measurements (Section 5.1.3), are eliminated. The oxygen content increases significantly indicating the oxygen deficient defect layer studied in Section 4.3, is also largely removed. Although the appropriate oxygen to metal stoichiometry is approached, the Y:Zr ratio is significantly lower, exhibiting Zr enrichment.

Changes in the elemental concentrations over sputtering time are more clearly presented in Figure 5-4. Here the Si, Na, and C concentrations are not included for clarity and as mentioned, are below detection level after 10 minutes. Over the 50 minute time scale the yttrium content is found to increase monotonically while the zirconium concentration, after an initial jump between 0 and 10 minutes due to removal of the defect layer, remains approximately constant in time.

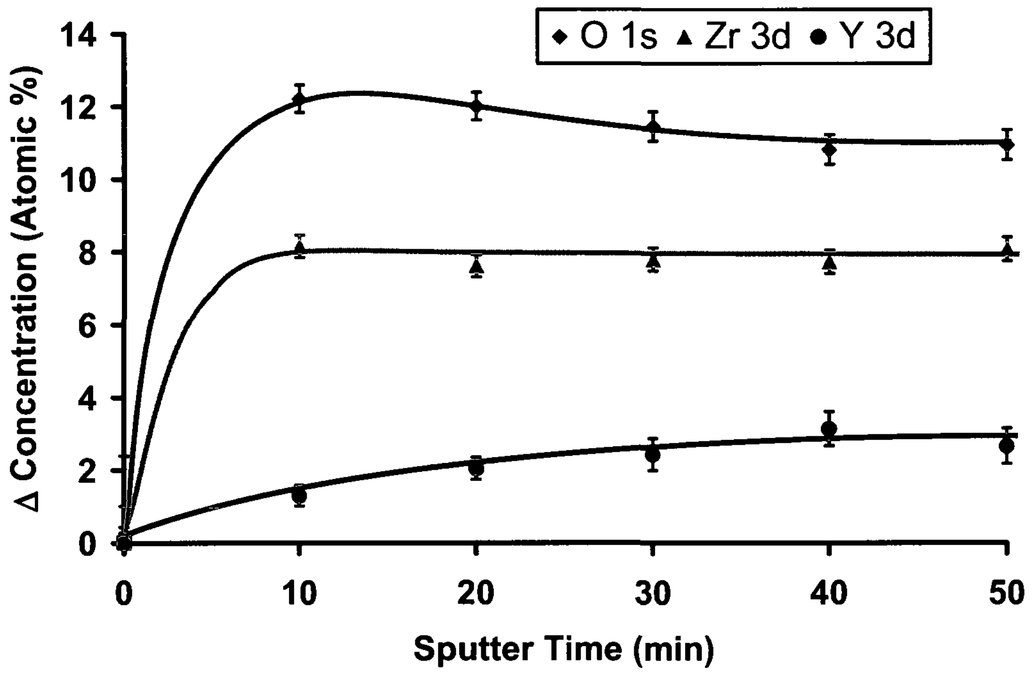

Figure 5-4 *The change (from time zero) in atomic concentration as a function Ar+ sputter time for the intrinsic elements of YSZ. Impurity elements are not included for clarity, however they are removed after 10 minutes. A sputter equilibrium of constituents is achieved between 30 and 40 minutes of bombardment. The sample was held at 300 °C during the series.*

After the removal of this defect layer, preferential sputtering of oxygen is observed until an equilibrium sputter chemistry is reached between 30 and 40 minutes. Though it is not entirely clear, the increase in yttrium concentration over this range suggests that zirconium is preferentially sputtered as well, in agreement with results of RF magnetron sputtering of YSZ targets with Ar[27]. Perhaps since oxygen is less strongly bound in zirconia than yttria, the oxygen correlated with zirconium is preferentially removed. That is, the zirconia molecule is preferentially sputtered over time. It appears that the largest contribution to the surface defect layer previously studied by AR-XPS is removed within the first ten minutes of sputtering, after which time the largest contribution to changes in stoichiometry results from ion bombardment.

After performing ion sputtering in time the sample was imaged by STM in order to view sputter induced changes to topography. In Figure 5-5a, the post air anneal (1000 °C, 5 hours) AFM micrograph is shown indicating a Type 1 surface topography. After sputtering, the sample was immediately transferred to the STM chamber, where it was held at 280 °C during imaging.

STM images were generally unstable and I/V curves often showed large hysteresis with sharply fluctuating curves. Though the origin has not been determined absolutely it is believed that much of the instability originates from sharp changes in the electronic structure across the surface. These changes may be due to clustering of oxygen vacancies, and presence of both reduced and oxidized phases. Morant *et al.* showed by core level and valence-band XPS that sputter induced defects in ZrO_2 results in an oxygen depleted region up to ~1.2 nm thick.[28] These defects allow emission within the band gap at 2.3 eV above the valence band. In the Morant study the sample was subject to high fluences of 3 keV Ar ions, which resulted in a clear reduction of Zr^{4+} to lower oxidation states including Zr^{0} or Zr^{1+} as seen by shifts in the Zr 3d x-ray photoemission peaks. In the present study the

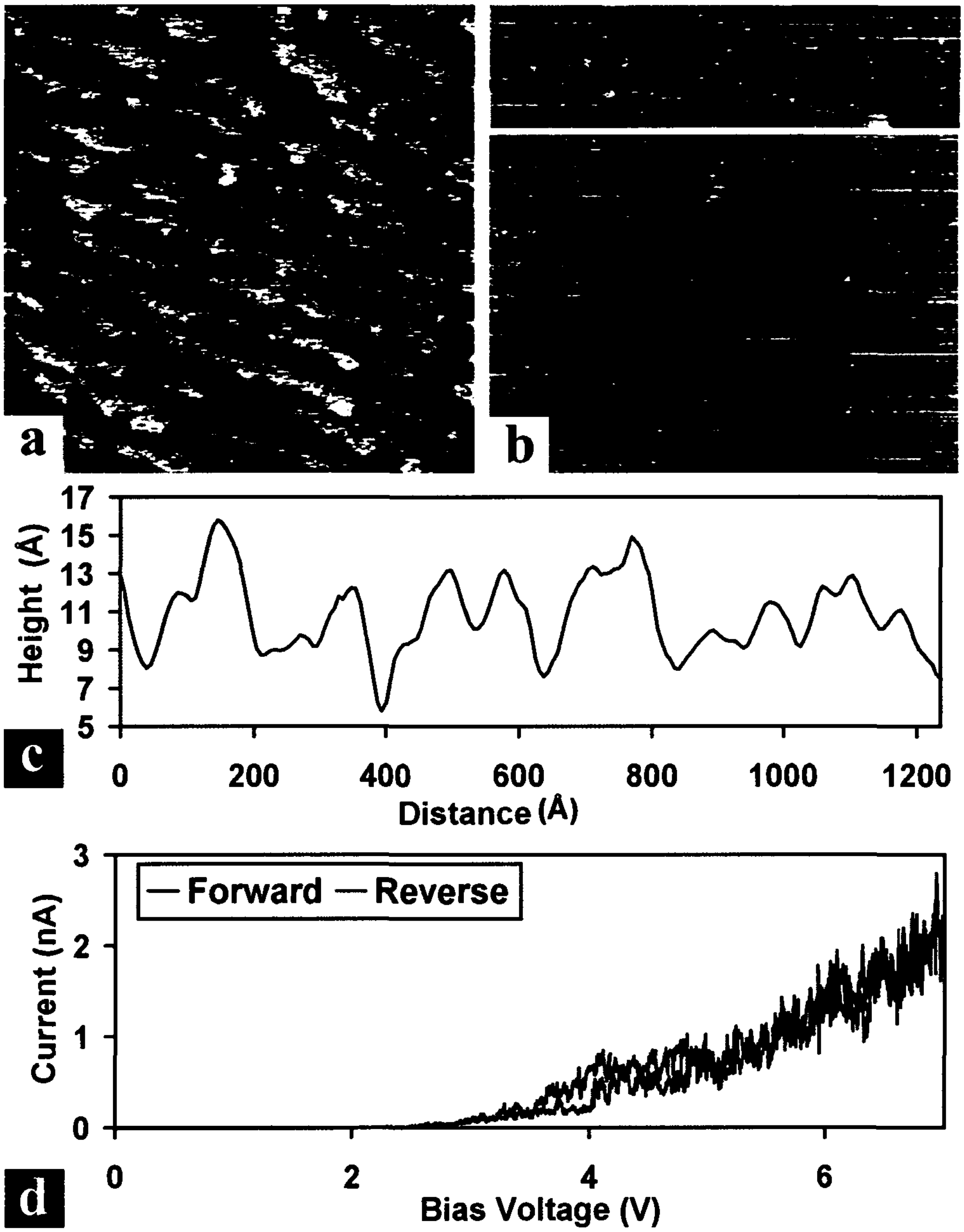

Figure 5-5 *(a) Ambient AF- micrograph (1400^2 nm^2, z_{range}=4 Å,* v=*1.3 l/s) acquired after air annealing to 1000 °C for 5 hours, Type 1 surface is apparent.(b) Scanning tunneling micrograph (278 °C, 3.01 V, 284 pA, 910 nm width, z_{range}=8 Å, v=2 l/s) exhibiting only a vague outline of steps and texture resulting from sputter damage. The inset at top (278 °C, 6.26 V, 145 pA, 340 nm width, z_{range}=20 Å,* v=*2 l/s) shows higher resolution micrograph with contours resulting from ion sputtering more clearly visible.(c) Representative line scan from the inset of (b), peak to valley spacing may be as large as 1 nm, though is more commonly 5 Å- 6 Å. (d) I/V curve (3 V, 220 pA) demonstrating the low bias voltage at which tunneling occurs due to the large number of oxygen vacancies produced during Ar+ sputtering.*

sample was subjected to ten times smaller fluences (~9 x 10^{16} ions/cm^2) at smaller kinetic energies (0.6 keV). A broadening in the Zr 3d doublets in combination with oxygen depletion is observed, however little or no Zr^0 or Zr^{1+} is seen.

Though sputter damage does occur, the main defects are in the form of Zr^{3+} or Zr^{2+} resulting in a broadening in the Zr 3d envelope. The large concentration of defects can be viewed by the I/V curve in Figure 5-5d, which shows a relatively high tunneling current for a small bias voltage. In fact, imaging was performed in Figure 5-5b at a bias voltage of 3.0 V at a set point of 284 pA. This indicates that a large number of empty electronic states have been produced at the surface providing a better overlap of filled states in the tip. This is in comparison to a more fully oxidized surface as discussed in the following section, in which a bias voltage greater than 10 V would be required to produce the same tunneling current.

The Figure 5-5b presents a scanning tunneling micrograph of the post sputter surface; only vague outline of the steps may be distinguished, and the surface has become flat and homogeneous. The inset of 5-5b shows higher resolution of the surface in which local corrugation of 6 Å to 8 Å is present. Due to the complete absence of carbon, these are considered to be true surface YSZ features, the corrugation may result from sputter induced roughening, or reconstruction derived from the addition of oxygen vacancies.

5.2.2. *Annealing in O_2*

Previously Ar$^+$ sputtering was shown to preferentially remove oxygen and possibly zirconium at 600 eV over time. The terrace structure characteristic of a YSZ(100) surface at thermodynamic equilibrium was largely removed. As determined from Chapter 3, in order to recover both proper stoichiometry, and step and terrace structure, annealing to temperatures of 1000 °C in back pressures of O_2 should be performed. In figures 5-6b, 5-7a and 5-7b scanning tunneling micrographs of a YSZ(100) single crystal are shown, which had previously undergone Ar^+ sputter for 40 minutes at 600 eV, followed by thermal oxidation in the preparation chamber to 1000 °C for two cycles of 45 minutes each in O_2 back pressures of 2.5×10^{-5} mbar.

As can be seen from Figure 5-6b, the step and terrace structure is reacquired after annealing for the given length of time. Though not atomically flat the terraces show corrugation of approximately 2 Å peak to valley (Figure 5-6c), which is significantly diminished in comparison to the post-sputtered corrugation of about 6 Å (Figure 5-5c). Tip induced reconstruction of the surface is apparent and particles up to 2 nm in height are formed (Figure 5-6c). The highly oxidized surface contains a much lower concentration of defect states with the I/V spectrum presented in Figure 5-6d, showing much lower tunneling current for a given bias voltage. In order to produce a sufficiently large tunneling current for a feedback signal, the bias voltage had to be held above 7 V; below this value noise at the junction would destabilize the imaging. This is in large contrast to the post sputter STM imaging parameters discussed previously in which 284 pA of tunneling current was obtained at 3 V. In order to image under lower voltages the temperature of the sample can be raised.

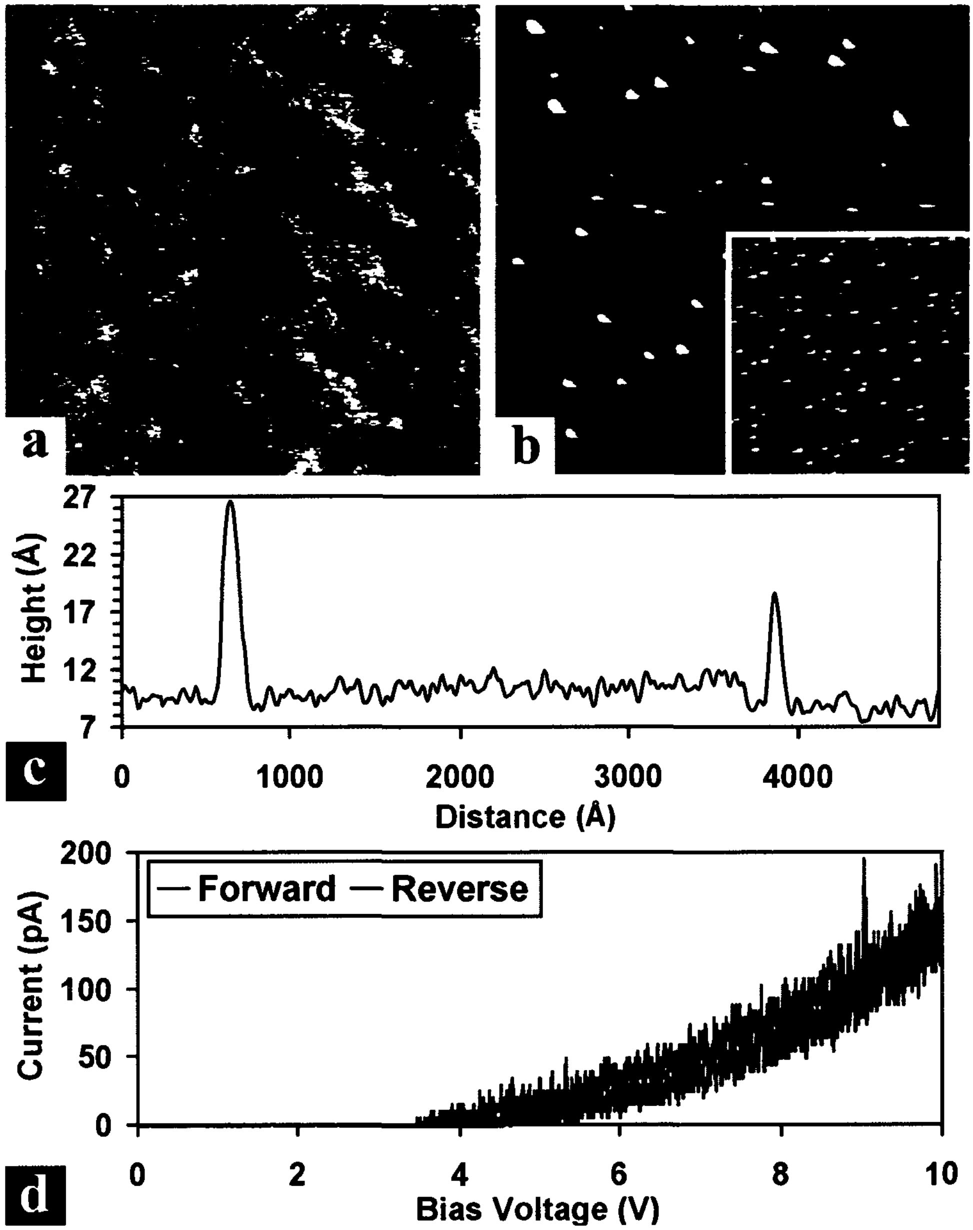

Figure 5-6 *(a) Ambient AF-micrograph (1000^2 nm^2, $z_{range}=5$ Å, v=1 l/s). (b) ST-micrograph (275 °C, 7.87 V, 75 pA, 450^2 nm^2, $z_{range}=9$ Å, v=2.5 l/s), inset (275 °C, 7.87 V, 88 pA, 650^2 nm^2, $z_{range}=9$ Å, v=2.5 l/s).(c) Line scan across (b) showing terrace corrugation of ~2 Å and large tip induced reconstructed particles.(d) I/V spectrum (9.75 V, 108 pA) showing a large decrease in current for the same bias voltage as compared to the sputtered sample observed in Figure 5-5.*

Imaging various spots on the same sample show its topography not to be entirely homogeneous. One out of five imaging positions on this particular sample demonstrates features like those in Figure 5-7a and 5-7b. Interestingly at these locations tip induced

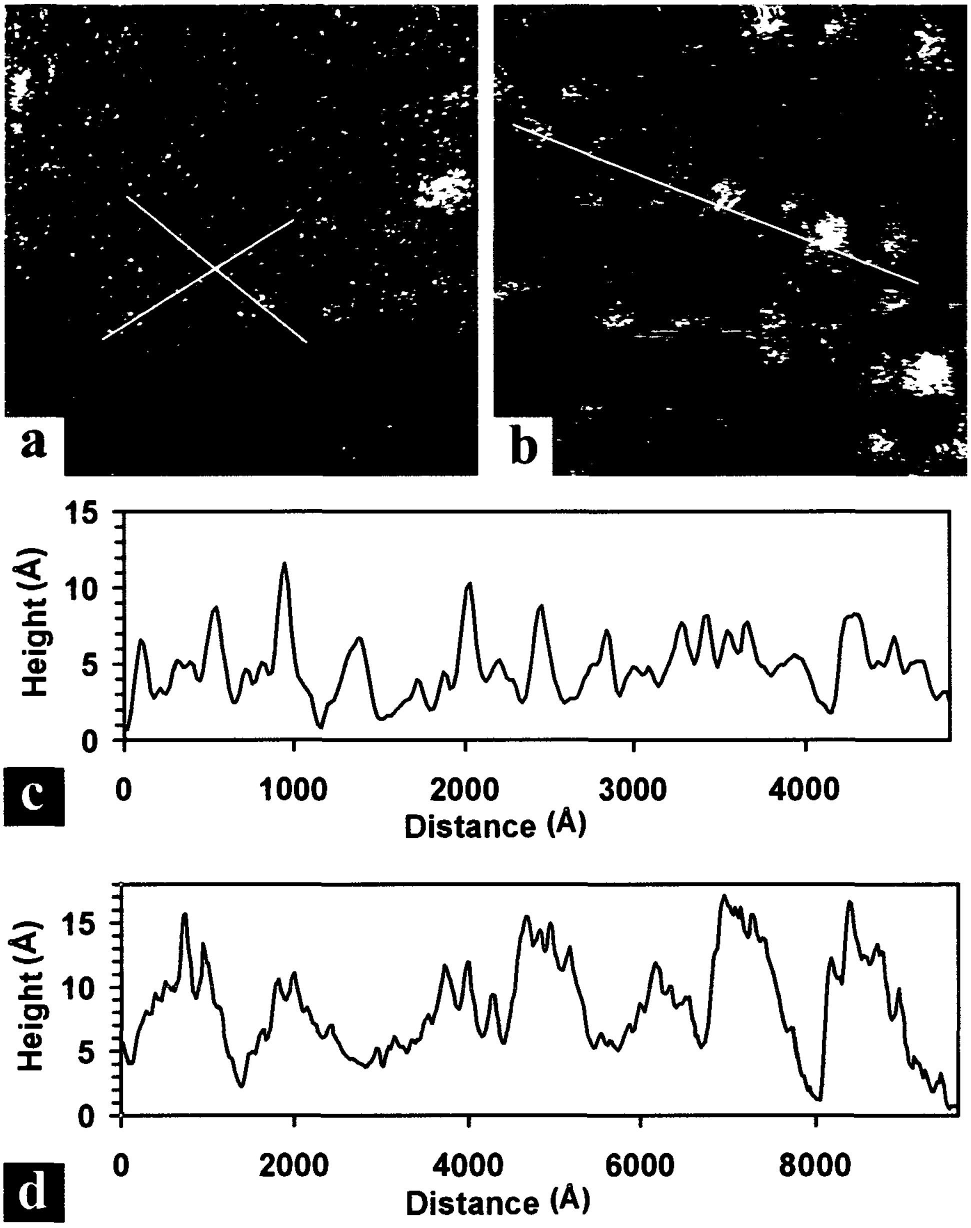

Figure 5-7 *New position on sample from Figure 5-6, (a) ST-micrograph (275 °C, 8.19 V, 62 pA,* 1^2 um^2, $z_{range}=25$ Å, v=2.5 *l/s) (b) ST-micrograph (275 °C, 8.28 V, 57 pA,* 1^2 um^2, $z_{range}=20$ Å, v=2.5 *l/s). Each image demonstrates the presence of large somewhat periodic superstructures. (c) Lines scan across (a) demonstrating height of particle growth. (d) Line scan across (b) showing contour of underlying superstructure as well as overlying particle heights.*

reconstruction is not apparent. The surface roughening and particle formation characteristic of this topography stabilizes the surface against tip induced effects, the particles formed may be up to approximately 1 nm in height (Figure 5-7c). The underlying basis for this reconstruction and subsequent stability is believed to be the presence of oxygen vacancies which have not had the opportunity to oxidize. Again lattice changes resulting from the presence of defects in combination with temperature induced mobility allow particle formation to occur. The reconstruction stabilized the surface preventing further changes resulting from the tip proximity and the corresponding electric field. The bottom third of Figure 5-7a shows what is attributed to a transition from the reconstructed zone to the terrace and step structure seen in 5-6b, in this region tip induced reconstruction does not occur.

Underlying the roughening and particle formation seen in the top two thirds of Figure 5-7a is a broader, seemingly periodic superstructure. Here contours are visible and they appear to run diagonally across the image along two oblique directions as indicated by the white lines. Super structures of this type are common in such materials as highly ordered pyrolytic graphite (HOPG), [29-35] the origin is usually considered to be a lattice size or angle mismatch between adjacent atomic layers. The largest lattice constant of the "super-lattices" seen for HOPG is about 9.1 nm [29]. The approximate periodicity on the present YSZ(100) sample in Figure 5-7a is approximately 100 nm, with a corrugation of up to 10 nm (Figure 5-7d). The formation of the patterns therefore extends many atomic layers into the surface. On HOPG these super-lattices are considered to be spurious, though the application of different surface preparations (NaOH, or electrochemical pretreatment)[29, 31] may enhance the probability of occurrence. The consequence of each of these treatments is the introduction of surface defects, the underlying origin believed to be in action in the case of YSZ.

In Figure 5-7b, these periodic structures are present. In this case higher layers of superstructures grow on top of others, with larger clusters growing in what is possibly bridge or top sites on the underlying super-lattice. Figure 5-7d shows a line scan from Figure 5-7b, in which the larger superstructures are measured showing spacing of about 100 nm or 200 nm, with heights of up to 15 Å.

Though the surface has been annealed in oxygen, it is clearly not entirely oxidized homogeneously, with surface reconstruction occurring in what are considered to be regions of higher defect concentration, likely in the form of oxygen vacancies. This sample had undergone thermal oxidation to 1000 °C for two cycles of 45 minutes each. XPS measurement after each of these cycles showed their stoichiometries were similar (Table 5-4). It is possible that at the partial pressures used (2.5 x 10^{-5} mbar), complete oxidation at the surface is not possible and there will always be some amount of dewetting of the surface layer. Samples which were supposedly fully oxidized, as seen in Figure 5-6b, showed two Angstrom corrugation along the terraces, and atomically flat regions were not observed. Moreover it seems that the more highly oxidized or flatter regions are more prone to tip induced surface reconstruction, likely through reduction.

Table 5-4 *Elemental atomic concentrations as determined from quantification of XP-spectra (90° takeoff) acquired after the given process.*

Process	O 1s (Atom %)	C 1s (Atom %)	Zr 3d (Atom %)	Y3d (Atom %)
Initial	49.6 ± 0.7	19.2 ± 0.9	23.5 ± 0.3	7.7 ± 0.2
Sputter/O_2 Anneal	62.7 ± 0.3	1.5 <	28.3 ± 0.3	9.0 ± 0.2
24 Hrs in Vac.	63.4 ± 0.4	1.5 <	28.2 ± 0.3	8.5 ± 0.2
O_2 Anneal	62.9 ± 0.3	1.5 <	28.1 ± 0.3	9.0 ± 0.2
Post Imaging	63.5 ± 0.4	1.5 <	27.8 ± 0.4	8.7 ± 0.2

Chemical compositions after several of the processes undertaken in the present experiment are summarized in Table 5-4 . It seems that when the sample is heated to

300 °C in vacuum for imaging, or when the sample is left in vacuum for prolonged periods, some changes may occur. However the changes are extremely small if not insignificant, moreover the chemical compositions may be re-equilibrated by annealing in oxygen.

5.3. Interaction of YSZ(100) with surface carbon

Surface carbon on YSZ, which has received little attention in the literature, has been found to be a major source of irreproducibility between samples. In some circumstances surface carbon will desorb from the surface at temperatures between 23 °C and 300 °C, in other samples more complicated reactions will occur. In this section these reaction are studied and a hypothesis is proposed as to why some samples exhibit these more complicated reactions and others do not.

5.3.1. Carbon and temperature

Yttria stabilized zirconia (100) was heated at a ramp rate of approximately 1 °C/s up to a predetermined temperature. It was then held for 5 minutes before being cooled to approximately 225 °C for XP-spectra acquisition. These steps were repeated for a series of temperatures from 325 °C to 725 °C at 100 °C increments.

X-ray photoelectron spectra of the carbon 1s envelope for adventitious carbon taken over the first three measurements (225 °C, 325 °C, 425 °C) are viewed in Figure 5-8. The binding energies have been referenced to the Zr $3d_{5/2}$ transition by adjusting the scale so that it lies at 182.6 eV. The Y $3p_{3/2}$ transition, whose position remains constant at elevated temperatures, is included in Figure 5-8 for illustration of the carbon shift. Heating of the YSZ sample over this range results in a (1.1 ± 0.1) eV down shift in the carbon 1s binding energy, from (284.9 ± 0.2) eV at room temperature to (283.8 ± 0.2) eV after heating to 325 °C and 425 °C for 5 minutes each.

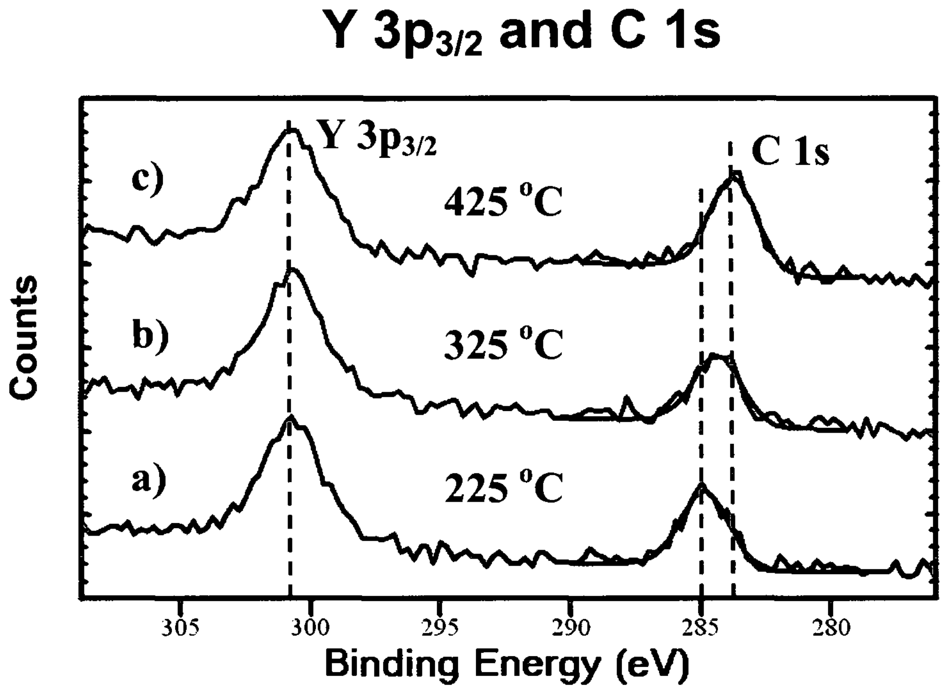

Figure 5-8 *X-ray photoemission results taken at 225 °C for YSZ (100) Y* $3p_{3/2}$ *(left-hand peak) and C 1s envelopes. (a) Sample spectra at 225 °C, (b) After heating to 325 °C for 5 minutes, and (c) sample after heating to 425 °C for 5 minutes. C 1s peak shows a stepwise shift, initially 0.4 eV (a-b) then 0.7 eV (b-c), to a total of 1.1 eV (a-c) toward lower binding energy. The shift is due to a simultaneous decrease in adsorbed carbon and segregation of carbon from near surface regions.*

Upon heating to 325 °C the carbon peak lies shifted partially by approximately 0.4 eV. This shift occurs coincident with an apparent decrease in the overall carbon concentration, a decrease consistently seen for other samples (Section 5.1.4 for example). This loss corresponds to desorption of hydrocarbons which are normally found at binding energies above 284.8 eV. The maximum of the convoluted carbon envelope will therefore appear to shift downwards as a result of the decrease in this high binding energy component. At 425 °C, the carbon peak has shifted by 1.1 eV, and there is a significant increase in the overall carbon concentration.

In Figure 5-9a the atomic concentrations of each element, as determined by XPS quantification, is plotted as function of annealing temperature. Carbon concentration is shown to reach an equilibrium value after 525 °C (for 5 minutes); the speed with which this equilibrium occurs makes segregation from the bulk unlikely. Instead, the increase may be a result of carbon from deeper near-surface regions diffusing toward the vacuum interface where the probability of inelastic scattering is much lower. Adsorption of carbon from the vapour phase due to local degassing of the sample holder may also result in an increase in carbon signal, although this seems unlikely since at 325 °C adventitious carbon tends to be removed from the surface rather than adsorbed. In either case the carbon is viewed in a chemically bound state corresponding to a 1.1 eV shift from the room temperature value and a 1 eV shift from free (graphitic) carbon (C-H). This shift may correspond to a carbon atom coordinating with a defect such as an F+ centre (singly ionized oxygen vacancy) or bonding to a partially reduced zirconia molecule (Zr^{3+}), or possibly even conversion to amorphous carbon.

Above 425 °C the carbon concentration continues to increase before stabilizing between 525 °C and 625 °C. The increase arrives with a simultaneous decrease in oxygen concentration, both concentration changes are equivalent in magnitude at approximately 4%. As heating cycles are continued to temperatures above 525 °C reduction of zirconia becomes apparent, not only through XPS, but the sample visually darkens. Figure 5-10 shows the progression of the Zr 3d, C 1s photoemission envelopes after heating cycles to 425 °C, 525 °C, 625 °C, and 725 °C. It can be seen that as the temperature is increased, the Zr transition begins to gain a shoulder shifted 3.8 eV ± 0.1 eV to lower binding energies. At these higher temperatures the Zr^{4+} peak at 182.6 eV is converted to a species of lower binding energy at approximately 178.8 eV. A simultaneous increase of a 2.7 eV ± 0.2 eV downshifted C 1s peak at 281.5 eV ± 0.2 eV corresponding to an RSF corrected area ratio of approximately 1:1 confirms the reduction of ZrO_2 to ZrC.[36-39]

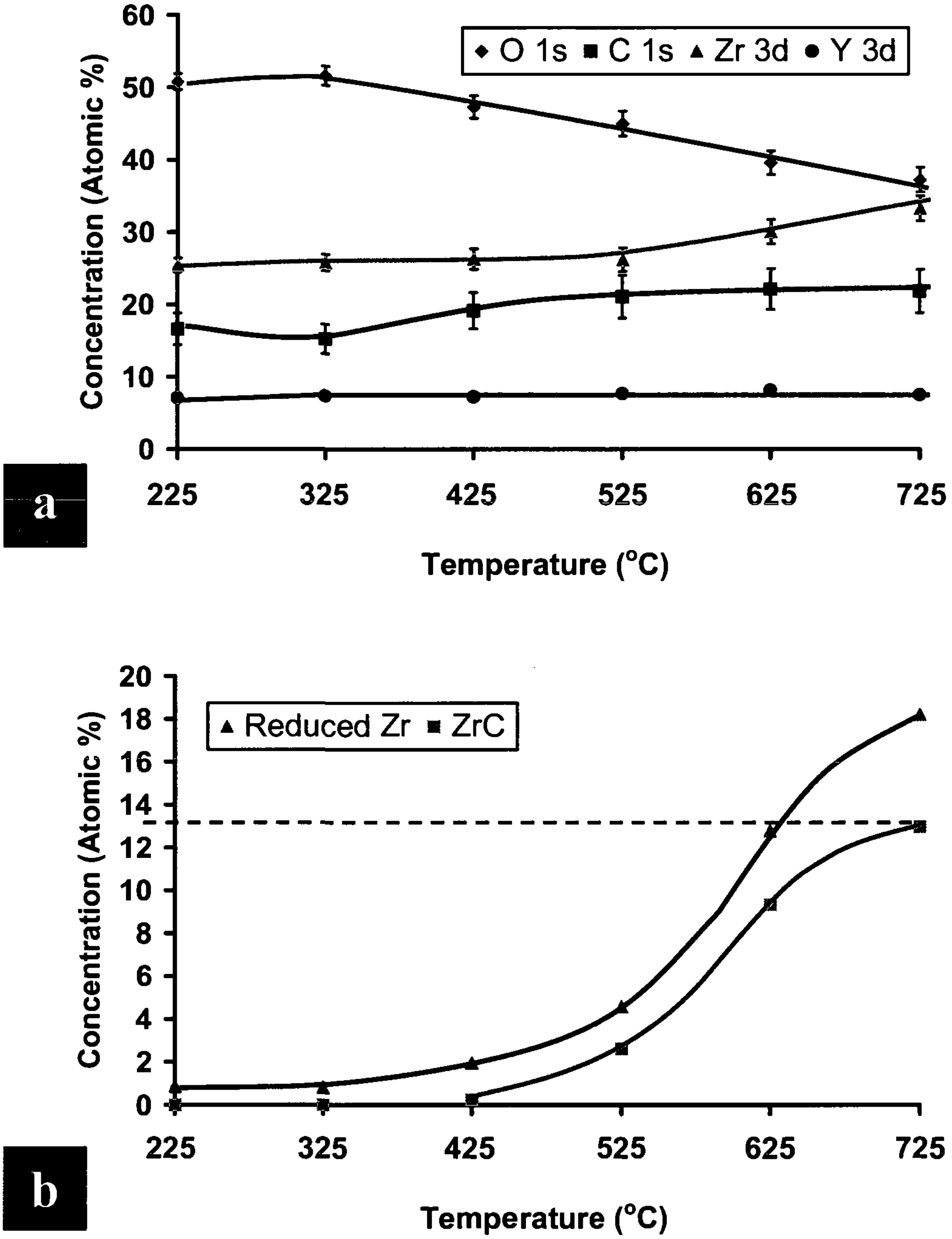

Figure 5-9 *(a) Quantification results of X-ray photoemission spectra show the total atomic concentrations of elements O, C, Zr and Y. (b) X-ray photoemission derived concentrations of the total reduced Zr components including carbide and sub-oxides, as well as the zirconium carbide concentration alone. The dotted line indicates the estimated limiting carbide coverage.*

In Figure 5-9b the concentration of the reduced Zr 3d and ZrC components determined from peak fitting of the Zr 3d envelope are plotted versus annealing temperature. Between 225 °C and 425 °C no zirconium carbide formation occurs within the allotted time (~10 minutes), though zirconia sub-oxides may exist in the form of Zr_2O_3 or ZrO corresponding to Zr^{3+} and Zr^{2+} oxidation states respectively. These components exist in concentrations totaling less than two percent.

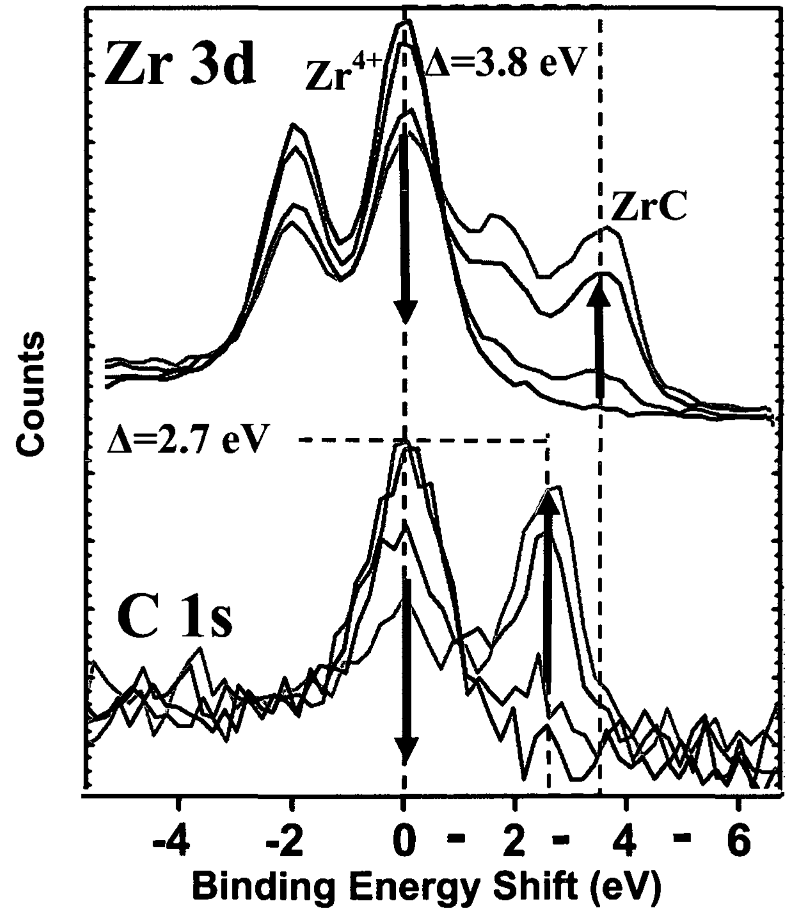

Figure 5-10 *Carbon 1s and zirconium 3d photoemission envelopes acquired after heating to successively higher temperatures (425 °C, 525 °C, 625 °C, and 725 °C) for five minutes each. Carbide formation indicated by the down shifted binding energy peaks on the right side of both the Zr 3d and Z 1s transitions, rises with each increasing temperature Black arrows indicate intensity change of peak with increasing temperature.*

Small amounts of carbide begin to form by 525 °C and the rate of formation increases with temperature up to 725 °C, after which, the rate of formation slows. Under conditions in which the reaction may produce unlimited product, it would be expected that the carbide concentration would invariably increase with temperature in the presence of excess carbon. The slowing of the reaction may indicate the formation of a terminating surface carbide layer.

The mechanism through which zirconium carbide formation proceeds becomes more apparent in viewing the C 1s envelope of Figure 5-10. It can be seen that as the carbide intensity increases at lower binding energy, it does so at the expense of the higher binding energy species. Since the total overall concentration of carbon remains constant, as seen in Figure 5-9a, a one to one transformation of carbon to carbide is concluded. At 725 °C when the rate of carbide formation begins to plateau (Figure 5-10a) the surface concentration of carbide is approximately 12.7 ± 0.5 %, while the total carbon concentration is (21 ± 3) %.

Measurement of the growth of carbide in time (at 400 °C) on a different sample (Figure 5-11) shows that even in the presence of a higher concentration of surface carbon ((27 ± 2) %), carbide formation ceases again at approximately 13 %. From Le Chatelier's principle and the temperature dependence of the equilibrium constant, one would expect the equilibrium concentration of carbide in this case to be different. This is not so, and therefore it is plausible that a complete and stable carbide layer forms at the interface between YSZ and surface carbon preventing further reduction.

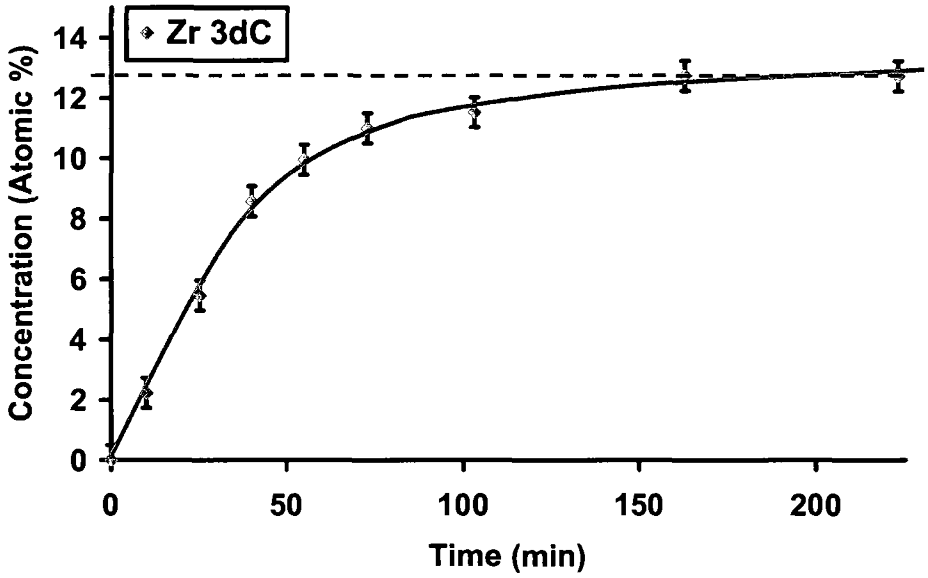

Figure 5-11 *Plot of the surface atomic concentrations of zirconium carbide as a function of vacuum anneal time. The surface concentration equilibrates at approximately 13 %,,similar to the value seen in Figure 5-9b, indicating a terminating carbide layer forms preventing further reduction.*

As shown in Figure 5-12a, the overall concentration of oxygen begins to decrease steadily above 325 °C, from a molar concentration of (51.6 ± 1.1) % to (37.2 % ± 1.6) % at 725 °C. The decrease in oxygen concentration arrives with a broadening of the full width at half maximum and 0.3 eV downward shift in the O1s signal. The changes in the oxygen electronic environment are better resolved in the O KLL (Figure 5-12) Auger peak in which a downshifted shoulder is seen at 525 °C. The origin of the shifted intensities are difficult to determine absolutely, however the existence of oxidation states in the Zr 3d envelope intermediate between Zr^{4+} and ZrC would support their assignment to suboxides.

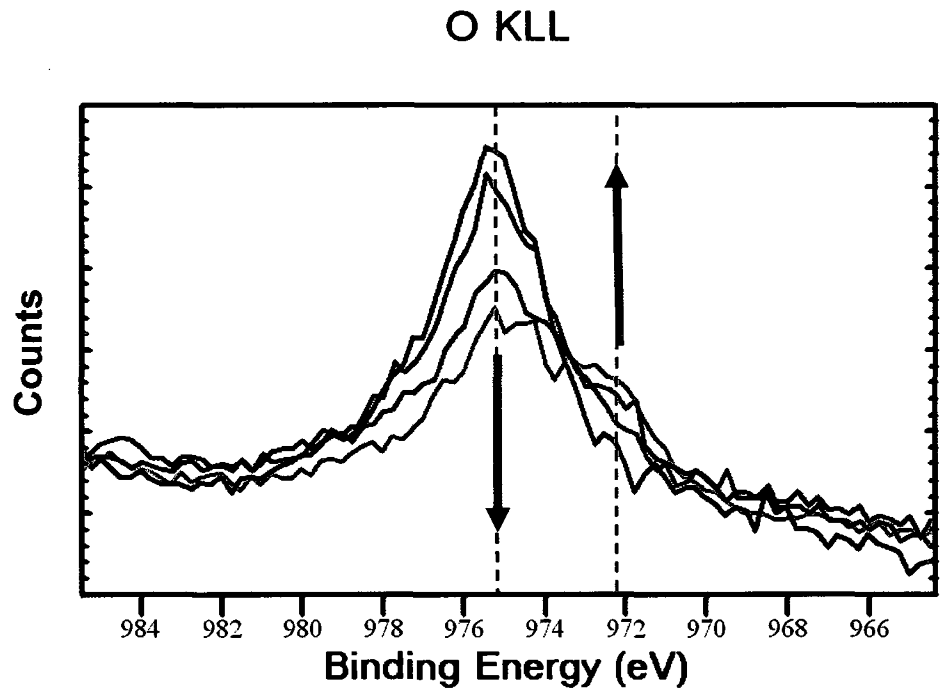

Figure 5-12 *O KLL Auger transition of the XPS spectrum acquired after heating at 425 °C, 525 °C, 625 °C, and 725 °C for five minutes at each temperature. The central component of the peak decreases with each temperature rise and an increasingly large shoulder is formed. Black arrows indicate intensity change of peak with increasing temperature.*

In Figure 5-9a after 525 °C as the oxygen content decreases the zirconium concentration increases, this may be a result of back diffusion of oxygen which forces zirconium closer to the surface. If this were merely a result of oxygen being removed from the surface an increase in all species should be seen, as their relative proportions would increase. Zirconium is preferentially increasing and so diffusion to surface regions must be occurring. This was also observed by Song *et al.* during the oxidation of a Ni/Zr alloy which contained a high level of impurity carbon.[36] In this paper the authors proposed two reaction pathways for zirconium carbide formation:

$$(x + 1)C + ZrO_2 \rightarrow ZrC + xCO \qquad \text{Equation 5-1}$$

$$C + ZrO_x \rightarrow ZrC + xO \quad (0 < x \leq 2) \qquad \text{Equation 5-2}$$

If the reaction given in equation 5-1 were responsible for the formation of carbide then as the reaction proceeded, either the overall carbon concentration would decrease due to the evolution of CO into the vacuum, or a large adsorbed CO peak should become apparent at binding energies at or near 286 eV.[23] Neither of these effects are observed, and as a result the second reaction given in equation 5-2 is preferred. The O released in this reaction would be available to diffuse into the bulk, causing the observed enrichment of zirconium.[36]

5.3.2. Carbon and oxygen partial pressure

A YSZ(100) sample which had been previously annealed in air for 2 hours to 1300 °C, was heated in vacuum to form a carbide. The carbon induced reduction of ZrO_2 was not permitted to form a terminating layer so that the effect of O_2 partial pressure on the reaction could be investigated. It is known from studies of as-received and air annealed YSZ(100) samples, that reduced carbon species are possible under ambient conditions, however peaks associated with fully reduced ZrC have not been observed. Carbide formation should therefore be dependent upon the partial pressure of O_2.

Figure 5-13 presents the x-ray photoelectron spectrum of the C 1s envelop after annealing in air and after vacuum annealing to 350°C for 30 minutes. Though not conclusive, our assignment of the component carbon peaks both before and after vacuum annealing are indicated. In can be seen that the air annealed sample contains peaks associated with C-O and C-H/C-C, bonds at 285.7 eV and 284.8 eV respectively. A component peak at 283.7 eV corresponding to the downshifted carbon species observed previously (Section 5.3.1), is attributed to carbon coordinating with an oxygen vacancy, perhaps a singly ionized vacancy (F^+), or possibly dissolved carbon located at interstitial sites within the lattice. A fourth peak located at approximately 282.4 eV is assigned to a reduced yet non-stoichiometric species (Zr_xC, $x>1$) or a C-Zr-O surface state reported elsewhere. [37, 40]

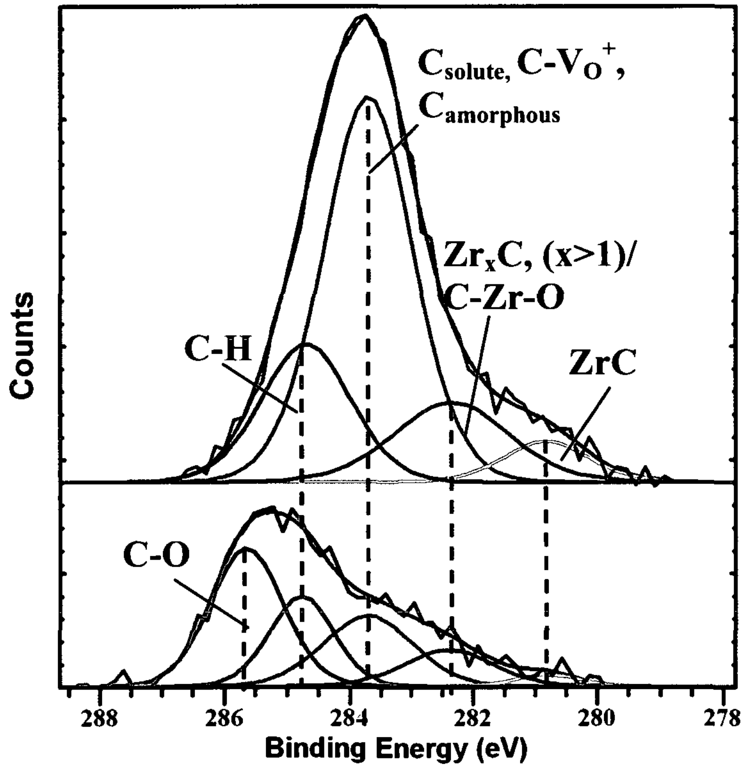

Figure 5-13 *High resolution photoemission C 1s envelope (10 eV pass, 0.1 eV step, and 4 s dwell, background subtracted) before (bottom) and after vacuum anneal to 350 °C. Peak fitting has been performed and component peaks can be observed to change, with the C-O component completely removed or reduced to C-C/C-H, all other components increase in intensity and ZrC is formed.*

As previously observed, the hydrocarbons evolve at elevated temperatures between 225 °C and 325 °C, this results in the loss of the high binding energy peak associated with the O-C bond in the post vacuum anneal spectrum. All other component peaks increase significantly resulting in an overall carbon concentration rise from (10.4 ± 1.7% to

17.5% ± 1.5 %). The largest contribution to this increase is associated with dissolved or vacancy coordinated carbon, however reduced carbon both in the form of ZrC (280.8 eV) and non-stoichiometric or C-Zr-O rise significantly. The atomic concentration of ZrC is found to be (1.2 ± 0.2) %.

Imaging of the carbide containing surface was performed by STM and the results are presented in Figure 5-14. Image 5-14a shows the surface to be covered in elongated pits with some pits nested within others. Their cumulative depths may be as high as 5 nm, with most being on the order of 2.5 nm to 3 nm (Figure 5-14c). These are higher than steps heights previously observed by AFM for samples annealed to 1300 °C (Chapter 3), though the pitting makes this sample distinct from those stepped and terraced surfaces. The feature which sets this sample apart from all other oxidized samples studied is the form of the I/V spectrum, which is similar to those which would be acquired for a conductor. Though the tunneling current is small between -1 V and 1 V, no obvious band gap is present, moreover the current is symmetric about 0 V (Fermi level) with significant tunneling achieved at negative voltage values. This is vastly different than I/V curves seen for oxidized, or even Ar^+ sputtered samples. Carbide formation, though only accounting for 1 % of surface species, produces significant change in the electronic surface structure transforming the insulator into a conductor.

Following STM measurement of the surface presented in Figure 5-14, the same sample was transferred to the Specs chamber for examination by x-ray photoelectron spectroscopy. In this experiment the sample was held at 400 °C in back pressure of O_2, while simultaneously collecting XP-spectra. Consecutive scans were performed producing one spectrum approximately every 7 minutes, and after every second scan the partial pressure of O_2 was increased. The time interval, and thus the time required to acquire one spectrum, was

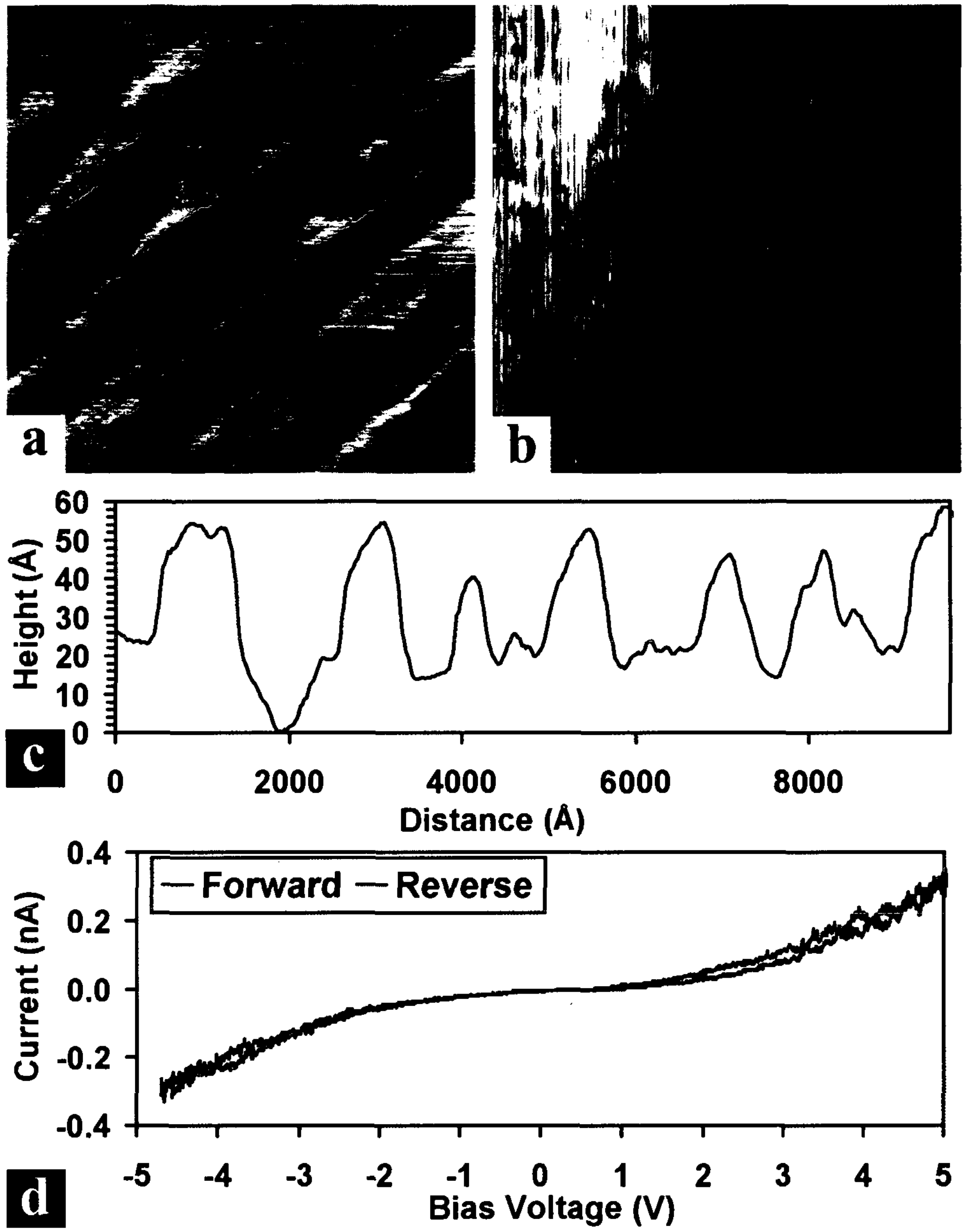

Figure 5-14 *(a) ST-micrograph (288 °C, 5.11V, 452 pA,* 1^2 *um*^{2}*,* z_{range}*=55 Å, v=3 l/s) (b) ST-micrograph (288 °C, 5.11 V, 487 pA,* 60^2 *nm*^{2}*,* z_{range}*=25 Å, v=3 l/s). (c) Lines scan across (a) demonstrating depth of pits. (d) I/V spectrum (5.11 V, 408 pA) in which the band gap has disappeared indicating that the formation of carbide has been sufficient to cause the surface to become conductive.*

selected as a balance between time resolution and spectra quality. The temperature was selected to provide appropriate reaction kinetics for the time scale. As a result changes in carbide formation could be observed within the time required to perform one or two spectra. Specifically changes in the O 1s, C 1s , Zr 3d and Y 3d envelopes were monitored in time.

Below O_2 partial pressure of 1.0 x 10^{-5} mbar the carbide formation continues above the initial ~2 atom%, the spectra given in figures 5-15 a and b show the Zr 3d and C 1s envelope during the carbide formation. Again the reaction proceeds through the peak found at 283.7 eV, attributed to dissolved or vacancy coordinated carbon, this species seems to act as an intermediate state between free carbon and carbide.

At approximately 1 x 10^{-5} mbar the formation of carbide slows and very little change is seen over two scans; by raising the pressure to 2.5 x 10^{-5} mbar the formation of carbide reverses. Figures 5-15 c and d show this reversal with spectrum (c) and (d) being respectively, the third and sixth spectra acquired after raising the oxygen pressure to 2.5 x 10^{-5} mbar. This corresponds to 21 minutes between the starts of each acquisition. In the C 1s envelope of spectrum (d) the carbide is not removed directly, it instead reverts back to the component at 283.7 eV. The free carbon contribution seen as a left side shoulder in (c), is apparently oxidized and removed, likely through the formation and evolution of CO or CO_2 . The remaining carbon is a single sharp peak correlated solely to the species at 283.7 eV.

This carbon species is extremely stable and does not decrease significantly over several more scan cycles at this temperature and pressure. Only by elevating the temperature while maintaining the high oxygen partial pressure can this carbon species be removed at a reasonable rate. This was in fact performed and the elemental concentrations are plotted as a function of time in Figure 5-16.

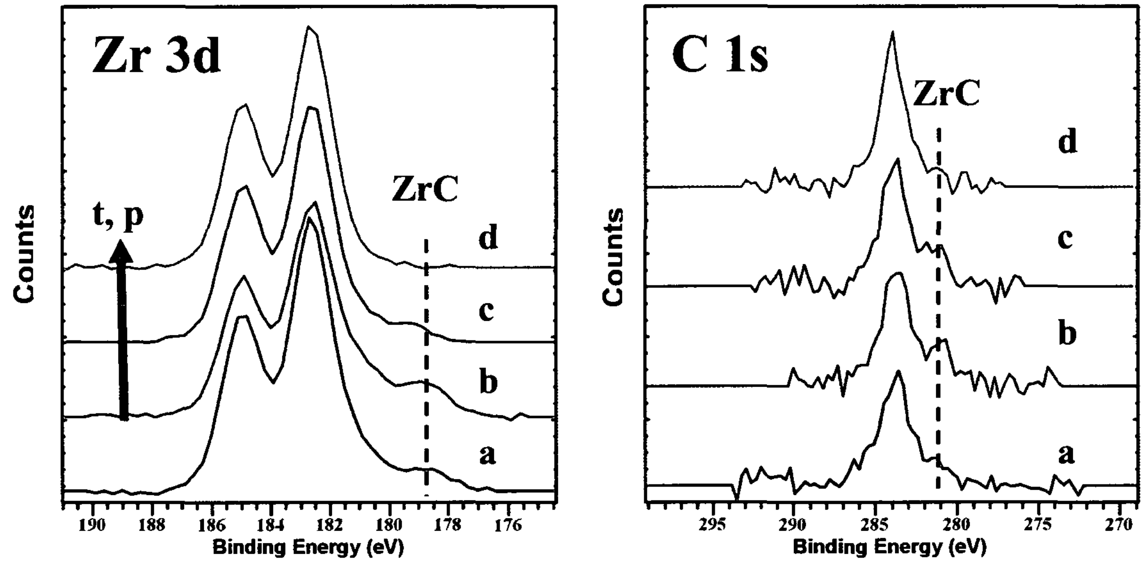

Figure 5-15 *XP-spectra for the Zr 3d and C 1s transitions acquired at increasing partial pressures of* O_2. *(a) and (b) taken at pressures below* 1×10^{-7} *mbar, spectrum (b) taken after (a) shows an increase in carbide formation. (c) and (d) acquired under pressure of* 2.5×10^{-5} *mbar* O_2, *(d) taken after (c) shows a reduction in both the ZrC shoulder on the right and the shoulder associated with C-H/C-C bonds.*

Here the plot begins after the pressure had been elevated to 2.5×10^{-5} mbar, and each point represents the start of an XPS scan. The temperature was raised in several cycles, each to a higher peak value than the last. Above 500 °C the Bremsstrahlung radiation background became too high to acquire accurate spectra (k_bT dependence), and so after each heating cycle above this value the sample was allowed to cool to 400 °C for spectrum acquisition. The temperature corresponding to each scan is plotted on the same chart (secondary axis on right) and is indicated by the dotted line.

Initially at 400 °C the only remaining carbon species is stable or extremely slow to be removed, the first three spectra plotted show little or no decrease in carbon concentration. The next spectrum, acquired after raising the temperature to 500 °C, results in a modest decrease in carbon. With each successive e heating cycle after this, first to 700 °C then

850 °C, the carbon decreases significantly, arriving with a corresponding and approximately equivalent increase in oxygen concentration. After 850 °C, carbon is almost entirely removed and a final cycle to 900 °C produces a carbon free, approximately stoichiometric sample (O: (64.3 ± 0.6) %, Zr: (27.0 ± 0.5) %, Y: (8.7 ± 0.3) %).

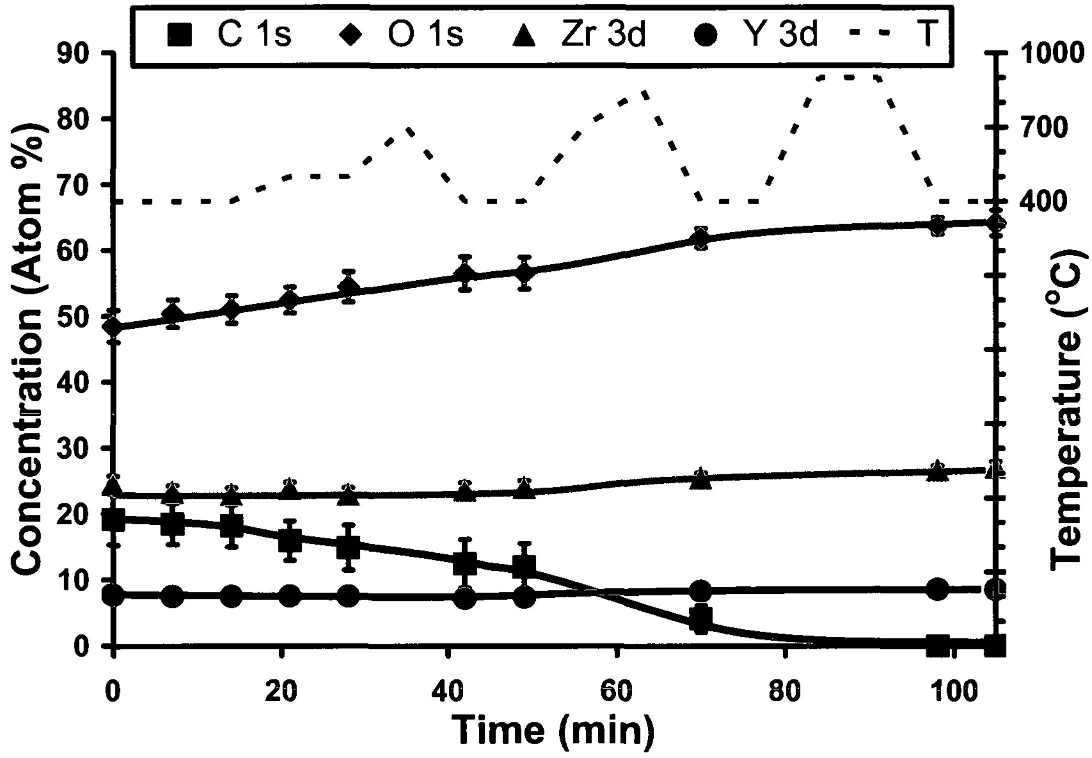

Figure 5-16 *X-ray photoelectron spectroscopy quantification results tracking the relative atomic concentrations of a YSZ(100) sample which was previously reduced in vacuum to form carbide. The elemental concentrations change in time in response to heating in 2.5 x 10^{-5} mbar back pressures of* O_2 according to the *temperature program indicated by the dashed line. Concentrations are plotted on the left axis with the temperature values for the program on the right. At 400 °C and 500 °C the kinetics for oxidation of the carbon and* ZrO_2 *are slow. Heating to 850 °C- 900 °C provides the greatest decrease in carbon*

Broad spectra acquired after the experiment shows that all cation impurities (Ni, Ca, K) as well as silicon have been removed during high temperature annealing in oxygen. Consequently thermal oxidation offers a mechanism through which to clean YSZ(100) without performing ion bombardment.

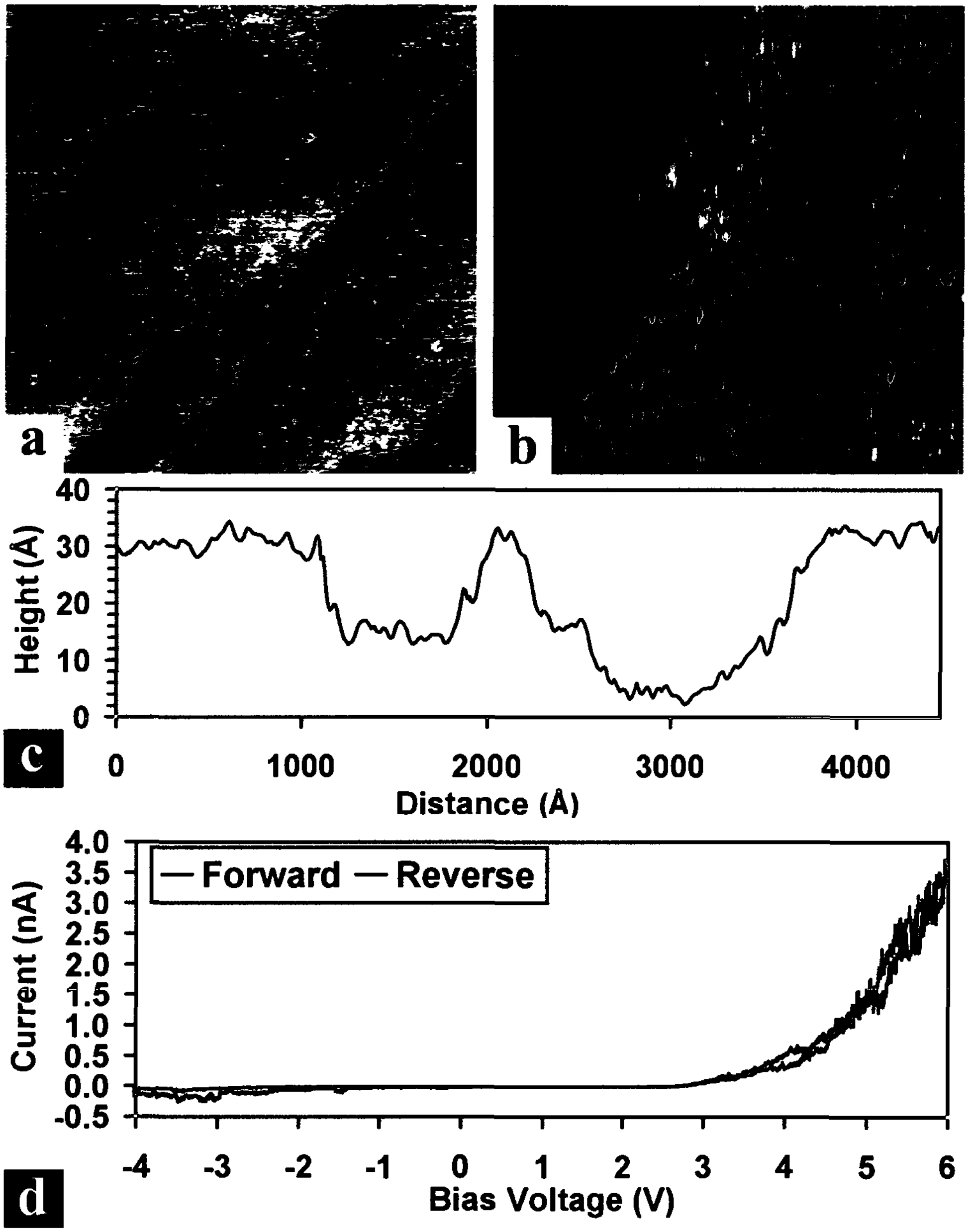

Figure 5-17 *(a) ST-micrograph (288 °C, 5.61 V, 247 pA, 500^2 nm^2, z_{range}=50 Å,* v=*3.5 l/s) (b) ST-micrograph (288 °C, 5.80 V, 390 pA, 160^2 nm^2, z_{range}=50 Å,* v=*3.5 l/s) Imaged after cycles of thermal oxidation up to temperatures as high as 900°C, carbide has been removed and dewet clusters are apparent. (c) line scan over (a) indicating terrace, and pit corrugation as well as their relative heights. (d) I/V spectrum (5.80 V, 390 pA) demonstrating the return to insulator properties with a band gap >7 eV.*

After the final heating cycle to 900 °C in oxygen, STM was performed. The resulting images are shown in Figure 5-17. As in previous images of oxidized samples, the surface is shown to be covered in partially dewet clusters, indicative of a partially reduced surface layer. The I/V spectrum (Figure 5-17d) has returned to the form of an insulator, in this case the band gap is greater than 7 eV, indicating that carbide formation is indeed the origin of the conductor type spectrum seen in Figure 5-14d.

Though normally reported to be in the range of 5.6 eV or less depending on the defect state,[41-43] the YSZ band gap has been argued to be as large as 7 eV to 8 eV by Morinaga *et al* and others. [44-46] The origin if the discrepancy is unknown, but perhaps the presence of surface impurities or defects in some studies offers electronic states within the YSZ bandgap that are probed, resulting in the observed differences.

Table 5-5 *Quantification results of XP-spectra acquired after air annealing to 1300 °C ("Initial"). After annealing in vacuum to 350 °C producing zirconium carbide ("Carbide"), and after thermal oxidation cycles at temperatures up to 900 °C in 2.5 x* 10^{-5} *mbar* O_2 *("Oxide"). Annealed in vacuum to 900 °C for 15 minutes.*

State	Figure	O 1s (Atom %)	C 1s (Atom %)	Zr 3d (Atom %)	Y3d (Atom %)
Initial	5-13	58.0 ± 1.1	10.4 ± 1.7	24.4 ± 0.5	7.6 ± 0.3
Carbide	5-13, 5-14	49.5 ± 1.1	17.5 ± 1.5	25.2 ± 0.6	7.7± 0.3
Oxide	5-17	64.3 ± 0.6	< 1.5	27.0± 0.5	8.7 ± 0..3
Cluster	5-18	62.4 ± 1.0	< 1.5	28.8± 0.5	8.8 ± 0..3

The corrugation of the terraces and pit bottoms in these images (Figure 5-17c) is larger than some of the oxidized samples seen previously, however at approximately 4 Å, it is smaller than the features of Figure 5-7c. If the corrugation is dependent upon the concentration of oxygen vacancies, then additional vacancy formation through reduction should produce further dewetting and hence larger particles should form and corrugation should increase.

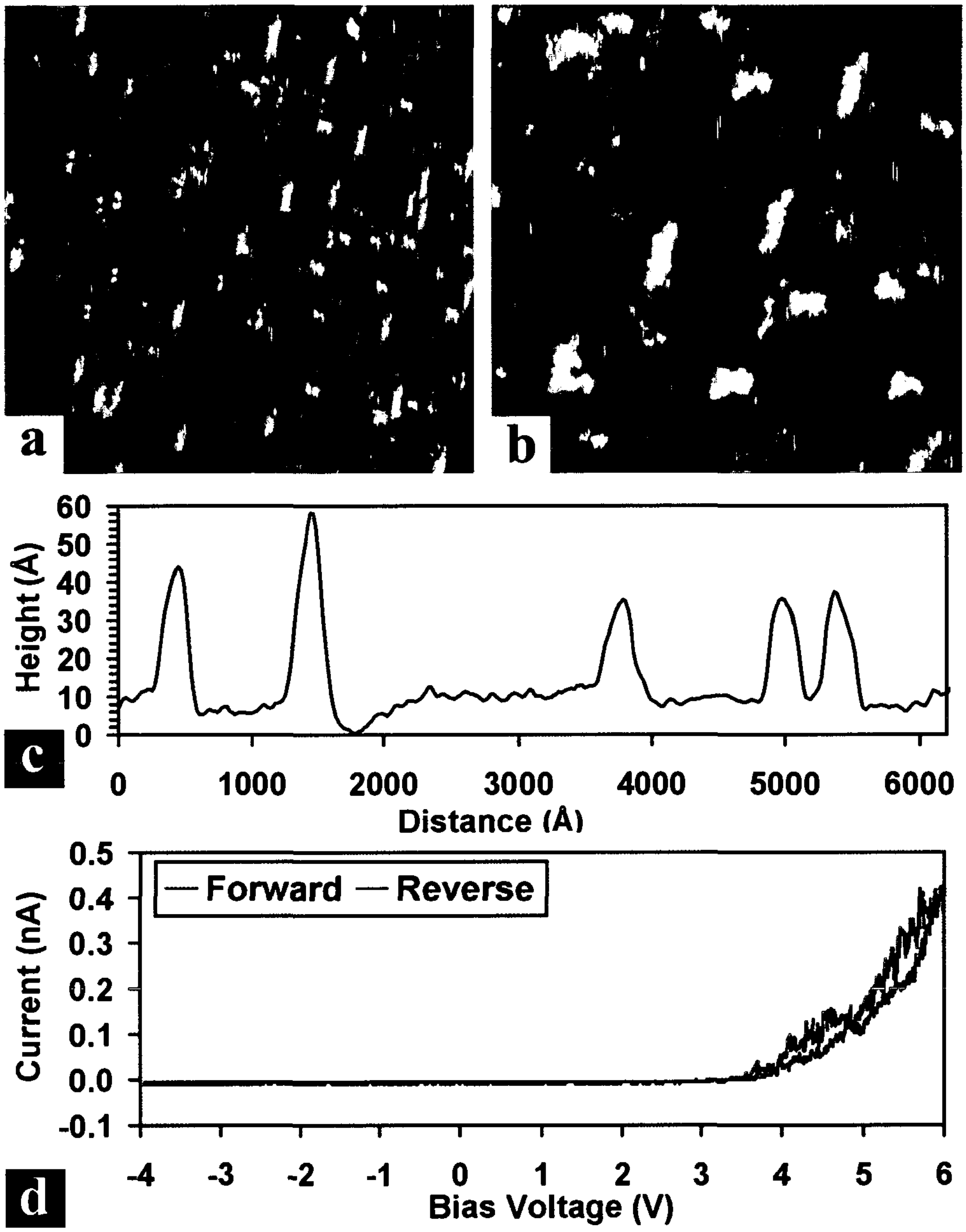

Figure 5-18 *(a) ST-micrograph (288 °C, 6.03 V, 134 pA,* 1^2 *um*^{2}, z_{range}*=50 Å,* v=3.2 *l/s) (b) ST-micrograph (288 °C, 6.03 V, 163 pA,* 160^2 *nm*^{2}, z_{range}*=45 Å,* v=3.2 *l/s) Imaged after high temperature vacuum anneal to 900°C for 15 minutes. Images show large dewet clusters up to 5 nm in height. (c) line scan over (a) indicating terrace corrugation and cluster heights. (d) I/V spectrum (6.03 V, 159 pA) demonstrating that insulator properties are maintained with a band gap >7 eV.*

Since high temperature annealing in vacuum is well known to create vacancies in oxides,[47, 48] the sample observed in image 5-17 was heated to 900 °C for 15 minutes at pressures ~ 2.0 x 10^{-10} mbar. A slight reduction was confirmed by XPS (Table 5-5) corresponding to an oxygen concentration loss of approximately 1.9 %. Figure 5-18 a and b presents the resulting surface topography acquired by STM after reduction. It can be seen clearly that dewetting of the surface does in fact occur, large particles have formed on the surface up to 5 nm in height. Moreover the particles appear to be preferentially aligned along two perpendicular directions, in a manner similar to the line defects observed in Chapter 3. At first glance the orientation of the alignment may seem a result of interaction with the tip during imaging, however adjusting imaging parameters so that the fast scan direction is perpendicular to the aligned features results in the same image. Therefore the preferential alignment represents a true surface property, with this self organization occurring as a result of strain minimization with the underlying less reduced YSZ.

The remaining question as to why certain samples exhibit carbide formation upon heating and others do not cannot be answered conclusively. However as seen in Chapter 3 there is a large variability in surface defect structure, with some samples exhibiting extremely thick defect layers in comparison to others. Since the reaction producing carbide has been concluded to proceed according to equation 5-2, it is very plausible that an intermediate within this reaction is carbon occupation of or coordination with an oxygen vacancy. The initial defect structure of YSZ resulting from the chemical and mechanical polishing by the crystal manufacturer may contain a variable quantity of vacancies or dissolved carbon within the lattice. Some samples will have sufficient quantities of both dissolved carbon and vacancies for the reaction to occur, while in others will not. Though an initial quantity of vacancies may increase the reduction rate, carbon is likely able to reduce even a fully stoichiometric, largely defect free YSZ surface in the presence of sufficient carbon. Often however surface carbon will desorb before having the opportunity to react.

5.4. Conclusion

The surface region of air annealed YSZ(100) single crystals have been shown to contain only a few of the impurities mentioned in the literature, these are Na, Ca, K, Si. While Ca and K are found in only very low concentrations below 1 atom percent, Na and Si exist at higher concentrations up to 2 to 4 percent. Through angle resolved XPS these impurities have been found to be highly localized at the surface though less so than carbon. The carbon envelope is predominantly composed of adsorbed species from ambient conditions which at low temperatures exists as an overlayer of hydrocarbons. At elevated temperatures around 300 °C, hydrocarbons desorb from the surface reducing the overall C content. Raising the temperature further to 400 °C causes diffusion of carbon from near surface regions to the interface, at the same time, oxygen may move to the surface region as well. Moreover at 400 °C the impurities K and Na become lower as they evaporate, while Si remains on the surface and can only be removed at a much high temperature of about 900 °C through thermal oxidation.

Even at low fluences the ion sputtering at 600 eV removes defective surface layers of Type 1 samples quite quickly; after 10 minutes of sputtering the sample is largely free of contaminants though extended periods of sputtering cause oxygen and zirconium to be removed preferentially. At approximately 30 to 40 minutes, a sputter equilibrium appears to be reached in which the elemental concentration distribution stabilizes. This provides a good target value for sputtering since if in fact it is an equilibrium condition then sputtering for extended periods of time should produce a similar chemical composition for all samples (not necessarily so for topography). Post-sputter STM imaging is difficult likely due to sharp changes in local electronic structure, though it has been possible to acquire some images showing high frequency contours on vague steps and terraces. The high level of oxygen vacancies caused by sputtering produces a large density of defect states which increase the tunneling current for a given bias voltage to much higher values than can be obtained for a fully oxidized surface.

After sputtering, thermal annealing in O_2 pressures of 2.5×10^{-5} mbar at 1000 °C causes samples to oxidize. Largely removing the defect states and increasing the bias voltage required for tunneling to occur. Scanning tunneling microscopy shows that thermal oxidation causes the samples to flatten, with some correlation between the extent of oxidation and the surface roughness apparent. Flatter, more highly oxidized samples are more prone to STM tip induced reconstruction, than are less oxidized, more rough samples. The clustering that occurs to a greater extent in only slightly reduced surfaces appears to be more stable and does not appear to reconstruct further through interaction with the tip while scanning. As in Chapter 3, the dewetting is attributed to the concentration of oxygen vacancies at the surface, and while oxidized samples may be flatter they are not atomically flat even after 90 minutes of thermal oxidation. It is possible that even in 2.5×10^{-5} mbar of oxygen the YSZ(100) surface will contain a sufficient number of vacancies to partially dewet. Upon intentional introduction of oxygen vacancies through thermal reduction, large clusters, elongated along two perpendicular directions were observed. Consequently future model anode experiments will have to be designed carefully to maintain a surface as close to stoichiometry in order to prevent this large dewetting. This will be necessary especially during catalysis studies in which the sample will have to be raised to high temperature.

The carbon induced reduction of YSZ is possible at low temperatures beginning at 320 °C - 425 °C. This is hypothesized to be especially true if the initial defect structure of YSZ contains a large amount of carbon and oxygen vacancies. The reaction which forms carbide (eq. 5.2) was shown to produce only oxygen as a byproduct, which is then free to desorb from the surface or diffuse into the bulk. Carbide formation seems to be self limited with a terminating layer forming at a coverage of approximately 13 atom %. At only 2 % coverage carbide was shown to alter the electronic structure of the surface with I/V spectroscopy exhibiting curves similar to those of conductive materials.

Upon heating to 400 °C, production of carbide can occur in pressures below approximately 1×10^{-5} mbar, above this pressure oxidation will occur with the carbon atom in the carbide being liberated, and the zirconium atom becoming oxidized. At higher temperatures above about 500 °C in back pressures of O_2 again greater than 1×10^{-5} the liberated carbon is removed from the surface probably as CO_x.

The fully oxidized YSZ(100) surface exhibits, by I/V spectroscopy, a band gap generally greater than the 5.6 eV reported in the literature. The discrepancy between that value and the observed bandgap (> 7eV) perhaps originates from the surface preparation or the STM technique used.

References

1. Nowotny, J., Sorrell, C.C. and Bak, T., *Segregation in zirconia: Equilibrium versus non-equilibrium segregation.* Surface and Interface Analysis, 2005. **37**(3): p. 316.

2. Nowotny, J., Bak, T., Nowotny, M.K. and Sorrell, C.C., *Charge transfer at oxygen/zirconia interface at elevated temperatures - part 2: Oxidation of zirconia.* Advances in Applied Ceramics, 2005. **104**(4): p. 154.

3. Nowotny, J., Bak, T., Nowotny, M.K. and Sorrell, C.C., *Charge transfer at oxygen/zirconia interface at elevated temperatures - part 3: Segregation induced interface properties.* Advances in Applied Ceramics, 2005. **104**(4): p. 165.

4. Anthony E. Hughes, *Segregation in single-crystal fully stabilized yttria-zirconia.* Journal of the American Ceramic Society, 1995. **78**(2): p. 369.

5. G.S.A.M. Theunissen, A.J.A.W., A.J. Burggraaf, *Surface and grain boundary analysis of doped zirconia ceramics studied by AES and XPS.* Journal of Materials Science, 1992. **27**: p. 5057.

6. Hughes, A.E. and Badwal, S.P.S., *Impurity segregation study at the surface of yttria-zirconia electrolytes by XPS.* Solid State Ionics, 1990. **40-1**: p. 312.

7. Hughes, A.E. and Badwal, S.P.S., *Impurity and yttrium segregation in yttria-tetragonal zirconia.* Solid State Ionics, 1991. **46**(3-4): p. 265.

8. Shibata, N., Oba, F., Yamamoto, T., Ikuhara, Y. and Sakuma, T., *Atomic structure and solute segregation of a sigma=3, 110 /{111} grain boundary in an yttria-stabilized cubic zirconia bicrystal.* Philosophical Magazine Letters, 2002. **82**(7): p. 393.

9. Theunissen, G., Winnubst, A.J.A. and Burggraaf, A.J., *Surface and grain-boundary analysis of doped zirconia ceramics studied by AES and XPS.* Journal of Materials Science, 1992. **27**(18): p. 5057.

10. Zhang, Z.M., Nowotny, J., Pigram, P.J., Lamb, R.N., Nakamura, S. and Yamana, K., *XPS study of surface cation segregation in mullite/zirconia composites.* Surface and Interface Analysis, 1996. **24**(9): p. 647.

11. Zhu, J.J., van Ommen, J.G., Knoester, A. and Lefferts, L., *Effect of surface composition of yttrium-stabilized zirconia on partial oxidation of methane to synthesis gas.* Journal of Catalysis, 2005. **230**(2): p. 291.

12. de Ridder, M., van Welzenis, R.G., van der Gon, A.W.D., Brongersma, H.H., Wulff, S., Chu, W.-F. and Weppner, W., *Subsurface segregation of yttria in yttria stabilized zirconia.* Journal of Applied Physics, 2002. **92**(6): p. 3056.

13. Eichler, A. and Kresse, G., *First-principles calculations for the surface termination of pure and yttria-doped zirconia surfaces.* Physical Review B, 2004. **69**(4).

14. Stanek, C.R., Grimes, R.W., Rushton, M.J.D., McClellan, K.J. and Rawlings, R.D., *Surface dependent segregation of* Y_2O_3 *in t-*ZrO_2. Philosophical Magazine Letters, 2005. **85**(9): p. 445.

15. Tanuma, S., Powell, C.J. and Penn, D.R., *Proposed formula for electron inelastic mean free paths based on calculations for 31 materials.* Surface Science Letters, 1987. **192**: p. L849.

16. Tanuma, S., Powell, C.J. and Penn, D.R., *Calculations of electron inelastic mean free paths for 31 materials.* Surface and Interface Analysis, 1988. **11**(11): p. 577.

17. Tanuma, S., Powell, C.J. and Penn, D.R., *Calculations of electron inelastic mean free paths .2. Data for 27 elements over the 50-2000 eV range.* Surface and Interface Analysis, 1991. **17**(13): p. 911.

18. Tanuma, S., Powell, C.J. and Penn, D.R., *Calculations of electron inelastic mean free paths .3. Data for 15 inorganic-compounds over the 50-2000 eV range.* Surface and Interface Analysis, 1991. **17**(13): p. 927.

19. Tanuma, S., Powell, C.J. and Penn, D.R., *Calculations of electron inelastic mean free paths (IMFPs) .4. Evaluation of calculated IMFPs and of the predictive IMFP formula tpp-2 for electron energies between 50 and 2000 eV.* Surface and Interface Analysis, 1993. **20**(1): p. 77.

20. Tanuma, S., Powell, C.J. and Penn, D.R., *Calculations of electron inelastic mean free paths .5. Data for 14 organic-compounds over the 50-2000 eV range.* Surface and Interface Analysis, 1994. **21**(3): p. 165.

21. Tanuma, S., Powell, C.J. and Penn, D.R., *Calculations of electron inelastic mean free paths (IMFPs) .6. Analysis of the Gries inelastic scattering model and predictive IMFP equation.* Surface and Interface Analysis, 1997. **25**(1): p. 25.

22. de Ridder, M., van Welzenis, R.G. and Brongersma, H.H., *Surface cleaning and characterization of yttria-stabilized zirconia.* Surface and Interface Analysis, 2002. **33**(4): p. 309.

23. Moulder, J.F., Stickle, W.F., Sobol, P.E. and Bomben, K.D., *Handbook of x-ray photoelectron spectroscopy*, ed. Chastain, J. and R.C.J. King. 1995: Physical Electronics, Inc.

24. Wikipedia, *Sodium.* www.wikipedia.org, 2008.

25. Simpson, W.C., Wang, W.K., Yarmoff, J.A. and Orlando, T.M., *Photon- and electron-stimulated desorption of O+ from zirconia.* Surface Science, 1999. **423**(2-3): p. 225.

26. Thome, T., Pham Van, L. and Cousty, J., *Evolution of yttria stabilized zirconia (100) surface morphology with temperature.* J. Eur. Ceram. Soc., 2004. **24**: p. 841.

27. Lee, Y.K. and Park, J.W., *Optical properties and stresses of rf magnetron sputtered yttria-stabilized zirconia thin films.* Journal of Materials Science Letters, 1996. **15**(17): p. 1513.

28. Morant, C., Sanz, J.M. and Galan, L., *Ar-ion bombardment effects on* ZrO_2 *surfaces.* Physical Review B, 1992. **45**(3): p. 1391.

29. Miyake, K., Akutsu, K., Yamada, T., Hata, K., Morita, R., Yamashita, M. and Shigekawa, H., *Giant superstructures formed on graphite surface treated with NaOH solutions studied by scanning tunneling microscopy.* Ultramicroscopy, 1998. **73**(1-4): p. 185.

30. Horiguchi, N., Kasuya, A. and Nishina, Y., *Scanning tunneling microscopy of clusters adsorbed on superperiodic lattice of highly oriented pyrolytic graphite.* Surface Review and Letters, 1996. **3**(1): p. 983.

31. Zhang, J.D. and Wang, E.K., *STM investigation of HOPG superperiodic features caused by electrochemical pretreatment.* Journal of Electroanalytical Chemistry, 1995. **399**(1-2): p. 83.

32. Valenzuelabenavides, J. and Delagarza, L.M., *Electronic superstructures on the graphite surface observed by scanning-tunneling-microscopy - an interference model.* Surface Science, 1995. **330**(2): p. 227.

33. Xu, H., Permana, H., Lu, Y. and Ng, K.Y.S., *STM study of Mo growth and induced surface-structure changes on HOPG.* Surface Science, 1995. **325**(3): p. 285.

34. Kuwabara, M., Clarke, D.R. and Smith, D.A., *Anomalous superperiodicity in scanning tunneling microscope images of graphite.* Applied Physics Letters, 1990. **56**(24): p. 2396.

35. Xhie, J., Sattler, K., Ge, M. and Venkateswaran, N., *Giant and supergiant lattices on graphite.* Physical Review B, 1993. **47**(23): p. 15835.

36. Song, Z., Bao, X., Wild, U., Muhler, M. and Ertl, G., *Oxidation of amorphous Ni-Zr alloys studied by XPS, UPS, ISS and XRD.* Applied Surface Science, 1998. **134**(1-4): p. 31.

37. Kato, S., Ozawa, K., Edamoto, K. and Otani, S., *Photoelectron spectroscopy study of the oxidation of ZrC(100).* Japanese Journal of Applied Physics Part 1-Regular Papers Short Notes & Review Papers, 2000. **39**(9A): p. 5217.

38. Edamoto, K., Nagayama, T., Ozawa, K. and Otani, S., *Angle-resolved and resonant photoemission study of the ZrO-like film on ZrC(100).* Surface Science, 2007. **601**(21): p. 5077.

39. Hakansson, K.L., Johansson, H.I.P. and Johansson, L.I., *High resolution core level study of ZrC(100) and its reaction with oxygen.* Phys. Rev. B, 1993. **48**: p. 2623.

40. Hwu, H.H. and Chen, J.G.G., *Surface chemistry of transition metal carbides.* Chemical Reviews, 2005. **105**(1): p. 185.

41. Dash, L.K., Vast, N., Baranek, P., Cheynet, M.C. and Reining, L., *Electronic structure and electron energy-loss spectroscopy of ZrO_2 zirconia.* Physical Review B, 2004. **70**(24).

42. Orera, V.M., Merino, R.I., Chen, Y., Cases, R. and Alonso, P.J., *Intrinsic electron and hole defects in stabilized zirconia single-crystals.* Physical Review B, 1990. **42**(16): p. 9782.

43. PaiVerneker, V.R., Petelin, A.N., Crowne, F.J. and Nagle, D.C., *Color-center-induced band-gap shift in yttria-stabilized zirconia.* Physical Review B, 1989. **40**(12): p. 8555 LP

44. Morinaga, M., Adachi, H. and Tsukada, M., *Electronic-structure and phase-stability of ZrO_2.* Journal of Physics and Chemistry of Solids, 1983. **44**(4): p. 301.

45. Abousekkina, M.M., *Further-studies on sintering characteristics of zirconium dioxide.* Indian Journal of Physics and Proceedings of the Indian Association for the Cultivation of Science-Part A, 1978. **52**(3): p. 244.

46. Frandon, J., Brousseau, B. and Pradal, F., *Electronic excitations in some transition-metals and their oxides - characteristic energy-loss measurements up to 50 eV.* Physica Status Solidi B-Basic Research, 1980. **98**(1): p. 379.

47. Esch, F., Fabris, S., Zhou, L., Montini, T., Africh, C., Fornasiero, P., Comelli, G. and Rosei, R., *Electron localization determines defect formation on ceria substrates.* Science, 2005. **309**(5735): p. 752.

48. Ganduglia-Pirovano, M.V., Hofmann, A. and Sauer, J., *Oxygen vacancies in transition metal and rare earth oxides: Current state of understanding and remaining challenges.* Surface Science Reports, 2007. **62**(6): p. 219.

6. Summary and Outlook

Yttria Stabilized Zirconia is an extremely dynamic system characterized by complicated defect surface layer composed of oxygen vacancies and impurities. Variation in the defect layer from sample to sample provides a serious source of irreproducibility for model catalyst studies since such variation has been shown to modify the growth mechanism of metal deposited through e-beam evaporation. The origin of the variability is proposed to result from the chemical and mechanical polishing technique used to prepare the surface by the crystal manufacturer. This process is believed to impregnate the surface region with oxygen vacancies, and carbon in concentrations that differ between samples. The presence of oxygen vacancies modifies the lattice geometry inducing strain between defective and non-defective layers that result in surface reconstruction and self-organization at elevated temperatures when the kinetic hindrance to diffusion is lifted. Depending on the size of the defect layer a host of complicated topographies may result. Sputtering and/or thermal annealing in air may drive the surface towards a specific equilibrium structure composed simple steps and terraces, however the conditions under which the such a topography may be obtained will depend strongly upon the starting point.

Imaging of a bulk YSZ(100) single crystal surface has been achieved for the first time by scanning tunneling microscopy in ultra high vacuum. Heating the crystal to elevated temperatures nearing 300 °C produces a sufficient increase in electronic conductivity so that the tunneling current may be dissipated. Studies combining STM and x-ray photoelectron spectroscopy have provided characterization of surface impurities, as well as methods to eliminate them through thermal oxidation at pressures greater than 1.0×10^{-5} mbar near

900 °C to 1000 °C. High temperature oxidation leads to sample smoothing though not to the extent of atomic corrugation. Such surfaces appear very prone to tip induced reconstruction, likely through reduction. Some surfaces which may be only slightly reduced exhibit an entire surface coverage in dewet clusters that appear to be less prone to further reconstruction upon interaction with an STM tip. With the introduction of an even greater concentration of oxygen vacancies through thermal reduction, catastrophic dewetting will occur. Particle formation of up to several nanometres in height has been observed. These particles self organize along preferential directions similar to features seen in ambient studies.

Near future studies should involve further characterization of the dewetting pathway. Initially producing a clean and nominally flat surface through thermal oxidation subsequent imaging can be performed at various stages of reduction. This should also be performed in the combinations of gases which would be used for model catalyst studies. Such catalysis studies should initially involve the oxidation of methane since this reaction is similar to the one which occurs at the solid oxide fuel cell anode (running on methane of course). Catalytic metal such as nickel or palladium, may be deposited in clean and oxidized type 1 YSZ surfaces, and temperature programmed desorption of methane may be performed to examine ad/desorption energies. Reaction studies may also be undertaken and it would be relevant to compare results on clean surfaces to those which are covered in impurity segregants. Since real systems all contain impurities this would help bridge the complexity gap between real and model systems.

Appendix A
Novel Work

During my PhD studies I have co-authored several peer review publications:

1) R.G.Green, J.B.Giorgi. Scanning Tunneling Microscopy of YSZ(100) *Surface Science.* **2009**, *In Preparation.*

2) M.A.Brown, R.G.Green, J.B. Giorgi, J.C.Heminger. AFM Studies of the Evolution of Oxidized KI in Ultra-Thin films of Water. **2009**, *In Preparation.*

3) C.M. Grgicak, R.G. Green, J.B.Giorgi. SOFC Anodes for Direct Oxidation of Hydrogen and Methane Fuels Containing H2S. *Journal of Power Sources.* **2008,** *179, 317-328.*

4) R.G. Green, L. Barré, J.B. Giorgi. Nano-Structures on the Surface of YSZ: Implications for Metal Deposition Experiments. *Surface. Science.* **2007**, 601, 792-802.

5) Tsyganok, P.J.E. Harlick, R.G. Green, J.B. Giorgi and A. Sayari. Non-oxidative Dehydrogenation of Ethane to Ethylene over Chromium Catalysts Prepared from Layered Double Hydroxide Precursors. *Catal. Commun.* **2007** 8 (12): 2186-2193.

6) C.M. Grgicak, R.G. Green, J.B.Giorgi. Control of Microstructure, Sinterability and Performance in Ni-YSZ, Cu-YSZ and Co-YSZ SOFC Anodes. *J. Mater. Chem.* **2006**, 16, 885-897.

7) C.M. Grgicak, R.G. Green, W.F. Du, J.B.Giorgi. Synthesis and Characterisation of NiO-YSZ Anode Materials: Precipitation, Calcination and the Effects on Sintering. *J. Am. Ceram. Soc.* **2005**, 88, 3081-3087.

My Contribution:

1: Near completion and will be submitted shortly it contains aspects of chapters 4 and 5. This will be the first published record in which scanning tunneling microscopy is used to study the surface of a bulk YSZ single crystal. I performed all work related to this publication

2: Derived from a collaboration with Matthew Brown from Prof. Heminger's group at UC Irvine. For this work I examined the surface modification of ozone treated KI single crystals under exposure to water vapour by XPS and FM-AFM in our UHV chamber. This publication is completed and awaiting final approval before submission.

3: A result of continuing work with Catherine Grgicak from our lab, this publication studied the catalytic properties of the anode of a real working solid oxide fuel cell in different fuels containing H_2S. All the experiments were performed on a real fuel cell setup that I designed and built, I also studied the reaction byproducts on postmortem anodes by XPS.

4: Paper number 4 represents the first statistical investigation of the YSZ(100) surface, and the first to study the effect of such defective topographies on sub-monolayer coverages of deposited metal. The content of this work relates largely to chapter 3. I performed all work related to this publication.

5: Derived from collaboration with the Sayari lab at the University of Ottawa in which a new series of catalysts were designed and tested by a host of techniques. For this work I examined a selection of this series by XPS and analyzed the results. XPS proved to be very valuable in confirming and expanding on results from other techniques.

6: This was the first work to use the fuel cell that I designed and built which continues to used by most members of our group

7: In this study the synthesis conditions were related to subsequent material properties. I performed the high temperature XRD setup and developed the methodology to correct for thermal and instrumental effects in the resulting data.